

The application of single specimen foraminiferal isotope analyses to investigate seasonality in the Southern Ocean

Anna Dora Mikis



Thesis submitted for the Degree of Doctor of Philosophy
Cardiff University

September 2017

Summary

The Antarctic Peninsula and the surrounding Southern Ocean are some of the most climatically sensitive regions on Earth. The West Antarctic Peninsula (WAP) experienced a $\sim 3.4^{\circ}\text{C}$ warming during the 20th century which was accompanied by widespread glacial melting. In contrast, 21st century air temperature records in the northern Antarctic Peninsula show a decreasing trend indicating large scale natural decadal-scale climate variability at that location. Atmospheric and oceanographic variability in the WAP have also been observed in Holocene climate records showing variable meltwater discharge relating to the frequency of La Niña events and summer insolation during the late Holocene.

Single specimen foraminiferal isotope analysis has been successfully used to study changes in seasonal variability in the tropical regions relating to El Niño-Southern Oscillation (ENSO). In this thesis, I investigate the applicability of this method to study seasonal changes in environmental conditions in the high latitudes over a range of timescales.

In the Scotia Sea, a modern record of the polar foraminifera species, *Neogloboquadrina pachyderma*, shows temperature related distribution and $\delta^{18}\text{O}$ signature, the presence of multiple morphotypes, as well as variable calcification depths and vital offsets related to biological processes and as determined by the single specimen isotope analysis. A six-year long sediment trap-derived *Neogloboquadrina pachyderma* record of abundance, morphology, and single specimen $\delta^{18}\text{O}$ showed that all these parameters are driven by seasonal changes in sea ice concentration and food availability - relating to chlorophyll α concentration and sea surface temperature - at the Antarctic Peninsula. The *Neogloboquadrina pachyderma* record highlights inter-annual variability, relating to the teleconnections between ENSO/Southern Annular Mode and the high latitude atmospheric setting, proving its suitability to investigate seasonality changes. Finally, in the Scotia Sea, single specimen *Globorotalia inflata* $\delta^{18}\text{O}$ record displayed variability during the Holocene relating to changes in Antarctic Intermediate source waters in the Southern Ocean.

DECLARATION

This work has not been submitted in substance for any other degree or award at this or any other university or place of learning, nor is being submitted concurrently in candidature for any degree or other award.

Signed (candidate) Date

STATEMENT 1

This thesis is being submitted in partial fulfillment of the requirements for the degree of Doctor of Philosophy

Signed (candidate) Date

STATEMENT 2

This thesis is the result of my own independent work/investigation, except where otherwise stated, and the thesis has not been edited by a third party beyond what is permitted by Cardiff University's Policy on the Use of Third Party Editors by Research Degree Students. Other sources are acknowledged by explicit references. The views expressed are my own.

Signed (candidate) Date

STATEMENT 3

I hereby give consent for my thesis, if accepted, to be available online in the University's Open Access repository and for inter-library loan, and for the title and summary to be made available to outside organisations.

Signed (candidate) Date

STATEMENT 4: PREVIOUSLY APPROVED BAR ON ACCESS

I hereby give consent for my thesis, if accepted, to be available online in the University's Open Access repository and for inter-library loans **after expiry of a bar on access previously approved by the Academic Standards & Quality Committee.**

Signed (candidate) Date

“All we have to decide is what to do with the time
that is given to us.”

J. R. R. Tolkien

Acknowledgements

I would begin by thanking my main supervisor, Jenny Pike for her continuous support, guidance, and encouragement not only during the past four years of this PhD but during my undergraduate degree as well. I would also like to thank Vicky Peck and Kate Hendry for giving me the opportunity to work on this project and for helping to find solutions whenever a problem arose. I am also very grateful to Mike Meredith for all the time he has given, and to Melanie Leng for supporting my isotope work.

I am very grateful to Hugh Ducklow, Deborah Steinberg, and Sharon Stammerjohn for sharing their samples and their data, which ultimately allowed me to complete this thesis. I would also like to thank Frank Peeters and Suzan Verdegaal – Warmerdam at VU, Amsterdam for the isotope measurements, as well as Hilary Sloane at NERC Isotope Geoscience Laboratory for the additional isotope measurements. My thanks also goes to the Antarctic Science International Bursary for awarding me with a grant that enabled me to carry out most of the isotope analysis. I am also grateful to Dani Schmidt at Bristol and Kirsty Edgar, now in Birmingham, for allowing and helping me to work in their facilities to complete the morphometric analysis, and for extensive discussions that led me to understand all that the data could reveal. I would also like to thank Dani and Kirsty for fuelling my scientific curiosity and inspiring me to dig deeper into the science. Additionally, I am also grateful to the British Antarctic Survey for enabling me to take part in the BAS scientific cruise JR304 aboard the RRS James Clark Ross. I would like to thank the research staff and the crew for helping me to collect vital samples as well as for making the cruise a truly enjoyable once in a lifetime experience.

I am forever grateful to the paleoclimate group in Cardiff for all their support, in particular to Paola, for all her guidance, advice, and scientific discussions. I would like to thank my past and present office mates for providing endless discussions both about science and everyday life. Particularly, thanks to Freya, Amy, Hennie, Micky, Elaine, Kim, Steph, and Rachel for all your support, for being wonderful friends, and making these last four years so memorable. I would also like to thank Emmanuela, Sophie, and Bethan for all their support too. Special thanks go to Kim and Steph who helped me get through the most difficult times, for being amazing people, teaching me how to unwind during stressful times, and for letting me crash with them whenever I was in Bristol.

I would like to thank Louise for being a great friend who has always been there to listen and have some cake and tea when needed. Most of all, I am hugely grateful to Paul for his love and support, and for always being ready with a cwtch. Finally, I would like to thank my family for teaching and encouraging me to forever expand my knowledge.

Commonly used symbols and Abbreviations

| | |
|-----------------------------------|---|
| ACC | Antarctic Circumpolar Current |
| AAIW | Antarctic Intermediate Water |
| AASW | Antarctic Surface Water |
| AAWW | Antarctic Winter Water |
| Chl α | Chlorophyll α concentration |
| $\delta^{18}\text{O}_{\text{np}}$ | <i>Neogloboquadrina pachyderma</i> oxygen isotope |
| $\delta^{18}\text{O}_{\text{eq}}$ | Equilibrium $\delta^{18}\text{O}$ |
| EH | Early Holocene |
| ENSO | El Niño-Southern Oscillation |
| G. inflata | <i>Globorotalia inflata</i> |
| LCDW | Lower Circumpolar Deep Water |
| LH | Late Holocene |
| MD | Maximum diameter |
| Np | <i>Neogloboquadrina pachyderma</i> |
| PCA | Principal Component Analysis |
| PF | Polar Front |
| SACCF | Southern ACC Front |
| SAF | Subantarctic Front |
| SAM | Southern Annular Mode |
| SAMW | Subantarctic Mode Water |
| SB | Southern Boundary Front of the ACC |
| SIC | Sea Ice Concentration |
| SST | Sea Surface Temperature |
| TZW | Transition Zone Water |
| UCDW | Upper Circumpolar Deep Water |
| WAP | West Antarctic Peninsula |

Table of contents

| | |
|---|-----------|
| 1. Introduction | 1 |
| 1.1. Climate variability in the southern high latitudes..... | 1 |
| 1.2. Single specimen stable isotope analysis of planktonic foraminifera..... | 3 |
| 1.3. Aims and Objectives | 5 |
| 1.4. Outline of the Thesis | 7 |
| 2. Regional Setting and Oceanography | 9 |
| 2.1. Scotia Sea | 9 |
| 2.1.1. Modern Oceanography | 9 |
| 2.2. Western Antarctic Peninsula | 13 |
| 2.2.1. Glacial setting..... | 13 |
| 2.2.2. Oceanography | 14 |
| 2.2.3. Atmospheric setting | 15 |
| 2.3. Atmospheric teleconnections between the southern high latitudes and the tropics | 16 |
| 2.3.1. El Niño-Southern Oscillation..... | 16 |
| 2.3.2. Southern Annular Mode | 18 |
| 3. Background information on proxies | 21 |
| 3.1. Planktonic foraminifera..... | 21 |
| 3.1.1. Foraminifera life cycle and ontogeny | 21 |
| 3.1.2. <i>Neogloboquadrina pachyderma</i> (Ehrenberg, 1861) | 22 |
| 3.1.3. <i>Globorotalia inflata</i> (d’Orbigny, 1839b) | 25 |
| 3.2. Foraminifera morphology | 27 |
| 3.3. Stable isotopes | 29 |
| 3.3.1. Seawater stable isotopes..... | 29 |
| 3.3.1.1. <i>Oxygen isotopes</i> | 29 |
| 3.3.1.2. <i>Carbon isotopes</i> | 30 |
| 3.3.2. Stable isotopes of foraminifera | 32 |
| 3.3.2.1. <i>Neogloboquadrina pachyderma</i> | 32 |
| 3.3.2.2. <i>Globorotalia inflata</i> | 34 |
| 4. Materials and Methods | 35 |
| 4.1. JR304 cruise materials and methods | 35 |
| 4.1.1. Sampling for foraminifera..... | 36 |
| 4.1.2. Water column profiling | 38 |
| 4.1.3. Seawater stable isotope analysis | 39 |

| | |
|---|-----------|
| 4.1.4. <i>Neogloboquadrina pachyderma</i> stable isotope analysis | 40 |
| 4.1.5. Predicting equilibrium $\delta^{18}\text{O}$ value of calcite | 41 |
| 4.2. PAL-LTER Time series | 42 |
| 4.2.1. <i>Neogloboquadrina pachyderma</i> flux measurements | 43 |
| 4.2.2. Measurements of morphology | 48 |
| 4.2.2.1. <i>Automated image acquisition</i> | 48 |
| 4.2.2.2. <i>Manual image acquisition</i> | 51 |
| 4.2.3. Stable isotope analysis | 52 |
| 4.2.4. Predicting the equilibrium $\delta^{18}\text{O}$ value of calcite | 52 |
| 4.2.5. Environmental parameters | 53 |
| 4.3. Falkland Plateau sediment core | 54 |
| 4.3.1. Stable isotope analysis of <i>Globorotalia inflata</i> | 55 |
| 5. Results and Discussion | 59 |
| 5.1. <i>Neogloboquadrina pachyderma</i> abundance, stable isotope composition, vital effects, and calcification depth variability in the Scotia Sea: results from vertical plankton hauls | 59 |
| 5.1.1. Oceanographic setting | 59 |
| 5.1.1.1. <i>Temperature profiles</i> | 60 |
| 5.1.1.2. <i>Salinity profiles</i> | 63 |
| 5.1.1.3. <i>Fluorescence and density profiles</i> | 63 |
| 5.1.2. <i>Neogloboquadrina pachyderma</i> abundance in the Scotia Sea | 64 |
| 5.1.2.1. <i>Neogloboquadrina pachyderma</i> morphotypes | 67 |
| 5.1.3. <i>Neogloboquadrina pachyderma</i> stable isotopic signatures and water column $\delta^{18}\text{O}$ gradients | 70 |
| 5.1.3.1. <i>Neogloboquadrina pachyderma</i> oxygen isotopic ratios | 70 |
| 5.1.3.2. <i>Neogloboquadrina pachyderma</i> carbon isotopic ratios | 72 |
| 5.1.3.3. <i>Seawater $\delta^{18}\text{O}$ trends</i> | 74 |
| 5.1.4. Foraminiferal and seawater oxygen isotopes: equilibrium, vital effects, and calcification depths | 75 |
| 5.1.4.1. <i>Relationships between $\delta^{18}\text{O}_{\text{sw}}$ and salinity in the Scotia Sea</i> | 75 |
| 5.1.4.2. <i>Neogloboquadrina pachyderma</i> shell weight vs $\delta^{18}\text{O}_{\text{np}}$: impact of size on oxygen isotope ratio | 75 |
| 5.1.4.3. <i>Exploration of vital effects during isotope fractionation by Neogloboquadrina pachyderma in the Scotia Sea</i> | 78 |
| 5.1.5. Summary and Conclusion | 83 |
| 5.2. Seasonal variability of <i>Neogloboquadrina pachyderma</i> abundance, morphology, and stable isotope composition at the West Antarctic Peninsula | 85 |

| | |
|---|-----|
| 5.2.1. Statistical methods for data analysis | 86 |
| 5.2.1.1. Spearman's rank correlation coefficient..... | 86 |
| 5.2.1.2. Interquartile range..... | 87 |
| 5.2.1.3. Mann-Whitney U-test | 87 |
| 5.2.1.4. Levene's test for Equality of Variances..... | 87 |
| 5.2.1.5. Principal Component Analysis | 88 |
| 5.2.1.6. Anderson-Darling test for normality | 88 |
| 5.2.1.7. Redundancy Analysis | 89 |
| 5.2.2. Assessment of <i>Neogloboquadrina pachyderma</i> flux, morphology, and stable isotope chemistry from a six year-long time series | 89 |
| 5.2.2.1. Physical properties and seasonality at Palmer Deep | 89 |
| 5.2.2.2. <i>Neogloboquadrina pachyderma</i> flux between 2006 and 2013 | 90 |
| 5.2.2.3. The morphological variability of <i>Neogloboquadrina pachyderma</i> at Palmer Deep..... | 97 |
| 5.2.2.4. <i>Neogloboquadrina pachyderma</i> stable isotopes..... | 116 |
| 5.2.3. A typical year at Palmer Deep | 125 |
| 5.2.3.1. Phase 1 – Winter sea ice season | 126 |
| 5.2.3.2. Phase 2 – Sea ice break up season..... | 126 |
| 5.2.3.3. Phase 3 – Summer season..... | 128 |
| 5.2.3.4. Phase 4 – Late summer season | 128 |
| 5.2.3.5. Phase 5 – Autumn season..... | 129 |
| 5.2.3.6. Phase 6 – Early winter season | 129 |
| 5.2.4. Annual flux patterns: What controls foraminiferal flux in the high latitudes? | 129 |
| 5.2.4.1. Inter-annual variability in <i>Neogloboquadrina pachyderma</i> shell flux..... | 131 |
| 5.2.5. The role of environmental variability on <i>Neogloboquadrina pachyderma</i> shell size and morphology | 132 |
| 5.2.5.1. Morphotypes of <i>Neogloboquadrina pachyderma</i> | 132 |
| 5.2.5.2. <i>Neogloboquadrina pachyderma</i> morphological variability and the role of environmental parameters | 133 |
| 5.2.6. <i>Neogloboquadrina pachyderma</i> calcification and stable isotope variability | 135 |
| 5.2.6.1. Depth and seasonality of calcification..... | 136 |
| 5.2.6.2. Intra- and inter-annual variability in <i>Neogloboquadrina pachyderma</i> $\delta^{18}\text{O}$ | 138 |
| 5.2.7. Seasonal variability of <i>Neogloboquadrina pachyderma</i> $\delta^{18}\text{O}$ derived from single specimen analysis | 140 |
| 5.2.7.1. Relationship between <i>Neogloboquadrina pachyderma</i> size and single specimen stable isotopes | 144 |
| 5.2.8. Exceptional <i>Neogloboquadrina pachyderma</i> flux event of 2010: What is the role of the Southern Annular Mode and the El Niño-Southern Oscillation..... | 146 |
| 5.2.8.1. Variability in sea ice advance and retreat due to Southern Annular Mode and El Niño-Southern Oscillation | 147 |

| | |
|---|------------|
| 5.2.8.2. <i>Recent trends in wind-driven sea ice variability in the Palmer region</i> | 148 |
| 5.2.9. Synthesis and Conclusion..... | 152 |
| 5.3. Investigating intermediate water mass variability in the Southern Ocean during the Holocene..... | 157 |
| 5.3.1. Comparison of paired and single specimen <i>Globorotalia inflata</i> | 157 |
| 5.3.2. Single specimen stable isotope record of the Holocene..... | 162 |
| 5.3.2.1. <i>Single specimen oxygen isotope record</i> | 163 |
| 5.3.2.2. <i>Single specimen carbon isotope record</i> | 165 |
| 5.3.3. <i>Globorotalia inflata</i> stable isotope variability during the Holocene | 167 |
| 5.3.4. <i>Globorotalia inflata</i> as an Antarctic Intermediate Water proxy species | 168 |
| 5.3.5. Does <i>Globorotalia inflata</i> stable isotope variability reflect changes in local or regional environmental conditions? | 172 |
| 5.3.6. Temperature- and size-dependency in single specimen <i>Globorotalia inflata</i> $\delta^{18}\text{O}$ measurements..... | 174 |
| 5.3.7. The role of biological and chemical processes on <i>Globorotalia inflata</i> $\delta^{13}\text{C}$ | 177 |
| 5.3.8. A changing regime of Antarctic Intermediate Water sources during the Holocene | 179 |
| 5.3.8.1. <i>SAMW variability and its impact on AAIW properties and <i>Globorotalia inflata</i> $\delta^{18}\text{O}$ due to Holocene climate variability in the Southeast Pacific</i> | 181 |
| 5.3.8.2. <i>AAWW variability and its impact on AAIW properties and <i>Globorotalia inflata</i> $\delta^{18}\text{O}$ due to Holocene climate variability at the Antarctic Peninsula and South Atlantic</i> | 184 |
| 5.3.9. Summary and Conclusion..... | 186 |
| 6. Conclusions and Recommendations..... | 189 |
| 6.1. <i>Neogloboquadrina pachyderma</i> abundance, stable isotope composition, vital effects, and calcification depth variability in the Scotia Sea: results from vertical plankton hauls..... | 189 |
| 6.2. Seasonal variability of <i>Neogloboquadrina pachyderma</i> abundance, morphology, and stable isotope composition at the West Antarctic Peninsula | 191 |
| 6.3. Investigating intermediate water mass variability in the Southern Ocean during the Holocene..... | 193 |
| 6.4. Recommendations to improve methods | 194 |
| 7. References | 197 |
| Appendix | 217 |

1. Introduction

1.1 Climate variability in the southern high latitudes

Antarctica and the surrounding Southern Ocean are one of the most climatically sensitive regions on the planet, with certain areas experiencing some of the most rapid warming observed globally in recent decades. The West Antarctic Peninsula (WAP) experienced a $\sim 3.4^{\circ}\text{C}$ warming during the 20th century (Vaughan et al., 2003), which is approximately five times the global average of $0.6 \pm 0.2^{\circ}\text{C}$ identified by the Intergovernmental Panel on Climate Change for the same period (Houghton et al., 2001). A similar, higher rate of warming was observed in West Antarctica, where the region around the Amundsen Sea experienced a $2.4 \pm 1.2^{\circ}\text{C}$ warming between 1958 and 2010 (Bromwich et al., 2013). The atmospheric warming was accompanied by increased glacier melting; 84% of 244 tidewater and marine glacier fronts experienced melting between 1945 and 2005 (Cook et al., 2005). The flow rate of these melting glaciers has increased by approximately 12% between 1992 and 2005 due to frontal thinning related to the increased oceanic temperatures (Pritchard and Vaughan, 2007, Pritchard et al., 2012). The increased glacial melting along the Antarctic Peninsula has been shown to be the result of warm and warming Circumpolar Deep Water at mid-depths (Cook et al., 2016). Together, the rate and extent of the recent glacial melting experienced along the WAP is unparalleled for the past 120 years (Hendry and Rickaby, 2008).

In contrast to the 20th century warming, 1999-2014 surface air temperature records from northern Antarctic Peninsula stations show decreasing trends ($-0.47 \pm 0.25^{\circ}\text{C}$ per decade), especially during austral summer. The decreasing surface air temperature has been the result of a strengthening of the midlatitude jet that drives cold, southeasterly winds over the Peninsula more frequently (Turner et al., 2016). The variability between the 20th and 21st centuries have been shown to be within the boundaries of large natural decadal-scale climate variability at this location.

The variability in atmospheric processes observed along the Antarctic Peninsula and further afield can have considerable impact on the Antarctic marine ecosystem, from top predators to phytoplankton (Clarke et al., 2007; Ducklow et al., 2012) and on oceanographic processes (e.g. Matthews and Meredith, 2004; Meredith et al., 2008; Stammerjohn et al., 2008b; Meredith et al., 2016). Long-term records show that the sea ice season over the Antarctic Peninsula shelf area decreased by 30-40 days in 1992-2004 compared to 1979-1991 in response to changing atmospheric processes (Stammerjohn et al., 2008b). Additionally, lower number of sea ice days between 1998

and 2001 compared to the 1992-1997 period were associated with persistent northerly winds deriving from sustained La Niña and positive Southern Annular Mode conditions (Massom et al., 2006; Stammerjohn et al., 2008a). Variable sea ice melt and glacial meltwater distribution along the West Antarctic Peninsula between 2011 and 2014 have also been shown to be strongly linked to regional wind forcing related to the Southern Annular Mode and the El Niño-Southern Oscillation (Meredith et al., 2016). A multidecadal record of phytoplankton abundance has shown that a five-fold interannual variability in annual peak chlorophyll concentrations are strongly related to wind forcing (Ducklow et al., 2012), and that a factor of two decline between 1979 and 2006 in the northern parts of the West Antarctic Peninsula is most likely due to an up to 60% increase in surface winds in that time period (Montes-Hugo et al., 2009). Concurrently, the southern regions of the West Antarctic Peninsula experienced increasing phytoplankton biomass by up to 66%, driven by periods of low sea ice concentrations, wind, and cloud cover (Montes-Hugo et al., 2009). The Antarctic coastal shelf waters, including the West Antarctic Peninsula, serve as important atmospheric CO₂ sinks through the high rates of primary production (Arrigo et al., 2008). As a result, the high rates of interannual spatial variability of primary production could have significant impact on the drawdown of atmospheric CO₂.

Variability in the atmospheric and oceanographic conditions in the southern polar regions have been observed during the Holocene period, similarly to modern times. A record of oxygen isotope composition of marine diatoms deriving from a sediment core at Palmer Deep, West Antarctic Peninsula has identified variations in glacial meltwater fluxes (Swann et al., 2013, Pike et al., 2013). These variations in the glacial meltwater flux were related to the increasing frequency of La Niña events and increasing summer insolation during the late Holocene (Pike et al., 2013). Additionally, ocean-driven frontal melting of glaciers was linked to meltwater discharge during the mid to late Holocene (Pike et al., 2013). Further south along the WAP, in Marguerite Bay, a multi-proxy sediment record (including foraminifera) highlighted the intermittent upwelling of Upper Circumpolar Deep Water (UCDW) onto the continental shelf during the late Holocene which was most likely the result of an enhanced sensitivity to ENSO forcing (Peck et al., 2015). The periodic incursion of UCDW is the most likely explanation for the intermittent melting and freezing of sea ice indicated by the multiproxy record. In comparison, weakened UCDW upwelling during the early to mid Holocene was the result of the northward movement of the Southern Westerly Winds and resulted in decreased primary productivity compared to the early Holocene (Peck et al., 2015). In order to better constrain the relationship between frontal melting of glaciers, sea ice patterns, upwelling of UCDW onto the

continental shelves and atmospheric variability during the Holocene, high resolution records need to be studied with proxies, such as single specimen foraminiferal stable isotopes, that allow for the examination of past seasonal variability in the region.

1.2 Single specimen stable isotope analysis of planktonic foraminifera

Foraminifera are single celled marine zooplankton that secrete a calcite test and either float in the water column at various depths (planktonic) or live on or within the seafloor sediment (benthic) (Hemleben et al., 1988). They have long been used to study past climate variability thanks to their calcite shell and their ubiquity in the world ocean (Ravelo and Hillaire-Marcel, 2007). The first stable isotope measurement of a foraminifera for paleoclimate reconstruction was undertaken by Cesare Emiliani (Ravelo and Hillaire-Marcel, 2007) who used the oxygen isotope of foraminiferal calcite to reconstruct glacial-interglacial climate variability during the Pleistocene (Emiliani 1955). The development of opening and closing plankton nets (e.g. Bé 1962) enabled studies to investigate the modern distribution of foraminifera species, linking them with specific environmental conditions (e.g. Bé, 1969; Tolderlund and Bé, 1971; Boltovskoy, 1971; Fairbanks et al., 1980; Boltovskoy et al., 1996). Furthermore, the use of piston and gravity cores from the 1960s onwards allowed the study of past foraminifera distribution and stable isotope composition and thus the study of past climates (e.g. Kennett, 1968; CLIMAP, 1976; Boltovskoy, 1994).

The investigations of past climate variability utilising the oxygen and carbon isotope signature of foraminiferal calcite over the last 60 years were accompanied by an increasing number of studies examining the biological controls on foraminifera test size, shell development, reproduction, habitat, calcification depths, and stable isotope composition (e.g. Hemleben et al., 1977; Spindler et al., 1978; Ketten and Edmond, 1979; Spindler et al., 1979; Bé, 1980; Brummer et al., 1986; Spero and Lea, 1993; Spero et al., 1997). Often, these studies utilised laboratory culture experiments of planktonic foraminifera (e.g. Bé and Spero, 1981; Spero, 1987; 1992; Lea et al., 1995; Bemis et al., 1998; 2000). The abundance of investigations into foraminiferal biology, abundance, habitat, and stable isotope compositions have allowed researchers to develop highly effective proxies for paleoclimate research.

Traditionally, studies that used the stable isotope signature of foraminiferal calcite to infer past climate variability combined and crushed a number of foraminifera tests (20-40) from one sediment sample to produce a single homogenous foraminifera sample for

stable isotope analysis. Each centimetre of a sediment core, and thus an assemblage of foraminifera from which the 20-40 tests are picked, spans a large temporal range. As a result, the single stable isotope value obtained from the amalgamation of the tests is an average of the environmental conditions recorded by the foraminifera. Coincidentally, short duration events (e.g. periodic meltwater input to coastal regions), as well as seasonal and interannual variability are masked by the average environmental signal. With improvements in technology it has become possible to analyse single specimens of foraminifera for their stable isotope ratio to reveal past short-term events and changes in seasonal and interannual configuration of oceanography.

Single specimen foraminiferal stable isotope analysis has been commonly used during the past 20 to 30 years to study variability in oceanographic conditions on seasonal timescales in the low latitude regions (e.g. Spero and Williams, 1990; Koutavas et al., 2006; Wit et al., 2010; Ganssen et al., 2011; Feldmeijer et al., 2013; Ford et al., 2015; Metcalfe et al., 2015). One of the earliest single specimen studies (Spero and Williams, 1990) utilised *Orbulina universa*, a large (>500 µm) and heavy (~30µg) planktonic foraminifera, that secretes a terminal spherical chamber around the entire test during the last 3-5 days of its life cycle making it suitable for studying short-term environmental events. Between 11 and 35 individual specimens were individually analysed for stable isotopes from sediment samples. The single specimen stable isotope analysis identified the periodic presence of low-salinity surface waters at the end of the last glacial period (~11.8 ka BP) and during the end of the Younger Dryas (~9.5 ka BP) most likely as a result of meltwater input to the Gulf of Mexico (Spero and Williams, 1990). This early single specimen stable isotope study highlights the suitability of the method for the assessment of seasonal or periodic introduction of meltwater into surface waters as result of short-term climate variability.

The majority of recent single specimen studies utilised the proxy to investigate variability in the El Niño-Southern Oscillation during the Holocene (Koutavas et al., 2006; Leduc et al., 2009; Khider et al., 2011; Koutavas and Joanides, 2012), or earlier time periods (Leduc et al., 2009; Scroxton et al., 2011; Koutavas and Joanides, 2012; Ford et al., 2015). Other studies have employed the method to investigate more regional seasonal changes, such as seasonal variability in the Central Mediterranean during prominent climate events of the Holocene (Goudeau et al., 2015) and sea surface temperature ranges in the Arabian Sea during the last 20 ka (Ganssen et al., 2011). Single specimen foraminiferal stable isotopes have also been used to gain greater insight into the role of environmental changes and hydrography on specific species' habitat preferences and calcification patterns (Metcalfe et al., 2015; Steinhardt et al., 2015).

Paleoclimate studies of Southern Ocean marine sediments routinely utilise siliceous microfossils, such as diatoms, due to their high abundance in surface waters (e.g. Leventer et al., 1993; Taylor and McMinn, 2001; Taylor et al., 2001; Leventer et al., 2006; Heroy et al., 2007; Allen et al., 2011; Shevenell et al., 2011; Etorneau et al., 2013; Pike et al., 2013). Diatom assemblage studies can reveal variability in primary production and sea ice; however, the stable isotope analysis of these siliceous organisms is still technologically challenging, leading to only a handful of direct assessments of sea ice and glacial meltwater variability using this proxy (e.g. Panizzo et al., 2013; Pike et al., 2013; Swann et al., 2013; Abelmann et al., 2015). Stable isotope analysis of the dominant planktonic foraminifera in the polar waters, *Neogloboquadrina pachyderma*, has been utilised in the past to study climate variability in the Holocene (e.g. Matsumoto et al., 2001; Peck et al., 2015) and in glacial times (e.g. Vautravers et al., 2013; Benz et al., 2016). High resolution, single specimen stable isotope analysis of *Neogloboquadrina pachyderma* could potentially enable us to bridge the gap in our understanding of the impact of seasonal variability of UCDW upwelling and of large-scale atmospheric processes, such as ENSO and SAM on past glacial meltwater and sea ice patterns along the West Antarctic Peninsula.

1.3 Aims and Objectives

The original aim of the study was to investigate changes in seasonality in the Southern Ocean and around the West Antarctic Peninsula using single specimen stable isotope analysis of a single species, *Neogloboquadrina pachyderma* (Np). Through this approach, constraints and region-specific information would have been developed on the single specimen stable isotope method by assessing living and recently alive specimens with co-located environmental parameters. The information derived from this study would then have been used in an assessment of seasonal and interannual variability over a longer timescale, made possible by a time-series sediment trap. This would have revealed how the surface water signal travels through the water column, and provided a picture on how an annual signal might get built up in the sediment. Finally, the lessons learnt in the two modern studies would have been applied to data derived from a high resolution sediment core to provide a rounded assessment of seasonal variability over long timescales (hundreds or thousands of years). However, the sediment core specified for this study experienced geochemical changes post-recovery which prevented the collection of foraminifera. An alternate core was found, albeit, at a location under different environmental and climate regimes. Additionally, the *Neogloboquadrina pachyderma* specimens identified in the new core were not sufficient in size to be analysed individually, therefore an alternate species, *Globorotalia inflata*, was used for the single

specimen analysis. As a result, the focus of the downcore study changed, moving from a surface water perspective to an intermediate water one, and the findings of the modern studies did not apply to the interpretation of the paleoceanography record. Furthermore, the changes in location and species meant that the aims and objectives of the final part of the thesis needed to be adapted.

The overall aim of this thesis is to investigate the applicability of single specimen stable isotope analysis of foraminifera to study seasonal changes in environmental conditions in the Southern Ocean on a range of timescales. In addition, emphasis is placed on the relationship between environmental changes and biochemical variability of foraminifera in the high latitudes.

The specific objectives of the thesis are:

- To study modern *Neogloboquarina pachyderma* single specimen stable isotope variability in the mid to high latitudes in order to create a region-specific record of vital effects.
- To create a modern record of seasonal and interannual variability of *Neogloboquarina pachyderma* in relation to environmental changes at the West Antarctic Peninsula. This investigation will include:
 - the assessment of foraminifera abundance and flux from a six-year long sediment trap and its relationship to food availability, water temperatures, and sea ice presence.
 - the detailed study of *Neogloboquarina pachyderma* morphology, the identification of different morphospecies, and their dominance under different environmental conditions.
 - the analysis and interpretation of single specimen *Neogloboquarina pachyderma* stable isotopes in relation to morphological variability, as well as to seasonal changes of temperatures, food availability, and sea ice.
 - the assessment of the *Neogloboquarina pachyderma* record in light of interannual atmospheric and oceanographic variability relating to teleconnections with El Niño-Southern Oscillation and/or Southern Annular Mode, and its impact on the potential use of *Neogloboquarina pachyderma* stable isotopes in this region.
- To investigate intermediate water variability in the Scotia Sea during the Holocene period by utilising a single specimen *Globorotalia inflata* stable isotope record from the Falkland Plateau. This will provide potential insight into the role

of the polar regions on intermediate water mass variability in the mid latitude regions.

1.4 Outline of the Thesis

In Chapter 2, the regional setting and the associated oceanography of the two main regions involved in the thesis (the Scotia Sea and the Antarctic Peninsula) are presented. Additionally, the two main climate phenomena, impacting the Southern Ocean regions, (El Niño-Southern Oscillation and Southern Annular Mode) are described and their impact on high latitude atmospheric and oceanographic conditions is discussed.

In Chapter 3, the proxies used throughout the thesis are reviewed. The first part of the chapter provides information on the life cycle of foraminifera and gives an assessment about the two planktonic foraminifera species, *Neogloboquadrina pachyderma* and *Globorotalia inflata*, utilised in the study. The second part of the chapter reviews foraminiferal morphology and its use in paleoclimate studies. In the final part of the chapter, stable isotope analysis of seawater and foraminifera is discussed.

In Chapter 4, a detailed description is provided on the materials and methods used in the thesis. The chapter is divided into three main sections reflecting the three studies that form the thesis. The first section covers the JR304 cruise materials and the associated stable isotope analysis. The second section constitutes the time series samples at Palmer Deep and the flux, morphological, and stable isotope analysis that derive from those samples. Finally, in the third section, the sediment samples from the Falkland Plateau are described together with the stable isotope analysis undertaken on them.

The following chapter (Chapter 5) and its constituent three sections present and discuss the results obtained during this study. Each of the three sections focuses on a different application of the single specimen analysis in the southern mid to high latitudes and provides a scientific assessment of the foraminifera species utilised.

Neogloboquadrina pachyderma is the most abundant planktonic foraminifera in the high latitudes and is commonly used in studies that employ planktonic foraminifera to investigate recent and past high latitude climatic variations. As a result, information about species habitat, behaviour, environmental preferences, and response to environmental changes are widely available. However, an assessment of past studies highlights the species' environment-specific nature. In Chapter 5.1, a detailed assessment of vertical plankton tow-derived *Neogloboquadrina pachyderma* abundance, morphology, and single specimen stable isotope signature is provided in relation to environmental

conditions. The first part of the results and discussion section describes the oceanographic conditions during the sample collection in the austral spring of 2014 while the rest of the results and discussion covers the distribution of *Neogloboquadrina pachyderma* in the Scotia Sea and the relationship between *Neogloboquadrina pachyderma* stable isotopes, shell weights, calcification depths, and isotope fractionation-derived vital effects.

The West Antarctic Peninsula is one of the most climatically sensitive regions of the high latitudes and particularly, of Antarctica. A high degree of intra- and interannual variability has been observed in the regional climate and sea ice distribution around the WAP impacting all levels of the food web and is modulated by teleconnections with El Niño-Southern Oscillations and the Southern Annular Mode. The holistic assessment of *Neogloboquadrina pachyderma* abundance, morphology, and single specimen stable isotope variability over a period of six years (2006-2013) from a sediment trap at the continental shelf off Palmer Deep is presented in Chapter 5.2. Detailed statistical analysis is carried out on the *Neogloboquadrina pachyderma* data in relation to environmental parameters to investigate the relationship between the two. The results are discussed in terms of seasonal and environmental variability along the West Antarctic Peninsula and the role Southern Annular Mode and El Niño-Southern Oscillation plays on *Neogloboquadrina pachyderma* at the study site.

The Southern Ocean and the southern mid-latitude climate experienced variability during the long-term gradual cooling of the Holocene period, with oscillations in Southern Westerly Wind stress, changes in El Niño-Southern Oscillation frequency, and variability in glacial meltwater flux from the Antarctic Peninsula. In chapter 5.3, single specimen *Globorotalia inflata* stable isotope record from the Falkland Plateau is used to reconstruct intermediate water variability during the Holocene. The biological factors behind *Globorotalia inflata* stable isotope composition is fully explored before utilising it as a proxy for oceanographic variability and is discussed in relation to existing records of Holocene climate variability from the southern mid to high latitudes.

A summary of key findings in relation to the original aims and objectives is presented in Chapter 6 together with improvements to methods.

2 Regional Setting and Oceanography

2.1 Scotia Sea

The Scotia Sea is an area of the Southern Ocean bounded to the west by the Drake Passage and to the north, east, and south by the Scotia Arc (Figure 2.1). The Scotia Arc was formed during the mid-Cretaceous (120-83 Ma) as a result of the westward movement of the South American plate, which led to the uplift of the southern tip of the Andes and the proto North Scotia Ridge (Dalziel et al., 2013). Due to the uplift of the North Scotia Ridge the South Georgia microcontinent began moving eastward towards its current position (Figure 2.1). The Antarctic and South American continental plates began to spread apart around 55 Ma (early Eocene) beginning the development of the Drake Passage, as well as the South Scotia Sea, the South Scotia Ridge, and the Scotia Plate itself (Eagles, 2010). A deep water connection between South America and Antarctica is thought to have developed by 34-40 Ma. The youngest part of the Scotia Sea to experience spreading is the West Scotia Sea, where the last of the seafloor spreading has been dated to 6.6-5.9 Ma (Livermore et al., 2005).

2.1.1 Modern Oceanography

The modern oceanography of the Drake Passage and the Scotia Sea region is well known due to a long history of oceanographic research in the area. The main feature of the Scotia Sea region, and of the Southern Ocean as a whole, is the eastward/northeastward flow of the Antarctic Circumpolar Current (ACC) (Figure 2.1), which is driven by the Southern Westerly Winds between 45°S and 55°S (Orsi et al., 1995). The ACC is the largest current system in the global ocean, transporting 136.7 ± 6.9 sverdrup (Sv) of water (Meredith et al., 2011), together with heat, salt, nutrients, and other chemical properties between the Atlantic, Indian and Pacific Oceans (Orsi et al., 1995). The flow of the ACC is linked to the steep shoaling of isopycnals towards southern latitudes through the entire water column (Figure 2.2), as well as to large geostrophic shear (Deacon, 1937).

The ACC is defined by three frontal regions which are characterised by fast-flowing currents and separated by calmer waters (Meredith et al., 2011). The position of the frontal boundaries can be defined as areas of steep shoaling/deepening of isopycnal surfaces (Orsi et al., 1995). The three fronts from north to south (Figure 2.2): Subantarctic Front (SAF), Polar Front (PF) and Southern ACC Front (SACCF) (Whitworth, 1980; Orsi et al., 1995). An additional front, the Southern Boundary of the

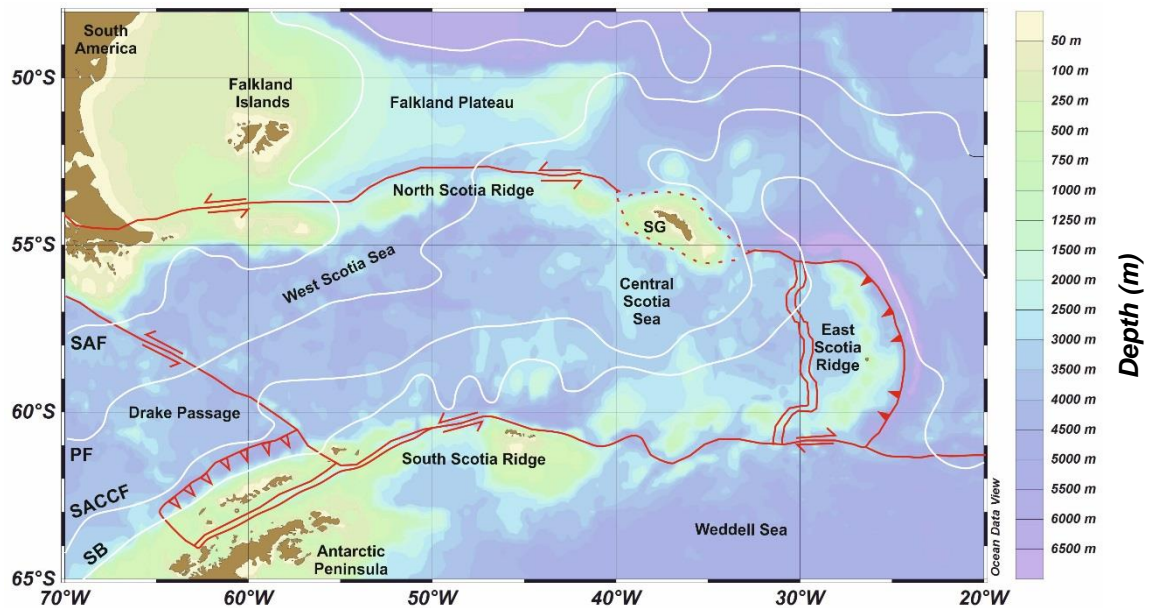


Figure 2.1: Bathymetry and geological setup (after Dalziel et al., 2013) of the Scotia Sea region with the frontal systems of the Antarctic Circumpolar Current (after Garabato et al., 2003). Red lines denote plate boundaries, double red lines are spreading ridges, red arrows represent direction of transform fault, and teeth indicate direction of subduction zone (Dalziel et al., 2013). SG, South Georgia microcontinent; SAF: Subantarctic Front; PF: Polar Front; SACC: Southern Antarctic Circumpolar Current Front; SB: Southern Boundary of the ACC. The SAF, PF, and SACC are the three main fronts of the ACC transporting most of the water mass (Orsi et al., 1995).

ACC (SB) is recognised south of the SACC as the area where the Upper Circumpolar Deep Water (UCDW) shoals to a shallow depth of ~200 m (Orsi et al., 1995). The SAF separates the ACC from the influence of subtropical waters, while the SB separates the ACC from the subpolar waters (Figure 2.1).

Within the Scotia Sea, bathymetry controls the paths of both surface and deep water currents and water masses associated with the three fronts creating meanders and eddies leading to increased water mixing through the water column and across the frontal boundaries (Peterson and Whitworth, 1989). East of South America, the ACC turns northward due to the bathymetry of the basin and the Scotia Arc (Figure 2.1). The SAF, the most northerly of the main ACC fronts hugs the continental slope around the Falkland Islands, while the water masses along the PF cross the West Scotia Sea and travel through the North Scotia Ridge west of South Georgia (Figure 2.1; Garabato et al., 2003). In contrast, the currents along the SACC transport water out of the Scotia Sea through the gaps between the South Georgia microcontinent and the East Scotia Ridge (Figure 2.1). The northward movement of the water masses along the SAF allows for some of the water to escape from the ACC, forming the Malvinas Current, that closely follows the

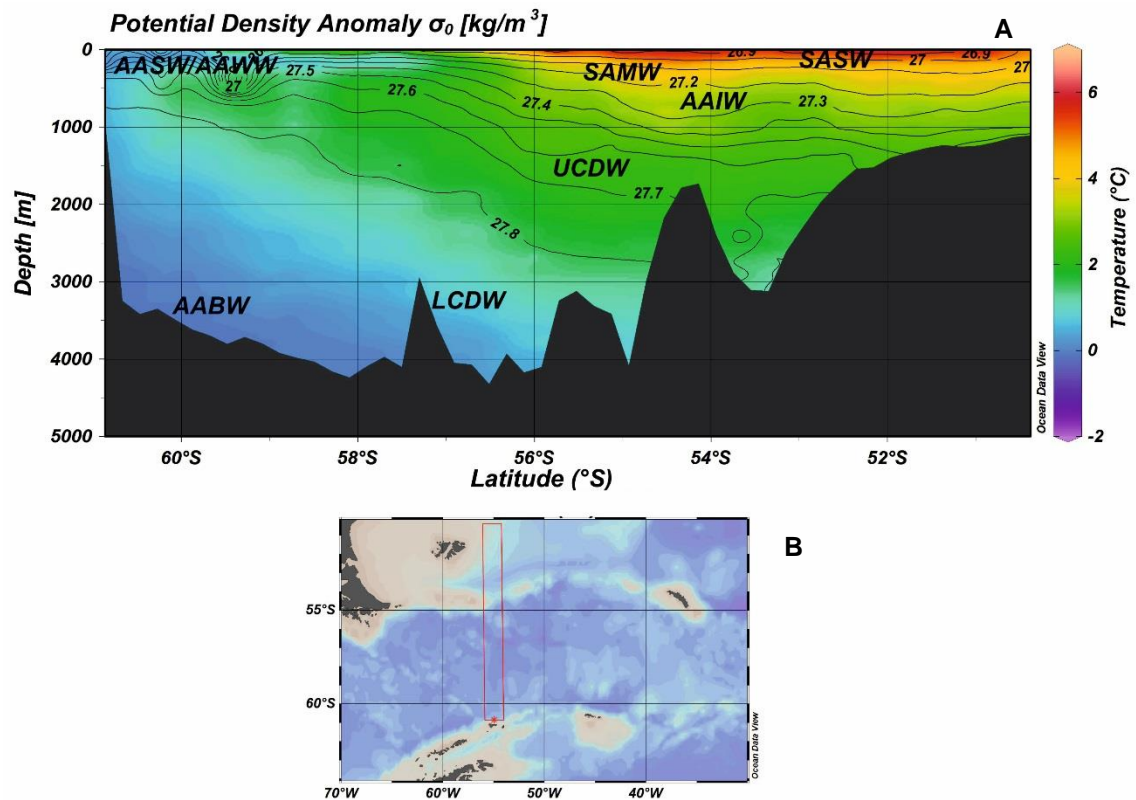


Figure 2.2: A): Cross-section of Scotia Sea, displaying latitudinal temperature (colour bar) and potential density (black contour lines) changes, and the water masses of the Southern Ocean as defined by Orsi et al., 1995; Garabato et al., 2002; and Meredith et al., 1999. The contour lines of potential density highlight the shoaling of the isopycnals from the north to the south across the Antarctic Circumpolar Current (54°S-60°S). AASW: Antarctic Surface Water; AAWW: Antarctic Winter Water; SAMW: Subantarctic Mode Water; SASW: Subantarctic Surface Water; AAIW: Antarctic Intermediate Water; UCDW: Upper Circumpolar Deep Water; LCDW: Lower Circumpolar Deep Water; AABW: Antarctic Bottom Water. B) Scotia Sea bathymetry map highlighting the cross-sectional area (red box).

South American continent as it travels north, feeding Antarctic-sourced waters into the global thermohaline circulation (Boltovskoy et al., 1996).

The main water masses associated with the ACC and the Scotia Sea are Subantarctic Surface Water (SASW), Subantarctic Mode Water (SAMW), Antarctic Surface Water (AASW), Antarctic Winter Water (AAWW), Antarctic Intermediate Water (AAIW), Upper Circumpolar Deep Water (UCDW), and Lower Circumpolar Deep Water (LCDW) (Figure 2.2). Antarctic Bottom Water is found at the bottom of the Scotia Sea as it spreads from its source regions along the Antarctic continents equatorward (Orsi et al., 1995).

Subantarctic Surface Water (SASW) denotes the northern boundary of the Antarctic Circumpolar Current (ACC), and is found on the poleward side of the Subtropical Front (Orsi et al., 1995). SASW makes up some of the warmest and saltiest waters of the ACC

structure, with potential temperature between 5 °C and 6°C and salinity ~34.15 practical salinity unit (PSU) within the Scotia Sea (Meredith et al., 1999).

Subantarctic Mode Water (SAMW) is found north of the SAF (Figure 2.2) and is formed by the deepening of the winter mixed layer on the northern edge of the ACC (Meredith et al., 2011) and has significant South Pacific contribution in the form of fresh and cold freshwater runoffs from Chile (Meredith et al., 1999). It is also modified due to density mixing as it flows along the SAF across the Southern Ocean. As a result, temperature and the salinity of this water mass display a wide range across the three ocean basins, with temperature (salinity) ranging from 4-5°C (34.2-34.3 PSU) in the eastern South Pacific to 14-15° (35.4-35.5 PSU) in the western South Atlantic (McCartney et al., 1977).

Antarctic Surface Water (AASW) is found south of the PF (Figure 2.2) all the way to the continental margin of Antarctica (Orsi et al., 1995). Its properties are determined by the air-sea interactions, formation and melting of sea ice, and advection (Gordon and Huber, 1984), with temperatures ranging on average from -1.0 to 1.0 °C, and salinities ranging from 34.0 PSU to 34.6 PSU (Emery et al., 2003). Due to its low salinity and temperature it readily mixes with UCDW at the southern edge of the ACC where the UCDW shoals closer to the surface (Smith and Klink, 2002). Once mixed with UCDW, AASW flows north towards the Polar Front (Orsi et al., 1995).

Antarctic Winter Water (AAWW) is formed in the spring/summer when the melting sea ice and glacial ice along the Antarctic Peninsula freshens the cold surface waters (Meredith et al., 1999) along the continental margin leading to the isolation of the cold winter mixed layer (Mosby, 1934). This isolated cold mixed layer becomes AAWW with very low potential temperatures (less than -1.0°C) and low salinity (~33.9 PSU) (Meredith et al., 1999) which then flows equatorward, deepening south of the PF (Figure 2.2).

Towards the northern edge of the ACC, Antarctic Intermediate Water (AAIW) is found beneath SAMW, while south of the PF it is located directly below AASW (Orsi et al., 1995) (Figure 2.2). AAIW can originate from a number of sources. It can form from AASW that undergo subduction at the Polar Front (Orsi et al., 1995), from AAWW, originating from the winter mixed layer of the Bellingshausen Sea, that flows north towards the Polar Front (Meredith et al., 1999; Naveira Garabato et al., 2009), or from modified cold, fresh SAMW that flowed eastwards from the South Pacific through the Drake Passage into the Scotia Sea (McCartney, 1977). The source waters that make up the AAIW result in temperatures that range between 2°C and 6°C, and salinities between 33.8 PSU and 34.8 PSU across the Southern Ocean (Emery et al., 2003). The low salinity source

waters of the AAIW lead to a very low salinity profile for the AAIW itself, resulting in a salinity minimum at intermediate depths (Talley, 1996).

Upper Circumpolar Deep Water (UCDW) is found below AAIW in the northern part of the ACC, and below AASW in the southern part of the ACC (Figure 2.2). It is easily recognised by its low-oxygen, high nutrient concentration properties, as well as its high temperature ($>1.5^{\circ}\text{C}$) and high salinity (34.65 PSU to 34.7 PSU) (Orsi and Whitworth III, 2005). UCDW shoals from depths of up to 3500 m at the SACCF towards the surface at the SB where it mixes with AASW (Orsi et al., 1995).

Lower Circumpolar Deep Water (LCDW) is the high salinity (~ 34.5 PSU), cold (0°C to -0.5°C) and thus dense branch of the Circumpolar Deep Water that penetrates the southern regions of the Pacific, Indian, and Atlantic Ocean basins (Sloyan and Rintoul, 2001) thanks to its density. It is formed south of the ACC through brine rejections and direct mixing with shelf waters (Orsi et al., 1995; Sloyan and Rintoul, 2001). Similarly to UCDW, it is found at shallower depths at the southern edge of the ACC, and deepens equatorward (Figure 2.2).

2.2 Western Antarctic Peninsula

The Antarctic Peninsula (AP) is a narrow (<250 km wide), long (~ 1250 km) mountainous body, rising to a height of 3500 m at its highest with only a few areas dropping below 2000 m (King and Turner, 1997). The northernmost point of AP reaches 63°S at Prime Head, while the majority of the landmass lies between 63°S and 75°S (Figure 2.3) and is subjected to subpolar climates with significantly contrasting meteorological and oceanographic conditions on the opposing sides of the peninsula. The spine of the AP is made up of Mesozoic-Tertiary igneous granitoids now capped by a permanent ice cap (Domack et al., 2003), the AP Ice Sheet.

2.2.1 Glacial setting

Glaciation of the AP most likely started around 30 million years ago during the Eocene, as recorded in the South Shetland Islands (Dingle and Lavelle, 1998), while large-scale expansion of glaciation across the continental shelf during the Miocene and the Pliocene-Pleistocene has also been identified (Barker and Camerlenghi; 2002). The present physical setting is the result of the decline of the AP Ice Sheet, sea level rise and isostatic adjustment following the Last Glacial Maximum. The contrasting glacial setting of the eastern and western side of the peninsula is due to the different precipitation patterns over the areas. The WAP is characterised by regular cyclonic activity related to the prevailing southern Westerlies which carry large quantities of snow to the area. This

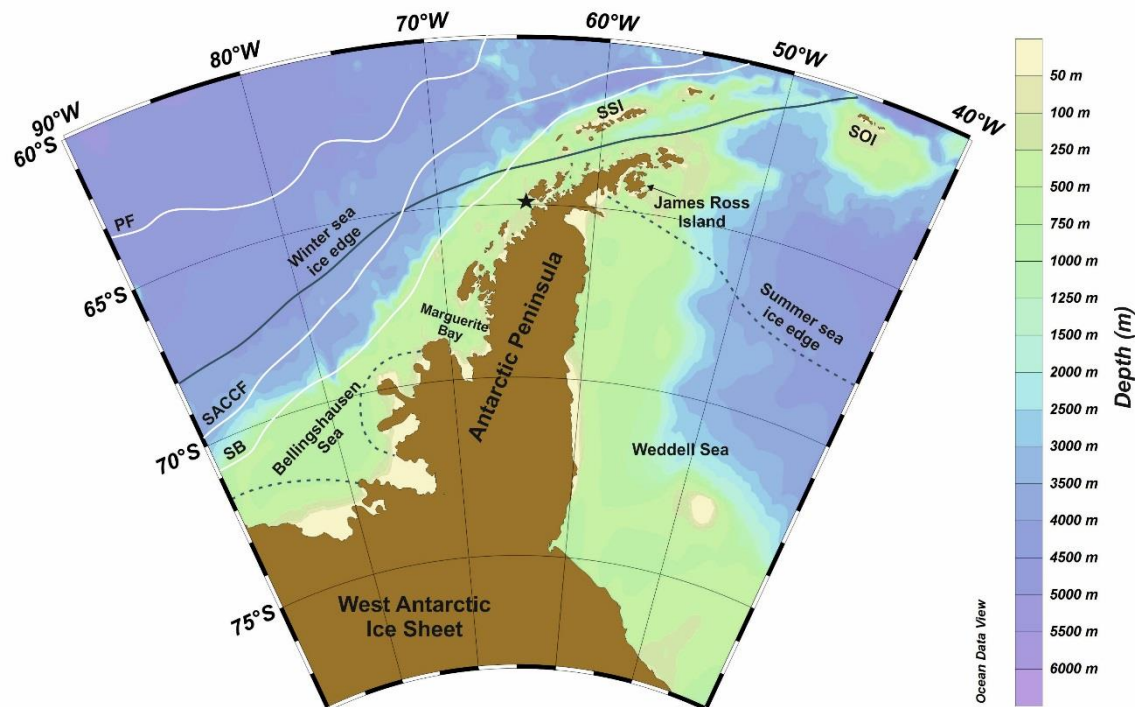


Figure 2.3: Bathymetry map of the seas surrounding the Antarctic Peninsula showing frontal boundaries (white lines; after Naveira Garabato et al., 2002) and winter and summer sea ice extent (blue solid and dotted lines, respectively; after NASA, 2009). Black star denotes location of Palmer Deep. SSI: South Shetland Islands; SOI: South Orkney Islands.

results in high accumulation rates of snow and a markedly lower equilibrium line altitude despite the higher average summer temperatures (Domack et al., 2003). The East Antarctic Peninsula (EAP) is characterised by lower levels of snowfall, lower average annual temperatures and higher equilibrium line altitude. This contrast results in marked differences in the development and characteristics of glaciers and ice shelves on the two sides of the peninsula. Ice shelves on the eastern side have low elevation surfaces susceptible to rapid changes in meltwater production, while the tidewater and outlet glaciers of the western side have significant snow pack and higher snow lines which are less prone to changes in meltwater production (Skvarca and DeAngelis, 2003).

2.2.2 Oceanography

The Antarctic Circumpolar Current is driven by the Southern Westerly Winds (SWW) and travels past the AP from west to east, entering the Atlantic sector of the Southern Ocean through the Drake Passage (Figure 2.3). The western side of the peninsula is bathed by Upper Circumpolar Deep Water (UCDW) (Figure 2.3) that upwells at the Southern Boundary of the ACC and is carried to the WAP via the ACC (Orsi and Whitworth III, 2004). The UCDW acts as the most important source of heat and nutrients along the WAP (Martinson and McKee, 2012) as it is significantly warmer than the surface waters around the Peninsula. Above UCDW, Antarctic Surface Water readily mixes with UCDW

due to its density (Meredith et al., 1999). Vertical mixing between AASW and UCDW creates a water mass that has surface temperatures above freezing during the winter (Smith and Klinck, 2002). Characteristics of the surface waters along the AP vary with the freezing and the melting of the sea ice, significantly affecting salinity and density.

The contrasting water masses and different atmospheric settings create different sea ice regimes along the EAP and WAP. Sea ice is present all year round in most years in the Weddell Sea (only the northernmost areas experience ice-free times). In contrast, the sea surface along the WAP experiences large inter-annual variations in sea ice presence (King et al., 2003). During the winter months sea ice extends to the northernmost regions of the peninsula, however, by March it melts back all the way to the southern parts of the Bellingshausen Sea (Figure 2.3).

2.2.3 Atmospheric setting

Due to the geography of the peninsula a strong marine influence exists over the area. SWW have the main influence over the climate of the WAP, carrying moist, comparatively warm air masses from the mid-latitudes over the peninsula (Bentley et al., 2009). The EAP experiences significantly colder conditions as the cold continental air masses from the interior of the continent descend into the Weddell Sea embayment (Domack et al., 2003). Due to a large equator-to-pole atmospheric air temperature difference the Southern Ocean and the coastal areas around the continent endure the development of regular forceful weather systems. In the areas of climatic fronts (e.g. Antarctic Polar Front – APF- and the increased thermal gradient along the coast of the continent) strong horizontal temperature gradients exist together with frequent cyclogenesis, cloud cover and strong wind activity (King and Turner, 1997).

The WAP experiences the largest interannual variability in surface air temperatures on the Antarctic continent. This interannual atmospheric variability is controlled by the twice-yearly poleward movement and intensification of the atmospheric low-pressure trough in the spring and the autumn around the high latitudes, termed the semi-annual oscillation (SAO) (van Loon, 1967). The interactions between sea ice and the atmosphere due to the SAO drive the seasonal cycle of sea ice advance and retreat (e.g. Watkins and Simmonds, 1999; Stammerjohn et al., 2003). Surface air temperature at Faraday station, found at the northern half of the peninsula, has a mean annual temperature range of $\sim 11^{\circ}\text{C}$ with a standard deviation of $\sim 1.1^{\circ}\text{C}$ (King, 1994). The variation derives from the large temperature change observed during the winter months, between June and September, which persist into the following year (King and Turner, 1997), suggesting that the temperature change is related to changes in ocean circulation and in sea surface

temperature (SST). At Marguerite Bay (Figure 2.3), average annual temperature is around -9°C and average precipitation is in excess of 300 mm/year (Allen et al., 2011).

Surface air temperatures along the WAP display sensitivity to the extent of sea ice cover over the Bellingshausen Sea on a seasonal scale. During times of maximum sea ice extent (winter and spring) surface air temperatures display a negative correlation with sea ice (Jacobs and Comiso, 1997). The exact relationship between the two factors has not been determined yet due to the diversity of processes effecting sea ice extent and SST. The role of upwelling UCDW and the influence of the EL Niño-Southern Oscillation on the development of the sea ice remains elusive (Domack, et al., 2003), thereby the effect of the sea ice on the surface air temperature is difficult to decipher.

Larger scale atmospheric circulation is determined by the location of the peninsula itself in relation to the circumpolar trough (CPT) of low sea level pressure. This in turn varies as part of the larger-scale Southern Hemisphere circulation, in which pressure levels across the atmosphere vary inversely between the mid and high latitudes (King and Turner, 1997). This mode of variability of Southern Hemisphere circulation is called the Southern Annular Mode (SAM). Part of the CPT is the Amundsen Low, an extensive area of low pressure found over the Amundsen Sea and which drives mild, northwesterly winds over the coast of the WAP (King et al., 2003). The high topography of the peninsula prevents the transport of this warmer air mass from the WAP to the EAP, thereby creating a significant surface temperature gradient ($5\text{-}10^{\circ}\text{C}$) between the two sides (Bentley et al., 2009).

2.3 Atmospheric teleconnections between the southern high latitudes and the tropics

On inter-annual timescales, atmospheric variability around the south Pacific section of the Southern Ocean, and thus variability in sea ice advance and retreat along the Antarctic Peninsula are mostly controlled by the teleconnections between El Niño-Southern Oscillation/Southern Annular Mode and the high latitudes as these modulate the Semi-Annual Oscillation (Thompson and Wallace, 2000).

2.3.1 El Niño-Southern Oscillation

El Niño-Southern Oscillation (ENSO) is an interannual cycle in the atmospheric and ocean circulation of the Pacific region (Figure 2.4) that has significant effect on the climate of the rest of the globe. The Southern Oscillation (SO) is one of the largest interannual climate variations on the planet (Rasmusson and Wallace, 1983). In the tropical Pacific Ocean the SO is linked to large-scale fluctuations in SST, rainfall and in

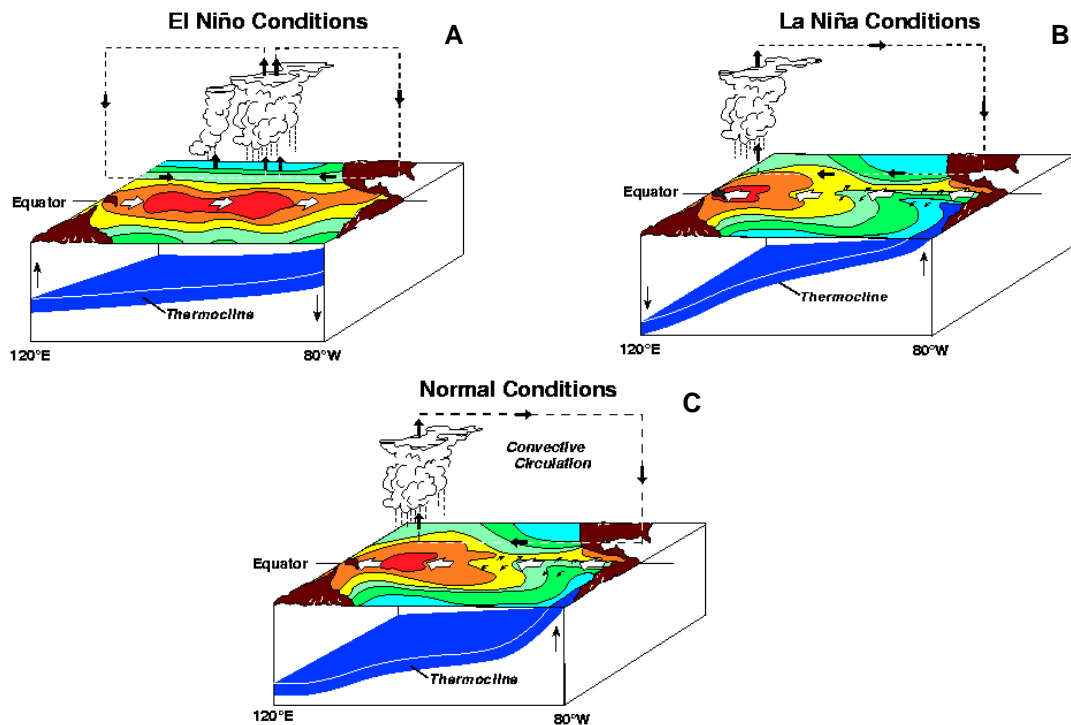


Figure 2.4: Schematic representation of the atmospheric and oceanographic conditions in the tropical Pacific during El Niño (A), La Niña (B), and normal conditions (C) highlighting the changes in the depth of the thermocline, in the location of the warm pool, and in the position of the convective cell (Pacific Marine Environmental Laboratory, NOAA, [Accessed: August 2017]).

the intensity of the trade winds, while in the subcontinent of India it is associated with severe droughts. Over North America the SO has been correlated with severe winter weather; while the Northern Hemisphere as a whole experiences large oscillations in mean atmospheric temperatures during SO events (Horel and Wallace, 1981; Philander, 1983).

The SO refers to the variation in the atmospheric mass over the Pacific Ocean, with cold, intermediate and warm conditions in the near-surface areas of the eastern Pacific Ocean (King and Turner, 1997). During the cold periods, termed La Niña, the tropics are characterised by stronger trade winds and a surface pressure difference between the eastern and western Pacific. The eastern Pacific around South America experiences the development of high pressure, while the western Pacific, around Indonesia and Australia, experiences low pressure (Figure 2.4B; Horel and Wallace, 1981). The low pressure system results in the development of active convective systems and prolonged heavy rainfall over that area. During the less frequent El Niño periods, the atmospheric and oceanic circulation undergoes a significant change (Philander, 1983). The strength of the trade winds decreases during these periods along with the surface pressure gradient between the east and west side of the Pacific Ocean, resulting in decreased convective

activity and precipitation in the western Pacific (Figure 2.4A), causing large-scale droughts most prominently in Australia (Rasmusson and Wallace, 1983).

The SO also affects surface ocean currents, with the presence of increased upwelling of nutrient-rich, cold waters off the coast of South America during La Niña (Figure 2.4B; Philander, 1983). El Niño events are characterised by weaker surface ocean currents and reduced upwelling off the coast of South America.

It has been well established that the variations in atmospheric and oceanic temperatures and ocean circulation due to the ENSO events have an effect on the climate around the AP (e.g. White and Peterson, 1998; Harangozo, 2000). Studies have shown that surface air temperatures and atmospheric circulation displayed variability relating to ENSO during the 1945-2005 period (White and Peterson, 1998; King et al., 2003; Meredith et al., 2004b; Meredith and King, 2005).

ENSO is a tropical phenomenon that has a great impact on the southeast Pacific section of the Southern Ocean through the development of Rossby waves over the Pacific Ocean (Hoskins and Karoly, 1981; Harangozo, 2000; Kwok and Comiso, 2002; Turner, 2004). Rossby waves develop over the mid-latitudes during El Niño events and travel poleward weakening the polar front jet while strengthening the subtropical jet (Hoskins and Karoly, 1981). As a result, positive pressure anomalies develop along the WAP region leading to a lack of cyclonic activity over the Amundsen/Bellinghausen Seas (Renwick, 2005) and dominant cold, southerly winds blowing off from the AP resulting in colder than average SST and increased sea ice cover and duration (Kwok and Comiso, 2002; Turner, 2004). La Niña events are associated with the opposite atmospheric and oceanic anomalies (Figure 2.5B), with the weakening of the subtropical jet and the strengthening of the polar front jet (Kwok and Comiso, 2002) resulting in greater cyclonic activity in the Bellinghausen Sea (Li, 2000) with warmer SST along the WAP (Yuan, 2000) stemming from the increased northerly winds that carry warm, moist air (Fogt and Bromwich, 2006; Stammerjohn et al., 2008a, Clem and Fogt, 2013).

2.3.2 Southern Annular Mode

Southern Annular Mode, and the variability between its positive and negative phases is associated with the development of zonally symmetrical atmospheric pressure differences of opposing signs between the polar regions and the midlatitudes centered around 45° latitude (Thompson and Wallace, 2000). Changes in the strength and mode of the SAM determine variability in the strength and positioning of the circumpolar westerly winds (Thompson and Wallace, 2000; Marshall et al., 2006; Marshall and Bracegirdle, 2015). Along with the zonal variability, SAM also has a strong meridional

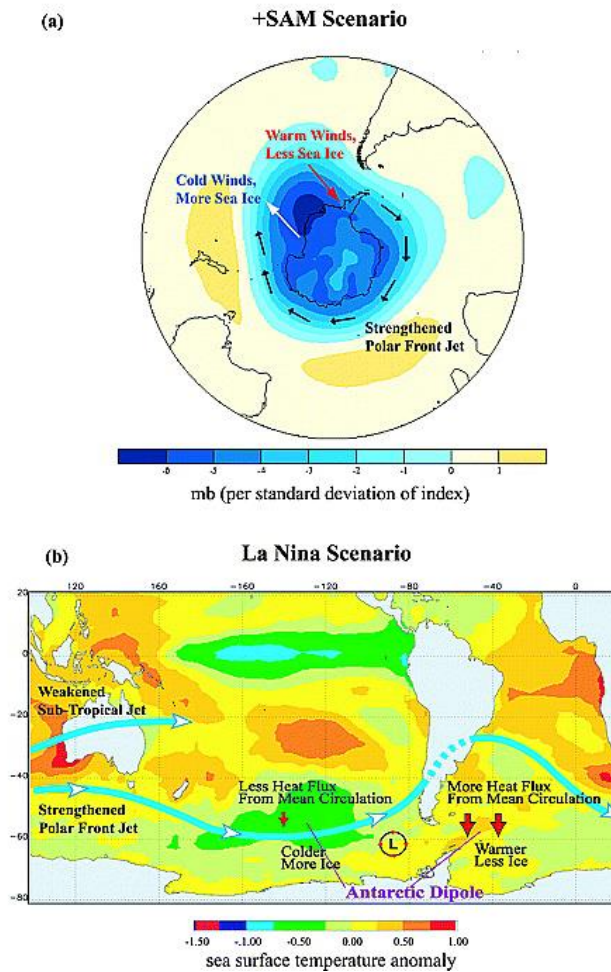


Figure 2.5: Schematic representation of the atmospheric response across the Southern Pacific sector of the Southern Ocean and the Antarctic Peninsula to positive SAM (A) and La Niña (B) (Stammerjohn et al., 2008). A) Black arrows depict the westerly winds around Antarctica, while the blue and yellow areas show differences in atmospheric pressure. B) Base map represents sea surface temperature variability (red areas are higher temperatures).

component, particularly around the Amundsen/Bellinghousen Sea and the Ross Sea (Marshall et al., 2003). During positive SAM periods positive pressure anomalies exist in the midlatitudes and negative anomalies are found in the high latitudes (Figure 2.5A) supporting the development of warm southerly winds along the WAP region and cold northerly winds in the Amundsen and Ross Seas (Kwok and Comiso, 2002; Lefebvre et al., 2004). This pattern switches to the opposite during negative SAM (Lefebvre et al., 2004). The warm northerly winds during +SAM create negative sea ice and positive SST anomalies along the WAP (Figure 2.5A). Negative SAM creates the opposite anomalies for both sea ice and SST (Kwok and Comiso, 2002; Lefebvre and Goose, 2005, Clem and Fogt, 2013). SAM has become more positive during the past few decades due to the combination of anthropogenic forcings and natural variability (Marshall et al., 2003). During the past thirty years co-variability between ENSO and SAM has increased: La Niña coincided with positive SAM, and El Niño with negative SAM (Kwok and Comiso,

2002; Stammerjohn et al., 2008a, Clem and Fogt, 2013). The impact of ENSO and SAM on the strength of sea level pressure (SLP) anomalies and sea ice advance on the WAP also intensified during the same period (Stammerjohn et al., 2003; Stammerjohn et al., 2008a). As a result, negative SLP anomalies during austral summer and autumn are observed on the WAP during La Niña events and positive SAMs, and vice versa for positive SLP. Concurrently variability in WAP sea ice trends has been closely linked to the SLP anomalies. Earlier wind-driven sea ice retreat and later sea ice advance is associated with the development of strong negative SLP anomalies along the WAP supporting anomalously warm northerly winds in the Bellingshausen Sea as a result of the increasingly positive SAM and strong La Niñas since the 1990s. Conversely, positive SLP anomalies during the autumn months in the Amundsen Sea region are associated with cold southerly winds over the WAP region resulting in early sea ice advance (Stammerjohn et al., 2008a, b).

Similarly to the Antarctic Peninsula, ENSO and SAM has had an impact on the water masses in the Scotia Sea. Interannual variability observed in the volume transport of the ACC has been found to coincide with variability in the strength and phase of SAM, suggesting that the long-term increase in SAM strength is accelerating the ACC volume transport (Meredith et al., 2011). Additionally, interannual variability in the salinity and potential temperature of AAIW (0.01-0.04 PSU; 0.1°C-0.5°C respectively) between 1965 and 2005 were found to be related to ENSO and SAM-driven variations in wintertime air-sea heat fluxes and net evaporation, due to changes in the Southern Westerly Wind (SWW) stress (Meredith et al., 2011). The salinity of AAIW decreased by ~0.05 PSU between the 1970s and the early 2000s with almost no change in temperature, most likely as a result of decreasing AAWW salinity in the Bellingshausen region (Naveira Garabato, 2009). This was related to increased precipitation and sea ice melt linked to interdecadal changes in the SWW, likely due to increased positive trend in SAM (Meredith and King, 2005; Meredith et al., 2011).

3 Background information on proxies

3.1 Planktonic foraminifera

Two species of planktonic foraminifera were used in this project, *Neogloboquadrina pachyderma* and *Globorotalia inflata*. Planktonic foraminifera are single celled surface dwelling protozoa which excrete a calcite shell. They have long been used as a means to study historical changes in oceanography and climate due to their excellent preservation potential and ubiquity in marine sediments. The two species were chosen based on their high abundances in the sediments and seawaters assessed. *Neogloboquadrina pachyderma* (sinistral) specimens were collected from surface waters of the Scotia Sea in 2014 and from sediment trap samples located offshore from Palmer Deep, WAP, covering a six-year period between 2006 and 2013. *Globorotalia inflata* specimens were collected from a marine sediment core recovered from the Falkland Plateau.

3.1.1 Foraminifera life cycle and ontogeny

Planktonic foraminifera reproduction takes place by the release of gametes (Bé et al., 1977; Spindler et al., 1978; Hemleben et al., 1989). Prior to gamete release the foraminifera shell can be thickened by the secretion of a calcite crust around the whole test (Bé, 1980; Hemleben et al., 1989). Foraminifera reproduction follows a lunar cycle (Spindler et al., 1979; Hemleben et al., 1989; Jonkers et al. 2015), where planktonic foraminifera release a large amount of gametes in a synchronised manner 3 to 7 days after a full moon, to increase the chances of successful reproduction. After release, the gametes fuse together to form a zygote (Figure 3.1), which is followed by the establishment of the first chamber, the proloculus, which may or may not be calcified. During the juvenile stage, the foraminifera calcifies the second chamber as the cytoplasm continues to grow (Figure 3.2), followed by the calcification of subsequent chambers of uniform morphology (Brummer et al., 1986). The juvenile foraminifera test has a wide umbilicus and an equatorial aperture. The surface of the shell is non-cancellate, and has a suturally perforate wall. Following the juvenile stage, during the neanic stage the chambers of the test inflate, the umbilicus closes, the aperture moves to its adult position and pores develop on the surface of the test while additional chambers are calcified (Figure 3.2), which are successively larger with greater food intake (Brummer et al., 1986). The adult stage of the foraminifera is associated with changes in chamber shape (Figure 3.2), alterations in coiling mode and the addition of a terminal chamber in some

species. The terminal stage of the foraminifera relates to reproduction, which can be manifested in the ontogeny by the thickening of the entire shell by the addition of a calcite crust that has a cancellate texture, the formation of spherical, kummerform, or sac-form final chamber, or the shedding of the spines in spinose species (Brummer et al., 1986; Hemleben et al., 1989).

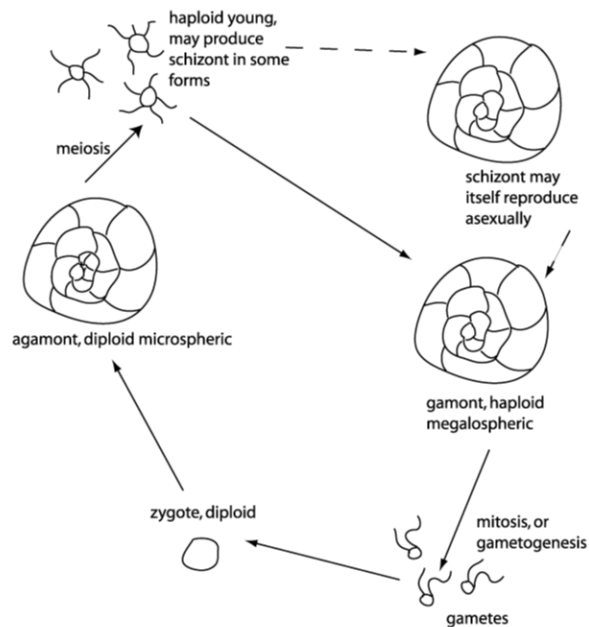


Figure 3.1: Generalised representation of foraminiferal life cycle showing the transformation between gametes, zygotes, gamonts and sexual and asexual reproduction (<http://www.ucl.ac.uk/GeolSci/micropal/foram.html>). Planktonic foraminifera undergo only sexual reproduction (Schiebel and Hemleben, 2005).

3.1.2 *Neogloboquadrina pachyderma* (Ehrenberg, 1861)

Neogloboquadrina pachyderma (Np) (Figure 3.3) is the dominant planktonic foraminifera species south (north) of the Polar Front on the Southern (Northern) Hemisphere (Pflaumann et al., 1996; Niebler and Gersonde, 1998). It has no symbionts, tolerates a wide range of SSTs, but has a preference for lower sea surface salinities (about 34 practical salinity unit (psu)) and small seasonal variations (NOAA, 1996; Spindler, 1996). Greatest Np abundances are commonly found in association with chlorophyll maxima (because of lack of symbiont), in areas of small vertical temperature gradients and minimal seasonal stratification; however, it is also found living in sea ice (Spindler, 1990; Mortyn and Charles, 2003). Np generally calcifies at 50-200 m water depth in the polar seas (Kohfeld et al., 1996; Bauch et al., 1997), however, the species can adjust its depth habitat in response to local hydrography (i.e. eddy mixing or advection of water masses) (Mortyn and Charles, 2003; Jonkers et al., 2013). Along the WAP, Np lives in the surface

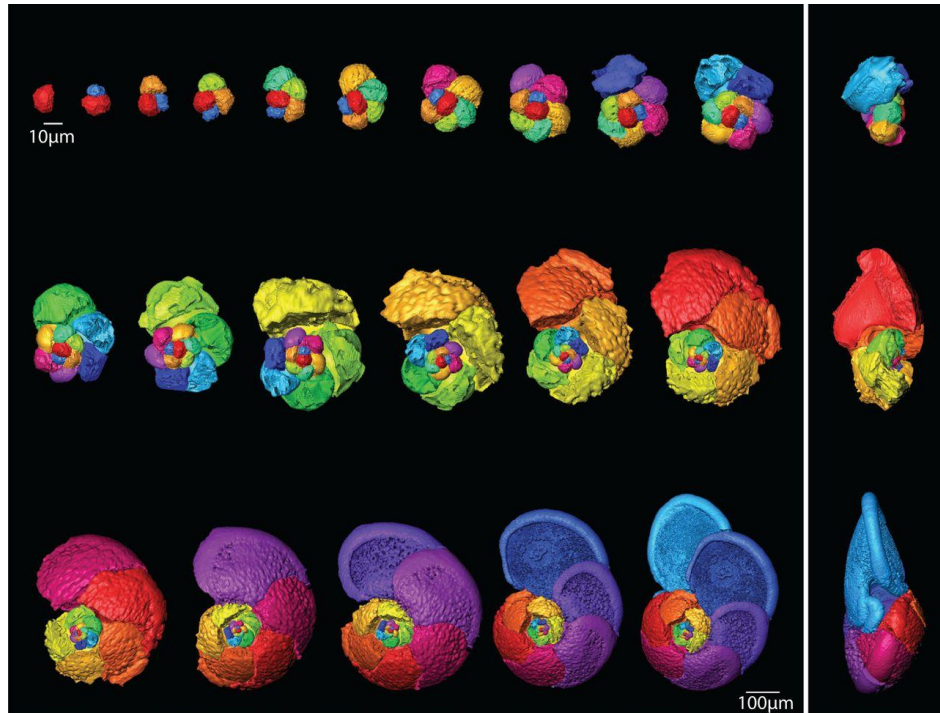


Figure 3.2: Ontogenic development of *Globorotalia tumida* showing the progression of growth stages from proloculus (top left) to mature, adult foraminifera (bottom right) (Caromel et al., 2015)

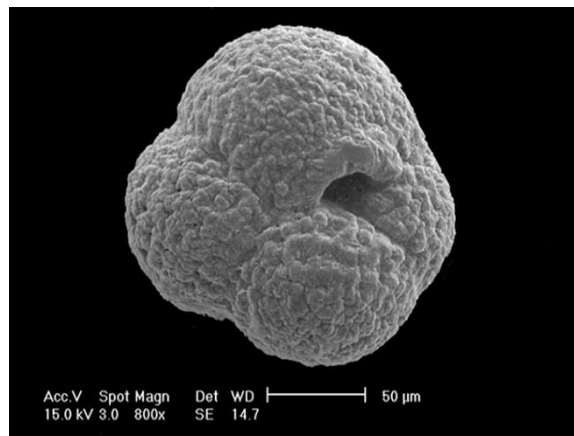


Figure 3.3: Scanning Electron Microscope image of an adult *Neogloboquadrina pachyderma* specimen (Np-A morphotype) from Palmer Long Term Ecological Research Programme sediment trap, 64.5°S, 66.0°W.

waters all year round, occupying the ice-water interface during the austral winter (Hendry et al., 2009). Peak flux of Np is associated with the warmer conditions of the late spring summer season (King and Howard, 2005).

A direct relationship exists between the water masses of the Southern Ocean and the genotypes of *Neogloboquadrina pachyderma*. South of the Antarctic Convergence, exclusively sinistral specimens are found. North of the Antarctic Convergence, the number of sinistral, left-coiling, specimens decreases while the abundance of dextral, right-coiling, specimens increases sharply (Boltovskoy, 1971; Niebler and Gersonde,

1998; Darling et al., 2004). These dextral coiling *Neogloboquadrina* specimens have been suggested to be designated their own species (*Neogloboquadrina incompta*) based on their genetics (Darling et al., 2006). The sudden change between *Neogloboquadrina pachyderma* and *Neogloboquadrina incompta* (*N. incompta*) marks the boundary between the Polar Front and the Subantarctic waters. Another distinct boundary is found between the northern edge of the Subantarctic Front and the southern edge of the Subtropical Front where *Np* virtually disappear and *N. incompta* dominates (Boltovskoy, 1996).

Genetic analysis of *Np* specimens collected from waters of the South Atlantic and the South Atlantic sector of the Southern Ocean revealed the existence of three different genotypes of *Neogloboquadrina pachyderma* (Types II, III, and IV) south of 50°S (Darling et al., 2004, 2006). Type II specimens were mostly found in the warm waters north of the Subantarctic Front and was absent from the cold waters south of the Polar Front (Figure

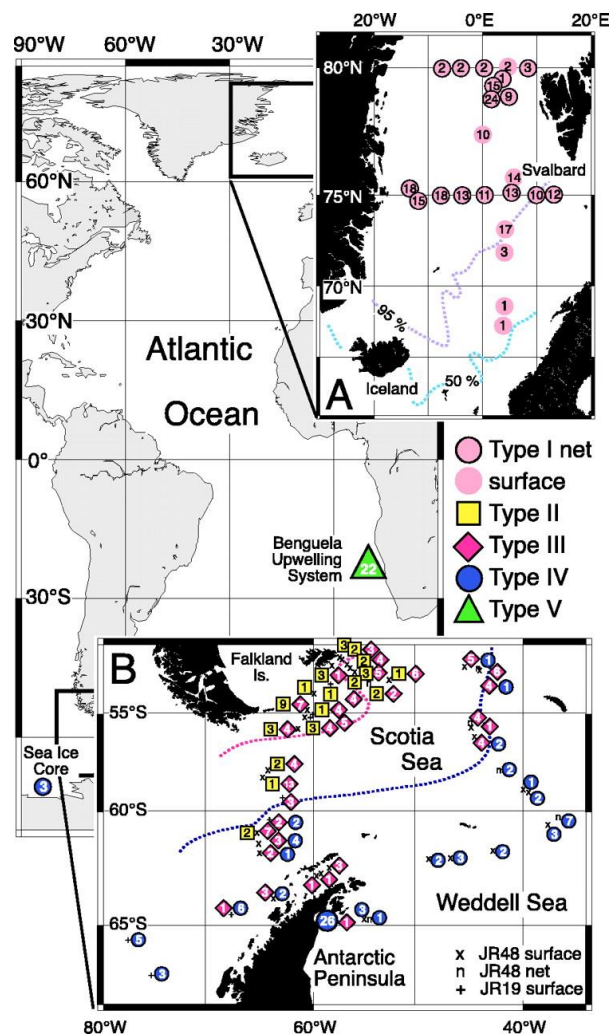


Figure 3.4: Distribution of *Neogloboquadrina pachyderma* genotypes in the North Atlantic (A) and in the subpolar/polar Antarctic (B) (Darling et al., 2004). The location of the Subantarctic Front and the Polar Front in the austral summer of 2000 are shown by the pink and blue contours respectively.

3.4). Type III specimens were widely distributed across the Southern Ocean (Figure 3.4), being most abundant north of the Polar Front. Type IV Np were only observed in the coldest waters, south of the Polar Front (Figure 3.3) (Darling et al., 2006).

During its life cycle, Np migrates through the water column – juvenile forms proliferate in the top 50 m of the surface waters and they migrate down as they mature, completing gametogenesis in deeper surface waters (Kozdon et al., 2009). During this time, Np adds new chambers and calcite layers to the test at varying temperature and salinity zones, thereby each specimen records distinct environmental conditions (Schiebel and Hemleben, 2005). As part of the final phase of the organism's life cycle a thick calcite layer might be added to the test (Kozdon et al., 2009). As this can take place at a much deeper depth (with considerably different environmental conditions) than the original calcification, the foraminifera test has two separate calcite layers. This secondary calcite makes Np a highly resistant species against dissolution, as evidenced by low dissolution indexes recorded in the Scotia Sea (Malmgren 1983).

Two distinct forms of Np have been identified in the Atlantic Ocean, one with heavy encrustation of calcium carbonate on the outer surface, and one without encrustation (Kohfeld et al., 1996; Kozdon et al., 2009). The encrustation results in average shell weights which are 3-4 times that of those without a secondary calcite crust. The non-encrusted Np has a shiny, smooth and translucent surface (Kohfeld et al., 1996) and is found to live in the top 80 m of the surface waters, in the cold, mixed layer of the water column. Peak abundance of encrusted Np in the Arctic region is found within the pycnocline, between 100 and 150 m water depth (Kohfeld et al., 1996; Bauch et al., 1997). In the Southern Ocean Np was found in water depths of up to 200 m (Mortyn and Charles, 2003). It appears that the secondary calcite crust is only added to the shell once the organism falls out of the main chlorophyll zone into the main pycnocline, possibly as part of its life cycle. $\delta^{18}\text{O}$ of Np in sediments, therefore, provide a record of temperature and salinity near/slightly above the main pycnocline (Kuroyanagi et al., 2011), while variations of $\delta^{18}\text{O}_{\text{calcite}}$ between different shell sizes reflect the strength of the pycnocline as well as possible water column stratification, which allows for the reconstruction of past water column structures.

3.1.3 *Globorotalia inflata* (d'Orbigny, 1839b)

Globorotalia inflata (*G. inflata*) (Figure 3.5) is a non-symbiotic deep-dwelling planktonic foraminifera (Bé 1969, Fairbanks et al., 1980, Hemleben et al., 1989) calcifying mainly within the mixed layer and the thermocline (Wilke et al., 2006). This species has been identified as a transitional species which is present in waters between the subtropical

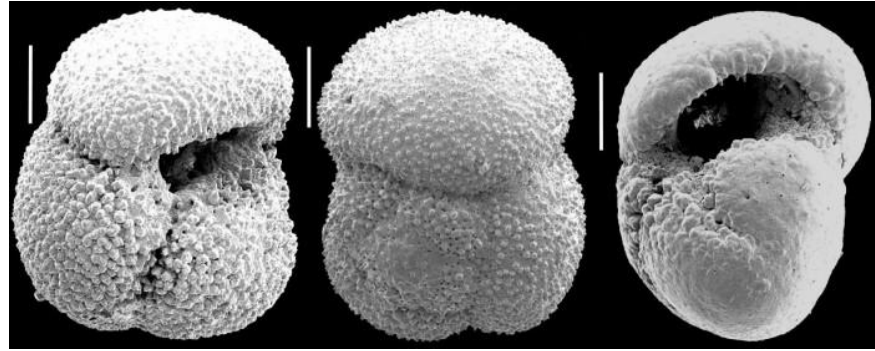


Figure 3.5: Scanning Electron Microscope image of *Globorotalia inflata* from New Zealand in ventral, dorsal, and side view (from left to right) (Hayward, 2011).

and the Subantarctic regions in the western side of the South Atlantic (Bé 1969, Portilho-Ramos et al 2014). It is found in high numbers in well mixed Brazil-Malvinas waters (warm and cold waters respectively, between $\sim 42\text{-}46^\circ$ S) (Boltovskoy et al. 1996, Portilho-Ramos et al., 2014, Morard et al., 2016). *G. inflata* is considered to have high preservation potential (Vincent and Berger, 1981), suggested by the close correlation between numbers present in surface waters and core top sediments (Malmgren, 1983, Kucera, 2007). Specimens can tolerate a wide range of sea water temperatures, from $\sim 8^\circ\text{C}$ to $\sim 27^\circ\text{C}$. Greatest abundances are found in waters with temperatures between 16°C and 20°C , which corresponds to the Subtropical Front in the South Atlantic (Niebler and Gersono, 1998; Kucera, 2007). In the South Atlantic *G. inflata* dominates assemblages during austral spring (October, November) making up as much as 70% of the total population (Bé 1969). This is consistent with findings in the Pacific sector of the Southern Ocean (King and Howard, 2005).

In both the North and South Atlantic this species has been found to dominate areas of consistently high nutrient concentrations (the bottom of the summer thermocline) associated with the deep chlorophyll maxima (Mortyn and Charles, 2003; Wilke et al., 2006; Cléroux et al., 2007, Salmon et al, 2015).

Apparent calcification depth of *G. inflata* range between 95 m and 1033 m water depth with calcification temperatures between 3.1°C and 16.5°C . On the Falkland Plateau calcification depth is found to be around 370 m and calcification temperature is 3.88°C (Groeneveld and Chiessi 2011). Calcification depths of between 300 - 500 m have been observed in other regions of the Atlantic Ocean as well (Elderfield and Ganssen, 2000; Cléroux et al., 2013) confirming *G.inflata* as a deep-dwelling species.

Genetic analysis of *G. inflata* revealed the existence of two genotypes (Type I and Type II) in the Atlantic and Southern Ocean (Morard et al., 2011). Type I specimens were found in both the Northern and Southern Hemisphere, in transitional and subtropical

waters (Morard et al., 2011). In the South Atlantic, the Type I genotype dominates the warm waters of the Brazil Current (Morard et al., 2016). The Type II genotype was only found in the subpolar waters of the Southern Ocean (Morard et al., 2011), in the cold waters of the Malvinas Current (Morard et al., 2016) and, within the Antarctic Circumpolar Current (Morard et al., 2011).

3.2 Foraminifera morphology

Morphology of planktonic foraminifera has been utilised as a proxy for past climate variability for over forty years (e.g. Bé, 1968; Malmgren and Kennett, 1972; Healy-Williams et al., 1992; Kucera and Kennett, 2002; Moller et al., 2013). *N. pachyderma* was one of the first planktonic foraminifera species chosen for morphological studies due to its abundance in surface sediments in the mid to high latitudes and the affinity of different morphologies for specific water masses and latitudinal positions (Malmgren and Kennett, 1972). The earliest morphology studies were carried out by splitting foraminifera samples between numerous size fractions and by visual assessments (Kennett, 1968; Malmgren and Kennett, 1972). These studies provided information on trends in maximum and median diameters, on % fraction of the samples with four/four and a half/five chambers in last whorl, and on the % fraction of sinistrally and dextrally coiling tests (early studies did not differentiate the different coiling directions as separate species). These early investigations highlighted the now well understood trend that *Neogloboquadrina pachyderma* abundance and size increases with increasing latitude between the mid-latitudes and the Polar Front.

With technological improvements it became possible to conduct more thorough morphological studies by first digitising foraminifera specimens (e.g. Healy-Williams and Williams, 1981; Williams et al., 1988) and then directly measuring aspects of the tests using automated microscopes and image analysis (Kucera and Kennett, 2002; Schmidt et al., 2004a; Moller et al., 2013). The morphology of *Neogloboquadrina pachyderma* specimens from Southern Indian Ocean (Williams et al., 1988; Healy Williams, 1992) and from North Atlantic core top samples (Healy Williams, 1992) were analysed by Fourier shape analysis. This approach revealed the existence of multiple morphotypes (six in the Southern Indian Ocean) each responding to different environmental conditions and parameters, such as temperature and the zonal distribution of water masses and frontal boundaries. These second-generation morphological studies integrated the stable isotope analysis of Np, which revealed isotopic differences of up to 1.6‰ in the $\delta^{18}\text{O}$ ratio between morphotypes relating to environmental processes (Williams et al., 1988). Smaller, 0.5‰ offset was found in the $\delta^{13}\text{C}$ ratios of morphotypes which were attributed

to biologically-controlled processes. Results also offered insight into Np calcification as specimens from the South Indian Ocean showed that morphotypes with greater pentagonality calcify with increasing disequilibrium from seawater (Healy-Williams 1992).

The morphological analysis of *Neogloboquadrina pachyderma* specimens by automated microscopes and image acquisition was used by numerous studies to investigate the evolutionary origins and improvements of Np (Huber et al., 2000; Kucera and Kennett, 2002) and other planktonic species (Schmidt et al., 2004a; Schmidt et al., 2004b). Mean and maximum shell size records revealed consistent increase in Np size since the mid-Pleistocene in both the North Atlantic (Huber et al., 2000) and in the North Pacific (Kucera and Kennett, 2002) as the species improved its adaptation to cold environmental conditions. The power of the automated morphological analysis is illustrated by the global sedimentary record of 23 planktonic foraminiferal species whose size distribution was analysed spatially and temporally (Schmidt et al., 2004a; Schmidt et al., 2004b). The automated analysis allowed the identification of environmental optima for the different planktonic foraminifera species based on the strong positive correlation between test size, abundance and temperature. An optimum temperature $\sim 0^{\circ}\text{C}$ was identified for Np, and $20\text{-}25^{\circ}\text{C}$ for *G. inflata* (Schmidt et al., 2004b) through this approach.

More recently, morphological studies have attempted to use *Neogloboquadrina pachyderma* morphology as a means to study past SST and environmental variability in climatically sensitive regions like the Arctic (Eynaud et al., 2009) and North Atlantic (Moller et al., 2013). Five morphotypes of Np were identified in the central Arctic (Eynaud et al., 2009), with 25% of the entire Np population (which make up the three largest morphotype groups) explained by warm, North Atlantic water intrusion into the Arctic Basin during the Quaternary. In one of the most recent Np morphology studies (Moller et al., 2013) Np size records were used to create an empirical formula to reconstruct past SST variability since the Last Glacial Maximum in the North Atlantic. The strong linear correlation between Np size and temperature in this region allowed the development of this empirical formula which can successfully be used in the polar regions where other palaeotemperature proxies struggle.

3.3 Stable isotopes

Stable oxygen and carbon isotopes of foraminiferal calcite are used to decipher global and regional climate change. Emiliani (1955) conducted one of the first research studies into Pleistocene climate change in which stable isotopes of oxygen and carbon were used. Since then, a wide range of research has taken place to determine what drives

variation in these isotopes (e.g. Shackleton and Opdyke, 1973; Erez and Luz, 1983; Gonfiantini, 1986).

Three stable isotopes of oxygen exist: ^{16}O , ^{17}O and ^{18}O . ^{16}O and ^{18}O are the most abundant isotopes with relative fractions of 99.76% and 0.20% respectively, leaving only 0.04% of all oxygen on Earth as ^{17}O (Rohling and Cook, 1999). There are two stable isotopes of carbon, ^{12}C and ^{13}C with a relative abundance of 98.89% and 1.11% respectively (Faure, 1986). Molecules which are made up of the lighter isotopes react more easily than those with the heavy isotopes. Partitioning of these isotopes between different substances is called fractionation (Rohling and Cook, 1999) and is a result of reactions during isotope exchange and of kinetic effects (e.g. diffusion).

In order to accurately quantify the abundance of the rarer isotopes the ratio between the less and more abundant isotope is determined ($^{18}\text{O}/^{16}\text{O}$ and $^{13}\text{C}/^{12}\text{C}$) then compared to a known standard, using the following equations (Ravelo and Hillaire-Marcel, 2007), expressed as a delta (δ) value have units of per mil (‰, per thousand) (Figure 3.6).

$$\delta^{18}\text{O} = \left(\frac{\left(\frac{^{18}\text{O}}{^{16}\text{O}} \right)_{\text{sample}}}{\left(\frac{^{18}\text{O}}{^{16}\text{O}} \right)_{\text{standard}}} - 1 \right) * 1000 \text{ ‰}$$

$$\delta^{13}\text{C} = \left(\frac{\left(\frac{^{13}\text{C}}{^{12}\text{C}} \right)_{\text{sample}}}{\left(\frac{^{13}\text{C}}{^{12}\text{C}} \right)_{\text{standard}}} - 1 \right) \times 1000 \text{ ‰}$$

Figure 3.6: Equations to calculate the ratios of stable oxygen and carbon isotopes (Ravelo and Hillaire-Marcel, 2007):

High δ values show the enrichment of the heavy isotope relative to the standard, while low δ values show the enrichment of the lighter isotope relative to the standard. Analysis of stable isotopes is done by using a mass spectrometer in which the mass ratios of CO_2 (calculated by reacting carbonate with phosphoric acid) are determined with reference to a standard CO_2 with known isotopic composition, the Pee Dee Belemnite (PDB) and later the Vienna PDB (VPDB) (Rohling and Cook, 1999). This will be explained in more detail in section 4.

3.3.1 Seawater stable isotopes

3.3.1.1 Oxygen isotopes

A number of processes can affect the $\delta^{18}\text{O}$ signature of seawater in which foraminifera thrive. Seawater $\delta^{18}\text{O}$ is closely linked to all the processes of the hydrological cycle, including evaporation, vapour transport, precipitation and iceberg melting (Hoffmann and Heimann, 1997; Rohling and Cook, 1999). The long-term storage of water in ice sheets and aquifers considerably affects $\delta^{18}\text{O}$, while seasonal sea-ice formation and melting

also affects the stable oxygen isotope composition of seawater, causing seasonal variability (Fairbanks, 1989; Ravelo and Hillaire-Marcel, 2007). Advection and mixing of water masses originating from different regions can also influence local $\delta^{18}\text{O}$ (Frew et al. 1995). Oxygen isotope ratios in foraminiferal calcite are affected by a number of factors, most importantly the equilibrium fractionation between seawater and the different carbonate species (Kim and O'Neil, 1997), which defines a strong and important temperature influence on the $\delta^{18}\text{O}$ of foraminiferal calcite. Disequilibrium in $\delta^{18}\text{O}$ is linked to changes in carbonate ion concentration, respiration, symbiont photosynthesis, ontogeny (changes in $\delta^{18}\text{O}$ with shell development) and gametogenic calcite (secretion of calcite, enriched in ^{18}O , on the surface of the shell before gamete release) (Spero and Lea, 1993; Rohling and Cook, 1999).

Modern data suggests that a clear seasonal variation exists in $\delta^{18}\text{O}_{\text{seawater}}$ in coastal Antarctic waters, with high values found during the austral winter (up to 0.05‰), and low values observed during the austral summer (approximately -0.9‰) (Meredith et al., 2008b). This seasonal variation is most likely due to seasonal changes in glacial meltwater input because sea ice processes alone would only affect the salinity of the surface waters as it accounts for only 1% of the freshwater input during the summer. As air temperature remains steadily below 0°C, the seasonal variation of seawater $\delta^{18}\text{O}$ is determined by the degree of glacial melting and SST during the austral summer (Meredith et al., 2013).

3.3.1.2 Carbon isotopes

The $\delta^{13}\text{C}$ of seawater is very closely linked to the organic carbon cycle and to sedimentary carbonate (Ravelo and Hillaire-Marcel, 2007). Photosynthesis, respiration and the export of organic matter leaves the terrestrial reservoir with a distinct $\delta^{13}\text{C}$ value of -25‰, compared to 0‰ for the carbonate reservoir in the ocean (Hoefs, 1997). A significant depth gradient exists in the $\delta^{13}\text{C}$ profile in seawater. During photosynthesis, ^{12}C is utilised leaving the surface waters enriched in ^{13}C . Remineralisation of organic matter in the mixed layer releases the lighter carbon isotope and somewhat balances the offset between ^{12}C and ^{13}C created by photosynthesis (Rohling and Cook, 1999). The export production of organic matter to the deeper waters removes ^{12}C to the deep water, resulting in seawater at depth being enriched in ^{12}C and depleted in ^{13}C (Figure 3.7). Increased export of organic matter creates a sharper gradient between the surface and deep water. Surface water $\delta^{13}\text{C}$ also depends on the air-water CO_2 exchange and the rate of carbon burial in sediments – the removal of carbon from the ocean-atmosphere systems.

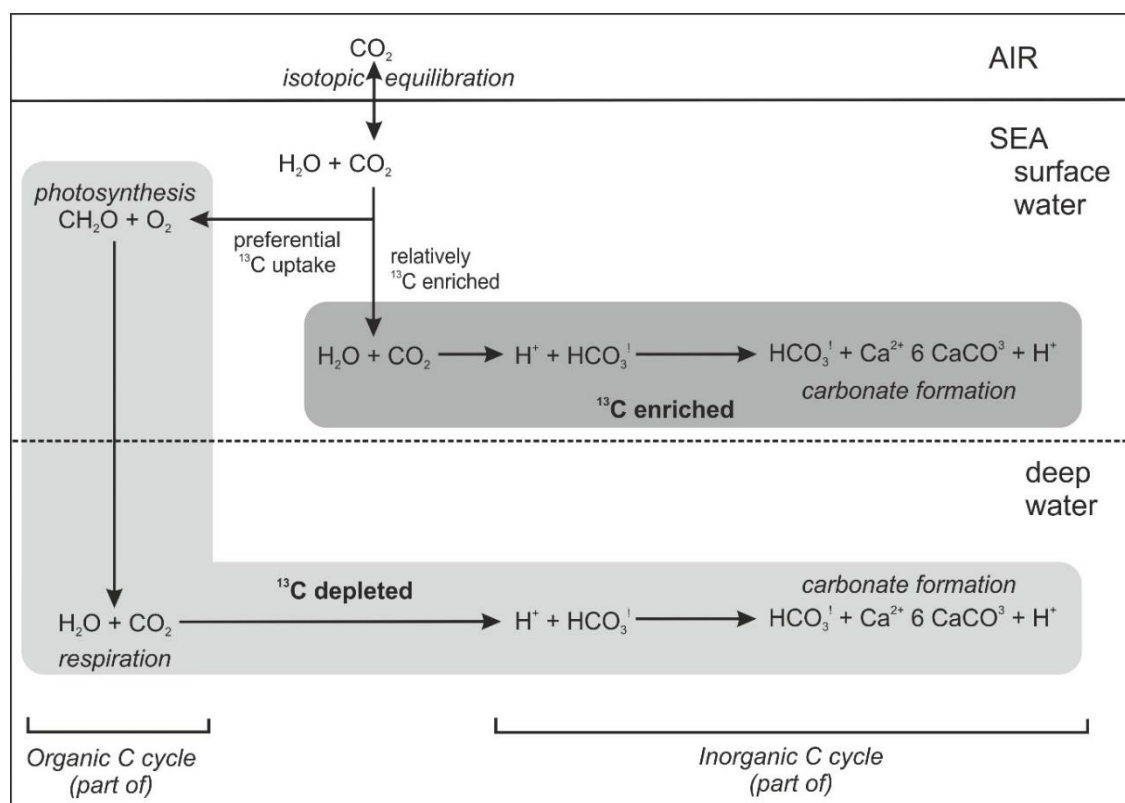


Figure 3.7: The schematic diagram displays the relationship between surface and deep water carbon isotope composition with relation to photosynthesis, export of organic matter through the water column and remineralisation at depth (Rohling and Cook, 1999).

Foraminiferal calcite carbon isotope ratios reflect the $\delta^{13}\text{C}$ of the dissolved inorganic carbon (DIC) of the seawater in which the organism calcified. However, the $\delta^{13}\text{C}$ of the foraminiferal carbonate is in disequilibrium with the seawater due to kinetic fractionation during comparatively rapid calcification and because of biological vital effects (Ravelo and Hillaire-Marcel, 2007). Foraminifera calcifies within an internal carbon pool that can have a different pH, $\delta^{13}\text{C}_{\text{DIC}}$, and DIC concentration than the surrounding seawater. (Zeebe et al., 1999). The $\delta^{13}\text{C}_{\text{DIC}}$ of the internal carbon pool is lowered when metabolic CO_2 with low $\delta^{13}\text{C}$ is respired by the organism. The $\delta^{13}\text{C}_{\text{DIC}}$ of the internal pool of symbiont-bearing foraminifera can increase during photosynthesis due to the removal of CO_2 with low $\delta^{13}\text{C}$ values. The rate of respiration, photosynthesis and calcification in relation to the turnover of DIC in the internal carbon pool all impact the $\delta^{13}\text{C}$ of the foraminiferal calcite (Spero et al., 1997). An additional parameter that affects the $\delta^{13}\text{C}$ of the foraminiferal calcite is the rate of isotopic equilibrium during the hydration and hydroxylation of CO_2 within the internal carbon pool with respect to the calcite precipitation. The rate of isotopic equilibration is generally slower than the rate of calcite precipitation and as such, the rate of calcite precipitation can influence the isotopic equilibration between the carbon species in the internal carbon pool. As a result, the $\delta^{13}\text{C}$

of the foraminiferal calcite is affected by the pH and CO_3^{2-} concentration and the rate of calcite precipitation. (McConnaughey, 1989a, 1989b).

$\delta^{13}\text{C}_{\text{DIC}}$ (stable carbon isotope ratio of DIC in seawater) varies through time and it is not uniform around the world's oceans or through the water column (Kroopnick et al., 1972), therefore calcification depth and, in turn, temperature are key factors that influence $\delta^{13}\text{C}$ of calcite. Important processes and factors which also affect the $\delta^{13}\text{C}$ of calcite include (i) the incorporation of low metabolic CO_2 into the calcite (vital effect) (Erez, 1978, Kohfeld et al., 1996; Ortiz et al., 1996); (ii) the photosynthetic activity of symbionts (increased light intensity results in ^{13}C enrichment in calcite shells of symbiont-bearing foraminifera) (Spero and Lea, 1993); (iii) the rate of growth (increasing shell size increases ^{13}C enrichment) (Spero and Parker, 1985); and (iv) the concentration of carbonate ion in the seawater ($\delta^{13}\text{C}$ decreases with increasing $[\text{CO}_3^{2-}]$) (Spero et al., 1997).

3.3.2 Stable isotopes of foraminifera

3.3.2.1 *Neogloboquadrina pachyderma*

Stable isotope ratios of *Neogloboquadrina pachyderma* calcite are useful palaeoceanographic and palaeoclimatic proxies as they correlate with surface water conditions in the polar regions (Kohfeld et al., 1996) which, in turn, are extremely sensitive to changes in climate. $\delta^{13}\text{C}$ and $\delta^{18}\text{O}$ of Np calcite have been widely used to determine variations in deep water circulation (Lehman and Keigwin, 1992), changes in upwelling and surface water productivity among others (Charles and Fairbanks, 1990). A fairly constant relationship exists between SST and $\delta^{18}\text{O}_{\text{calcite}}$: an approximately 4°C increase in SST (0-20 m depth) results in $\sim 1\text{‰}$ decrease in $\delta^{18}\text{O}_{\text{calcite}}$ (Epstein et al, 1953). $\delta^{18}\text{O}$ of Np in the Arctic region varies by 1.5‰ between 50 and 200 m water depth; $\delta^{13}\text{C}$ values do not vary significantly in the same depth zone, but remain within $0.50 \pm 0.14\text{‰}$ (Kohfeld et al., 1996).

A consistent offset of $\sim 1\text{‰}$ was observed in the $\delta^{18}\text{O}_{\text{calcite}}$ relative to the equilibrium calcite value measured from in-situ seawater $\delta^{18}\text{O}$ and temperature in the Arctic Ocean, and has been attributed to vital effects (Bauch et al., 1997). To accurately determine $\delta^{18}\text{O}_{\text{calcite}}$ these vital effects need to be accounted for. In polar regions, a correction factor of $0.73\text{‰} \pm 0.2$ can be included into calculations of foraminiferal $\delta^{18}\text{O}$ to account for vital effects when comparing with equilibrium $\delta^{18}\text{O}$ to determine calcification depths (Hendry et al., 2009). Size can affect $\delta^{18}\text{O}_{\text{calcite}}$ as smaller (125-180 μm) specimens show on average a -0.79‰ difference compared to larger specimens (180-250 μm) (Jonkers et al., 2013). This variation is due to different calcification depth between large and small specimens,

calcification rate and respiration. Plankton tow samples from the Northern Pacific (Kuroyanagi et al., 2011) show that large *Neogloboquadrina pachyderma* specimens secrete their shell more slowly and at shallower depth with both higher $\delta^{18}\text{O}$ and $\delta^{13}\text{C}$ values than smaller ones.

Calculating $\delta^{13}\text{C}_{\text{calcite}}$ of the tests is simplified at high-latitude regions because temperature is decoupled from other environmental factors in regions where seasonal sea ice conditions dominate. Due to decreased gas exchange between the surface waters and the atmosphere during the austral winter, $\delta^{13}\text{C}_{\text{calcite}}$ becomes 0.8‰ lower (Meredith et al., 2013). This is reversed once sea-ice melts during the spring season allowing the replenishment of CO_2 with lower $\delta^{13}\text{C}$ into the surface waters.

Seasonality variability of *Neogloboquadrina pachyderma* abundance and stable isotope composition:

Several modern studies of *Neogloboquadrina pachyderma* have attempted to constrain the species' calcification depth range, seasonal variability of abundance and stable isotope composition (e.g. Kuroyanagi et al., 2011; Jonkers et al., 2013; Sagawi et al., 2013; Asahi, et al., 2016). These studies covered a range of locations across the global ocean (e.g. North Atlantic, Arctic Ocean, Northern Pacific Ocean, Bering Sea, South Atlantic, Southern Ocean) and identified region-specific calcification depths and vital offsets relating to the hydrographic conditions of the areas (e.g. Volkmann and Mensch, 2001; Hillaire-Marcel et al., 2004; Kuroyanagi et al., 2011; Jonkers et al., 2013).

Neogloboquadrina pachyderma has been found to calcify in a wide part of the water column. Calcification within the mixed layer near the pycnocline was found in the Atlantic and in the Pacific Ocean (Ortiz et al., 1996; Volkmann and Mensch, 2001; Hillaire-Marcel et al., 2004; Kozdon et al., 2009; Asahi et al., 2015). Calcification within the shallower parts of the mixed layer was identified by Sagawa et al. (2013) in the western North Pacific. Other studies identified calcification below the surface mixed layer within the pycnocline – in the North Atlantic (Bauch et al., 1997; Jonkers et al., 2013) and in the South Atlantic (Mortyn and Charles, 2001). As the depth of the mixed layer varies across the oceans, calcification depths inevitably vary across the global ocean.

Calcification in equilibrium with the surrounding seawater was found in the North Atlantic (Jonkers et al., 2013) and in the Nordic Seas (Simstich et al., 2003). In contrast and more commonly, vital offsets of up to -1.0‰ were detected in the Arctic Ocean (Hillaire-Marcel et al., 2004), northern North Atlantic (Bauch et al., 1997; Kozdon et al., 2009); in the western North Pacific (Kuroyanagi et al., 2011); Bering Sea (Asahi et al., 2015) and in the South Atlantic (Mortyn and Charles, 2001).

Two main peak flux events have been observed in most of the sediment trap studies, including in the Bering Sea, (Asahi and Takahasi, 2007), northwestern North Pacific Ocean (Kuroyanagi et al., 2011, Sagawa et al., 2013), in the North Atlantic (Jonkers et al., 2013), and in the western Pacific/southern Australia sector of the Southern Ocean (King and Howard, 2004). The first peak in Np flux coincides with the spring bloom and the second with the time of maximum stratification in all these studies.

3.3.2.2 *Globorotalia inflata*

Core-top samples of *G. inflata* show that $\delta^{18}\text{O}_{\text{calcite}}$ of this species range between $\sim 1.5\text{‰}$ and 3.0‰ from 35°S to 50°S respectively while $\delta^{13}\text{C}$ values range from 0.8‰ to $\sim 1.8\text{‰}$ over the same latitudes (Groeneveld and Chiessi, 2011, Morard et al., 2016). $\delta^{13}\text{C}_{\text{calcite}}$ values show a clear trend towards more positive numbers with increasing latitudes, while the $\delta^{18}\text{O}_{\text{calcite}}$ values are more variable (Chiessi et al. 2007).

G. inflata moves deeper in the water column during its life cycle, to depths of up to 800 m. As the organism sinks from the surface water towards deeper waters it continues to add volume to its test by the addition of a secondary calcite crust which can account for as much as 50% of the total shell weight (Lohmann, 1995, Wilke et al., 2006, Chiessi et al. 2007). This continuous calcification results in the $\delta^{18}\text{O}$ values of deeper waters being incorporated into the calcite crust hence making this species a useful indicator of changes taking place in deeper waters. Seasonal variability of the Brazil-Malvinas Confluence is recorded in the variability of the $\delta^{18}\text{O}$ value and the calcification depth of *G. inflata* (Chiessi et al. 2007).

The $\delta^{13}\text{C}$ of *G. inflata* is mainly controlled by the $\delta^{13}\text{C}_{\text{DIC}}$ of the seawater and by the concentration of CO_3^{2-} ($[\text{CO}_3^{2-}]$) of the seawater as opposed to temperature (Wilke et al., 2006). $\delta^{13}\text{C}$ of this species becomes lighter with increased size and weight - a $\sim 1\text{‰}$ change between $250\mu\text{m}$ and $500\mu\text{m}$ - while a similar relationship is not observed between $\delta^{18}\text{O}$ and size/weight (Elderfield et al. 2002). This reflects the downward migration of *G. inflata* during calcification and the incorporation of lighter carbonate isotopes into the calcite crust at depth. Carbon isotope ratios of *G. inflata* show a positive correlation with nutrient concentrations in the South Atlantic (Chiessi et al. 2007).

4. Materials and Methods

The foraminifera used in this research were recovered from three different settings. Specimens obtained from plankton tows were collected during the RRS *James Clark Ross* cruise JR304 (Figure 4.1) in November-December 2014, as part of the scientific component of the cruise funded by the British Antarctic Survey (Watkins et al., 2016). The main goal of the cruise was to undertake the Western Core Box survey – a yearly assessment of krill distribution and biomass- and to carry out a series of 36 hour-long time stations across the Scotia Sea for collaborative biological studies. Specimens obtained from sediment trap samples (Figure 4.1) were recovered between 2006 and 2013 as part of the Palmer Station Antarctica Long Term Ecological Research (Palmer LTER) Network funded by the United States National Science Foundation. The main aim of the Palmer LTER study that began in 1993 off the coast of Palmer Station is to understand how the seasonality and interannual variability of sea ice extent and duration influence the ecosystems and biogeochemical cycle along the marginal sea ice zone (Smith et al., 1995). The marine sediment core JR244 - GC528 (Figure 4.1) used in this study was collected during the RRS *James Clark Ross* cruise JR244 between January and March 2011 as part of the Quaternary Sediments Workpackage within the Chemistry and Past Climate Programme funded the British Antarctic Survey. The main aim of the cruise was to gain new insight into the glacial maxima around the South Orkney Islands and in the southern Weddell Sea during the late Quaternary, to study past glacial retreats and to assess the changes in paleoceanographic conditions in these areas (Larter et al., 2011). The project aims for the three sample sets can be found in Chapter 1.3.

The aim of this chapter is to describe the regional setting of the localities the foraminifera specimens were collected from and to provide information on the methodologies used throughout my research.

4.1 JR304 cruise materials and methods

The JR304 cruise was a science and logistic leg of the 2014-15 passage of the RRS *James Clark Ross* to Antarctica, which took place between 15th November and 17th December 2014. The cruise combined base relief and replenishment work with research activities in the Scotia Sea. The science aspect of the cruise covered a number of objectives. These include the annual krill biomass survey (Western Core Box) in the South Georgia region, four time station investigations to study diel changes in the

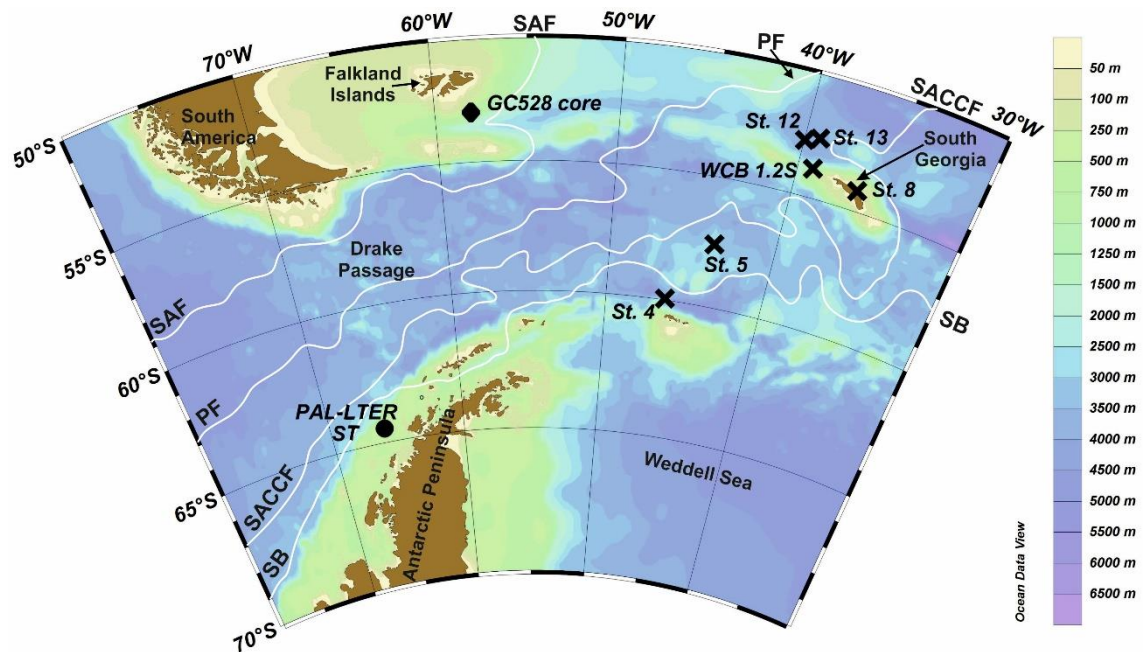


Figure 4.1: Bathymetry map (Schlitzer, R. 2016) of the South Atlantic section of the Southern Ocean highlighting the location of the samples used in the three studies. The location of the main Bongo net samples and CTD samples collected during the JR304 cruise are represented by black crosses. The Palmer LTER sediment trap (black circle) is located at 64.3°S 66.0°W, 130 km offshore from the Antarctic Peninsula. Sediment core JR244 - GC528 is located at 53.0°S 58°W, and is denoted by the black diamond. The main oceanic fronts are represented by white lines: SAF: Subantarctic Front, PF: Polar Front, SACCF: Southern Antarctic Circumpolar Current Front, SB: Southern Boundary of the Antarctic Circumpolar Current.

production and distribution of the pelagic food-web and the vertical plankton tow sampling of the water column for marine zooplankton (Watkins et al., 2016).

4.1.1 Sampling for foraminifera

Vertical plankton tow samples were collected with a motion-compensated Bongo net between 17th November and 14th December 2014 as part of the cruise activities. Samples were collected at 13 stations between 59.9° and 52.6°S and 58.2° and 36.45°W (Table 4.1). Sampling with the Bongo net was carried out as an additional, complementary activity to other planned activities at the stations. Bongo net deployments were made during the cruise transit phase to accompany Continuous Plankton Recorder (CPR) tows, during the 36-hour diel stations to sample the zooplankton community over the diel cycle, during the visit to one of the northern bay areas of South Georgia (Figure 4.1) with the primary aim of sampling for pteropods, and during the Western Core Box to characterise the zooplankton community compositions. The diversity of the locations spanning a 5°C SST range between north of the Polar Front and South of the Southern Boundary of the Antarctic Circumpolar Current (SB) offered ample opportunities to sample foraminifera from different environmental conditions.

Table 4.1: Foraminifera sampling localities during JR304 cruise with date, station name and number, latitude and longitude of sampling, bongo net mesh size, and the bottom depth of bongo net deployment. Highlighted rows represent the localities where seawater samples were also collected using a CTD.

| Date | Station No./name | Lat. (°) | Long. (°) | Mesh size (µm) | Depth (m) |
|------------------|-------------------------------------|----------|-----------|----------------|-----------|
| 17/11/2014 18:38 | Station 1 | -56.67 | -58.17 | 200 | 200 |
| 17/11/2014 19:07 | Station 1 | -56.67 | -58.17 | 100 | 200 |
| 18/11/2014 16:21 | Station 2 | -58.99 | -51.8 | 100 | 200 |
| 19/11/2014 11:24 | Station 3 | -60.77 | -46.48 | 100 | 115 |
| 25/11/2014 15:49 | Station 4 | -59.96 | -46.16 | 100 | 100 |
| 25/11/2014 15:53 | Station 4 | -59.96 | -46.16 | 100 | 200 |
| 25/11/2014 19:13 | Station 4 | -59.96 | -46.16 | 100 | 100 |
| 25/11/2014 19:28 | Station 4 | -59.96 | -46.16 | 100 | 200 |
| 26/11/2014 14:40 | Station 4 | -59.96 | -46.16 | 100 | 100 |
| 27/11/2014 13:10 | Station 5 - P2 | -57.61 | -43.67 | 100 | 200 |
| 28/11/2014 08:23 | Station 6 | -55.24 | -41.26 | 100 | 200 |
| 29/11/2014 15:17 | Station 6 | -55.25 | -41.26 | 100 | 100 |
| 29/11/2014 15:29 | Station 6 | -55.25 | -41.26 | 100 | 200 |
| 03/12/2014 15:38 | Station 8 | -54.2 | -36.45 | 100 | 100 |
| 03/12/2014 15:54 | Station 8 - Cumberland Bay | -54.2 | -36.45 | 200 | 200 |
| 08/12/2014 23:12 | WCB 1.2N Station | -53.49 | -39.25 | 100 | 200 |
| 09/12/2014 06:59 | WCB 1.2S station - Western Core Box | -53.85 | -39.14 | 100 | 200 |
| 10/12/2014 04:54 | WCB 2.2N station | -53.43 | -38.7 | 100 | 200 |
| 10/12/2014 04:54 | WCB 2.2N station | -53.43 | -38.7 | 200 | 200 |
| 11/12/2014 05:40 | WCB 3.2S station | -53.71 | -37.97 | 100 | 100 |
| 11/12/2014 05:40 | WCB 3.2S station | -53.71 | -37.97 | 200 | 200 |
| 13/12/2014 06:26 | Station 12 - P3 | -52.81 | -39.97 | 100 | 200 |
| 13/12/2014 21:17 | Station 12 | -52.81 | -39.97 | 200 | 200 |
| 13/12/2014 21:39 | Station 12 | -52.81 | -39.97 | 200 | 100 |
| 14/12/2014 08:27 | Station 13 | -52.6 | -39.2 | 100 | 100 |
| 14/12/2014 08:46 | Station 13 - Upwelling | -52.6 | -39.2 | 100 | 200 |
| 14/12/2014 15:57 | Station 13 | -52.6 | -39.2 | 100 | 200 |

Foraminifera samples were collected with a motion-compensated Bongo net (Figure 4.2) with two nets (100 µm and 200 µm mesh-size) attached to the two 57 cm wide net rings. Plastic bags were placed in the collection-end of the nets and tightened on the cod-end with jubilee clips. The Bongo net was lowered to 100 and 200 m water depth off the port side of the ship. Once the net was brought back to the ship the plastic bags were removed from the cod-ends and the contents were gently poured in to buckets partially filled with seawater. The 200 µm mesh samples were immediately poured over a pre-cut

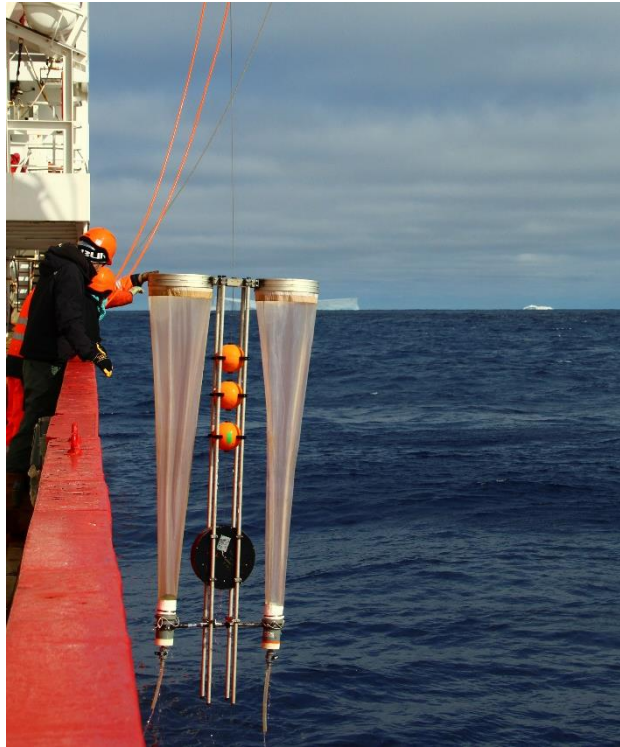


Figure 4.1: Motion-compensated bongo net being deployed on the port side of the ship.

200 μm filter mesh, folded and frozen at -80°C . The 100 μm mesh samples were sampled for zooplankton. At every station, foraminifera abundance was low enough to remove all the specimens from the buckets. These were placed in glass petri dishes and *Neogloboquadrina pachyderma* (Np) specimens were picked with a fine brush. The specimens were gently rinsed three times in dionised water to prevent the precipitation of salt crystals on/within the shells after which they were placed in microfossil slides, and counted, air dried and transported back to UK for stable isotope analysis.

4.1.2 Water Column profiling

Nineteen CTD casts were carried out to vertically profile the water column at 10 different stations. Six of the 19 casts (Stations 4, 5, 8, 12, 13 and WCB 1.2S) were selected to provide water column profiles at the main foraminiferal sampling locations (Figure 4.1). The CTD unit included a SBE32 carousel water sampler, 24 12-litre niskin bottles, a SBE9Plus CTD and a SBE11Plus deck unit (Figure 4.3). The SBE9Plus CTD unit included a temperature and a conductivity sensor, as well as a submersible pump. In addition, a SBE35 Deep Ocean Standards Thermometer was also attached to make temperature readings each time a niskin bottle was fired, allowing for the calibration of the SBE9Plus CTD unit. An altimeter, a fluorometer, a photosynthetically active radiation (PAR) sensor, two oxygen sensors and a transmissometer were also attached to the CTD unit to provide as much information on the water properties as possible. The CTD

data was collected at 24Hz and logged to a PC. The Seasave 7.22.3 by Sea-Bird Electronics, Inc. software was used to process the relayed data (Watkins et al., 2016).

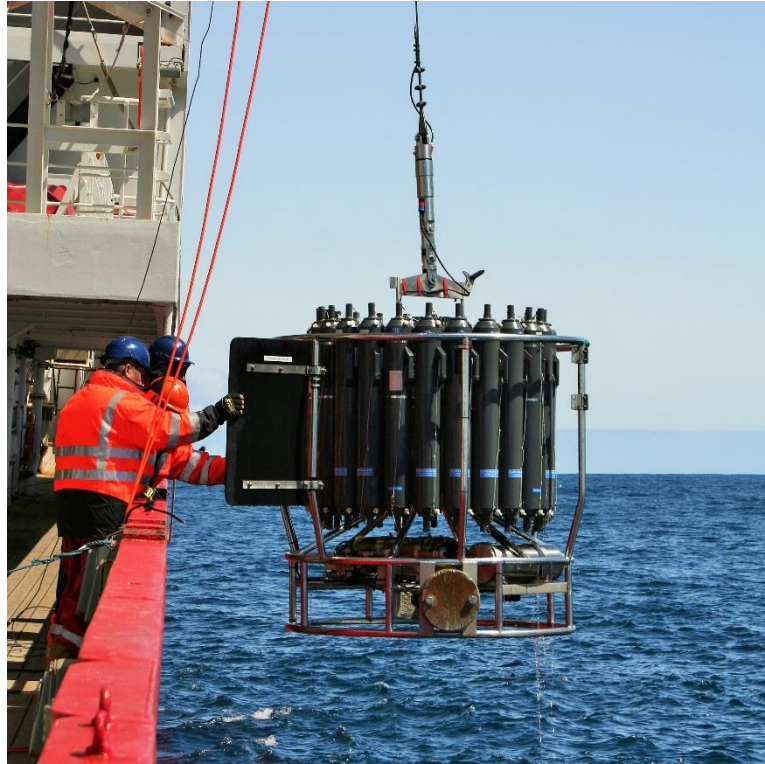


Figure 4.2: CTD unit with niskin bottles being deployed on the port side of the ship.

4.1.3 Seawater stable isotope analysis

The 24 niskin bottles attached to the CTD unit were used to collect water samples from discreet water depths simultaneously with the profiling. The niskin bottles were fired at predetermined depths that covered the depth range of the Bongo nets with an additional sample collected at 500 m water depth or the bottom of the cast, depending on which was deeper. Once back on deck the niskin bottles were sampled immediately for seawater stable oxygen isotope analysis. The samples for $\delta^{18}\text{O}$ analysis were collected as a priority to prevent any gas exchange between the niskin bottle and the air. The seawater from the niskin bottles was transferred into 30 mL Nalgene bottles via a tygon tube which was soaked in filtered seawater overnight to prevent bubble formation. The Nalgene bottles were left to overflow approximately three times to limit air bubbles in the bottle. The filled Nalgene bottles were capped, wrapped in parafilm and stored at 4°C until analysis. Altogether, 41 water samples were collected for $\delta^{18}\text{O}$ analysis. Water samples were also collected for TA/DIC analysis, $\delta^{13}\text{C}$ of Particulate Organic Carbon ($\delta^{13}\text{C}_{\text{POC}}$) and $\delta^{13}\text{C}$ of Dissolved Inorganic Carbon ($\delta^{13}\text{C}_{\text{DIC}}$) analysis to provide a complete dataset about surface water carbonate chemistry. Unfortunately, a third of the precipitated inorganic carbon samples contained insufficient material for analysis. The

other two-third of the samples were analysed for $\delta^{13}\text{C}_{\text{DIC}}$; however, the analysis yielded measurements which were outside the expected $\delta^{13}\text{C}_{\text{DIC}}$ variation: average value of -9.95‰ instead of the expected $0.4\text{-}1.0\text{‰}$ range in the South Atlantic Ocean (Kroopnick, 1985). Therefore further analyses for carbonate and nutrients were abandoned.

The 30 mL water samples were analysed for stable oxygen isotope ratios at the Stable Isotope Facility of the British Geological Survey in Keyworth, UK. The samples were analysed using an IsoPrime 100 instrument equipped with an Aquaprep. The seawater $\delta^{18}\text{O}$ analysis followed the equilibrium method for oxygen (Epstein and Mayeda, 1953). Every sample was run three times to establish precision, with an average of $\pm 0.02\text{‰}$ achieved. All isotopic measurements are reported as per mil deviation from the Vienna Standard Mean Ocean Water2 (‰ VSMOW2).

4.1.4 *Neogloboquadrina pachyderma* stable isotope analysis

Stable isotope measurements on the Np specimens from the plankton tows and from the sediment trap were carried out at the Faculty of Earth and Life Sciences, Vrije University, Amsterdam, which were visited in person between 15th January 2016 and 13th February 2016. The laboratory was chosen based on the capability of the mass spectrometer, which can measure carbonate material weighing as little as 6-7 μg reliably. Prior to analysis we attempted to chemically clean the specimens to remove any organic or inorganic matter present on/in the tests. As a test, 10 specimens were placed in a vial with a 3% H_2O_2 solution for 30 minutes followed by three dionised water rinses. After the final rinse, methanol was added to the vial which was placed in a sonic bath for 15 seconds. The specimens were rinsed again three times with dionised water and air-dried. At the end of this test, the specimens were inspected under a microscope to assess potential damage caused by the cleaning procedure. Out of the 10 specimens only four survived the cleaning procedure intact. The rest of the tests broke into multiple pieces or disintegrated entirely. As a result, the chemical cleaning step was abandoned. The specimens were recovered live from surface waters hence it is unlikely that the tests contained any other carbonate material (chiefly coccolithophores) which could alter the stable isotope signal of the test and we are confident that the chemical cleaning step was not a pre-requisite of the stable isotope analysis.

Np specimens were weighed individually on a Mettler Toledo XPR2U high precision microbalance ($d=0.1 \mu\text{g}$) in pre-weighed aluminium foil boats in Amsterdam. The specimens were placed into the foil boats with a dry-brush to prevent adding additional moisture to the sample. The stable isotope measurements were carried out on a Finnigan GasBench II carbonate preparation device interfaced with a Finnigan Delta isotope ratio

mass spectrometer. Each specimen was placed into a glass vial for analysis. Approximately 4-6 glass beads were placed on top of the specimens to prevent them from agitated in the vial when the acid is injected. The carbonate samples were acidified in helium flushed sample vials, creating CO₂. The resulting CO₂-helium mixture was transferred to the isotope ratio mass spectrometer to determine the $\delta^{18}\text{O}$ and $\delta^{13}\text{C}$ ratio of the gas. During this process, the mass spectrometer measures the available gas in each vial eight times in succession. As a result, at the first measurement, all the gas is available while for the last measurement, only a fraction of the originally available gas remains. Each of the eight measurements provide a $\delta^{18}\text{O}$ and a $\delta^{13}\text{C}$ value so the standard deviation for each sample is derived from the variability between the eight measurements. The spectrometer was calibrated through the international standard IAEA-CO1 and the laboratory's own in-house standard VICS. A range of weights of VICS standards were measured on a microbalance to ensure that the mass spectrometer was generating enough signal at all weights. The IAEA-CO1 standard was placed into vials with a special pipette to place exact amount of material into vial. A range of masses (approximately 5-40 μg) of IAEA-CO1 standard was run alongside the samples to provide accurate calibration. All isotopic measurements are reported as per mil deviation from the Vienna Pee Dee Belemnite scale (‰ VPDB). Analytical reproducibility of carbonate industrial standards run concurrently with the Np specimens was between 0.10‰ and 0.12‰ for $\delta^{13}\text{C}$ and between 0.07‰ and 0.12‰ for $\delta^{18}\text{O}$.

4.1.5 Predicting equilibrium $\delta^{18}\text{O}$ value of calcite

The single specimen *Neogloboquadrina pachyderma* $\delta^{18}\text{O}$ ($\delta^{18}\text{O}_{\text{np}}$) measurements were compared with expected equilibrium $\delta^{18}\text{O}$ calcite ($\delta^{18}\text{O}_{\text{calcite}}$) values to determine calcification depths, temperature and potential vital effects. The equilibrium $\delta^{18}\text{O}$ value of foraminiferal calcite was calculated using the Kim and O'Neil (1997) equation (Eq. 1). This equation is particularly stable at low temperatures (Bemis et al., 1998). Equilibrium $\delta^{18}\text{O}$ ($\delta^{18}\text{O}_{\text{eq}}$) values were calculated for water depths which had corresponding available seawater $\delta^{18}\text{O}$ ($\delta^{18}\text{O}_{\text{sw}}$) measurements.

$$\delta^{18}\text{O}_{\text{eq}} = [25.778 - 3.333 \times (43.704 + T)^{0.5}] + \delta^{18}\text{O}_{\text{sw}} \quad \text{Equation 1}$$

where T is temperature, and $\delta^{18}\text{O}_{\text{sw}}$ is the corresponding stable isotope value of the seawater. To calculate accurate $\delta^{18}\text{O}_{\text{eq}}$ values, depth specific temperature values collected by the CTD units and $\delta^{18}\text{O}_{\text{sw}}$ measurements provided by the seawater $\delta^{18}\text{O}$ analysis were used. The $\delta^{18}\text{O}_{\text{sw}}$ measurements (which are reported against Standard Mean Ocean Water (versus SMOW - VSMOW)) were converted to Vienna Pee Dee Belemnite (VPDB) scale prior to $\delta^{18}\text{O}_{\text{eq}}$ calculation using the Bemis et al. (1998) equation

(Eq. 2) in order to be comparable to calcite stable isotope measurements which are routinely reported against VPDB:

$$\delta^{18}O_{sw(VPDB)} = 0.9998 \times \delta^{18}O_{SMOW} - 0.2 \quad \text{Equation 2}$$

No vital effect corrections were made to the $\delta^{18}O_{eq}$ calculations because the aim was to investigate the presence/absence of any vital effect in the $\delta^{18}O_{np}$ signal.

4.2 PAL-LTER Time series

Foraminifera specimens taken from the Palmer Long Term Ecological Research project (LTER) sediment trap (Figure 4.1), deployed since 1993 collecting surface water particle flux, were used for this part of the project. The Palmer LTER sediment trap is moored in 350 m water depth at 64° 30'S, 66° 00'W, approximately 130 km offshore from Palmer Station in the west Antarctic Peninsula midshelf region (Gleiber et al. 2012). The trap is suspended at 170 m water depth (Ducklow et al. 2008) where it collects sinking particles through its 0.5 m² surface area. The time series sediment trap is a PARFLUX Mark 78H 21-sample trap (by McLane Research Labs, Falmouth, MA) which collects particles in 500 ml bottles (Figure 4.4). The traps are recovered and redeployed during January of each year. Sampling intervals vary according to expected sedimentation trends, resulting in shorter sampling intervals (7 days) during strong flux periods and longer ones (up to 92 days) during periods of slower sedimentation (Table 4.2) (Ducklow et al. 2008). The collected sediment trap samples are held at 5°C until arrival to the laboratory. The samples are gently rinsed to separate out any larger swimmers present in the samples. Zooplankton found within the trap samples are archived in 2% formaldehyde under cold conditions. The processed samples were split until 2002 by employing a PARFLUX Wet

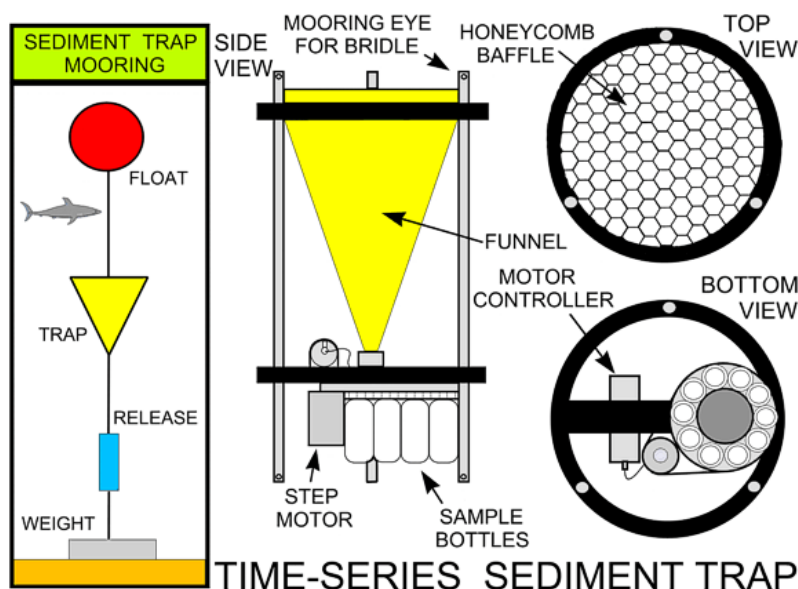


Figure 4.3: McLane PARFLUX Mark 78H 21-sample trap of the type deployed at the Palmer LTER site (Pope et al. 2000).

Sample Divider (by McLane Research), and since 2002 a plankton splitter has been used. Sediment trap samples with exceptionally high sedimentation were split up to 1/512 for analysis. All the samples were first analysed for total mass dry weight, organic carbon, particulate nitrogen and particulate phosphorus before any other analysis took place. Archived samples collected after 2002 are stored at Virginia Institute of Marine Sciences (VIMS), United States, in formalin. Any samples not archived are placed in 100 ml plastic cups, freeze-dried and stored at VIMS. More detailed information on the sample processing can be found in Ducklow et al. (2008).

4.2.1 *Neogloboquadrina pachyderma* flux measurements

Ninety-three (from a total of 125) sediment trap samples covering the time period between 18/01/2006 and 27/01/2013 were received from VIMS for the foraminifera flux study. To determine the flux of foraminifera, specimens were examined using a Zeiss optical microscope under 5-fold magnification.

Twenty-nine percent of the samples were whole, unsplit samples, while the rest (71%) were split portions of larger samples, with the split factor varying between 0.05 and 0.5 (Table 4.2). Inspection of the samples using the microscope revealed diatom concentrations of up to 90% in some cases. This can be attributed to the high-latitude location of the sediment trap. High percentage of faecal pellets were observed in samples with high sediment flux, relating to strong productivity. The majority of the sediment in the samples were made up of marine snow (organic material derived from dead plants and animals as well as from faecal matter) (Figure 4.5). This marine snow became clumped during the freeze-drying process, resulting – in some cases – in foraminifera becoming encased.

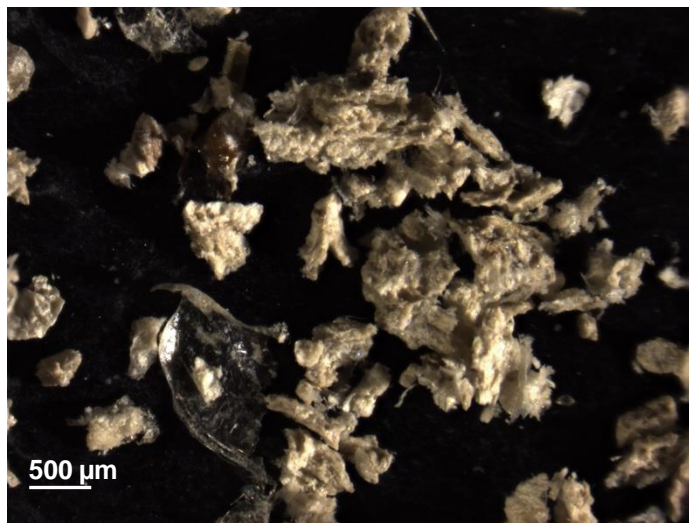


Figure 4.4: Clumped marine snow in 22/02/2012 sediment trap sample.

Table 4.2: Palmer LTER sediment trap collection periods, sediment trap cup ID numbers and sample split factors. Samples highlighted blue were not received as these have been depleted by other studies already.

| Start Date | End Date | Duration | Mid-Date | Sediment Trap Cup # | Split Factor |
|------------|------------|----------|------------|---------------------|--------------|
| 15/01/2006 | 22/01/2006 | 7 | 18/01/2006 | 1 | 0.50 |
| 22/01/2006 | 29/01/2006 | 7 | 25/01/2006 | 2 | 0.50 |
| 29/01/2006 | 12/02/2006 | 14 | 05/02/2006 | 3 | 0.10 |
| 12/02/2006 | 01/03/2006 | 17 | 20/02/2006 | 4 | 0.10 |
| 01/03/2006 | 01/04/2006 | 31 | 16/03/2006 | 5 | 0.10 |
| 01/04/2006 | 01/05/2006 | 30 | 16/04/2006 | 6 | 0.50 |
| 01/05/2006 | 01/06/2006 | 31 | 16/05/2006 | 7 | 0.50 |
| 01/06/2006 | 01/07/2006 | 30 | 16/06/2006 | 8 | 0.50 |
| 01/07/2006 | 01/09/2006 | 62 | 01/08/2006 | 9 | 0.50 |
| 01/09/2006 | 01/10/2006 | 30 | 16/09/2006 | 10 | 0.50 |
| 01/10/2006 | 01/11/2006 | 31 | 16/10/2006 | 11 | 0.50 |
| 01/11/2006 | 08/11/2006 | 7 | 04/11/2006 | 12 | 0.50 |
| 08/11/2006 | 15/11/2006 | 7 | 11/11/2006 | 13 | 0.50 |
| 15/11/2006 | 22/11/2006 | 7 | 18/11/2006 | 14 | 0.50 |
| 22/11/2006 | 29/11/2006 | 7 | 25/11/2006 | 15 | 0.50 |
| 29/11/2006 | 06/12/2006 | 7 | 02/12/2006 | 16 | 0.50 |
| 06/12/2006 | 13/12/2006 | 7 | 09/12/2006 | 17 | 0.50 |
| 13/12/2006 | 20/12/2006 | 7 | 16/12/2006 | 18 | 0.50 |
| 20/12/2006 | 27/12/2006 | 7 | 23/12/2006 | 19 | 0.50 |
| 27/12/2006 | 03/01/2007 | 7 | 30/12/2006 | 20 | 0.50 |
| 03/01/2007 | 10/01/2007 | 7 | 06/01/2007 | 21 | 0.50 |
| 15/01/2007 | 22/01/2007 | 7 | 18/01/2007 | 1 | 0.33 |
| 22/01/2007 | 29/01/2007 | 7 | 25/01/2007 | 2 | 0.33 |
| 29/01/2007 | 12/02/2007 | 14 | 05/02/2007 | 3 | 0.50 |
| 12/02/2007 | 01/03/2007 | 14 | 20/02/2007 | 4 | 0.50 |
| 01/03/2007 | 15/03/2007 | 14 | 08/03/2007 | 5 | 0.10 |
| 15/03/2007 | 01/04/2007 | 17 | 23/03/2007 | 6 | 0.10 |
| 01/04/2007 | 01/05/2007 | 30 | 16/04/2007 | 7 | 0.10 |
| 01/05/2007 | 01/06/2007 | 31 | 16/05/2007 | 8 | 0.33 |
| 01/06/2007 | 01/07/2007 | 30 | 16/06/2007 | 9 | No Split |
| 01/07/2007 | 01/09/2007 | 92 | 01/08/2007 | 10 | No Split |
| 01/09/2007 | 01/10/2007 | 31 | 16/09/2007 | 11 | No Split |
| 01/10/2007 | 01/11/2007 | 31 | 16/10/2007 | 12 | No Split |
| 01/11/2007 | 15/11/2007 | 14 | 08/11/2007 | 13 | No Split |
| 15/11/2007 | 22/11/2007 | 7 | 18/11/2007 | 14 | No Split |
| 22/11/2007 | 29/11/2007 | 7 | 25/11/2007 | 15 | No Split |
| 29/11/2007 | 06/12/2007 | 7 | 02/12/2007 | 16 | No Split |
| 06/12/2007 | 13/12/2007 | 7 | 09/12/2007 | 17 | No Split |
| 13/12/2007 | 20/12/2007 | 7 | 16/12/2007 | 18 | No Split |
| 20/12/2007 | 27/12/2007 | 7 | 23/12/2007 | 19 | No Split |
| 27/12/2007 | 03/01/2008 | 7 | 30/12/2007 | 20 | No Split |
| 03/01/2008 | 10/01/2008 | 7 | 06/01/2008 | 21 | No Split |

| Start Date | End Date | Duration | Mid-Date | Sediment Trap Cup # | Split Factor |
|------------|------------|----------|------------|---------------------|--------------|
| 15/01/2008 | 22/01/2008 | 7 | 18/01/2008 | 1 | 0.40 |
| 22/01/2008 | 29/01/2008 | 7 | 25/01/2008 | 2 | No Split |
| 29/01/2008 | 12/02/2008 | 14 | 05/02/2008 | 3 | 0.40 |
| 12/02/2008 | 01/03/2008 | 18 | 21/02/2008 | 4 | No Split |
| 01/03/2008 | 15/03/2008 | 14 | 08/03/2008 | 5 | 0.30 |
| 15/03/2008 | 01/04/2008 | 17 | 23/03/2008 | 6 | No Split |
| 01/04/2008 | 01/05/2008 | 30 | 16/04/2008 | 7 | 0.50 |
| 01/05/2008 | 01/06/2008 | 31 | 16/05/2008 | 8 | 0.50 |
| 01/06/2008 | 01/07/2008 | 30 | 16/06/2008 | 9 | No Split |
| 01/07/2008 | 01/09/2008 | 62 | 01/08/2008 | 10 | No Split |
| 01/09/2008 | 01/10/2008 | 30 | 16/09/2008 | 11 | No Split |
| 01/10/2008 | 01/11/2008 | 31 | 16/10/2008 | 12 | No Split |
| 01/11/2008 | 15/11/2008 | 14 | 08/11/2008 | 13 | 0.50 |
| 15/11/2008 | 22/11/2008 | 7 | 18/11/2008 | 14 | No Split |
| 22/11/2008 | 29/11/2008 | 7 | 25/11/2008 | 15 | 0.10 |
| 29/11/2008 | 06/12/2008 | 7 | 02/12/2008 | 16 | 0.50 |
| 06/12/2008 | 13/12/2008 | 7 | 09/12/2008 | 17 | No Split |
| 13/12/2008 | 20/12/2008 | 7 | 16/12/2008 | 18 | No Split |
| 20/12/2008 | 27/12/2008 | 7 | 23/12/2008 | 19 | No Split |
| 27/12/2008 | 03/01/2009 | 7 | 30/12/2008 | 20 | No Split |
| 03/01/2009 | 10/01/2009 | 7 | 06/01/2009 | 21 | No Split |
| 03/03/2010 | 19/03/2010 | 16 | 11/03/2010 | 1 | 0.50 |
| 19/03/2010 | 02/04/2010 | 14 | 26/03/2010 | 2 | 0.50 |
| 02/04/2010 | 16/04/2010 | 14 | 09/04/2010 | 3 | 0.15 |
| 16/04/2010 | 30/04/2010 | 14 | 23/04/2010 | 4 | 0.50 |
| 30/04/2010 | 30/05/2010 | 30 | 15/05/2010 | 5 | 0.15 |
| 30/05/2010 | 30/06/2010 | 31 | 14/06/2010 | 6 | 0.50 |
| 30/06/2010 | 30/07/2010 | 30 | 15/07/2010 | 7 | 0.75 |
| 30/07/2010 | 30/08/2010 | 31 | 14/08/2010 | 8 | 0.50 |
| 30/08/2010 | 30/09/2010 | 31 | 14/09/2010 | 9 | 0.50 |
| 30/09/2010 | 15/10/2010 | 15 | 07/10/2010 | 10 | 0.50 |
| 15/10/2010 | 22/10/2010 | 7 | 18/10/2010 | 11 | 0.50 |
| 22/10/2010 | 03/11/2010 | 12 | 28/10/2010 | 12 | 0.50 |
| 03/11/2010 | 15/11/2010 | 12 | 09/11/2010 | 13 | 0.05 |
| 15/11/2010 | 23/11/2010 | 8 | 19/11/2010 | 14 | 0.05 |
| 23/11/2010 | 30/11/2010 | 7 | 26/11/2010 | 15 | 0.50 |
| 30/11/2010 | 07/12/2010 | 7 | 03/12/2010 | 16 | No Split |
| 07/12/2010 | 14/12/2010 | 7 | 10/12/2010 | 17 | 0.50 |
| 14/12/2010 | 21/12/2010 | 7 | 17/12/2010 | 18 | 0.50 |
| 21/12/2010 | 28/12/2010 | 7 | 24/12/2010 | 19 | No Split |
| 28/12/2010 | 04/01/2011 | 7 | 31/12/2010 | 20 | 0.50 |
| 04/01/2011 | 10/01/2011 | 6 | 07/01/2011 | 21 | No Split |
| 15/01/2011 | 22/01/2011 | 7 | 18/01/2011 | 1 | 0.15 |
| 22/01/2011 | 29/01/2011 | 7 | 25/01/2011 | 2 | 0.15 |
| 29/01/2011 | 12/02/2011 | 14 | 05/02/2011 | 3 | 0.05 |

| Start Date | End Date | Duration | Mid-Date | Sediment Trap Cup # | Split Factor |
|------------|------------|----------|------------|---------------------|--------------|
| 12/02/2011 | 01/03/2011 | 17 | 20/02/2011 | 4 | 0.05 |
| 01/03/2011 | 15/03/2011 | 14 | 08/03/2011 | 5 | 0.05 |
| 15/03/2011 | 01/04/2011 | 17 | 23/03/2011 | 6 | 0.05 |
| 01/04/2011 | 01/05/2011 | 30 | 16/04/2011 | 7 | 0.10 |
| 01/05/2011 | 01/06/2011 | 31 | 16/05/2011 | 8 | 0.50 |
| 01/06/2011 | 01/07/2011 | 30 | 16/06/2011 | 9 | 0.50 |
| 01/07/2011 | 01/09/2011 | 62 | 01/08/2011 | 10 | 0.50 |
| 01/09/2011 | 01/10/2011 | 30 | 16/09/2011 | 11 | 0.50 |
| 01/10/2011 | 01/11/2011 | 31 | 16/10/2011 | 12 | 0.50 |
| 01/11/2011 | 15/11/2011 | 14 | 08/11/2011 | 13 | No Split |
| 15/11/2011 | 22/11/2011 | 7 | 18/11/2011 | 14 | 0.50 |
| 22/11/2011 | 29/11/2011 | 7 | 25/11/2011 | 15 | 0.50 |
| 29/11/2011 | 06/12/2011 | 7 | 02/12/2011 | 16 | 0.50 |
| 06/12/2011 | 13/12/2011 | 7 | 09/12/2011 | 17 | 0.50 |
| 13/12/2011 | 20/12/2011 | 7 | 16/12/2011 | 18 | 0.50 |
| 20/12/2011 | 27/12/2011 | 7 | 23/12/2011 | 19 | 0.50 |
| 27/12/2011 | 03/01/2012 | 7 | 30/12/2011 | 20 | No Split |
| 03/01/2012 | 01/02/2012 | 17 | 23/01/2012 | 1 | 0.10 |
| 15/01/2012 | 15/02/2012 | 14 | 08/02/2012 | 2 | 0.30 |
| 01/02/2012 | 01/03/2012 | 15 | 22/02/2012 | 3 | 0.10 |
| 15/02/2012 | 01/04/2012 | 31 | 16/03/2012 | 4 | 0.10 |
| 01/03/2012 | 01/05/2012 | 30 | 16/04/2012 | 5 | 0.30 |
| 01/04/2012 | 01/06/2012 | 31 | 16/05/2012 | 6 | No Split |
| 01/05/2012 | 01/09/2012 | 92 | 17/07/2012 | 7 | No Split |
| 01/06/2012 | 01/10/2012 | 30 | 16/09/2012 | 8 | No Split |
| 01/10/2012 | 01/11/2012 | 31 | 16/10/2012 | 9 | No Split |
| 01/11/2012 | 15/11/2012 | 14 | 08/11/2012 | 10 | No Split |
| 15/11/2012 | 22/11/2012 | 7 | 18/11/2012 | 11 | No Split |
| 22/11/2012 | 29/11/2012 | 7 | 25/11/2012 | 12 | No Split |
| 29/11/2012 | 06/12/2012 | 7 | 02/12/2012 | 13 | 0.30 |
| 06/12/2012 | 13/12/2012 | 7 | 09/12/2012 | 14 | 0.30 |
| 13/12/2012 | 20/12/2012 | 7 | 16/12/2012 | 15 | No Split |
| 20/12/2012 | 27/12/2012 | 7 | 23/12/2012 | 16 | No Split |
| 27/12/2012 | 03/01/2013 | 7 | 30/12/2012 | 17 | No Split |
| 03/01/2013 | 10/01/2013 | 7 | 06/01/2013 | 18 | No Split |
| 10/01/2013 | 17/01/2013 | 7 | 13/01/2013 | 19 | No Split |
| 17/01/2013 | 24/01/2013 | 7 | 20/01/2013 | 20 | 0.50 |
| 24/01/2013 | 31/01/2013 | 7 | 27/01/2013 | 21 | 0.75 |

A number of different techniques were employed in order to break up the clumps of marine snow and free any foraminifera trapped within the samples. First, samples were gently rinsed through a sieve with di-ionised water to break up clumps. This proved insufficient as not all clumps broke up and samples became static after the rinse. In order

to dissolve the organic material the samples were treated with a 3% solution of H₂O₂ for 30 minutes. Samples were sonicated in a sonic bath for 30 seconds to break up clumps. After sonication the samples were rinsed with di-ionised water to remove any dissolved or loosely clumped organic material. This approach was also unsuccessful because the organic material did not break up or dissolve sufficiently to release the foraminifera tests. Raising the sonication period to 1 minute resulted in the breakage of the foraminifera specimens. Another approach was to introduce di-ionised water to the samples placed in a petri dish. The aim was to collect foraminifera specimens with a pipette as the less dense organic material would float to the surface while the foraminifera would collect on the bottom of the petri dish. This approach was slightly more successful as it countered problems with static behaviour (created by the freeze-drying process), however, it did not aid the break-up of clumps. As none of these approaches helped with releasing the foraminifera from the organic material, individual specimens were picked from samples with a wet brush. Although this was time consuming it ensured that all specimens were removed from the trap samples. A soft fine brush was placed in di-ionised water for a couple of seconds, then without drying, clumps of organic matter were gently separated in a sampling tray. Every foraminifera specimen found within the samples was removed and placed in holding trays.

Once all foraminifera specimens were removed from the sediment trap cups the specimens were counted using a specimen tally counter. Results are presented as number of specimens per m² per day. Collection periods vary during the course of an annual cycle therefore results were averaged to a one day period. To account for the production and settling time the flux records were shifted by 1 week based on Np sinking speeds of 0.189 to 0.431 cm/s reported by Von Gyldenfeldt et al (2000). This shift was applied to all the foraminifera records in Chapter 5.2. The time-shifted Np flux and stable isotope records were used to create average annual composite figures following methods used by Jonkers et al (2010) in order to average out inter-annual variability in Chapter 5.2. To create the average annual composite figures the calendar dates of the Np flux records were converted to year days. The daily values of flux, organic carbon, organic nitrogen and sea ice concentration were each averaged over consecutive seven-day periods in the six different years (2006, 2007, 2008, 2010, 2011, and 2012) to make a composited year, described by weekly averages. Sea surface temperature and chlorophyll α concentration values were already presented as weekly averages. These weekly average values were used to create a synthetic sedimentary signal with the mid-dates of the weekly averages used to present the records in Chapter 5.2.

4.2.2 Measurements of morphology

One of the aims of the sediment trap study was to assess the morphological variability of *N. pachyderma* shells that lived under different environmental conditions. Morphological parameters of the foraminifera specimens were collected by two different methods.

4.2.2.1 Automated image acquisition

Selected multi-specimen samples were measured using an automated microscope and image analysis system (Bollmann et al., 2004) at the University of Bristol (Figure 4.6). The system utilises an incident light microscope analyser to view samples placed in glass/plexi trays. The glass trays are held in a plastic holder equipped with adjustable feet for levelling the trays. Underneath the trays a sheet of black velvet is placed which enhances the contrast of the calcite specimens (which are naturally white in colour) and absorbs any reflected light. The system automatically scans the holding trays placed on a motorised stage and captures images via a CCD video camera attached to a Wild MZ3 incident light stereomicroscope. Foraminifera samples were carefully evenly distributed on each of the six glass trays to prevent specimens clumping together. Once the image acquisition is completed Analysis5.0 software is used to identify individual specimens on the images. This is achieved by thresholding, whereby the differences in grey value distribution are used to differentiate between objects in the foreground and the background itself. To achieve high precision it is essential that light intensity is constant throughout the image acquisition –which can take up to 4-6 hours–, a high contrast is set

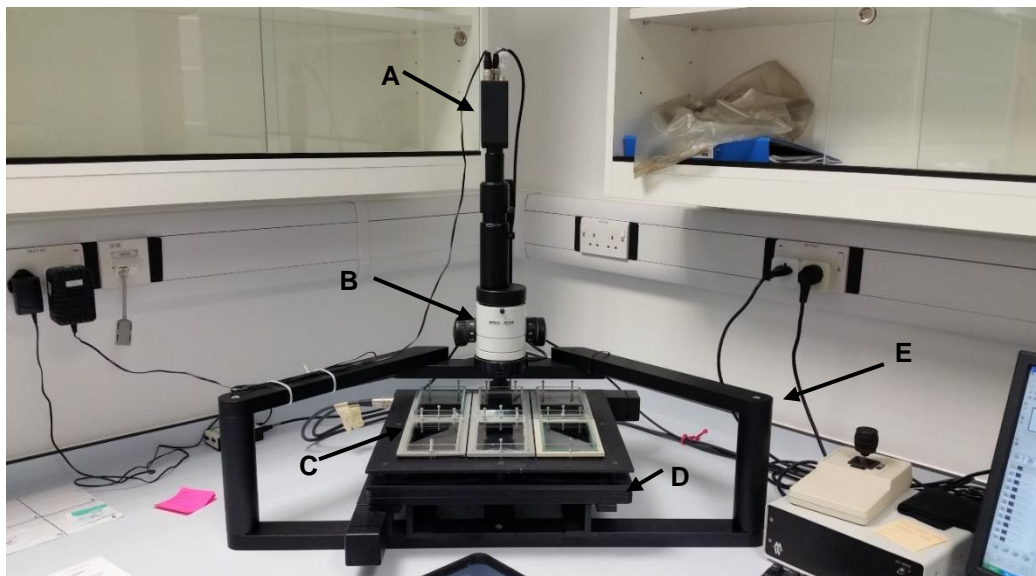


Figure 4.5: Automated microscope system set up at Bristol University. A: CCD video camera; B: Incident light microscope; C: Glass trays with adjustable feet for levelling; D: Tray for black velvet; E: Computer controlled motorised stage

prior to acquisition, illumination of the trays is uniform and all the trays are level. To achieve uniform and constant light illumination it is essential to only introduce known light sources, therefore the system is set up in a dark room and only the fibre optic ring light attached to the microscope should be illuminated. The glass/plexi trays have low light reflectance properties which, together with the light absorbing black velvet, makes it possible to detect the outline of bright objects correctly.

Analysis5.0, the image analysis software, provides morphological data on 21 different parameters derived from the identified specimens. Out of the 21 parameters, the following 8 were used for statistical analysis and assessment: area, perimeter, minimum diameter, maximum diameter, aspect ratio, elongation, sphericity and mean grey value. A further four parameters are derived using equations (Table 4.3; Mollar et al. 2013): circularity ratio, elongation ratio, box ratio and compactness coefficient.

Although this approach is a relatively simple and quick way to acquire morphological data it suffers from a number of drawbacks. In previous studies of morphological parameters (Healy-Williwams et al., 1992; Moller et al., 2013) it was suggested that foraminifera specimens should only be measured in umbilical view in order to provide

Table 4.3: Definition of secondary morphological parameters derived from measured parameters (after Moller et al. 2013).

| Primary parameters | | Secondary morphological parameters | |
|--------------------|-------------------------|---|--------------------------------|
| p | <i>Perimeter</i> | $R_c = A \cdot 4 \cdot \pi / p^2$ | <i>Circularity ratio</i> |
| A | <i>Area</i> | $R_e = 2 \cdot \sqrt{A} / (X_{max} \cdot \sqrt{\pi})$ | <i>Elongation ratio</i> |
| X_{max} | <i>Maximum diameter</i> | $B = X_{min} / X_{max}$ | <i>Box ratio</i> |
| X_{min} | <i>Minimum diameter</i> | $C = p / 2 \cdot \sqrt{\pi} \cdot \sqrt{A}$ | <i>Compactness coefficient</i> |



Figure 4.6: Example of foraminifera specimens captured only in parts by the automated microscope system.

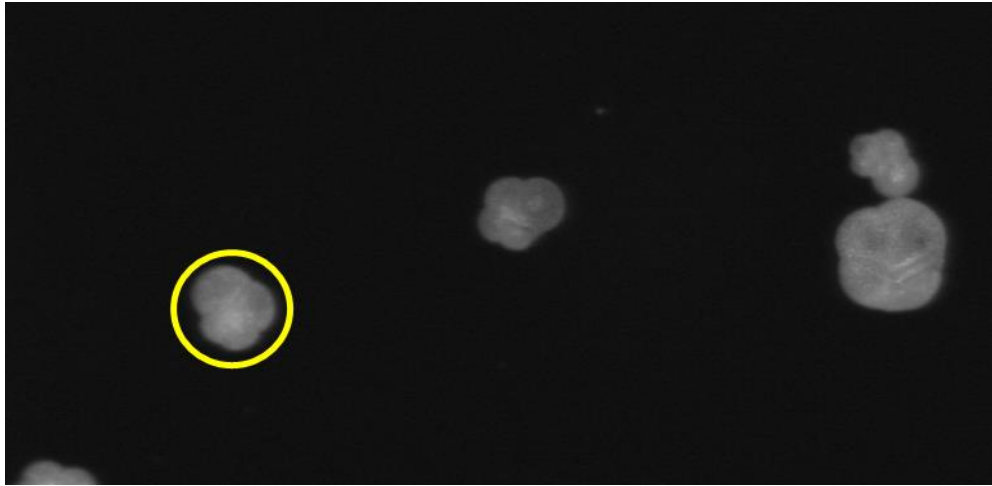


Figure 4.7: Slight halo is visible around the specimen encircled. This attests itself as a fuzzy edge around the boundary of the test.

consistent and comparable data. As the foraminifera samples are gently poured onto the trays it is possible that some specimens do not land in an umbilical position but on their side. It is also possible that some specimens are not analysed as they are only captured on the edges of images and, with only a small overlap between images (to prevent duplication), specimens could be missed (Figure 4.7). These problems were considered and steps were taken to reduce the effect of these before the analysis took place.

Samples were placed onto the trays carefully and were assessed under an optical microscope to ensure that all specimens are positioned in the standard umbilical position. Specimens were also placed sufficiently far apart from each other so that they did not touch. It was hoped that these measures were sufficient to reduce the number of incorrect data points produced by the scanning.

Another drawback of this approach is the automatic object recognition itself. The software uses a thresholding method utilising differences in grey values between object and background. This is a successful approach when dealing with relatively large objects (0.5-1 mm diameter), however, some of the specimens studied here only measure ~100-120 μm in diameter. All specimens display a slight halo around the perimeter of the test, due to slight light reflection, which can make the tests appear larger and this becomes problematic in the case of small specimens (Figure 4.8). This halo effect can be reduced by manually adjusting the thresholding boundary in the image analysis software by increasing the grey value threshold. External reproducibility of the automated system was tested on the maximum diameter dataset and was found to be $\pm 1.70 \mu\text{m}$ (Couderc, personal communication).

The main advantage of the automated image acquisition is the possibility to analyse a large number of specimens (maximum number of specimens analysed in one tray was approximately 2000) in a short amount of time (one hour/tray), providing a reasonably robust dataset.

4.2.2.2 Manual image acquisition

Samples with a large number of specimens (> 100) were split using a microsplitsper until only approximately 50 specimens remained in aliquot with the aim to maintain a consistent sample size aiding statistical analysis. Average sample size was 42 (with a range of 6-65). Prior to analysis, specimens were transferred onto a glass slide and oriented in umbilical position. A weak water-based wallpaper glue solution was used to ensure the specimens stayed in place. The glue was water based and is commonly used for combined morphology and stable isotope work as it does not affect the stable isotope measurements. The glue did not hinder the imaging process as it was transparent, and the solution was weak enough that it easily dissolved when a wet brush was used to remove the specimens without any damage later on. The glass slides were placed over standard sample slides which have a black paper base.

The fixed specimens were placed under Olympus SZX7 transmitted light microscope equipped with a QImaging FAST 1394 camera. Images were taken under five-fold magnification with the Q-Capture software. Prior to analysis a microscale was used to create an accurate scale for the image. Light intensity, contrast and focus were all adjusted prior to each image being captured to ensure clarity. Once captured, a scale was attached to every image to aid further processing. Due to the presence of the wallpaper glue some glare was present on the images which prohibited the correct identification of the specimens in ImageProPlus 6.2, the software used for the analysis of morphological parameters. To remove this glare the images were transferred into Adobe PhotoshopCC 2015, where the background of each image was changed to black. A smoothing factor of 5 was also applied to the outline of each specimen on the images to prevent the pixels creating an artificially angular outline. This small smoothing factor ensured that angular lines from pixels were rounded off without altering the natural outline of the specimens. The images were then transferred into ImageProPlus 6.2 for analysis where thresholding (using the differences in grey value distribution to differentiate between objects in the foreground and the background) was used to identify the specimens from the background. The scales attached to the images were used to set up the correct scale for each measurement. The following parameters were measured using the software: area, major axis, minor axis, maximum diameter, and minimum diameter, mean diameter, perimeter, roundness, size (length) and size (width).

These primary parameters were used to calculate the secondary morphological parameters - circularity ratio, elongation ratio, box ratio and compactness coefficient (Table 4.3).

4.2.3 Stable Isotope Analysis

Stable isotope analysis was carried out on individual and multiple Np specimens at the Faculty of Earth and Life Sciences, Vrije University, Amsterdam. The methods described in Section 4.1.4 were followed for the single specimen analysis of the PAL-LTER specimens. A multi-specimen stable isotope record was created in addition to the single specimen record from the sediment trap samples. To create the multi-specimen record, foraminifera samples were used from sediment trap cups which either had no sufficient number of specimens to allow for single specimen analysis or had an abundance of specimens to allow for additional analysis. Twenty-seven multi-specimen analyses were carried out in total. For each analysis Np specimens were placed in a pre-weighed foil boat until each sample reached a minimum of 30 µg. Average sample mass for the 27 multi-specimen samples was 42.5 µg, with a minimum of 24.7 µg and maximum of 66.4 µg. The samples were placed in glass vials with 4-6 glass microbeads. Stable isotope analysis was carried out using the same Finnigan GasBench II carbonate preparation device interfaced with a Finnigan Delta isotope ratio mass spectrometer, as described in Section 4.1.4. The spectrometer was calibrated through the international standard IAEA-CO1 and the laboratory's own in-house standard VICS. A range of weights of VICS standards were measured on a microbalance to ensure that the mass spectrometer was generating enough signal at all weights. The IAEA-CO1 standard was placed into vials with a special pipette to place exact amount of material into vial. A range of masses (approximately 5-40 µg) of IAEA-CO1 standard was run alongside the samples to provide accurate calibration. All isotopic measurements are reported as per mil deviation from the Vienna Pee Dee Belemnite scale (‰ VPDB). Analytical reproducibility of carbonate industrial standards run concurrently with the Np specimens was between 0.08‰ and 0.24‰ for $\delta^{13}\text{C}$ and between 0.09‰ and 0.22‰ for $\delta^{18}\text{O}$.

4.2.4 Predicting the equilibrium $\delta^{18}\text{O}$ value of calcite

One of the objectives of the sediment trap study was to investigate the calcification depth of Np in this polar setting. To this end, the expected equilibrium $\delta^{18}\text{O}$ calcite ($\delta^{18}\text{O}_{\text{eq}}$) values were calculated following the same method described in Section 4.1.5. In order to calculate $\delta^{18}\text{O}_{\text{eq}}$ values, $\delta^{18}\text{O}_{\text{sw}}$ measurements are needed. Due to lack of sampling $\delta^{18}\text{O}_{\text{sw}}$ values are not widely available along the Antarctic Peninsula. In order to calculate the $\delta^{18}\text{O}_{\text{eq}}$ values we calculated predicted $\delta^{18}\text{O}_{\text{sw}}$ values from salinity values derived from

the World Ocean Atlas 13 dataset. Two different equations were used to calculate the predicted $\delta^{18}\text{O}_{\text{sw}}$. The first one (Eq. 3) was based on the salinity - $\delta^{18}\text{O}_{\text{sw}}$ relationship derived from measured $\delta^{18}\text{O}_{\text{sw}}$ (Meredith et al., 2017). The $\delta^{18}\text{O}_{\text{sw}}$, seawater temperature and salinity datasets were collected each January in 2011 and 2012 during the annual PAL-LTER cruise. The dataset included measurements down to depths of 600 m providing a robust salinity - $\delta^{18}\text{O}_{\text{sw}}$ relationship for the summer period.

It is expected that the salinity - $\delta^{18}\text{O}_{\text{sw}}$ relationship is stable when significant amount of freshwater is not injected to the ocean. In a coastal position, such as the PAL-LTER sediment trap site, the injection of freshwater during the melt-season causes the salinity - $\delta^{18}\text{O}_{\text{sw}}$ relationship to break down (Meredith et al., 1999) therefore a second equation (Eq. 4) was needed to reflect the change in water column structure. Equation 4 was based on salinity and $\delta^{18}\text{O}_{\text{sw}}$ measurements for the October-December time period. The seawater samples were collected by hand from a RIB from in close proximity to the coast of Palmer Station, Anvers Island. The drawback of this dataset is the limited depth range (surface to 10 m) which means that no $\delta^{18}\text{O}_{\text{eq}}$ values could be calculated below the mixed layer where salinity values would deviate from surface values. The following two equations were used to calculate the predicted $\delta^{18}\text{O}_{\text{sw}}$ values:

$$\text{Predicted } \delta^{18}\text{O}_{\text{sw}} = (0.3387 \times S) - 11.796 \quad \text{Equation 3}$$

$$\text{Predicted } \delta^{18}\text{O}_{\text{sw}} = (0.0458 \times S) - 1.8883 \quad \text{Equation 4}$$

Where S is salinity. Note that due to the low temperatures of the polar sea temperature has a negligible impact on the predicted $\delta^{18}\text{O}_{\text{sw}}$. The predicted $\delta^{18}\text{O}_{\text{sw}}$ values were converted to VPDB scale using Eq. 2 in Section 4.1.5. Predicted $\delta^{18}\text{O}_{\text{eq}}$ values were calculated following Eq. 3 utilising temperature values derived from the WOA13 dataset. Vital effect corrections were not included in the $\delta^{18}\text{O}_{\text{eq}}$ as one of the aims of the stable isotope analysis was to investigate the presence/absence of any biological effects on isotope fractionation during calcification.

No $\delta^{18}\text{O}_{\text{eq}}$ values could be calculated for the winter sea ice season due to the lack of $\delta^{18}\text{O}_{\text{sw}}$ values.

4.2.5 Environmental parameters

The environmental dataset, including the chlorophyll α concentration, sea surface temperature and sea ice concentration, is generated as part of the PAL-LTER program (Smith et al., 1995; Ducklow et al., 2007).

Water samples are collected off the coast of Palmer Station from discreet depth intervals to determine chlorophyll α concentration, by hand from a RIB. Samples are collected

once or twice per week between October and March each year and Chl α concentrations are extracted by fluorescence analysis at Palmer Station and available on the Palmer LTER Data System (www.pal.lternet.edu/data).

Weekly sea surface temperatures (SST) were provided by Sharon Stammerjohn (Co-Principal Investigator at Palmer-LTER, Institute of Arctic and Alpine Research, University of Colorado Boulder, USA) for the Palmer vicinity, centred on 64.5°S and 64.5°W. These SST fields were blended from ship, buoy and satellite data on a 1 degree by 1 degree grid (Reynolds and Smith, 1994; Reynolds et al., 2002). The dataset is available at http://iridl.ldeo.columbia.edu/SOURCES/.NOAA/.NCEP/.EMC/.CMB/.GLOBAL/.Reyn_SmithOlv2/.weekly/.sst/

Daily sea ice concentration dataset for the sediment trap site was also provided by Sharon Stammerjohn. The dataset is from the NASA Goddard Space Flight Center's Scanning Multichannel Microwave Radiometer and the Defence Meteorological Satellite Program's Special Sensor Microwave/Imager time series derived from the Bootstrap algorithm (Stammerjohn et al., 2003) and is presented as % cover.

4.3 Falkland Plateau sediment core

Sediment core JR244 - GC528 (Figure 4.1) was collected during the JR244 British Antarctic Survey cruise of the RRS *James Clark Ross* in March 2011. JR244 - GC528 is a 7.9 m long gravity core which was recovered from the South Falkland Slope Drift on the Southern Falkland Plateau (53.00'78 S, 58°02'43 W, 598 m water depth, Figure 4.1). The top 58 cm of the core consists of carbonate-rich coarse sand with a high abundance of foraminifera (Figure 4.9). Below 58 cm the core abruptly changes to a finer-grained, darker sediment with more organic material and less carbonate, hence foraminifera, than the overlying material. This unit gradually changes into a coarser carbonate-poor unit below 108 cm. This unit makes up the majority of the sediment core, finishing at 575 cm. More organic material-rich sediment is found below 58 cm, which contains a greater amount of carbonate than the unit above it but still less than the top 58 cm of the core. The sediment core was dated by radiocarbon dating benthic foraminifera and the Bayesian statistical approach was used to constrain the final age model (Table 4.4, Figure 4.10) (Roberts et al., 2016). A detailed discussion on the construction of the age model can be found in Roberts, J. (2016).

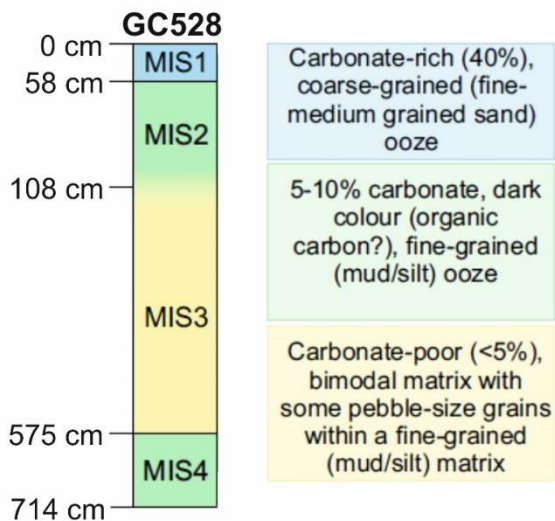


Figure 4.8: JR244 - GC528 sediment core log representing the main sediment units and the Marine Isotope Stages (MIS) the core encompasses (Roberts, 2016).

4.3.1 Stable isotope analysis of *Globorotalia inflata*

A paleoceanographic record from core JR244 - GC528 was generated using single specimen *Globorotalia inflata* stable isotope analysis. The first 100 cm of the core was sampled at 5 cm intervals, the wet sediment was weighed, washed over a 63 μm sieve using a fine water spray and then dried in the oven at 40°C for at least 24 hours. The fine (<63 μm) and the coarse (>63 μm) fractions were weighed and then placed into vials and bags, respectively. The coarse fraction was dry sieved into narrow size ranges (<125 μm , 125-250 μm , 250-350 μm and >350 μm) and all the available *G. inflata* were picked out of the samples. The number of *G. inflata* specimens in each sample varied between 19 and 95. Prior to stable isotope analysis, the specimens were cleaned of organic matter by soaking in a 3% H_2O_2 solution for 30 minutes in a glass vial, after which the specimens were rinsed with di-ionised water followed by sonication with methanol in an ultrasonic bath set at 20% power for 20 seconds. After the sonication the samples were rinsed with di-ionised water and dried in the oven at 40°C. During this cleaning process approximately a third of the total specimens in each sample were lost as a result of breakage. The dried specimens were individually weighed on a Mettler Toledo XP6 high precision microbalance ($d=1 \mu\text{g}$) in pre-weighed aluminium foil boats. Twelve sets of single specimen stable isotope measurements on the *G. inflata* shells were carried out on the Isoprime 100 with Multiprep at the Stable Isotope Facility, British Geological Survey, Keyworth. The mass spectrometer is capable of analysing carbonate samples weighing as little as 5-6 μg with precision. For the single specimen analysis 30 specimens were selected from each time horizon. Unfortunately, some specimens from three different samples were lost during transportation and, as a result, samples representing 7224 (49-50 cm), 8688.5 (55-56 cm) and 9601.25 yr BP (59-60 cm) have

Table 4.4: Radiocarbon dates for core JR244 - GC528, Falkland Plateau, obtained from the benthic foraminifera *Uvigerina bifurcate* and used in the Bchron age model (Roberts, et al., 2016).

| Core depth (cm) | ¹⁴ C AMS age (yr B.P) | 1 σ (yr) | Reservoir age (yr) | 1 σ (yr) | Laboratory |
|-----------------|----------------------------------|-----------------|--------------------|-----------------|---------------|
| 0 | 2540 | 30 | 967 | 110 | Beta Analytic |
| 5.5 | 2090 | 30 | 967 | 110 | Beta Analytic |
| 30 | 4972 | 45 | 967 | 110 | Godwin/UB |
| 41 | 6178 | 39 | 967 | 110 | Godwin/UB |
| 49 | 7150 | 30 | 967 | 110 | Beta Analytic |
| 58 | 9383 | 48 | 967 | 110 | Godwin/UB |
| 61 | 7876 | 51 | 967 | 110 | Godwin/UB |
| 61 | 9026 | 48 | 967 | 110 | Godwin/UB |
| 66 | 11925 | 48 | 987 | 110 | Godwin/UB |
| 72 | 12562 | 55 | 1031 | 110 | Godwin/UB |
| 78 | 12652 | 53 | 1040 | 110 | Godwin/UB |
| 82 | 12295 | 53 | 1077 | 110 | Godwin/UB |
| 88 | 12611 | 47 | 1077 | 110 | Godwin/UB |
| 98 | 13251 | 50 | 1084 | 110 | Godwin/UB |
| 109.5 | 12234 | 65 | 1150 | 110 | Godwin/UB |
| 111.5 | 13079 | 63 | 1175 | 110 | Godwin/UB |
| 119 | 13670 | 70 | 1298 | 110 | Godwin/UB |
| 124 | 14410 | 81 | 1325 | 110 | Godwin/UB |
| 139.5 | 14651 | 80 | 1330 | 110 | Godwin/UB |
| 149 | 16380 | 90 | 1364 | 110 | Beta Analytic |
| 199 | 17340 | 101 | 1364 | 110 | Godwin/UB |
| 229 | 17220 | 70 | 1364 | 110 | Beta Analytic |
| 289 | 18260 | 108 | 1364 | 110 | Godwin/UB |
| 350 | 20628 | 140 | 1364 | 110 | Godwin/UB |
| 416 | 29475 | 372 | 1364 | 110 | Godwin/UB |
| 448 | 33440 | 210 | 1364 | 110 | Beta Analytic |

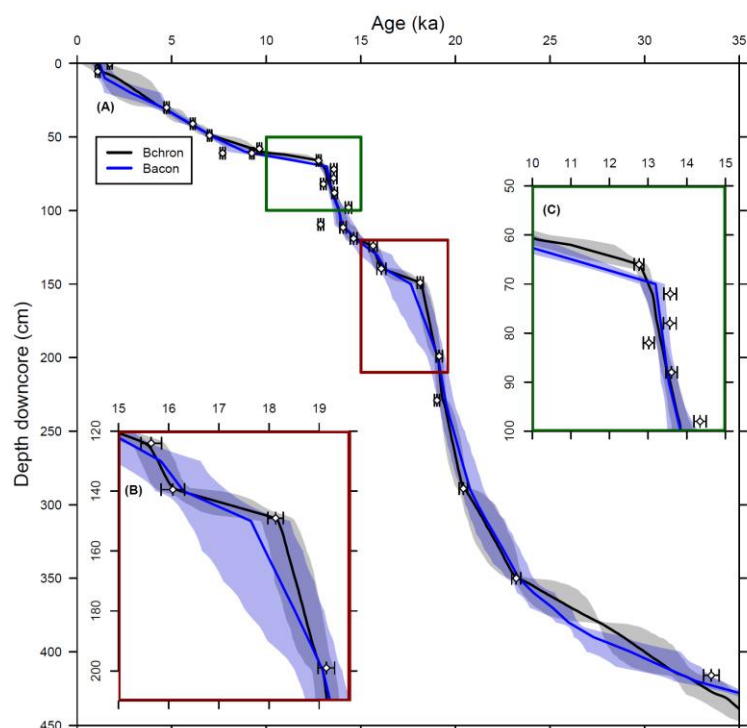


Figure 4.9: Age-depth model for top 450 cm section of core JR244 - GC528, produced by Roberts et al. (2016). Bchron age model (black line) is used to date the core.

less than 30 individual measurements. All isotopic measurements are reported as per mil deviation from the Vienna Pee Dee Belemnite scale (‰ VPDB). The values were normalised to the VPDB scale using a calcite laboratory standard (KCM) run concurrently with the foraminifera specimens and calibrated against SRM19 NIST reference material. Analytical reproducibility of the laboratory standards was between 0.03‰ and 0.07‰ for $\delta^{13}\text{C}$ and between 0.03‰ and 0.04‰ for $\delta^{18}\text{O}$. Due to a number of technical issues with the Isoprime 100 mass spectrometer, 8 sets of samples were analysed using a GV Isoprime mass spectrometer with Multiprep and VG Optima at the Stable Isotope Facility, British Geological Survey, Keyworth. This mass spectrometer is capable of analysing carbonate material weighing 20 μg or more. To achieve the required amount of carbonate two *G. inflata* specimens were analysed together. This approach was necessary to produce a dataset for the eight set of analysed samples with acceptable precision; however, by analysing two specimens in one vial the range of the isotope measurements in each time horizon is potentially reduced. Due to the limited availability of *G. inflata* in the sediment core the number of paired analysis per time horizon varied between 18 and 31. The isotopic measurements are reported as ‰VPDB and were normalised to the VPDB scale using the KCM standards ran concurrently with the *G. inflata* samples. Analytical reproducibility of the KCM laboratory standard was 0.03‰ for $\delta^{13}\text{C}$ and 0.05‰ for $\delta^{18}\text{O}$.

5 Results and Discussion

5.1 *Neogloboquadrina pachyderma* abundance, stable isotope composition, vital effects, and calcification depth variability in the Scotia Sea: results from vertical plankton hauls

Neogloboquadrina pachyderma is the most abundant planktonic foraminifera in the high latitudes (Kipp, 1976; Hilbrecht, 1996). It has been widely used to assess recent and past high latitude climatic changes (e.g. Kohfeld et al., 1996; Little et al., 1997; Ninnemann and Charles, 1997; Multiza et al., 1997; Bauch et al., 2000; Hillaire-Marcel et al., 2004; Eynaud et al., 2009; Hanslik et al., 2010; Hibbert et al., 2010; Smith et al., 2010; Moller et al., 2013; Vautravers et al., 2013; Berben et al., 2017; Jennings et al., 2017). Studies of modern *Neogloboquadrina pachyderma* from plankton tows and sediment traps have shown significant variability in abundance, calcification depths, vital effects, and stable isotope composition linked to local oceanographical conditions (e.g. Ortiz et al., 1996; Bauch et al., 1997; Bauch et al., 2002; Mortyn and Charles, 2003; Kuroyanagi et al., 2011; Jonkers et al., 2013; Asahi et al., 2015). Because of these regional variations it is important to provide local calibrations for future paleoceanographic investigations. Here, a detailed assessment of vertical plankton tow-derived *Neogloboquadrina pachyderma* record of abundance, morphology, and single specimen stable isotope composition is provided for the Scotia Sea. First, the oceanographic conditions during the sampling period are assessed to determine the environmental controls on the foraminifera record. This is followed by a detailed description of *Neogloboquadrina pachyderma* abundance, morphology and stable isotope variability in the study area within the Scotia Sea. These records are used to evaluate the relationship between *Neogloboquadrina pachyderma* stable isotopes, shells weights, calcification depths, and isotope-fractionation-derived vital effects.

5.1.1 Oceanographic setting of the Scotia Sea

The physical and chemical structure of the water column along the JR304 cruise track is assessed in order to constrain controls on the spatial distribution of *Neogloboquadrina pachyderma* (Np) in the modern Scotia Sea. A first order assessment of the oceanographic setting can be made by analysing World Ocean Atlas 2013 (WOA13) data for the period of October-December, which gives oceanographic data that is averaged over decadal periods, in this case between 2005 and 2012 with 0.25° latitudinal and longitudinal data coverage (Locarnini et al., 2013; Zweng et al., 2013). The WOA13

temperature profile shows that average surface temperature ranges from -1°C in the south to 1°C in the north, across the 8.5° latitudinal span of the cruise transect (Figure 5.1A). The southern part of the transect is characterised by a more defined density structure with cold and fresh Winter Water (WW, a result of deep winter mixing (Meredith et al., 2010)) occupying the top 200-400 m of the surface waters. WW overlays warmer and saltier Upper Circumpolar Deep Water (UCDW) between $\sim 58^{\circ}\text{S}$ and $\sim 56^{\circ}\text{S}$. This warmer water mass reaches ~ 1500 m water depth and lies above the colder and less salty Lower Circumpolar Deep Water (LCDW). UCDW is not detected south of 58°S ; WW directly overlays LCDW which shoals towards the surface along the 27.8 kg/m^3 isopycnal (Orsi et al., 1995). At the deepest part (below 3000 m) of the Scotia Sea just north of the South Orkney shelf, cold ($<0^{\circ}\text{C}$) and dense ($<27.85\text{ kg/m}^3$) Antarctic Bottom Water (AABW) is present (Orsi et al., 1995) (Figures 5.1A, B). In contrast, the surface waters at the northern end of the transect are warmer and fresher than the WW to the south. This warmer water mass is the Antarctic Surface Water (AASW), which becomes Antarctic Intermediate Water (AAIW) as it moves north beyond the Polar Front and is subducted from surface waters to more intermediate depth due to density differences (Orsi et al., 1995; Talley, 1996; Garabato et al., 2003; Evans et al., 2014). The AASW reaches ~ 400 m water depth, below which lies the warmer and saltier UCDW followed by the colder and denser LCDW (Figure 5.1A,B). Water column profiles can be constructed from the CTD deployments undertaken at the sampling localities (Figure 5.2) during the cruise. These CTD-derived profiles show similar patterns to the WOA13 profiles in both temperature and salinity (Figure 5.3).

5.1.1.1 Temperature profiles

Sea surface temperature (SST) (based on CTD measurements taken during the JR304 cruise) is coldest at Station 4 which is located south of the Southern Boundary of the Antarctic Circumpolar Current (SB, Figure 5.2). North of the SB, a 1.6°C SST temperature gradient exists between the most southerly location (Station 5) and the northern end of the transect (Station 12 and Station 13) where SSTs reach up to $\sim 2.5^{\circ}\text{C}$ (Figure 5.3A). Station 5 is located south of the Southern Antarctic Circumpolar Current Front (SACCF, Figure 5.2) and hence shows surface temperatures which are $\sim 0.5^{\circ}\text{C}$ colder (Figure 5.3A) than localities north of the SACCF (Station 8, WCB 1.2S, Station 12, 13). Between the SB and the Polar Front (PF) at Station 5, subsurface temperatures converge below 200 m depth. At all localities water temperatures in the upper 25-50 m remain close to the SST, defining the mixed layer, then decrease to a minimum from 90-120 m depth (the thermocline) below which they increase within the UCDW. At the

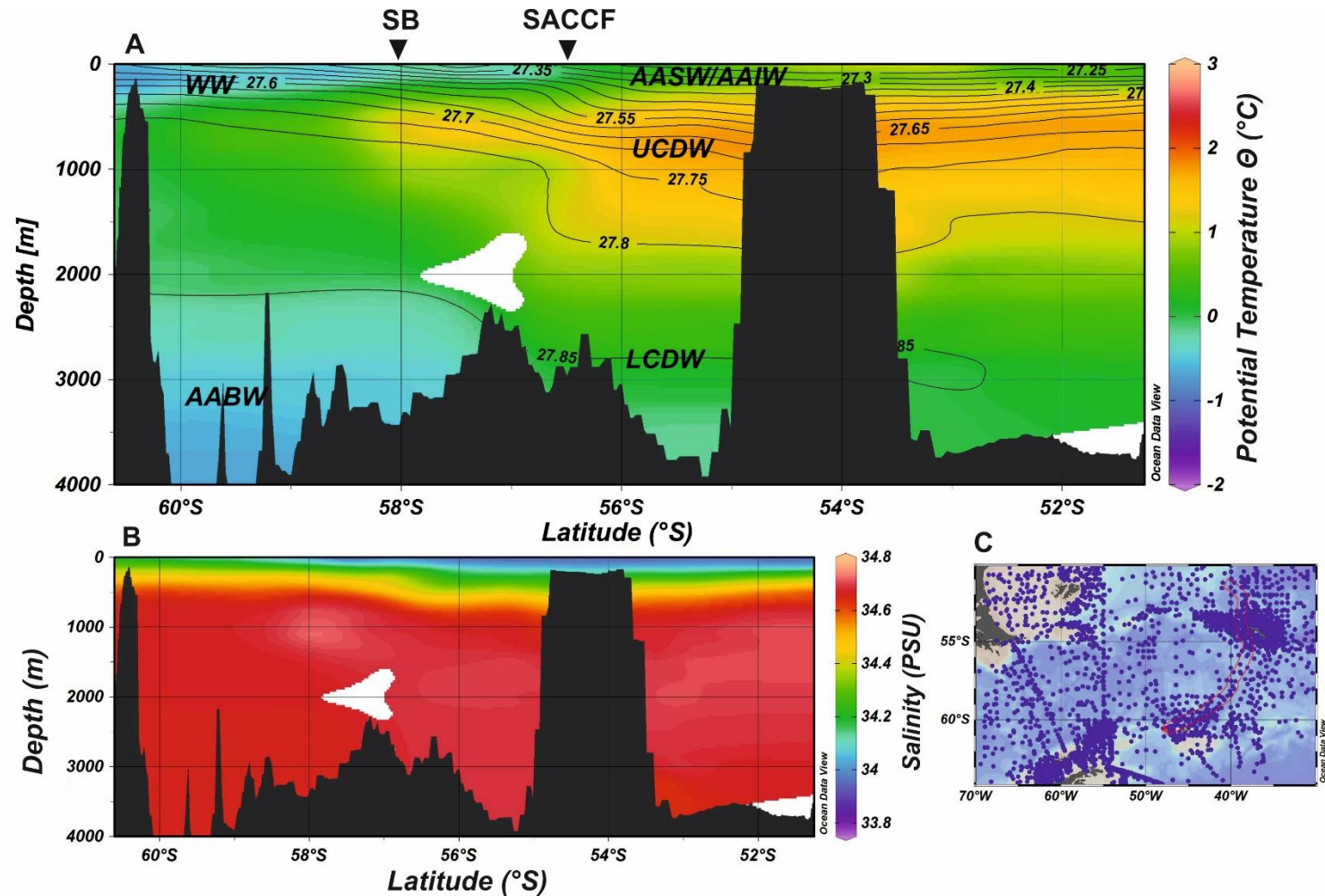


Figure 5.1: Temperature (A) and salinity (B) cross-section of the water column through JR304 cruise track (C). Black lines in temperature cross-section are isopycnals representing potential density. Black triangles depict the approximate location of two fronts, the Southern Boundary of Antarctic Circumpolar Current (SB) and the Southern Antarctic Circumpolar Current Front. Major water masses are identified based on temperature, salinity and potential density properties from Orsi et al. (1995) and Garabato et al. (2003). WW: Winter Water; AASW: Antarctic Surface Water; AAIW: Antarctic Intermediate Water; UCDW: Upper Circumpolar Deep Water; LCDW: Lower Circumpolar Deep Water; AABW: Antarctic Bottom Water. The cross section is highlighted by the red polygon in bottom right figure (C).

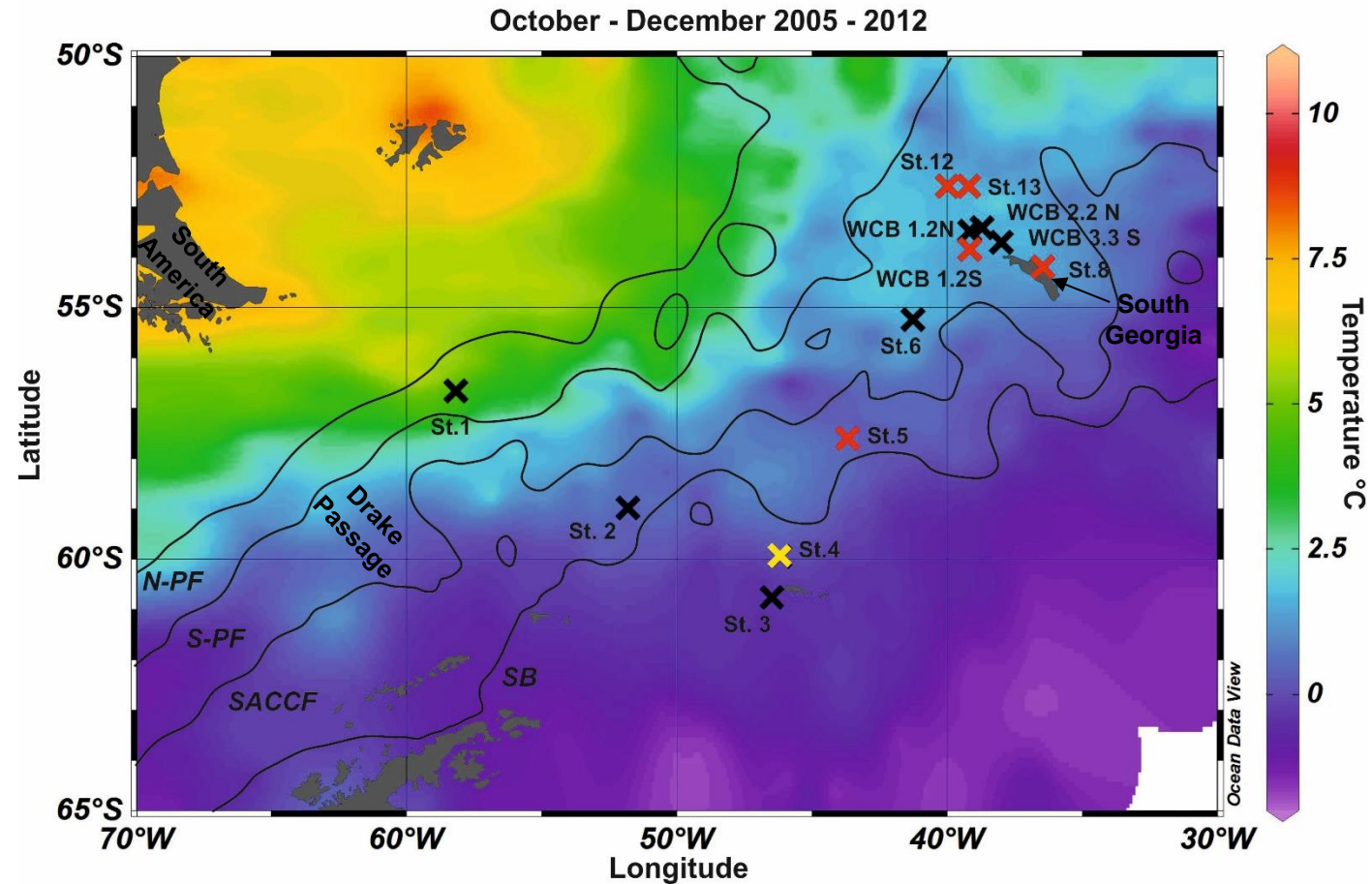


Figure 5.2: Surface temperature map of the Scotia Sea. Major oceanic fronts are annotated on the map. N-PF: Northern Boundary of Polar Front; S-PF: Southern Boundary of Polar Front; SACCF: Southern Antarctic Circumpolar Current Front; SB: Southern Boundary of Antarctic Circumpolar Current. Front positions based on dynamic heights in Venables et al. (2012). Vertical plankton tow sampling locations are identified by crosses (see Table 5.1 for grid reference of localities). Red crosses represent locations of samples where water samples and foraminifera specimens were analysed for stable isotopes. Yellow cross represent Station 4 where only seawater oxygen isotope data is available. Stations identified as WCB indicate annual Western Core Box krill survey grid locations.

southernmost station (Station 4) the water temperature minimum is reached at around 90 m water depth and; at the northern end of the transect (Station 13), the water temperature minimum is reached around 120 m water depth. The two sampling locations on the continental shelf (Station 8 and WCB 1.2S; Figure 5.2) show similar temperature profiles to the other stations; however, water temperature minima are reached at 160 m and 150 m respectively, close to the seafloor (Station 8: 250 m, WCB 1.2S: 201 m).

5.1.1.2 Salinity profiles:

Salinity shows a uniform pattern across the open ocean transect north of the SB (Station 5, 12, 13 and WCB 1.2S). Surface salinity is ~33.9 PSU at every station (apart from coastal Station 8) and remains uniform to 100-120 m water depth, after which it increases rapidly (halocline) between 120-175 m, followed by a more gradual increase with depth. South of the SB (at Station 4) surface salinity is ~34.4 PSU and increases with depth gradually. The salinity profile of Station 8, off the coast of South Georgia, is distinct from the open ocean profiles north of the SB. Surface water salinity at Station 8 is lower (33.3 PSU) than at all other locations with a strong shallow halocline between 12 and 18 m water depth. Between 18 and 100 m water depths at Station 8, salinity is similar to the open ocean stations, but below 100 m it remains 0.5 PSU below the open ocean stations. The anomalous salinity pattern at Station 8 can be attributed to its close proximity to the glaciers terminating within Cumberland Bay and the reduced influence of UCDW.

5.1.1.3 Fluorescence and density profiles:

Phytoplankton are an important source of food for foraminifera and it has been shown that the depth of maximum phytoplankton abundance is closely associated with foraminiferal calcification depth (Kohfeld et al., 1995; Bauch et al., 1997). Fluorescence, which is a measure of the amount of photosynthetic microorganisms (phytoplankton that synthesise chlorophyll α) in the water column, is highest within the mixed layer at all localities along the transect (Figure 5.3C). Surface concentrations range from 0.11 mg/m³ at Station 5 to 1.99 mg/m³ at Station 12. Apart from Station 8, maximum concentrations of fluorescence are reached in the mixed layer above the pycnocline (the depth of steepest density change; Fig 3C, 3D), at ~75 m water depth, which is consistent with observations of Mortyn and Charles (2003). Although the absolute concentration of maximum fluorescence varies between sites, the relative changes with depth are similar. At Station 8 the shallow halocline controls the density structure of the water column and fluorescence maximum is reached at the bottom of the pycnocline (~25 m), followed by a decrease to surface concentrations (<0.3 mg/m³) by around 50 m water depth. The density profile of Station 4, south of the SACCF, shows a consistent offset from the other

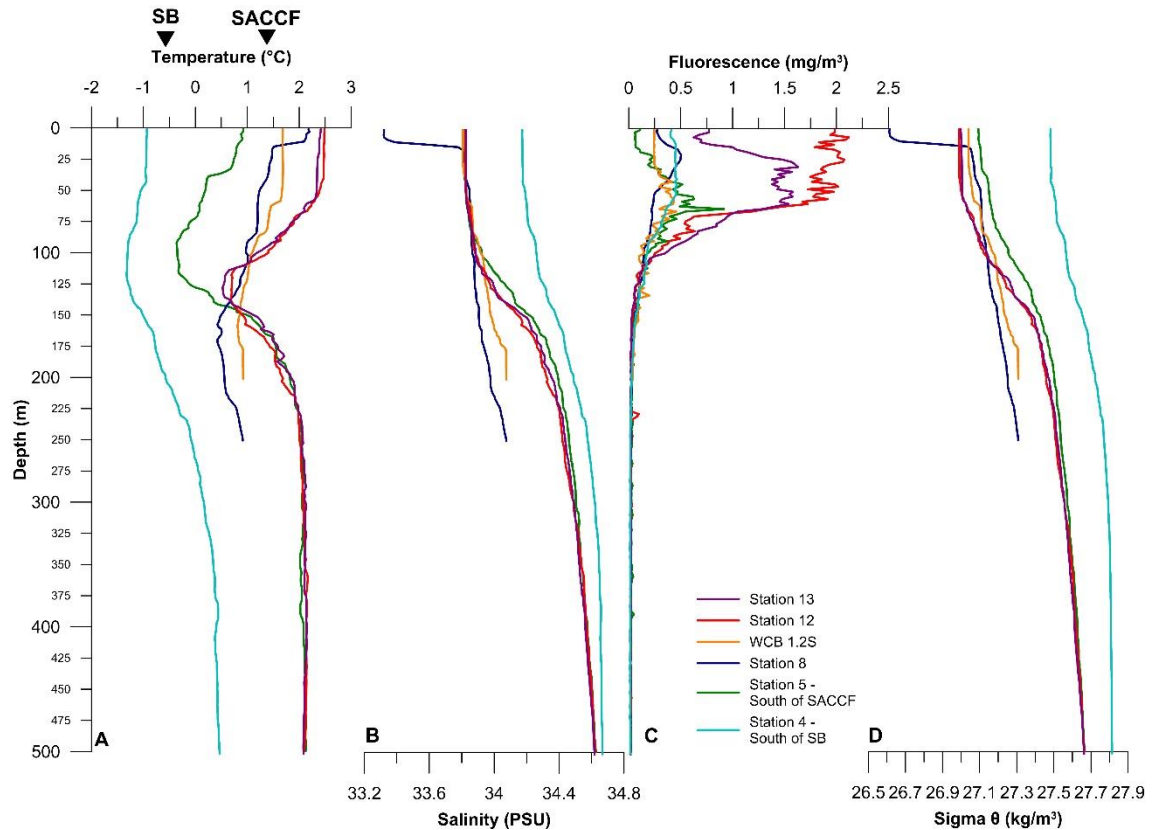


Figure 5.3: CTD water column profiles of the six water sampling stations. A) Temperature, triangles denote approximate location of Southern Boundary Front (SB) and Southern Antarctic Circumpolar Current Front (SACCF); B) Salinity; C) Fluorescence; D) Potential Density (θ).

stations, with surface and deeper water (below 150 m) values ~ 0.5 and ~ 0.2 kg/m^3 higher, respectively, than the average values of the open ocean locations (Figure 5.3D). This difference between the density profile of Station 4 and the others is the result of the offsets in temperature and salinity identified in Section 5.1.1.1 and 5.1.1.2. The fluorescence profile of Station 4 is similar to the other open ocean locations, albeit with lower fluorescence concentrations (Figure 5.3C).

5.1.2 *Neogloboquadrina pachyderma* abundance in the Scotia Sea

The majority of the planktonic foraminifera captured by the motion-compensated Bongo nets across the study area were *Neogloboquadrina pachyderma* (*Np*) specimens. Occasionally, at the northern end of the cruise transect *Globigerina bulloides* and *Globorotalia inflata* specimens were recovered by the plankton tow in single digit numbers. For this reason, *Np* will be the focus of the discussion. For information on the sampling with the motion-compensated Bongo nets, see Chapter 4.1.1.

Np abundance varies considerably from station to station, by up to two orders of magnitude between Station 4 and Station 12 (Table 5.1). The highest number of

foraminifera (100-200, 22, and 354 specimens in three plankton hauls, where the first and third were 12 hours apart; Table 5.1.) were collected at Station 12, one of the most northerly sampling locations, associated with higher water temperatures in the top 100 m of the water column. Station 12 has the highest surface water fluorescence ($\sim 2 \text{ mg/m}^3$) and thus, the greatest concentration of chlorophyll α of the study. High foraminifera numbers are also observed at other northern localities, at Stations 1, 6, 12 and 13 (Table 5.1). Lowest Np numbers were found at the southernmost end of the transect at Station 4, where the number of Np specimens recovered by the individual plankton tows was as low as three (Table 5.1). The low Np abundance at Station 4 coincide with low fluorescence (indicating low chlorophyll α concentration), the lowest sea water temperatures recorded along the water column at any station, the highest salinities and a weak density gradient. The low Np abundance at Station 4 cannot be attributed solely to the low chlorophyll α concentration because lower fluorescence values recorded at Station 5 and at WCB 1.2S are accompanied by higher Np abundances. The low Np numbers at Station 4 can most likely be attributed to the sampling location being south of the SB, and thus characterised by low water temperatures, and to an absence of a phytoplankton bloom.

There is no consistent picture about the preferred depth habitat of Np at the stations where the Bongo net was deployed to both 100 and 200 m water depth (Stations 4, 6, 8, 13, and WCB 3.2S). At Station 4, a greater number of Np were recovered from the plankton tow which was deployed to 100 m compared to the subsequent one released to 200 m water depth. In comparison, at Stations 13 and at the WCB 3.2S station, Np abundances were greater in the 200 m plankton tow and, at Stations 6 and 8, the abundances were approximately equal.

Although peak Np abundance clearly has a wide range within the 8° latitudinal cruise transect, a definite gradient in Np numbers can be observed from north to south, with Np abundance decreasing from the highs (up to 354) of Station 12 in the north to the low values (down to 3) of Station 4. Peak Np abundance is found at greater depth at the north end of the transect and it gradually shallows towards the south. This wide range of peak Np abundance depths is similar to that found by Mortyn and Charles (2003) further north and east in the South Atlantic sector of the Southern Ocean. The distribution of Np along the transect is inconsistent and patchy (Table 5.1). For example, two deployments at Station 12, 20 minutes apart on the 13/12/14, recovered 22 and 354 Np, representing a 15-fold change in abundance. Additionally, as described above, Np abundance inconsistently varies between the 100 and 200 m deployments. The high degree of

Table 5.1: Foraminifera sampling localities during JR304 cruise with date, station name and number, latitude and longitude of sampling, bongo net mesh size, bottom depth of bongo net deployment and the number of *Np* specimens captured in the plankton tow. Highlighted rows represent samples that underwent stable isotope analysis. At stations where precise numbers could not be provided, an upper or lower limit is given based on approximate recorded numbers.

| Date | Station No./name | Lat. (°) | Long. (°) | Mesh size (µm) | Depth (m) | No. of <i>Np</i> |
|------------------|-------------------------------------|----------|-----------|----------------|-----------|------------------|
| 17/11/2014 18:38 | Station 1 | -56.67 | -58.17 | 200 | 200 | <200 |
| 17/11/2014 19:07 | Station 1 | -56.67 | -58.17 | 100 | 200 | 90 |
| 18/11/2014 16:21 | Station 2 | -58.99 | -51.8 | 100 | 200 | 100 |
| 19/11/2014 11:24 | Station 3 | -60.77 | -46.48 | 100 | 115 | 50 |
| 25/11/2014 15:49 | Station 4 | -59.96 | -46.16 | 100 | 100 | 40 |
| 25/11/2014 15:53 | Station 4 | -59.96 | -46.16 | 100 | 200 | 6 |
| 25/11/2014 19:13 | Station 4 | -59.96 | -46.16 | 100 | 100 | 25 |
| 25/11/2014 19:28 | Station 4 | -59.96 | -46.16 | 100 | 200 | 3 |
| 26/11/2014 14:40 | Station 4 | -59.96 | -46.16 | 100 | 100 | 7 |
| 27/11/2014 13:10 | Station 5 - P2 | -57.61 | -43.67 | 100 | 200 | 59 |
| 28/11/2014 08:23 | Station 6 | -55.24 | -41.26 | 100 | 200 | <200 |
| 29/11/2014 15:17 | Station 6 | -55.25 | -41.26 | 100 | 100 | <200 |
| 29/11/2014 15:29 | Station 6 | -55.25 | -41.26 | 100 | 200 | <200 |
| 03/12/2014 15:38 | Station 8 | -54.2 | -36.45 | 100 | 100 | >50 |
| 03/12/2014 15:54 | Station 8 - Cumberland Bay | -54.2 | -36.45 | 200 | 200 | >50 |
| 08/12/2014 23:12 | WCB 1.2N Station | -53.49 | -39.25 | 100 | 200 | 31 |
| 09/12/2014 06:59 | WCB 1.2S station - Western Core Box | -53.85 | -39.14 | 100 | 200 | 94 |
| 10/12/2014 04:54 | WCB 2.2N station | -53.43 | -38.7 | 100 | 200 | 18 |
| 10/12/2014 04:54 | WCB 2.2N station | -53.43 | -38.7 | 200 | 200 | <20 |
| 11/12/2014 05:40 | WCB 3.2S station | -53.71 | -37.97 | 100 | 100 | 63 |
| 11/12/2014 05:40 | WCB 3.2S station | -53.71 | -37.97 | 200 | 200 | 109 |
| 13/12/2014 06:26 | Station 12 - P3 | -52.81 | -39.97 | 100 | 200 | <200 |
| 13/12/2014 21:17 | Station 12 | -52.81 | -39.97 | 200 | 200 | 22 |
| 13/12/2014 21:39 | Station 12 | -52.81 | -39.97 | 200 | 100 | 354 |
| 14/12/2014 08:27 | Station 13 | -52.6 | -39.2 | 100 | 100 | <100 |
| 14/12/2014 08:46 | Station 13 - Upwelling | -52.6 | -39.2 | 100 | 200 | <200 |
| 14/12/2014 15:57 | Station 13 | -52.6 | -39.2 | 100 | 200 | 100 |

variability in the *Np* abundance record highlights caveats associated with the sampling method. The Bongo nets were lowered first to 100 m water depth, brought back to the deck to empty the sampling buckets, then lowered back down to 200 m water depth. In some cases as much as 20 minutes passed between the collection of the 100 and 200 m deployments. During that time, the water mass underneath the ship constantly changed due to currents, allowing the lateral transport of water masses away from, and

to the sampling locality. This means, that in the time period between the 100 m and 200 m deployments foraminifera could have been transported away from the site, or could have been introduced to the location. This lateral advection of foraminifera by the water currents impedes good reproducibility of net catches at any one location. The limited number of Bongo net deployments hinders the thorough assessment of Np abundance in the Scotia Sea. A more structured sampling strategy, where Bongo nets are deployed at a regular distance from each other (for example, a 0.5° gap could be applied between sampling localities) could improve the spatial assessment of Np abundance. Sampling at either side of the frontal boundaries (SB, SACCF, Northern and Southern boundary of PF, SAF) could also improve our understanding of Np abundance in the Scotia Sea. In addition, the use of a depth-integrated plankton tow (e.g. Multiple Opening/Closing Net and Environmental Sensing System: MOCNESS), as opposed to the single-depth Bongo nets, would greatly enhance our understanding of Np habitat and calcification depth by highlighting specific depth intervals (e.g. 0-20 m, 20-50 m, 50-100 m, etc.) where Np is abundant .

5.1.2.1 Neogloboquadrina pachyderma morphotypes

Prior to stable isotope analysis specimens from five plankton tow hauls (Table 5.1) were inspected under the light microscope to ensure that morphotype-related variability in the stable isotope data is limited. It is recognised that high resolution SEM images would be helpful in the determination of the different morphotypes; however, visual inspection under a light microscope was the only means of morphotype separation for this study. Overall, three different morphotypes are present in the samples.

A review of existing literature reveals that *Neogloboquadrina pachyderma* specimens have been placed into different categories based on several different aspects of their morphological features. To date, no consistent morphological group classification method has been developed, leading to arbitrary determination of groups. Kennett (1968) separated Np specimens in the South Pacific and in the Southern Ocean based on chamber numbers in the final whorl, wall thickness and shape, and identified two groups. Group one, located south of 54-55°S was dominated by 4-chambered, thick-walled and compact specimens. In comparison, group two, located north of 54-55°S was dominated by 4 ½-to 5-chambered, thinner-walled and more lobate specimens. Vautravers et al. (2013) also used shape and size to identify two separate morphotypes (Morphotypes A and B) in sediment samples from the Antarctic Peninsula. Specimens belonging to Morphotype A were larger, quadrate and showed signs of a secondary crust, while specimens in the Morphotype B group were smaller, more lobate and had thinner shells than Morphotype A, and were considered to be juvenile forms of Morphotype A.

Morphological assessments carried out on northern hemisphere specimens were based on similar characteristics to the southern hemisphere ones. Stehman (1972) identified three different *Neogloboquadrina pachyderma* groups (Forms 1, 2, and 3) in the Labrador Sea which were based on shape, calcification, and aperture. Specimens which belonged to Form 1 had a compact, heavily calcified shell with a small aperture, 4 chambers in the final whorl, and were common in the coldest waters of the region. Form 2 specimens had a quadrate/square appearance, the shells were heavily calcified and had 4 ½ to 5 chambers in the final whorl. Form 3 specimens were more elongated, less square, were less encrusted, had an arched, sinuous lip around the aperture, had 5 chambers in the final whorl, and were found in warmer waters. Kohfeld et al. (1996) found two groups of Np in the Northern North Atlantic, and used the shape and surface texture of the shells to separate the groups. Np specimens that belonged to Group one were heavily encrusted, opaque, quadrate, and had heavier shells with crystalline surfaces. Group two specimens had smooth, reticulate surfaces, were nonencrusted, and more elongated with a lower shell mass and were suggested to be juvenile (or pre-encrustation) forms of Group one. A more recent study by Eynaud (2011) carried out on Arctic Ocean samples has provided the most thorough assessment of Np morphology to date and identified five different groups (Nps-1, 2, 3, 4, and 5) based on specimen size, shape, number of chambers, aperture size, and encrustation. Of particular interest from the five morphotypes, are the Nps-2, Nps-3 and Nps-5 groups. Nps-2 specimens were quadrate, encrusted and had 4 globular chambers and a large aperture. Nps-3 specimens were more elongated, had 4 to 4 ½ chambers and a large aperture. In contrast, Nps-5 specimens were smaller than the rest, lozenge-shaped and elongated, and had 4, nonencrusted chambers with small, deep suture lines.

Genetic analysis of North and South Atlantic, and Southern Ocean *Neogloboquadrina pachyderma* specimens revealed the existence of five different genotypes (Darling et al., 2004). Only one genotype (Type I) was found in the North Atlantic, while four genotypes (Type II, III, IV, and V) were identified in the Southern Hemisphere samples. Type V specimens are only found in the Benguela Upwelling system, while the other three genotypes dominate in different regions of the Southern Ocean. Type II is dominant north of the Subantarctic Front, Type III is widespread north of the Polar Front, while Type IV is only found south of the Polar Front.

Based on the above studies, three different morphotypes (Np-A, B, and C) of *Neogloboquadrina pachyderma* have been identified. Np-A specimens have compact, quadrate, cancellate shells with 4 globular chambers in the final whorl, and a prominent, large aperture and no clearly visible suture lines. Np-A specimens look similar in shape

to the Nps-2 morphotype (Figure 5.4A) identified by Eynaud (2011), Group one of Kennett (1968) and Kohfeld et al. (1996), Morphotype A of Vautravers et al. (2013), and Form 1 of Stehman (1972). Np-A morphotype dominates the Station 5 and Station 8 samples, the most southerly stations (Figure 5.2), and also makes up a greater portion of the Station 12, and Station 13 assemblages than the other morphotypes. In contrast, at WCB 1.2S Np-A only makes up a small portion of the population, as identified under a microscope. Under the light microscope the specimens from Station 5 look smaller than the specimens from the rest of the plankton tows.

Np-B specimens have more lobate, elongated, 4 to 4 ½ chambered cancellate shells with signs of encrustation and not very clear suture lines. In this group, the final chamber of the shell is more deflated, not globular and smaller than the other chambers. This group, Np-B, looks similar to the Nps-3 (Figure 5.4B) morphotype identified by Eynaud (2011) and Group two of Kennett (1968). Np-B morphotype is found in the Station 12 and Station 13 populations but altogether makes up a smaller portion than Np-A.

Np-C specimens have smaller (than Np-A and B) elongated, lobate shells with a shiny surface and 4 ½ chambers with distinct suture lines. These specimens do not show signs of encrustation and look similar to the Nps-5 morphotype (Figure 5.4C) identified by Eynaud (2011), Morphotype B of Vautravers et al (2013), and Group two of Kohfeld et al (1996). In some instances, the cytoplasm of the foraminifera was still intact at collection. Based on the lack of encrustation, presence of cytoplasm, highly elongated shape and similarity to the above morphotypes, Np-C specimens can be considered as juvenile, pre-gametogenic specimens that have not gone through reproduction. Np-C morphotype is found at all stations, making up a small portion of the population at Stations 5, 8, 12 and 13, and dominating the WCB 1.2S population. Np-C specimens in the Station 5, 8

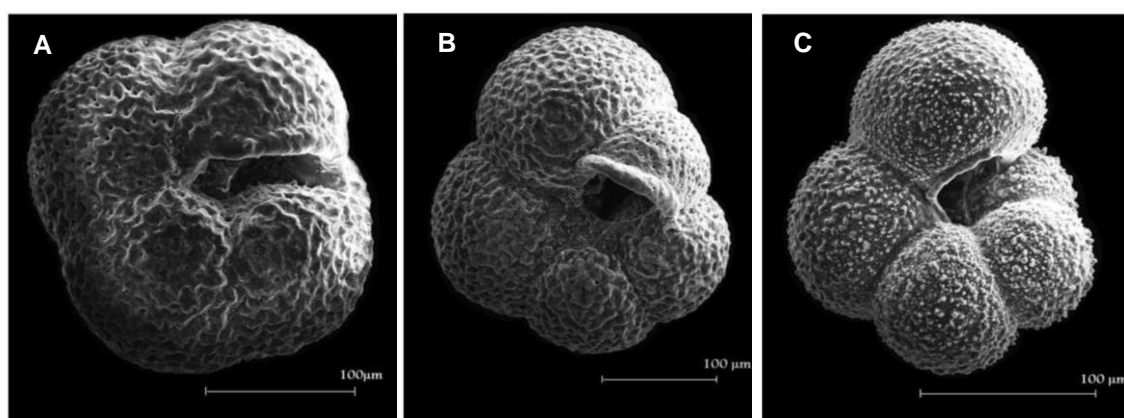


Figure 5.4: Scanning Electron Microscope images of Nps-2 (A), Nps-3 (B), and Nps-5 (C) *Neogloboquadrina pachyderma* morphotypes in ventral view from Eynaud (2011). Specimens derive from Central Arctic sediments (IODP-ACEX Hole 4C) and show the diversity of morphology observable in this species.

and WCB 1.2S populations generally still contained their cytoplasm at collection, while specimens belonging to the Station 12 and 13 population were missing the cytoplasm when collected by the Bongo net plankton hauls.

Three right-coiling *Neogloboquadrina pachyderma* specimens were present in the Station 12 samples (total of 112 specimens). As Darling et al. (2006) discussed, <3% of *Np* is right coiling in Atlantic and Southern Ocean populations, and therefore we assume that those present in the Station 12 sample are aberrant version of *Np* instead of *Neogloboquadrina incompta* specimens.

Using the spatial distribution of *Np* genotypes as identified by Darling et al (2004) it can be hypothesised that the *Np*-A morphotype (dominant at Station 5 and 8, south of the SACCF) belongs to the Type IV genotype group, while *Np*-B morphotype (present at Station 12 and 13, north of the SACCF, close to the PF) specimens most likely belong to the Type III genotype group. As the *Np*-C morphotype represents pre-reproduction specimens, this morphotype cannot be placed into either genotype group. Genetic analysis, akin to the Darling et al (2004) study is required to confirm the genotypes of the plankton tow samples. To reduce within-sample variability due to morphotype mixing, I aimed to choose only the dominant morphotypes for stable isotope analysis from each sample, i.e. *Np*-A specimens from the Station 5, 8, 12, and 13 samples; *Np*-C specimens from the WCB 1.2S samples (Table 5.2).

5.1.3 *Neogloboquadrina pachyderma* stable isotopic signatures and water column $\delta^{18}\text{O}$ gradients

Single specimen stable isotope ratios were measured on *Np* from five different plankton tow hauls, deployed to 200 m water depths. A minimum of 30 single specimens were analysed from each station; however, only 20, 15 and 29 reliable data points could be derived from Station 8, WCB 1.2S and Station 12, respectively. Variability between specimens can be observed in both the oxygen and carbon isotopic records (Figure 5.5).

5.1.3.1 *Neogloboquadrina pachyderma* oxygen isotopic ratios

Average oxygen isotope values of *Np* ($\delta^{18}\text{O}_{\text{np}}$) vary from $+2.22 \pm 0.34\text{‰}$ at WCB 1.2S to $+3.38 \pm 0.22\text{‰}$ at Station 5 (Figure 5.5A). The data show a maximum inter-station spread of 2.22‰ across the stations - between the highest value, $+3.77\text{‰}$, at Station 5 (*Np*-A specimens) and lowest value, $+1.5\text{‰}$, at WCB1.2S, (*Np*-C specimens) (Table 5.2). Largest variability of $\delta^{18}\text{O}_{\text{np}}$ values within a locality is recorded at WCB 1.2S (*Np*-C specimens) with a 1.27‰ range and a 0.12 variance. The smallest variability is recorded at Station 12 (*Np*-A specimens), where $\delta^{18}\text{O}_{\text{np}}$ values have a range of 0.62‰ , and a

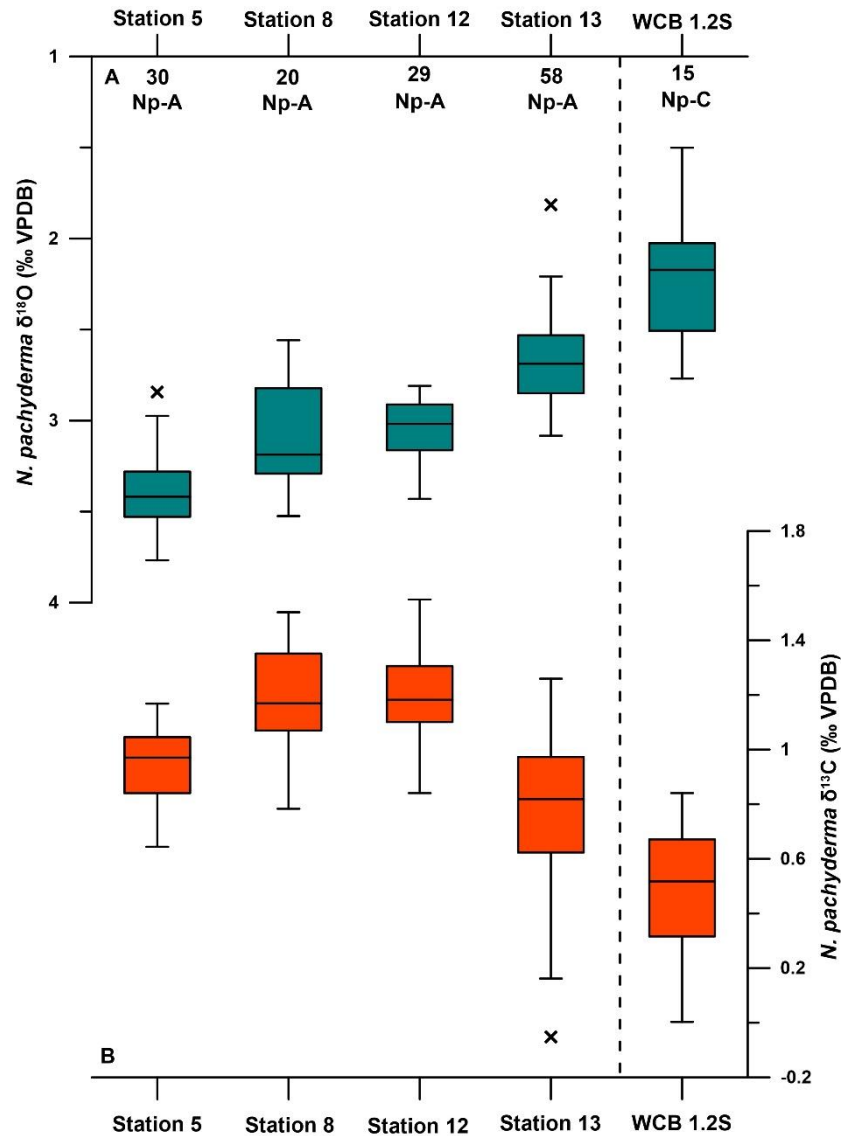


Figure 5.5: Single specimen *N. pachyderma* $\delta^{18}O$ (A) and $\delta^{13}C$ (B) boxplots arranged by morphotypes and latitude. Station 5 is the most southerly location, Station 13 is most northerly location. WCB1.2S sample contained Np-C morphotype specimens, the rest all contain Np-A morphotype specimens. Black crosses represent outliers (data points outside 1.5 x IQR), numbers denote the number of single specimens analysed.

variance of 0.03. The range of $\delta^{18}O_{np}$ values recorded at Station 13 (Np-A specimens) (1.27‰) is as high as at WCB 1.2S; however, this is skewed by a single data point (+1.81‰) outside the 1.5xInterquartile range. This is also reflected by the smaller variance (0.05 vs 0.12 at WCB 1.2S) and by the smaller standard deviation (0.23‰ vs 0.34‰ at WCB 1.2S). Although the lowest oxygen isotope values are not observed at the most northerly location, a clear latitudinal gradient exists in the record with values decreasing from south to north (Figure 5.5A).

Table 5.2: Summary statistics of single specimen Np $\delta^{18}\text{O}$ and $\delta^{13}\text{C}$ values from five plankton tow haul stations in the Scotia Sea.

| $\delta^{18}\text{O}$ | Station 5 | Station 8 | WCB 1.2S | Station 12 | Station 13 |
|---------------------------|-----------|-----------|----------|------------|------------|
| <i>No of specimens</i> | 30 | 20 | 15 | 29 | 58 |
| <i>Mean</i> | +3.38 | +3.09 | +2.22 | +3.04 | +2.67 |
| <i>Median</i> | +3.42 | +3.19 | +2.17 | +3.02 | +2.69 |
| <i>Standard deviation</i> | 0.22 | 0.29 | 0.34 | 0.17 | 0.23 |
| <i>Variance</i> | 0.05 | 0.08 | 0.12 | 0.03 | 0.05 |
| <i>Max</i> | +3.77 | +3.52 | +2.77 | +3.43 | +3.08 |
| <i>Min</i> | +2.84 | +2.56 | +1.50 | +2.81 | +1.81 |
| <i>Range</i> | 0.92 | 0.97 | 1.27 | 0.62 | 1.27 |
| <i>Morphotype</i> | Np-A | Np-A | Np-C | Np-A | Np-A |
| $\delta^{13}\text{C}$ | | | | | |
| <i>No of specimens</i> | 30 | 20 | 14 | 29 | 58 |
| <i>Mean</i> | +0.93 | +1.17 | +0.49 | +1.19 | +0.80 |
| <i>Median</i> | +0.97 | +1.17 | +0.52 | +1.18 | +0.82 |
| <i>Standard deviation</i> | 0.15 | 0.19 | 0.26 | 0.17 | 0.25 |
| <i>Variance</i> | 0.02 | 0.04 | 0.07 | 0.03 | 0.06 |
| <i>Max</i> | +1.17 | +1.50 | +0.84 | +1.55 | +1.26 |
| <i>Min</i> | +0.64 | +0.78 | +0.00 | +0.84 | -0.05 |
| <i>Range</i> | 0.52 | 0.72 | 0.84 | 0.71 | 1.31 |

An F_{\max} test (statistical test to assess differences between variance) conducted on the $\delta^{18}\text{O}_{\text{np}}$ dataset reveal statistically significant difference ($p=0.0001$) between the $\delta^{18}\text{O}_{\text{np}}$ -derived variances of the different localities. For further statistical tests parametric analysis techniques need to be employed due to the statistically significant differences between the variances. A Kruskal-Wallis test (non-parametric equivalent of ANOVA) reveals statistically significant difference between any of the medians of the five localities ($p = 6.65 \times 10^{-22}$). Furthermore, Mann-Whitney pairwise tests (non-parametric equivalent of t-test), highlight the existence of statistically significant difference between the medians of most localities, regardless of morphotype, with the exception of Station 8 and 12 (Table 5.3)

5.1.3.2 Neogloboquadrina pachyderma carbon isotopic ratios

Average carbon isotope values ($\delta^{13}\text{C}_{\text{np}}$) range between $+0.49 \pm 0.26\text{‰}$ at WCB 1.2S and $+1.19 \pm 0.17\text{‰}$ at Station 12 (Figure 5.5B). The record shows an inter-station spread of 1.6‰ across the stations: highest $\delta^{13}\text{C}_{\text{np}}$, $+1.55\text{‰}$, measured at Station 12, lowest value

Table 5.3: Bonferroni corrected *p* values of pairwise Mann-Whitney *U* tests conducted on the single specimen *Np* $\delta^{18}\text{O}$ and $\delta^{13}\text{C}$ dataset (Figure 5.5). Highlighted cells indicate statistically significant difference between samples ($p < 0.05$).

| $\delta^{18}\text{O}$ | Station 5 | Station 8 | WCB 1.2S | Station 12 |
|-----------------------|------------------------|-----------------------|-----------------------|------------------------|
| Station 5 | | | | |
| Station 8 | 3.90x10 ⁻⁴ | | | |
| WCB 1.2S | 6.41x10 ⁻⁸ | 1.70x10 ⁻⁶ | | |
| Station 12 | 3.21x10 ⁻⁷ | 0.502 | 7.72x10 ⁻⁸ | |
| Station 13 | 8.26x10 ⁻¹⁴ | 1.92x10 ⁻⁶ | 7.49x10 ⁻⁶ | 4.87x10 ⁻¹⁰ |
| $\delta^{13}\text{C}$ | | | | |
| Station 5 | | | | |
| Station 8 | 3.62x10 ⁻⁵ | | | |
| WCB 1.2S | 2.74x10 ⁻⁶ | 2.10x10 ⁻⁶ | | |
| Station 12 | 3.33x10 ⁻⁷ | 0.722 | 1.75x10 ⁻⁷ | |
| Station 13 | 0.013 | 1.97x10 ⁻⁷ | 3.17x10 ⁻⁴ | 3.45x10 ⁻¹⁰ |

of -0.05‰ measured at Station 13 (Table 5.2). The largest within-sample variability in the single specimen $\delta^{13}\text{C}_{\text{np}}$ record is found at Station 13, where a 1.31‰ range and a 0.06 variance is observed. The smallest within-sample variability is recorded at Station 5, where $\delta^{13}\text{C}_{\text{np}}$ values have a range of 0.52‰ and a variance of 0.02. While the largest range of $\delta^{13}\text{C}_{\text{np}}$ value is at Station 13, the largest variance and thus standard deviation is recorded at WCB 1.2S (0.07 and 0.26 respectively). The accompanying range of $\delta^{13}\text{C}_{\text{np}}$ values at WCB 1.2S is 0.84‰ (Table 5.2). The discrepancy between the largest range and variance is related to the presence of a very low $\delta^{13}\text{C}_{\text{np}}$ value (-0.05‰) at Station 13, which is outside the 1.5xInterquartile range (Figure 5.5B).

The within-sample $\delta^{13}\text{C}_{\text{np}}$ variance reveals statistically significant difference between the five stations when analysed through an F_{max} test ($p=0.01$). Similarly to the $\delta^{18}\text{O}_{\text{np}}$ record, the $\delta^{13}\text{C}_{\text{np}}$ values display normal distribution at every station; however, due to the significant difference between the variance of the different stations, non-parametric statistical tests need to be employed for further analysis. A Kruskal-Wallis test shows statistically significant difference between any of the medians of the different stations ($p = 2.03 \times 10^{-16}$). Additionally, Mann-Whitney pairwise tests also show similar results to the $\delta^{18}\text{O}$ dataset (Table 5.3), with statistically significant difference recorded between the medians of most stations (exception is the Station 8: Station 12 relationship). There is no clear latitudinal gradient in the $\delta^{13}\text{C}_{\text{np}}$ measurements (Figure 5.5B).

Seawater samples were collected at every CTD station to determine the carbon isotope variability of dissolved inorganic carbon (DIC), to help the interpretation of the $\delta^{13}\text{C}_{\text{np}}$ dataset. However, the amount of DIC collected was not enough to provide accurate figures. Therefore it is not possible to assess whether $\delta^{13}\text{C}_{\text{DIC}}$ or biological processes (kinetic fractionation and vital effects) exert a greater influence on the $\delta^{13}\text{C}_{\text{np}}$.

5.1.3.3 Seawater $\delta^{18}\text{O}$ trends

Seawater samples from a range of water depths, collected at the same locations as foraminifera samples for stable isotope analysis (Figure 5.2) were analysed for their oxygen isotope values. The $\delta^{18}\text{O}$ of the seawater ($\delta^{18}\text{O}_{\text{sw}}$) shows a consistent pattern along the transect (Figure 5.6). The maximum surface water $\delta^{18}\text{O}_{\text{sw}}$ difference between all stations is 0.34‰, while only a 0.04‰ difference exists between four of the northerly locations (Stations 5, 12, 13 and WCB 1.2S). The lowest surface water $\delta^{18}\text{O}_{\text{sw}}$ value (-0.43‰) is recorded at Station 8, proximal to the South Georgia coast, most likely as a result of the low surface water salinity (Figure 5.3B). The highest surface water $\delta^{18}\text{O}$ (-0.17‰) is found at the most southerly location, Station 4, south of the Southern Boundary of the ACC. $\delta^{18}\text{O}_{\text{sw}}$ through the water column is similar at each open ocean

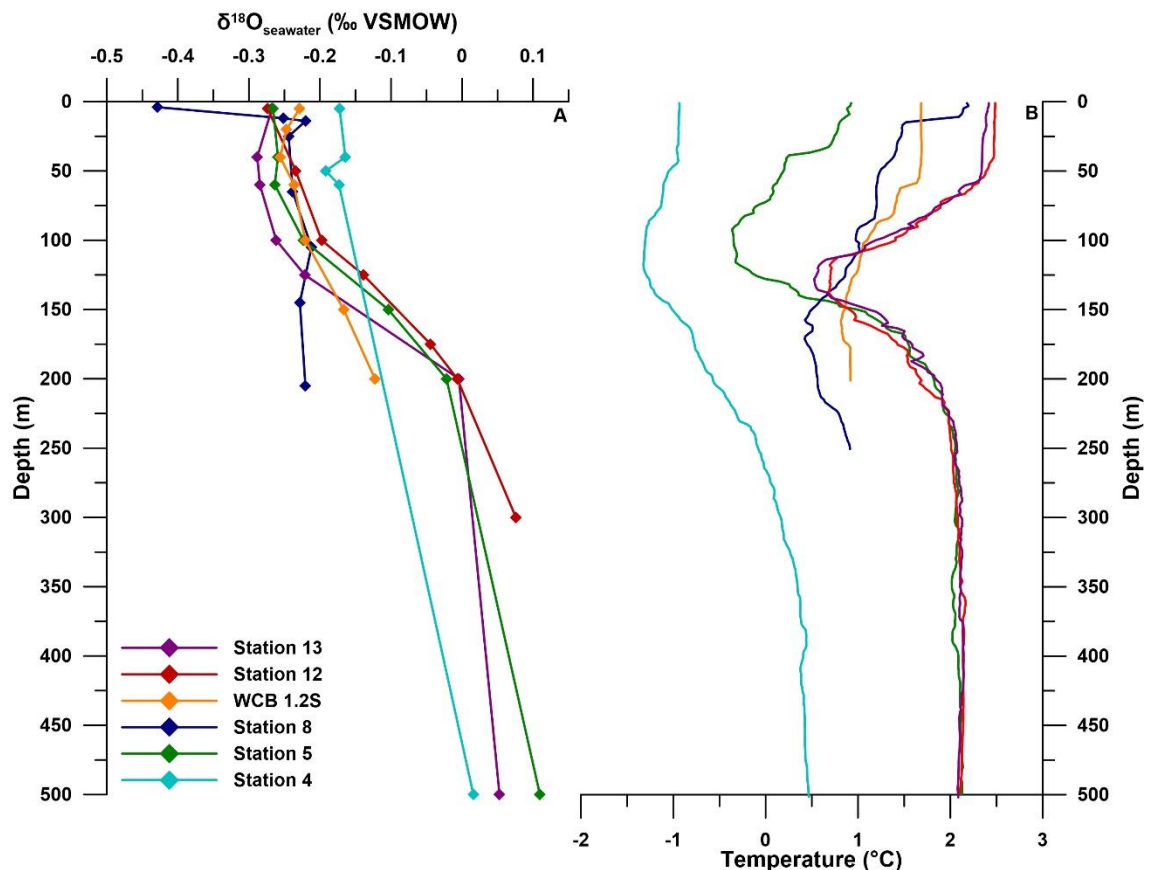


Figure 5.6: Seawater $\delta^{18}\text{O}$ (A) and temperature (B) profiles at the six sampling locations. Station 4 is south of the SB, Station 5 is located south of the SACCF. All other stations are north of the SACCF and south of the PF.

station, generally increasing with increasing depth (Figure 5.6). The general consistency of the $\delta^{18}\text{O}_{\text{sw}}$ values between the stations suggests that the same water masses were sampled across the study area and differences in $\delta^{18}\text{O}_{\text{np}}$ are most likely due to the effect of temperature.

5.1.4 Foraminiferal and seawater oxygen isotopes: equilibrium, vital effects, and calcification depths

In the following section the plankton tow-derived *Neogloboquadrina pachyderma* $\delta^{18}\text{O}_{\text{np}}$ record will be assessed with respect to existing Np records from mid- and high-latitudes. The observed stable isotope variability is investigated in relation to physical, environmental and biological processes.

5.1.4.1 Relationship between $\delta^{18}\text{O}_{\text{sw}}$ and salinity in the Scotia Sea

The $\delta^{18}\text{O}_{\text{sw}}$ values (Figure 5.6) mirror the CTD-derived salinity values (Figure 5.3B). The highest surface water $\delta^{18}\text{O}_{\text{sw}}$ values across the study area, found at Station 4 (the most southerly location), are accompanied by the highest surface water salinity values. Similarly, the lowest surface $\delta^{18}\text{O}_{\text{sw}}$ values, found at Station 8 (enclosed Cumberland Bay), are complemented by the lowest surface water salinity values. When a linear regression is applied to the $\delta^{18}\text{O}_{\text{sw}}$ and salinity values (Figure 5.7) a significant positive correlation ($r=0.95$) is found, indicating a near 1:1 relationship between the two. This 1:1 relationship is typical in open ocean areas where sea ice formation, and thus the introduction of brines, or fluvial input with low $\delta^{18}\text{O}$ signature is not a common feature (e.g. Rohling and Bigg, 1998; Meredith et al., 1999; Hillaire-Marcel et al., 2004; Ravelo and Hillaire-Marcel, 2007). Due to the observed strong coupling between $\delta^{18}\text{O}_{\text{sw}}$ and temperature in the Scotia Sea, it is expected that the significant cross-transect variability in $\delta^{18}\text{O}_{\text{np}}$ is an expression of either temperature change or biological processes.

5.1.4.2 *Neogloboquadrina pachyderma* shell weight vs $\delta^{18}\text{O}_{\text{np}}$: impact of size on oxygen isotope ratio

Co-variability between shell weight of *Neogloboquadrina pachyderma* and $\delta^{18}\text{O}_{\text{np}}$ have been recorded at a number of locations in past studies, for example, the Arctic Ocean (Bausch et al., 1997; Volkman and Mensch, 2001; Hillaire-marcel et al., 2004), North Atlantic (Kozdon et al., 2009), and the North Pacific Ocean (Kuroyanagi et al., 2011). However, this co-variability is not consistent, as some studies have found no relationship between shell weight/size and $\delta^{18}\text{O}_{\text{np}}$. Huber et al. (2000) and Jonkers et al. (2013) found no correlation between shell size and $\delta^{18}\text{O}_{\text{np}}$ in the North Atlantic, while only a seasonal correlation was identified in the North Pacific by Kuroyanagi et al. (2011). Therefore it is

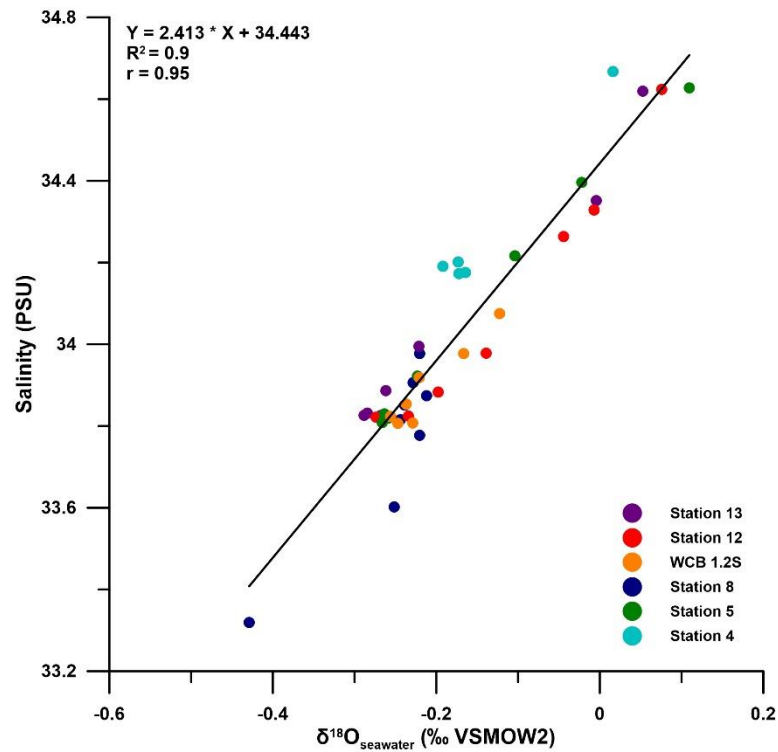


Figure 5.7: $\delta^{18}O$ -salinity relationship at six CTD stations across the Scotia Sea showing statistically significant correlation ($r=0.95$) indicating that salinity is the dominant factor on $\delta^{18}O_{\text{sw}}$ values in the Scotia Sea.

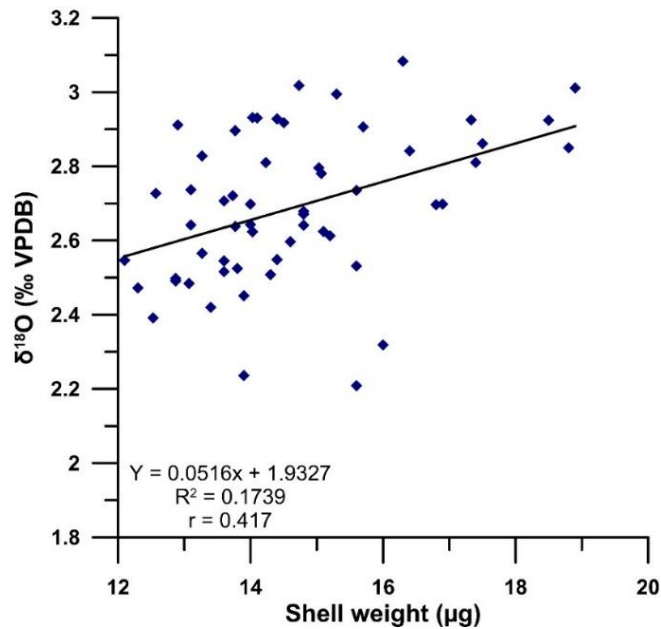


Figure 5.8: Linear regression figures of shell weight: $\delta^{18}O_{\text{np}}$. Specimens originate from Station 13 plankton tow haul. Statistically significant correlation is found between shell weight and $\delta^{18}O_{\text{np}}$, as indicated by the r value (greater than 0.25 at 95% significance).

important to determine whether such a link exists in the Scotia Sea before equilibrium calcification patterns are discussed.

The weight of 58 *Np*-A specimens was recorded for Station 13 which and can be compared with accompanying $\delta^{18}\text{O}_{\text{np}}$ values (Figure 5.8). Linear regression analysis reveals significant correlation between weight and $\delta^{18}\text{O}_{\text{np}}$, supporting previously published size-dependent $\delta^{18}\text{O}$ records (e.g. Bausch et al., 1997; Hillaire-Marcel et al., 2004; Kuroyanagi et al., 2011). Heavier specimens have higher $\delta^{18}\text{O}_{\text{np}}$ values, most likely due to deeper calcification depths (in colder and more saline waters) and the addition of secondary crust at those deeper depths. In contrast, smaller, and thus lighter specimens have lower $\delta^{18}\text{O}_{\text{np}}$ values, most likely as a result of shallower calcification depths (in warmer and less saline waters) and possible lack of secondary calcite crust. This trend is observable across the study area (Figure 5.9), with the highest average $\delta^{18}\text{O}_{\text{np}}$ values accompanying high shell weights of the adult morphotype, *Np*-A (Station 5:) and the lowest average $\delta^{18}\text{O}_{\text{np}}$ values are coupled with the lowest shell weights found in the pre-reproduction *Np*-C specimens of WCB 1.2S: *Np*-A specimens. The combination of the lowest shell weights and lowest $\delta^{18}\text{O}_{\text{np}}$ measurements in the WCB 1.2S sample most likely reflects the lack of secondary crust of the *Np*-C morphotype specimens, and a shallower calcification depth than *Np* specimens elsewhere in the study region. This agrees well with previous assessment of pre-gametogenic *Np* (Kohfeld et al., 1996; Kozdon et al., 2009), where *Np* specimens with ontogenic calcite only have been recorded to have lower shell mass and $\delta^{18}\text{O}_{\text{np}}$ values (Kohfeld et al., 1995; Kozdon et al., 2009). However, variabilities are present in this trend. Relatively low, average shell weight of $7.3 \pm 0.97 \mu\text{g}$ at Station 8 is accompanied by relatively high $\delta^{18}\text{O}_{\text{np}}$ values, centred on $3.09 \pm 0.29\text{‰}$. The combination of such high $\delta^{18}\text{O}_{\text{np}}$ values and low shell

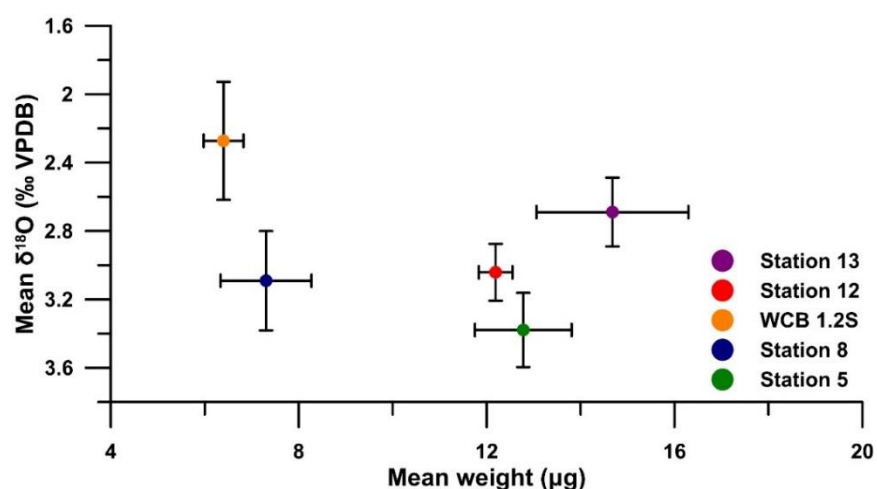


Figure 5.9: Average shell weight and $\delta^{18}\text{O}_{\text{np}}$ (A) variability at five stations across the Scotia Sea. Error bars depict one standard deviation range. WCB 1.2S specimens belong to the juvenile, *Np*-C morphotype. The other four stations represent adult, *Np*-A morphotypes.

weight most likely relates to the cold water temperatures (Figure 5.3A) present at calcification depth at the time of sampling coupled with probable secondary calcification and morphological differences. Station 8 is located closer to shore than the rest of the stations, off the coast of South Georgia (Figure 5.2). Glacial meltwater runoff from nearby South Georgia would have introduced nutrients (e.g. nitrate and phosphate) to the coastal waters, allowing Np to complete its life cycle, reproduce and secrete a secondary calcite crust more rapidly than if nutrients were more limited resulting in the calcification of smaller shells compared to ones achieved during a longer calcification period. The overall variability in the shell weight- $\delta^{18}\text{O}_{\text{np}}$ relationship is most likely the result of the latitudinal temperature increase between the most southerly and northerly sites (Figure 5.3A) combined with the impact of morphological variability (as discussed in Section 5.1.2.1).

5.1.4.3 Exploration of vital effects during isotope fractionation by Neogloboquadrina pachyderma in the Scotia Sea

The influence of temperature on the $\delta^{18}\text{O}_{\text{np}}$ is reflected well in the predicted calcite equilibrium values ($\delta^{18}\text{O}_{\text{eq}}$, Figure 5.10) which shows a $\sim 0.4\text{‰}$ difference at the surface between Station 5 and Station 13 even when $\delta^{18}\text{O}_{\text{sw}}$ is identical at -0.27‰ (Figure 5.6). Highest $\delta^{18}\text{O}_{\text{eq}}$ values are observed at Station 5 (0-150 m water depth), as a result of the lowest water temperature values of the five stations. $\delta^{18}\text{O}_{\text{eq}}$ values are almost identical at Station 12 and 13, showing consistently lower values between 40 m and 100 m than the rest of the stations (Figure 5.10) as a result of similar temperature trends across the water column (Figure 5.11D,E).

Previous plankton tow and sediment trap studies have identified the depth habitat of Np as within or just below the mixed layer, the exact depth of which depends on local hydrography and can range from 35 m to 150 m (Volkman and Mensch, 2001; Jonkers et al., 2010; Kuroyanagi et al., 2011; Asahi et al., 2015). The long held assumption in Np ontogeny is that the development of the secondary calcite crust takes place in deeper waters than the secretion of the ontogenic calcite shell (Hemleben and Spindler, 1983; Kohfeld et al., 1996; Kozdon et al., 2009). The calcification of the secondary crust has been linked to the pycnocline or just below the pycnocline (Ortiz et al., 1996; Mortyn and Charles, 2003; Simstich et al., 2003; Hillaire-Marcel et al., 2004; Kozdon et al., 2009). By using the depth of the mixed layer and that of the pycnocline as a guide, $\delta^{18}\text{O}$ equilibrium offsets of Np can be assessed across the Scotia Sea.

The depth of the mixed layer and of the pycnocline varies across the sites (Figure 5.11). The shallowest mixed layer (surface to 12 m water depth) is found at Station 8 (Figure

5.11B) as the result of the low-salinity lens in the enclosed Cumberland Bay. Here, average $\delta^{18}\text{O}_{\text{np}}$ values (with $\pm 1\sigma$) follow the $\delta^{18}\text{O}_{\text{eq}}$ without significant offset below the mixed layer, within the thermocline. The average $\delta^{18}\text{O}_{\text{np}}$ value (+3.09‰) converge onto the $\delta^{18}\text{O}_{\text{eq}}$ at ~100 m water depth.

At the rest of the stations the mixed layer is between 50 and 75 m deep (Figure 5.11A-E) and thus both the pycnocline and the thermocline are found much deeper than at Cumberland Bay. At Station 5 and 12, the relationship between the average $\delta^{18}\text{O}_{\text{np}}$ and $\delta^{18}\text{O}_{\text{eq}}$ is similar to Station 8. At these stations *Np*-A morphotypes dominate and were chosen for stable isotopic analysis. The average $\delta^{18}\text{O}_{\text{np}}$ value ($\pm 1\sigma$) follows the $\delta^{18}\text{O}_{\text{eq}}$ below the mixed layer without any significant offset and it converges onto the $\delta^{18}\text{O}_{\text{eq}}$ value at ~100 m water depth.

This equilibrium calcification below the mixed layer only agrees well with one other plankton tow study conducted in the northern Pacific Ocean (Asahi et al., 2015). Most plankton tow studies conducted in the Arctic Ocean (Bausch et al., 1997; Bausch et al., 2002; Hillaire-Marcel et al., 2004), in the North Atlantic (Kohfeld et al., 1996; Volkmann and Mensch, 2001; Kozdon et al., 2009) and in the Southern Ocean (Mortyn and Charles,

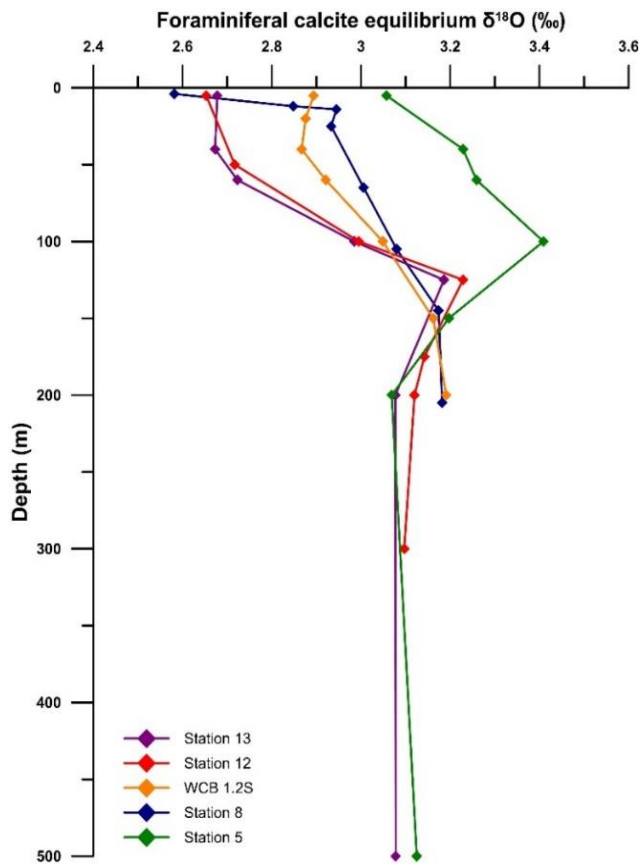


Figure 5.10: Calculated foraminiferal calcite equilibrium $\delta^{18}\text{O}$ values against depth at Station 5, 8, 12, 13 and WCB 1.2S. These locations were chosen based on the availability of sufficient number of *Np* for stable isotope analysis.

2003) have identified negative vital offsets up to 1‰. Lack of vital offsets in Np are commonly identified in sediment trap studies across the oceans (Jonkers et al., 2010; Jonkers et al., 2013; Sagawa et al., 2013; Asahi et al., 2015) and have been linked to the dominance of the encrusted specimens in the sediment traps. However, it is important to note that differences in vital offsets have been recorded in both plankton tows and sediment traps conducted at the same location (e.g. -1‰ vital offset recorded in sediment trap study of Kuroyanagi et al., 2011).

Different dynamics in the $\delta^{18}\text{O}_{\text{np}}:\delta^{18}\text{O}_{\text{eq}}$ relationship are observed at WCB 1.2S and Station 13. WCB 1.2S, where the Np-C morphotype dominates, is the only station where the range of single specimen $\delta^{18}\text{O}_{\text{np}}$ falls outside the $\delta^{18}\text{O}_{\text{eq}}$ profile (Figure 5.11C). At this location $\delta^{18}\text{O}_{\text{eq}}$ values across the entire water profile are higher than the maximum single specimen $\delta^{18}\text{O}_{\text{np}}$. The bottom of the mixed layer is approximately at 50 m water depth. The average $\delta^{18}\text{O}_{\text{np}}$ value ($+2.27 \pm 0.35\text{‰}$) at WCB 1.2S shows a negative offset of 0.6‰ from mixed layer $\delta^{18}\text{O}_{\text{eq}}$ value (at 20 m) and a 0.65‰ negative offset from the $\delta^{18}\text{O}_{\text{eq}}$ value just below the mixed layer (60 m).

At Station 13, where Np-A morphotype dominates, 50% of the $\delta^{18}\text{O}_{\text{np}}$ falls outside the $\delta^{18}\text{O}_{\text{eq}}$ profile (Figure 5.11E). The average $\delta^{18}\text{O}_{\text{np}}$ follows the $\delta^{18}\text{O}_{\text{eq}}$ profile in the mixed layer (top 50 m) without any offset. However, the $\delta^{18}\text{O}_{\text{eq}}$ values diverge from $\delta^{18}\text{O}_{\text{np}}$ and increase below the mixed layer in line with the increasing water temperature. As a result only 50% of the single specimen $\delta^{18}\text{O}_{\text{np}}$ values show no vital offset within the thermocline. The rest of the specimens show negative fractionation of up to 0.46‰ compared to mixed layer $\delta^{18}\text{O}_{\text{eq}}$ values and a -0.78‰ offset compared to thermocline $\delta^{18}\text{O}_{\text{eq}}$ value (at 100 m water depth).

A common theme of all stations is the presence of single specimen $\delta^{18}\text{O}_{\text{np}}$ values that either exhibit a negative offset from or fall within mixed layer $\delta^{18}\text{O}_{\text{eq}}$ values. The negative offset from $\delta^{18}\text{O}_{\text{eq}}$ across the entire water profile, coupled with the low $\delta^{18}\text{O}_{\text{np}}$ (+1.5 to +2.77‰) observed at WCB 1.2S are additional confirmation that these *Neogloboquadrina pachyderma* specimens are nonencrusted, having only secreted ontogenic calcite and belong to the Np-C morphotype. At this station the specimens still contained their cytoplasm when collected, with some showing signs of transitioning between juvenile and adult stages, indicating that the specimens were most likely still alive during collection. Ontogenic calcite exhibits a negative fractionation of minimum of 1‰ relative to $\delta^{18}\text{O}_{\text{eq}}$ (Volkman and Mensch, 2001; Kozdon et al., 2009) as a result of faster calcification in the juvenile and pre-adult stages that require higher respiration rates (Hemleben et al., 1989). As the $\delta^{18}\text{O}$ of respired CO_2 is significantly lower than the $\delta^{18}\text{O}$ of CO_2 in equilibrium with seawater (Epstein et al., 1977; McConnaughey, 1989),

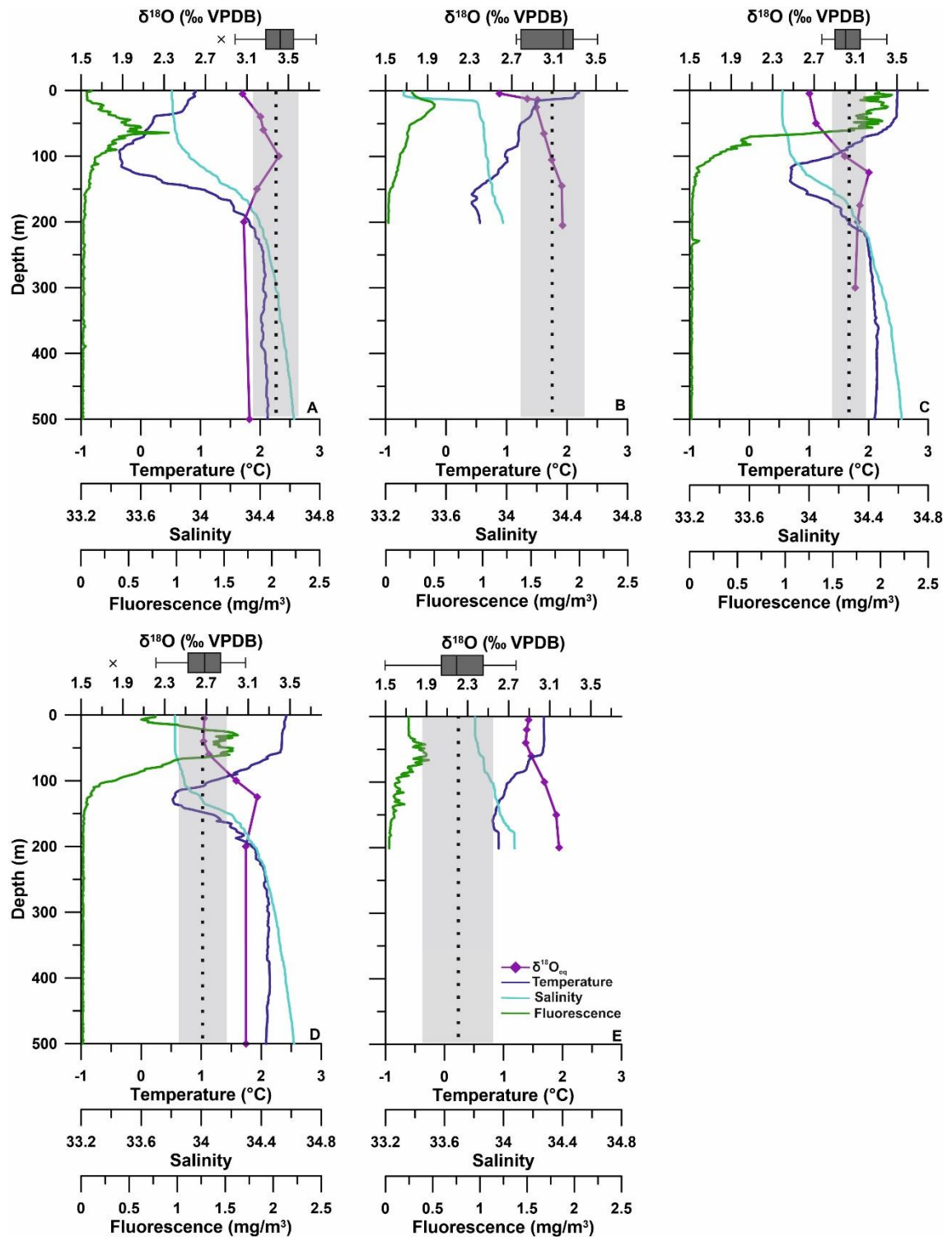


Figure 5.11: CTD and predicted $\delta^{18}\text{O}_{\text{eq}}$ profiles of the water column at each sampling locations in comparison with the single specimen *Np* $\delta^{18}\text{O}$ range (dark grey box plots on top). A) Station 5, B) Station 8, C) Station 12, D) Station 13, E) WCV 1.2S. Stations arranged by morphotype (*Np*-A morphotype in Stations 5, 8, 12, and 13, *Np*-C morphotype in WCV 1.2S) and by latitude, with Station 5 located in the south, station 13 in the north of the study area. The boxplots represent the same ranges as in Figure 5.4A. Dashed vertical line is the mean *Np* $\delta^{18}\text{O}$ value, light grey boxes around mean value represent one standard deviation range.

the faster calcification rate or smaller test size results in a significant negative fractionation (Kozdon et al., 2009). The negative fractionation identified in the mixed layer agrees well with previous studies conducted in the Atlantic sector of the Southern Ocean, where vital offsets of up to -1.2‰ compared with $\delta^{18}\text{O}_{\text{eq}}$ values above 100 m have been recorded (Donner and Wefer, 1994; Mortyn and Charles, 2003).

The negative fractionation exhibited by 50% of the specimens at Station 13 and equilibrium calcification within the mixed layer (instead of below it) exhibited by specimens at Stations 5, 8, and 12 could be explained by a number of reasons. One possibility, is that specimens were chosen incorrectly prior to stable isotope analysis and they are not Np-A morphotypes, but Np-C morphotypes instead. Another explanation could be the secretion of the secondary crust within the mixed layer. Np-C morphotypes were identified in all Bongo net hauls (Section 5.1.2.1), and at Station 5 and 8 these specimens contained their cytoplasm upon collection, indicating their pre-reproduction status. No shell was chosen with a cytoplasm from the Station 5 and 8 samples, therefore the picking of incorrect morphotype cannot explain equilibrium calcification within the mixed layer at these stations. Specimens at Stations 12 and 13 were without their cytoplasm, regardless of morphotype. Care was taken to avoid the picking of incorrect morphotypes. Only specimens that displayed signs of the secondary crust (large euhedral calcite crystals on surface and rough surface texture) were chosen, therefore the incorrect identification of morphotype can be discounted. Instead, it is likely, that specimens that show equilibrium calcification within the mixed layer or show negative fractionation in the mixed layer (Station 13) have secreted the calcite crust within the mixed layer.

The exact reasons and processes behind the secretion of the secondary crust of *Neogloboquadrina pachyderma* are still not known. In some planktonic foraminifera species the calcification of the secondary crust is related to gametogenesis (Bé, 1980). In the case of Np, early studies suggested that the secondary crust forms in response to declining water temperatures as the organism descends through the water column (Hemleben and Spindler, 1983; Kohfeld et al., 1996). However, a more recent study on North Atlantic Np from sediment traps found no indication that the secondary crust forms at greater depth (Jonkers et al., 2016). Additionally, secretion of the secondary crust at constant temperature has been observed in cultured specimens of *Neogloboquadrina incompta*, a close relative of Np (C. Davis, personal communication). Instead of a temperature control, it was suggested that crust formation is driven by tight biological controls, during late ontogeny at relatively shallow depths (Jonkers et al., 2012; Jonkers et al., 2016; Fehrenbacher et al., 2017). Therefore it is plausible that the large amplitude

in the single specimen $\delta^{18}\text{O}_{\text{np}}$ data across the Scotia Sea stations is due to this calcification within the mixed layer. The variability in vital offset within the Scotia Sea and the lack of agreement on the processes behind the secondary crust formation highlight the need for further studies of *Neogloboquadrina pachyderma* biology, morphology and stable isotope variability.

5.1.5 Summary and Conclusion

In this chapter, the aim was to investigate the variability of *Neogloboquadrina pachyderma* abundance, morphology, stable isotope composition and vital effects in the Scotia Sea in order to be able to provide constraints for time series and paleoclimate studies that utilise Np within the Southern Ocean.

Motion-compensated Bongo nets used to collect Np exhibit considerable variability in abundance across the study area. Np abundance varies by up to two orders of magnitude between a station south of the Southern Boundary of the Antarctic Circumpolar Current and a station on the southern edge of the Polar Front. Highest number of Np found in the most northerly location is associated with the highest surface water fluorescence (expression of chlorophyll α concentration) and highest water temperatures down to 100 m water depth. Lowest number of Np was recovered at the southernmost station, and is associated with low fluorescence values and low water temperatures across the water column. The equatorward increase in Np numbers is accompanied by increasing depth of peak abundance. The Bongo net hauls across the study area highlight the link between Np abundance, food availability and water temperature in the polar waters of the Scotia Sea and support previously published South Atlantic Np records (Mortyn and Charles, 2003).

Visual inspection of *Neogloboquadrina pachyderma* specimens under a light microscope revealed the existence of three morphotypes, whose distribution varies across the study area with latitude. The two adult morphotypes, Np-A and Np-B, are separated by the Southern Antarctic Circumpolar Current Front (SACCF). Np-B is found only north of the SACCF, while Np-A is present mostly in the colder waters south of it. The third morphotype, Np-C, represents juvenile, pre-gametogenic specimens, and is found across the study area, dominating one population west of South Georgia.

Stable isotope analysis of single specimens of *Neogloboquadrina pachyderma* reveals a latitudinal gradient in $\delta^{18}\text{O}_{\text{np}}$, decreasing from south to north with decreasing $\delta^{18}\text{O}_{\text{sw}}$ and increasing water temperatures. The $\delta^{18}\text{O}_{\text{np}}$ record shows co-variability with size, with heavier specimens showing higher $\delta^{18}\text{O}_{\text{np}}$. Highest $\delta^{18}\text{O}_{\text{np}}$ is recorded in the Np-A morphotypes at the southern stations, while the lowest $\delta^{18}\text{O}_{\text{np}}$ is recorded in the pre-

gametogenic Np-C morphotypes at WCB 1.2S. Comparison of single specimen $\delta^{18}\text{O}_{\text{np}}$ with $\delta^{18}\text{O}_{\text{eq}}$ across the study area reveals variable vital offsets. The $\delta^{18}\text{O}_{\text{np}}$ of the Np-C morphotype specimens, which calcify in the mixed layer, show negative offset of $\sim 0.6\text{‰}$ from mixed layer $\delta^{18}\text{O}_{\text{eq}}$. The Np-A morphotypes show equilibrium calcification below the mixed layer and within the mixed layer as well. Negative fractionation within the mixed layer is also recorded in this morphotype. The variable offset from $\delta^{18}\text{O}_{\text{eq}}$ of the Np-A morphotype specimens highlights the possibility for the calcification of the secondary crust within the mixed layer as well as below it. This finding supports previous studies of Np and closely related species that argued that the secretion of the secondary crust does not require colder temperatures, such as those found in deeper waters, but is instead biologically controlled, and can take place in shallower waters within the mixed layer (Jonkers et al., 2012; Jonkers et al., 2016; Fehrenbacher et al., 2017). This variable calcification of the secondary crust in the Np-A morphotype of *Neogloboquadrina pachyderma* means that any future study of Np stable isotopes within the polar regions should determine the morphotype as well as the calcification depths of the specimens prior to any assessment of stable isotope records.

5.2 Seasonal variability of *Neogloboquadrina pachyderma* abundance, morphology, and stable isotope composition at the West Antarctic Peninsula

The West Antarctic Peninsula is one of the most climatically sensitive regions in the world. It experienced a $\sim 3.4^{\circ}\text{C}$ warming during the 20th century (Vaughan et al., 2003), five times the global average of $0.6 \pm 0.2^{\circ}\text{C}$ for the same period (Houghton et al., 2001). The increasing atmospheric temperature was accompanied by increased melting of tidewater and marine glacier fronts; 84% of 244 has undergone melting between 1945 and 2005 (Cook et al., 2005) as a result of warm and warming Circumpolar Deep Water at mid-depths (Cook et al., 2016). Long-term records of sea ice concentration along the West Antarctic Peninsula show that the sea ice season shortened by 30-40 days in the 1992-2004 period compared to 1979-1991 as a result of the changes in atmospheric processes (Stammerjohn et al., 2008b). Interannual variability in the number of sea ice days over the Antarctic Peninsula shelf area has been linked to teleconnections between El Niño-Southern Oscillation and the high latitude atmospheric settings. Sea ice records show, that years with low number of sea ice days coincide with persistent northerly winds deriving from sustained La Niña in the tropical Pacific and positive Southern Annular Mode conditions in the high latitudes (Massom et al., 2006; Stammerjohn et al., 2008a). Changes in the atmospheric and oceanic conditions impact the Antarctic ecosystem, as seen by a factor of two decrease in annual peak chlorophyll concentration between 1979 and 2006 (Ducklow et al., 2012) relating to increased surface winds (Montes-Hugo et al., 2009).

In this chapter, a six-year long record of *Neogloboquadrina pachyderma* abundance, morphology, and single specimen stable isotope variability offshore of Palmer Station, Antarctica (Figure 5.12), is presented in relation to environmental conditions. Detailed statistical analysis is carried out on the all *Neogloboquadrina pachyderma* parameters in order to provide a robust assessment on the response of this polar species to environmental changes. The single specimen stable isotope record is used to assess intra- and inter-annual variability in vital effects and to provide a local constraint for future paleoceanographic investigations.

The first section provides information on the statistical analysis used throughout this study. The second section describes the results of the flux, morphology, and single specimen stable isotope analyses, while the rest of the chapter contains the discussion

of the results in the context of environmental variability along the West Antarctic Peninsula.

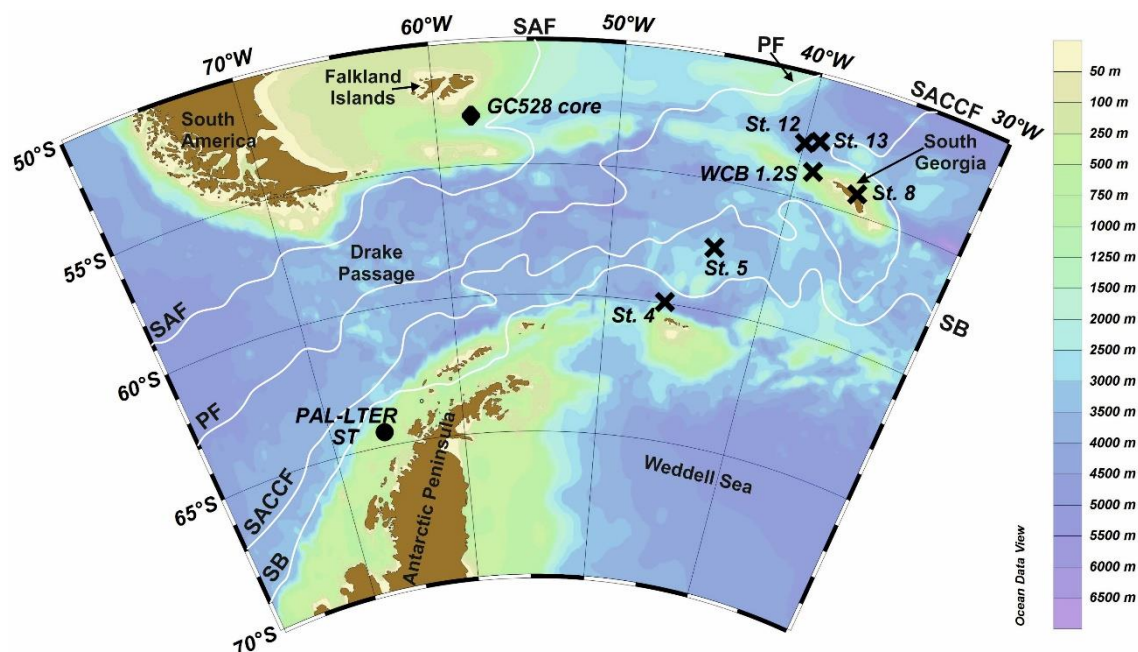


Figure 5.12: Bathymetry map (Schlitzer, R. 2016) of the South Atlantic section of the Southern Ocean highlighting the location of the Palmer LTER sediment trap (black circle) at 64.3°S, 66.0°W, 130 km offshore from the Antarctic Peninsula. The main oceanic fronts are represented by white lines: SAF: Subantarctic Front, PF: Polar Front, SACCF: Southern Antarctic Circumpolar Current Front, SB: Southern Boundary of the Antarctic Circumpolar Current. The location of samples used in Chapter 5.1 (crosses) and 5.3 (diamond) are also denoted as reference.

5.2.1 Statistical methods for data analysis

For data analysis the samples with the mid-date of collection period 9/12/2008, 16/05/2011, 22/02/2012 and 13/11/2013 were removed due to the very small specimen number (12, 6, 13 and 11 respectively) within the samples being below the threshold ($n=15$) identified through a rarefaction curve for statistical significance in statistical data analysis (Appendix 1).

5.2.1.1 Spearman's rank correlation coefficient

Spearman's rank correlation is a nonparametric test used to identify the strength and direction of a monotonic relationship between two series of data (Townend, 2002). Monotonic relationship differs from linear in that when one variable increases (or decreases) the other variable also increases (decreases) but not at the same time – linear relationship is also monotonic (Lehman and Romano, 2005). The test was used to assess the relationship between the *Neogloboquadrina pachyderma* (*Np*) flux record and the environmental variables (5.2.2). Non-paired values from each variable were removed prior to analysis. All remaining variables were ranked using the Excel function

“Rank.Avg” then sorted according to the ranking of the Np flux. Spearman’s correlation test was carried out using PAST v.3.15 (Hammer et al., 2016).

5.2.1.2 Interquartile range

Interquartile range measures the statistical dispersion or spread of data (Townend, 2002). It indicates the extent to which the central 50% of the data points (between 25th and 75th percentile) within a dataset are dispersed. It is a simple method to measure variability, by dividing the dataset into quartiles, with the central value identified by the median. The interquartile range is the difference between the upper (75th percentile, Q3) and the lower (25th percentile, Q1) quartile (Townend, 2002). This descriptive statistical method was used on the raw Np flux dataset to identify variability in the time-series, as indicated by the presence of outliers. Outliers are defined as follows:

$$OL = Q1 - 1.5 \times IQR \quad \text{Equation 5}$$

or

$$OL = Q3 + 1.5 \times IQR \quad \text{Equation 6}$$

where OL is outlier, Q1 is lower quartile, Q3 is upper quartile and IQR is interquartile range (Upton and Cook, 1996).

5.2.1.3 Mann-Whitney U-test

The Mann-Whitney U test is a nonparametric alternative to the t-test and is used to determine if two samples are likely to derive from the same population, utilising the value of the median (Townend, 2002). The main requirements and assumptions for the tests are: i) samples are not normally distributed; ii) samples should follow the same shape (i.e. if one sample is skewed right, the other should be too); and iii) the two samples should be independent (Hammer and Harper (2006). The Mann-Whitney U test was carried out on the morphological datasets collected by the manual and automated method (see section 4.2.2 in Methods). The number of samples analysed by the manual method was smaller than the number analysed by the automated method, hence samples (collected by the automated method) which did not make a pair were removed prior to analysis. Additionally, raw measurements were normalised before analysis to limit artificial results arising from large within-sample variances.

5.2.1.4 Levene’s test for Equality of Variances

Levene’s test is used to test if two or more samples have equal variances when the data displays a non-normal distribution (Levene, 1960). It is a non-parametric alternative to the Fmax test, which requires a normal distribution and prefers samples which have

equal number of data points (Hartley, 1950). Levene's test is a less sensitive test than Fmax test as it neither requires a normal distribution nor equal number of data points in the samples. The original version of the test used the mean of the samples for the statistical analysis; however, later developments explored the use of the medians (Brown and Forsythe, 1974) and this proved more beneficial in samples which showed a skewed distribution. In this chapter, here the median values of the samples are used to run Levene's test as some samples showed a skewed distribution.

5.2.1.5 Principal Component Analysis

Principal Component Analysis (PCA) is a type of multivariate analysis that identifies patterns in data, and highlights their similarities and differences through visual representation (Townend, 2002). Multivariate statistical analysis techniques can be used where several different types of measurements are made on each individual sample (Smith, 2002). PCA's primary function is to deconvolve the variation in a p-dimensional dataset and therefore the underlying assumptions do not include a Gaussian distribution of the dataset (Townend, 2002). PCA has a linear response model, and identifies hypothetical variables (components) that can explain most of the variance in the multidimensional dataset (Hammer and Harper, 2006). It can achieve this by reducing the dimensionality of the data while retaining most of the variation within the dataset (Jolliffe, 2002). At its most basic, PCA uses a series of least-squares regressions to fit straight lines through the data (Jongman et al., 1995). When represented visually, the first PCA axis embodies the first principal component (the hypothetical variable that explains the most variability within the dataset), the second PCA axis, the second principal component, and so on. The accompanying principal component scores correspond to the slope of the fitted linear regression line for the variable against the PCA axis, i.e. a positive score means an increase in the variable, and a negative score means a decrease in the variable (Jongman et al., 1995). Each principal component has an eigenvalue which is essentially the variance of the scores (Townend, 2002). PCA was used to analyse the manually collected morphometric dataset where the morphometric values were normalised, as well as on the means of log-transformed maximum diameter values together with the means of the size-invariant morphometric parameters.

5.2.1.6 Anderson-Darling test for normality

The Anderson-Darling test (A^2) is used to test if a sample of data derives from a population with a specified distribution (Stephens, 1974). It is related to the Kolmogorov-Smirnov test and is most commonly used to test for normal distribution (Stephens, 1986). The test calculates critical values based on a specific distribution (e.g. lognormal, normal,

and exponential) which allows it to be a more sensitive test than other statistical tests for normality (Stephens, 1974). The Anderson-Darling test is used to assess the distribution within the manually collected morphometrics dataset. The test was run on the log-transformed maximum diameter values of each sample. Additionally, the test was also carried out on the first principal component scores belonging to the Principal Component Analysis tests undertaken on the four size-invariant variables (see section 4.2.2 in Methods). Utilising the Anderson-Darling test on the first principal component scores can identify continuity in the morphospace — the representation of the possible shape, form and structure of an organism (Moller et al., 2013).

5.2.1.7 Redundancy Analysis

Redundancy analysis (RDA) is an extension of PCA analysis that requires both a set of response and a set of explanatory variables (Zuur et al., 2007). It is a non-symmetric alternative to Canonical Correlation Analysis (Van den Wollenberg, 1977). RDA models the response variables as a function of the explanatory variables. RDA utilises an extension of multiple linear regression, where multiple response variables are regressed on multiple explanatory variables. This is followed by a PCA on the matrix of the fitted values of all the response variables as generated by the multiple linear regression (Ter Braak 1986). The graphical output of the RDA is a triplot (two biplots on top of each other) which consist of three parts: i) qualitative explanatory variables are represented by squares, the quantitative ones by lines; ii) response variables are represented by lines or labels; iii) the samples themselves are denoted by points (Zuur et al., 2007). RDA was used on the means of the size-normalised, size-dependent morphological parameters, and on the size-normalised, size-invariant morphological parameters against the environmental parameters.

5.2.2 Assessment of *Neogloboquadrina pachyderma* flux, morphology, and stable isotope chemistry from a six year-long time series

5.2.2.1 Physical properties and seasonality at Palmer Deep

The physical properties of the environment are described to provide a context for the relationship of the abundance, morphology and geochemistry of Np to environmental parameters. Sea surface temperature (SST) (NOAA NCEP, 2015), sea ice concentration (SIC) (NSIDC, 2015), chlorophyll α concentration (chl α) and organic carbon and nitrogen fluxes (OCF and ONF respectively) (Palmer Station LTER Antarctica, 2015) recorded at the Palmer LTER site between Jan 2006 and Jan 2013 provide the environmental context (Figure 5.13). Throughout this 7 year period SST generally varies between 2°C

and -1.5°C between summer and winter (Figure 5.13A). Inter-annual variability of up to $\sim 1^{\circ}\text{C}$ is observed in the maximum difference between winter and summer SST values. Seawater temperatures at 100 m water depth display a smaller seasonal variability (maximum inter-annual range of 2°C) and exhibit less inter-annual variability than SST. We observe a strong seasonal stratification of the upper water column between late-spring and early-autumn throughout the record (increased offset between SST and 100 m temperature, Figure 5.13A). SIC and duration (Figure 5.13B) shows a strong seasonal cycle with pronounced inter-annual variability. Peak SIC occurs from July, and the exact timing and maximum values vary between years. Years where SIC approaches 100% are associated with minimum SST of -1.5°C , close to the freezing point of sea water. In 2010 and 2012, when SIC did not exceed 78.8% and 66.8% respectively, minimum SST was -1.28°C and -1.02°C respectively.

The length of the sea ice season also shows strong inter-annual variability, between 46 days in 2008 and 108 days in 2011 (Figure 5.13B). Although no direct measurement is available, it can be assumed that Chlorophyll α concentration is minimal during the sea ice season. Peak chl α concentration is reached after the end of the sea ice season (Figure 5.13D) when glacial meltwater introduces nutrients to the surface waters which together with the stratified water column, promote primary productivity, especially the development of diatom blooms (Smith et al., 1995; Pike et al., 2013; Peck et al., 2015). Peak chl α concentrations oscillate between 9.6 mg/m^3 and 35 mg/m^3 between 2006 and 2013 showing a strong inter-annual variability (Figure 5.13D). Total organic carbon flux varies from 0 to about $140\text{ mg/m}^2/\text{day}$ and are lowest between April and October (Figure 5.13E) when the water column is mixed (Figure 5.13A) and highest in the summer during times of maximum stratification. Variability in the organic carbon flux is also observed between the individual years throughout the record as well as within the years (Figure 5.13E). The greatest total organic carbon flux is recorded in 2006 while the lowest is in 2008. Total organic nitrogen flux follows the same trends as the organic carbon flux.

5.2.2.2 *Neogloboquadrina pachyderma* flux between 2006 and 2013

Foraminiferal flux will be described in the context of the annual and inter-annual changes in the environmental conditions outlined above (Section 5.2.2.1). *Neogloboquadrina pachyderma* (*Np*) was the only species found in the time series samples, which can be attributed to the polar location of the trap. Hence, from here on foraminifera flux is referred to as *Np* flux. *Np* flux generally range over two orders of magnitude from zero in winter months to over $300\text{ tests/m}^2/\text{day}$ in summer (Figure 5.13C). Exceptional fluxes of $1100 - 9500\text{ tests/m}^2/\text{day}$ were observed during the spring of 2010. Summer peak fluxes

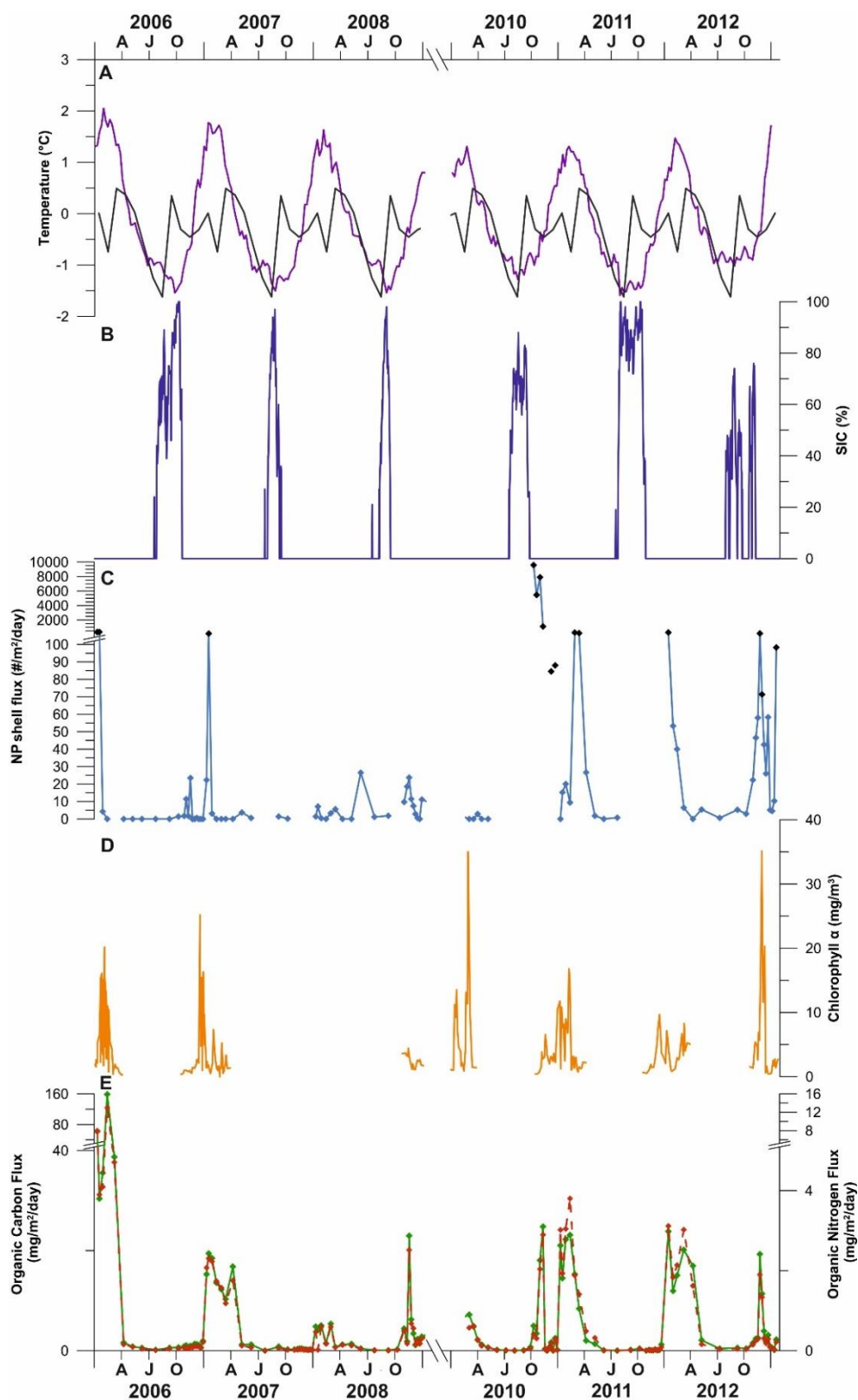


Figure 5.13: Time-series flux record in relation to environmental variables. A) Satellite-derived weekly sea surface temperature (purple line) and WOA13-derived monthly temperature at 100 m water depth (grey line) overlain onto the time-series interval. B) Satellite-derived sea ice concentration. C) Np shell flux. D) Chlorophyll α concentration between 10-20 m. E) Organic carbon (red line) and organic nitrogen (green line) flux record. Seasonal variability is observed in all three flux records. AJO: April, July, October

are generally above 100 tests/m²/day with the exception of 2008 when summer fluxes only reached ~5 tests/m²/day. Higher Np flux values of 13-26 tests/m²/day are recorded during the early summer period that year. Two distinct pulses of Np flux are recorded in the weekly-averaged annual flux record (Figure 5.14F). The first, broader pulse begins in late spring (end of October) and lasts until mid-summer (January) while the second, shorter-lived pulse arrives in late summer (mid-February) and dissipates by early autumn (April). The start of the first pulse in October coincides with the early chlorophyll bloom (Figure 5.14D) and takes place after the retreat of the seasonal sea ice (Figure 5.14C) reaching average fluxes of ~45 tests/m²/day by the second half of November (Figure 5.14F), and year on year ranging from 60 to 100 tests/m²/day.

Between the end of November and mid-January the shell flux of Np first drops slightly to an average of ~35 tests/m²/day (although fluxes vary from zero to ~50 tests/m²/day between the years). This decrease is followed by a peak in mid-January with average flux above 100 tests/m²/day. Note that the low averages of 10 tests/m²/day between late December and early January (Figure 5.14F) include gaps in the trap sampling hence, by comparison with other trap studies (Jonkers et al., 2010; Kuroyanagi et al., 2011), it is assumed that flux continues across this interval at the same rate as in early December. Significant inter-annual variability is found in the Np flux during this first pulse (e.g. Np flux of minimum of 1 tests/m²/day in 2006 December compared to maximum of 88 tests/m²/day in 2010 December, maximum of over 300 tests/m²/day in 2006 January compared to a minimum of 11 tests/m²/day in 2007 January). After mid-January Np flux decreases rapidly from its peak to an average of ~10 tests/m²/day (Figure 5.14F) coinciding with maximum water column stratification. The second pulse of Np flux, an abrupt increase to ~50 tests/m²/day at the end of February, coincides with the second chlorophyll bloom of the ice-free season (Figures 5.14D and 13B, respectively). By the end of March this second Np flux pulse dissipates and fluxes drop to ~4-5 tests/m²/day by April (Figure 5.14F). Np flux falls to background levels (zero to five Np tests/m²/day, Figure 5.14F) after March as SST and chl α decrease (Figures 5.14A and 12D) and the water column experiences greater mixing in the surface (Figure 5.14B). These low levels of Np flux remain the norm between April and late October (Figure 5.14F) with the exception of 2010 October, when the highest Np flux of the entire time series (1100 – 9550 tests/m²/day) was recorded (Figure 5.13C).

Seasonal and inter-annual variability in *Neogloboquadrina pachyderma* flux

To assess the foraminiferal flux variability through the time-series the interquartile range (IQR) and the outliers of the dataset are defined. Fourteen of the 92 samples are identified as outliers in the flux data set (Figure 5.15). These can be considered as data

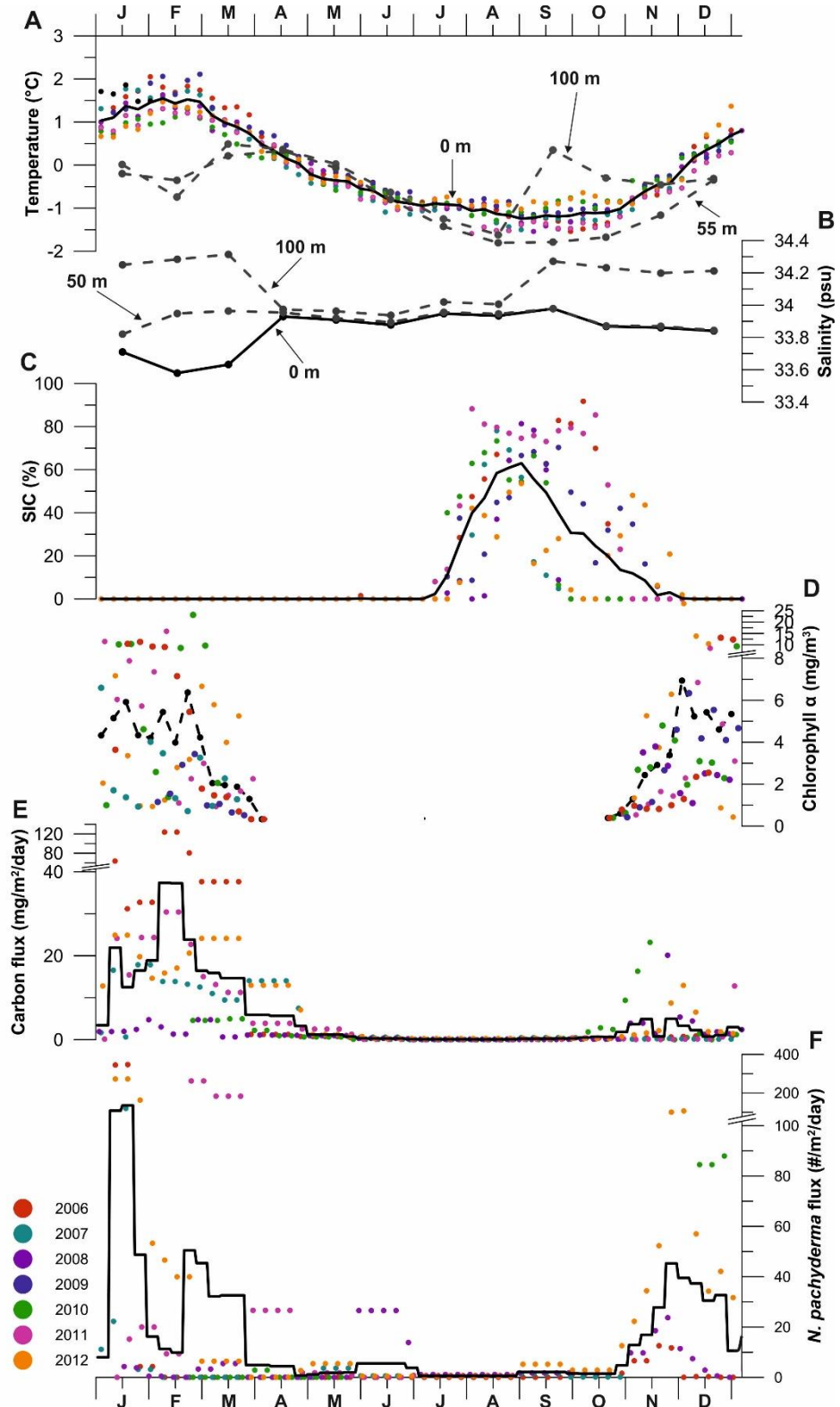


Figure 5.14: Weekly averaged and time-shifted time series flux record (black lines: average values, of 2006-2012 period; colour dots: individual years). A) Annual satellite-derived weekly SST, average SST (black line) and WOA13 monthly temperature at 55 m and 100 m water depths (grey lines). B) WOA13 monthly salinity record at surface (black line), 50 m and 100 m (grey lines) water depths. C) Annual satellite-derived daily sea ice concentration, average SIC (black line). D) Chlorophyll α concentration (10-20 m), average Chl α concentration (black line). E) Average carbon flux (black line) and annual records. F) *Nps* flux record (extremely high flux of October 2010 removed from calculation of average). The low fluxes of early January and the sudden drop off at the end of December are due to the gaps in sampling periods.

points that are outside the expected normal distribution and are different from the rest of the population, and that there is statistically significant variability in the flux. The significant variability is also indicated by the large difference between the average and the median value (Table 5.4). Statistically-determined high fluxes occur during January in 2006, January 2007, October, November, and December in 2010, March in 2011, January and December in 2012 and in January 2013 (Figure 5.16). These higher *Np* flux values occur mostly during times when carbon flux is high and/or chlorophyll α concentration is above or near 3 mg/m^3 . However, it is worth noting that while high fluxes of *Np* are always associated with increased carbon flux or chlorophyll α concentration, these factors do not always lead to higher *Np* flux, as highlighted in Figure 5.17.

To assess the relationship between the *Np* flux record and the environmental variables a series of Spearman's correlation tests were carried out. This test circumvents problems arising from the non-normal distribution of the datasets by ranking the values. Prior to analyses non-paired values were removed from the dataset and the rest of the dataset was ranked and sorted according to the *Np* flux record. The Spearman's Correlation tests revealed significant correlations for *Np* flux only with organic carbon and organic nitrogen flux, additionally, organic carbon and nitrogen flux are positively correlated with an r value close to 1 (Table 5.5). Significant correlation was found between chlorophyll α concentration and organic carbon and nitrogen flux. Significant correlation was also found between carbon/nitrogen flux and sea ice cover and SST.

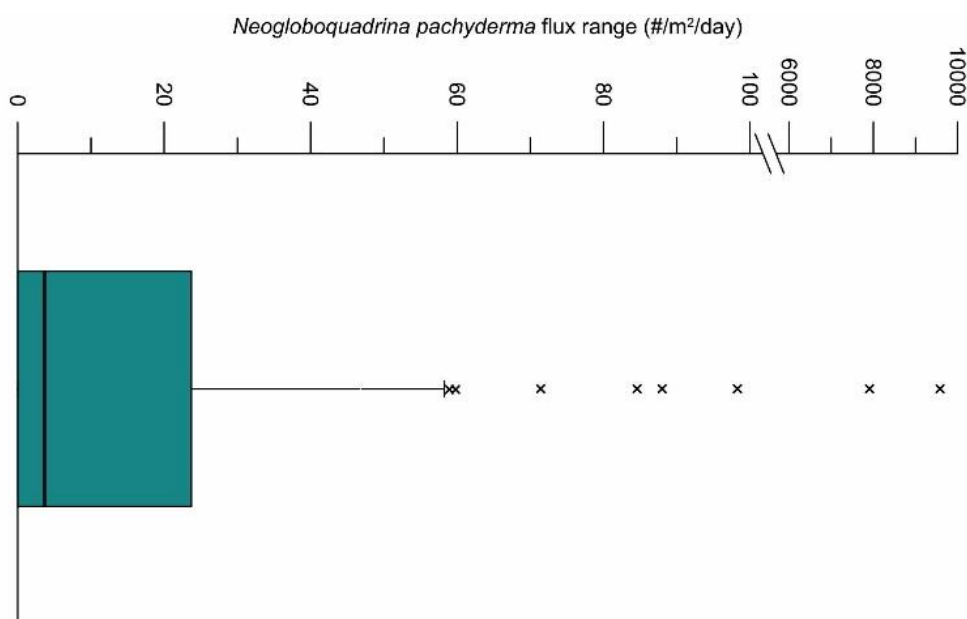


Figure 5.15: Boxplot of *Neogloboquadrina pachyderma* flux range. Crosses represent outliers, thick black line is median, grey dashed line is mean. Low outliers are not present as flux number cannot be below zero.

Table 5.4: *Neogloboquadrina pachyderma* flux data summary

| | |
|------------------------------------|------------|
| Mean | 286.76 |
| Median | 3.68 |
| Standard deviation | 1392.73 |
| Variance | 1939695.83 |
| Minimum | 0 |
| Maximum | 9586.29 |
| Mean + 1σ | 1679.49 |
| Mean + 2σ | 3072.22 |
| Quartile 1 | 0 |
| Quartile 2 | 3.68 |
| Quartile 3 | 23.7 |
| Top outliers (Q3+(1.5xIQR)) | >59.3 |

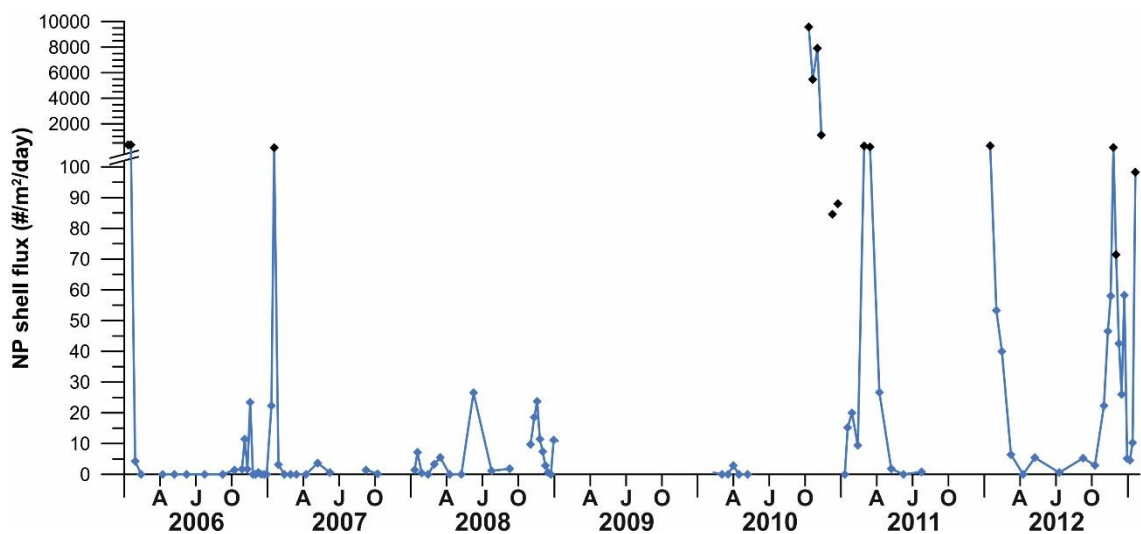


Figure 5.16: *Neogloboquadrina pachyderma* shell flux variability through the Palmer LTER time series. Black diamonds represent statistically significant outliers in the data. AJO: April, July, October.

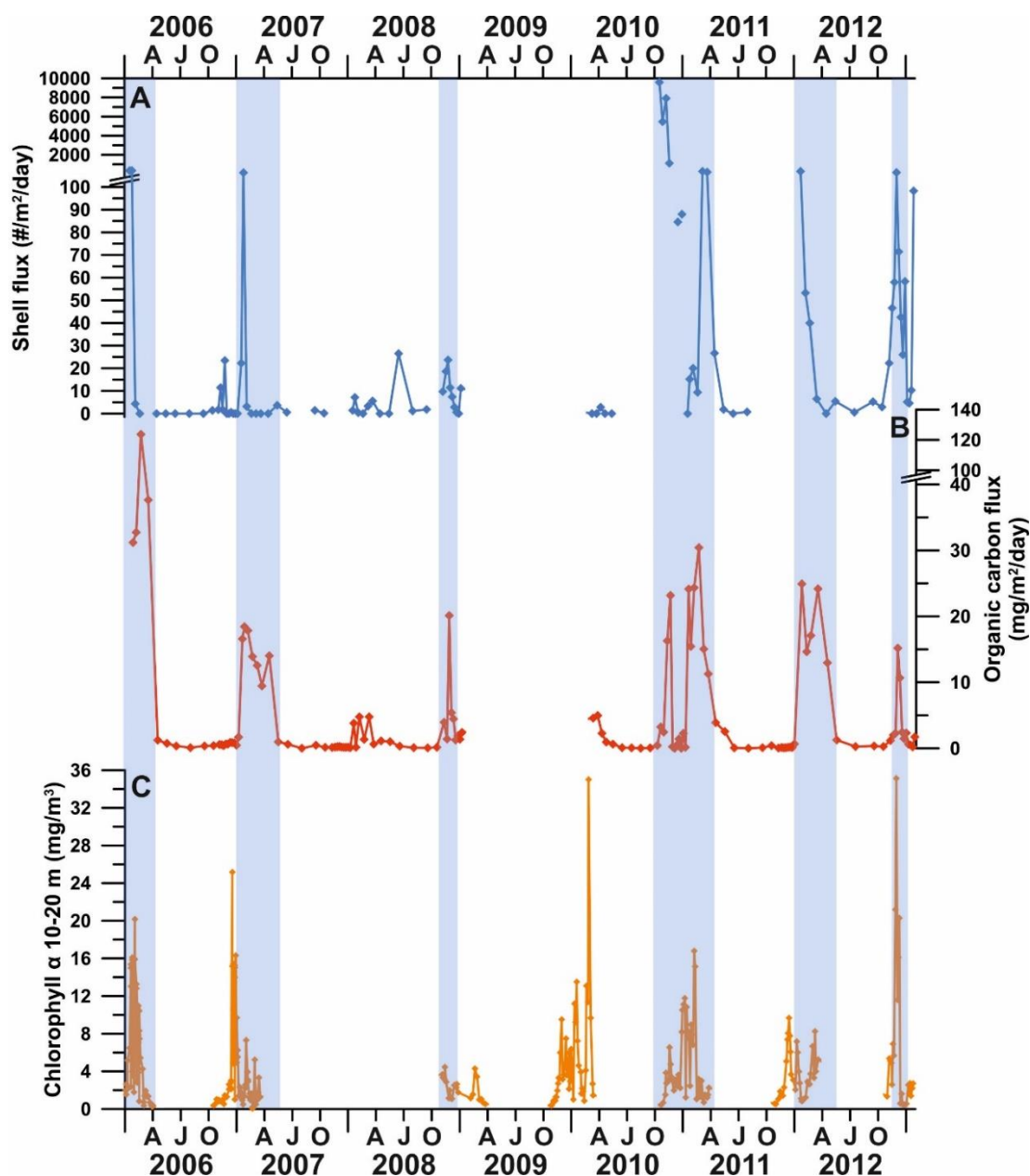


Figure 5.17: *Neogloboquadrina pachyderma* flux (A), organic carbon flux (B) and Chlorophyll α (C) concentration through time. Black symbols in (A) represent statistically significant outliers in the *Np* flux data. Highlighted areas show that some instances of increased organic carbon/chlorophyll concentration do not lead to higher *Nps* flux. AJO: April, July, October

Table 5.5: Spearman's correlation coefficient (r) values. Statistically significant ($p < 0.05$) results are highlighted in bold

| Variable | Nps flux | Carbon flux | Nitrogen flux | Sea Ice Conc. | SST | Chlorophyll α conc. |
|----------------------------|--------------|---------------|---------------|---------------|---------------|----------------------------|
| Nps flux | 1 | 0.229 | 0.219 | -0.035 | 0.112 | -0.005 |
| Carbon flux | 0.229 | 1 | 0.989 | -0.493 | 0.790 | 0.312 |
| Nitrogen flux | 0.219 | 0.989 | 1 | -0.480 | 0.770 | 0.309 |
| Sea Ice Conc. | -0.035 | -0.493 | -0.480 | 1 | -0.610 | 0.160 |
| SST | 0.112 | 0.790 | 0.770 | -0.610 | 1 | 0.077 |
| Chlorophyll α conc. | -0.005 | 0.312 | 0.309 | 0.160 | 0.077 | 1 |

5.2.2.3 The morphological variability of *Neogloboquadrina pachyderma* at Palmer Deep

In the next three sections the variability of Np morphology at Palmer Deep is analysed. The two data collection methods employed in this study will be evaluated and followed by an assessment of Np shape, size and translucency through the time series and, finally, the morphological variability will be considered from a statistical perspective.

Comparison of data collection methods: automated vs manual

Morphological analysis of the Np specimens was carried out both manually and using automated microscopy. A range of morphological parameters were analysed by both methods, including maximum, minimum and mean diameter, area, perimeter and sphericity. Mean grey values were analysed with the automated microscope. For a detailed description on the data collection methods please see Chapter 4.

The morphological datasets collected manually and by automated microscopy can be compared by carrying out a series of Mann-Whitney U-tests. In order to assess the interchangeability of the datasets it was important to analyse how closely related the results are from the two data collection methods. The maximum diameter (MD) parameter was chosen as the basis of the comparison because it was analysed using both methods and it is one of the parameters discussed most often in the literature (Healy-Williams et al. 1992; Eynaud et al, 2009, Moller et al. 2013). First, the absolute values were normalised to avoid any artificial results arising from the large range of values within some of the samples. The MD measurements were normalised to values ranging between 0 and 1 by using the following equation: $X_{\max,n} = (n - n_{\min}) / (n_{\max} - n_{\min})$ (Moller et al., 2013). By normalising the data, large differences in variance are also reduced (Table 5.6), which is a prerequisite of the Mann-Whitney U-test.

Samples were chosen for Mann-Whitney U-tests on the basis that both of the data collection methods were used for morphological analysis. Altogether MD values of 32 sets of samples were tested. The results of the tests showed that there is significant difference between the medians of 11 pairs of samples out of the 32 (Table 5.7). The results of the Mann-Whitney U-tests suggest that there is a significant difference between the MD obtained from the two methods and that samples analysed by the different methods cannot be combined into one dataset. The difference in the number of measurements collected by the different methods did not affect the results of the Mann-Whitney U-test. Some of the pairs of samples with large differences in the number of measurements (e.g. 19/11/2010: 63 and 471 measurements collected by the manual and automated method, respectively) showed no significant difference in mean MD,

while others did (e.g. 25/01/2006: 62 (manual) and 435 (automated)). Although the results of the two different techniques are not comparable overall, the 32 sets of data show similar trends when the manually-derived and microscope-derived datasets are visually displayed next to each other (Figure 5.18). This suggests that while the results of the different methods should not be considered as a single dataset, the automated microscopy method can be used just as effectively as the manual method when looking

Table 5.6: Comparison of the sample variances (σ^2) of raw and normalised maximum diameter dataset measured by the manual and automated method. By normalising the maximum diameter (X_{max}) values ($X_{max,n} = (n - n_{min}) / (n_{max} - n_{min})$) it is possible to reduce the large range in the between sample variance (Moller et al., 2013).

| Date | Manual | | Automated | |
|-------------------|----------|------------|-----------|------------|
| | Raw data | Normalised | Raw data | Normalised |
| 25/01/2006 | 1106.015 | 0.052 | 1541.667 | 0.044 |
| 11/11/2006 | 1507.080 | 0.079 | 1805.995 | 0.091 |
| 25/11/2006 | 1396.773 | 0.078 | 1589.419 | 0.077 |
| 25/01/2007 | 461.877 | 0.050 | 964.885 | 0.033 |
| 16/05/2007 | 835.982 | 0.049 | 1714.285 | 0.058 |
| 16/09/2007 | 535.423 | 0.088 | 612.345 | 0.080 |
| 23/03/2008 | 1447.136 | 0.047 | 1564.296 | 0.071 |
| 16/06/2008 | 1202.753 | 0.037 | 508.883 | 0.029 |
| 01/08/2008 | 1308.768 | 0.046 | 2194.566 | 0.089 |
| 16/09/2008 | 2103.138 | 0.057 | 1252.068 | 0.080 |
| 18/11/2008 | 1529.784 | 0.053 | 2121.510 | 0.055 |
| 09/12/2008 | 2016.842 | 0.110 | 2787.791 | 0.087 |
| 06/01/2009 | 2121.196 | 0.090 | 2236.071 | 0.107 |
| 18/10/2010 | 675.414 | 0.058 | 762.928 | 0.047 |
| 28/10/2010 | 2167.502 | 0.019 | 1067.015 | 0.050 |
| 19/11/2010 | 2192.987 | 0.053 | 2862.933 | 0.035 |
| 17/12/2010 | 3172.922 | 0.048 | 3424.120 | 0.031 |
| 31/12/2010 | 2380.290 | 0.042 | 2979.673 | 0.050 |
| 08/03/2011 | 1328.747 | 0.043 | 2385.108 | 0.045 |
| 23/03/2011 | 1983.947 | 0.081 | 2272.193 | 0.045 |
| 16/05/2011 | 853.053 | 0.164 | 2439.452 | 0.081 |
| 22/02/2012 | 849.344 | 0.088 | 1228.326 | 0.145 |
| 16/05/2012 | 870.636 | 0.075 | 1043.833 | 0.066 |
| 17/07/2012 | 1864.943 | 0.071 | 1637.209 | 0.088 |
| 16/09/2012 | 709.146 | 0.057 | 921.671 | 0.037 |
| 08/11/2012 | 1900.198 | 0.040 | 2139.616 | 0.036 |
| 18/11/2012 | 2299.111 | 0.041 | 2948.182 | 0.038 |
| 02/12/2012 | 4092.891 | 0.023 | 3841.313 | 0.026 |
| 09/12/2012 | 4066.276 | 0.052 | 1101.263 | 0.068 |
| 23/12/2012 | 3233.613 | 0.064 | 2968.266 | 0.059 |
| 30/12/2012 | 3637.243 | 0.053 | 2643.694 | 0.037 |
| 27/01/2013 | 1717.861 | 0.053 | 2575.266 | 0.031 |

Table 5.7: Results of Mann-Whitney U-tests (*p* values) and number of data points. Statistically significant ($p < 0.05$) results are highlighted in bold

| <i>Date</i> | <i>p values</i> | <i>No. of data points (manual)</i> | <i>No. of data points (automated)</i> |
|-------------------|--------------------|------------------------------------|---------------------------------------|
| 25/01/2006 | 0.013 | 62 | 435 |
| 11/11/2006 | 1.000 | 17 | 11 |
| 25/11/2006 | 0.714 | 38 | 27 |
| 25/01/2007 | 0.532 | 63 | 129 |
| 16/05/2007 | 0.912 | 17 | 12 |
| 16/09/2007 | 0.625 | 18 | 15 |
| 23/03/2008 | 0.626 | 39 | 35 |
| 16/06/2008 | < 0.0001 | 55 | 313 |
| 01/08/2008 | 0.004 | 48 | 10 |
| 16/09/2008 | 0.531 | 22 | 24 |
| 18/11/2008 | 0.018 | 49 | 36 |
| 09/12/2008 | 0.877 | 12 | 17 |
| 06/01/2009 | 0.506 | 18 | 14 |
| 18/10/2010 | 0.021 | 64 | 62 |
| 28/10/2010 | < 0.0001 | 63 | 57 |
| 19/11/2010 | 0.117 | 63 | 471 |
| 17/12/2010 | 0.597 | 62 | 96 |
| 31/12/2010 | 0.494 | 62 | 103 |
| 08/03/2011 | 0.529 | 43 | 38 |
| 23/03/2011 | 0.203 | 23 | 48 |
| 16/05/2011 | 0.649 | 6 | 17 |
| 22/02/2012 | 0.947 | 13 | 9 |
| 16/05/2012 | 0.105 | 29 | 23 |
| 17/07/2012 | 0.346 | 24 | 11 |
| 16/09/2012 | 0.275 | 49 | 52 |
| 08/11/2012 | 0.018 | 56 | 59 |
| 18/11/2012 | 0.036 | 65 | 110 |
| 02/12/2012 | < 0.0001 | 64 | 108 |
| 09/12/2012 | 0.414 | 50 | 35 |
| 23/12/2012 | 0.773 | 50 | 59 |
| 30/12/2012 | 0.005 | 64 | 136 |
| 27/01/2013 | 0.021 | 61 | 155 |

into broad-scale variability in the morphology of foraminifera. The automated method is a faster way to collect data as it does not rely on manual orientation and placement of individual specimens onto slides which can be time consuming when dealing with 1000s of specimens. Steps were taken prior to data collection to ensure that the specimens are orientated in the same way in order to create a dataset which is truly comparable with the manual dataset. As shown by the results of the statistical analyses these steps did not eliminate entirely the possibility that some specimens are measured in their side view instead of their umbilical view. The manual placement, orientation, image acquisition and analysis of each individual specimen took 3.5-4 hours per sample, depending on the number of specimens within a sample. This is approximately 24 times longer than what

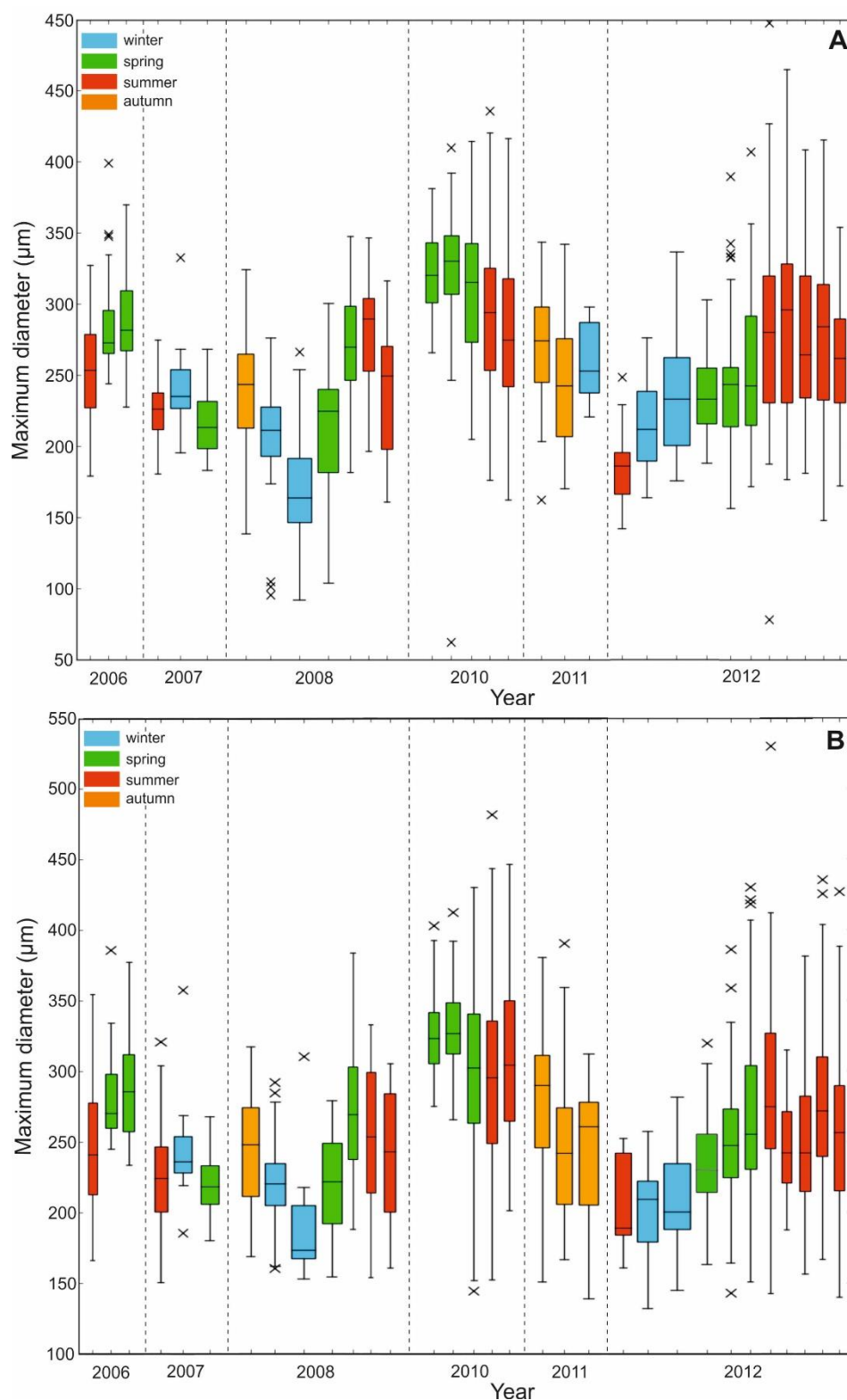


Figure 5.18: Comparison of manual and automatic image acquisition and analysis using the maximum diameter record. Absolute range of values can be slightly different between manually derived values (A) and those produced by the automatic microscope and image analysis system (B) primarily due to difference in the number of specimens analysed. However trends are similar. Note the successively increasing max. diameter between winter and summer 2012 (phase 1-phase 4) and the successively decreasing values between spring 2010 and autumn 2011 (phase 2-phase 5) observed by both methods. The width of the boxes varies in accordance with the length of time each cup was open in the sediment trap. Slimmest box represents 7 days, thickest box indicates 92 days.

is required for the automated microscopy. The use of an automated microscope and image analysis of the manually mounted individual specimens could, in a future study, provide an ideal solution for acquiring high precision, high accuracy data in a time efficient manner.

Variability of *Neogloboquadrina pachyderma* shape, size and translucency

To inspect the morphological variability of Np three parameters were used: MD, sphericity and mean grey value – each measured using the automated microscopy method. These parameters describe the overall morphology of the specimens well. MD is variable with size while sphericity and mean grey value are not variable with size. MD is a representation of the size of the test, with the assumption that older and/or less stressed organisms would have a larger maximum diameter than younger and/or more stressed organisms. Sphericity refers to the shape of the shell, i.e. how round/elongated the foraminiferal test is and is a reflection of the ratio between the longest and shortest distance measured on the shell, with the perfect sphere represented by the highest value of 1. The mean grey values are the expression of translucency as the grey value represents the brightness of a pixel. The brighter (whiter) the pixel the higher the grey value with a maximum of 255 in an 8-bit image (Johnson, 2006). The brightness of the pixels express the amount of calcification of the shell, with more heavily calcified specimens displaying whiter, less translucent tests.

Np shell size, expressed as MD, displays intra-and inter-annual variability (Figure 5.19C). Minimum, mean and maximum MD of the spring-summer months (October-April) are consistently higher compared to the corresponding winter (June-September) values of the same year. The highest maximum MDs were recorded during Nov-Jan 2010-11 and Dec 2012. The maximum MD recorded in these two summers exceed the summer maximum MD of 2006, 2007 and 2008 by as much as 200 μm (Figure 5.19C). Average and minimum MD display similar trends to the maximum MD, but with smaller overall variability. While Np shell size displays seasonal variability throughout the time series, the sphericity of the shells remain relatively unchanged (Figure 5.19B). The variability in the spread of the sphericity data remains similar to the MD dataset: largest ranges recorded in the spring-summer (October-April) and smallest ones in the winter (May-September) (Figure 5.19B). The translucency (hence calcification) of the shells, expressed by the mean grey value (Figure 5.19A) shows clear intra-annual variability, similar to that observed in the maximum diameter time series. The maximum winter mean grey values are lower than the corresponding year's summer mean grey values (Figure 5.19A), i.e. there is greater calcification of specimens collected in the summer and less calcification of those collected in the winter. The recorded range in mean grey

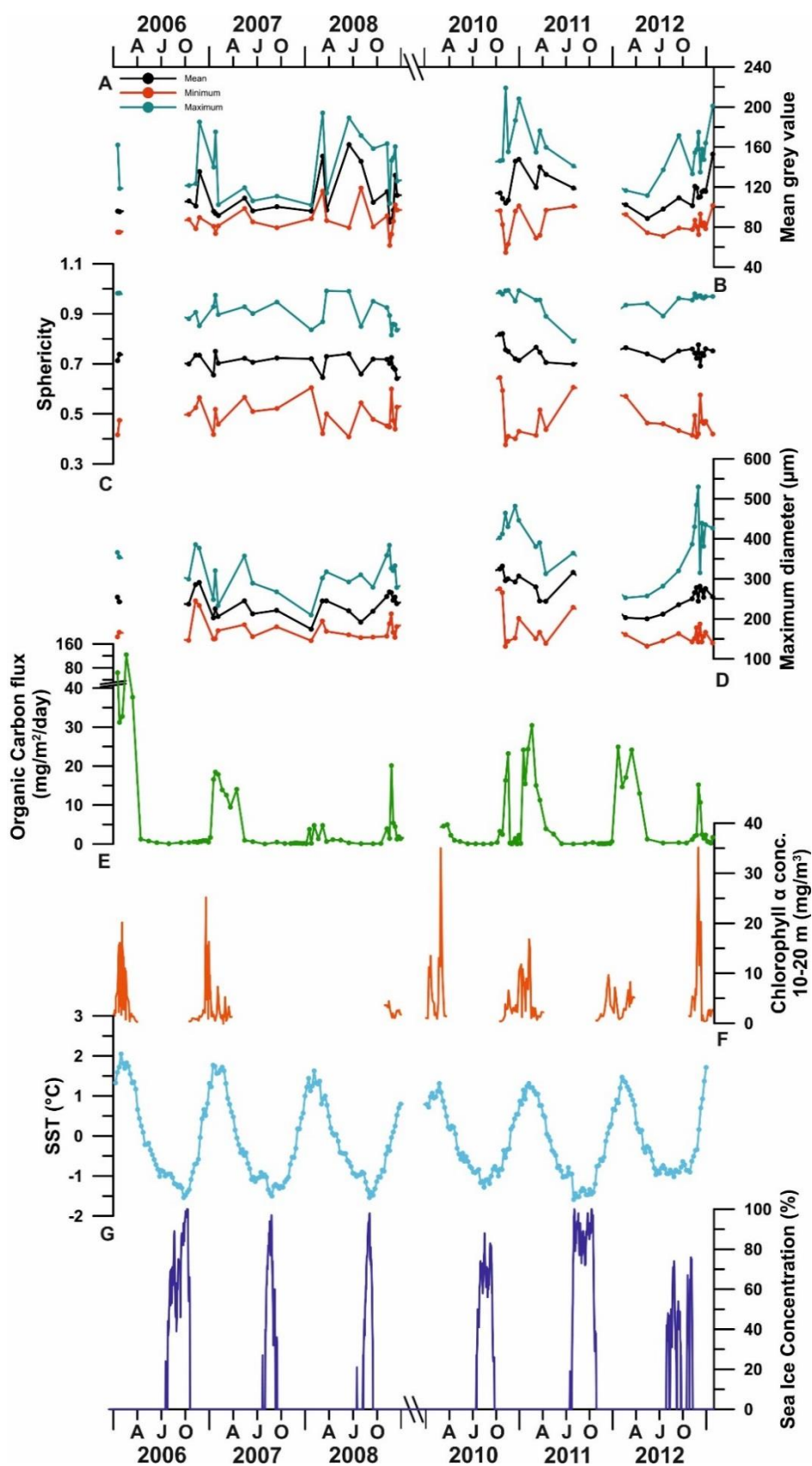


Figure 5.19: Time-series record of the foraminiferal morphological parameters (collected by automated method) and environmental variables. A) Mean grey values as a measure of translucency and calcification; B) Sphericity; C) Maximum diameter; D) Organic carbon flux; E) Chlorophyll *a* flux; F) Sea surface temperature; G) Sea ice concentration. AJO: April, July, October

value is typically smallest during the winter months and largest during the summer. The data range of each sample set can also be assessed by analysing the relative frequency distribution of each parameter (Figure 5.20). The relative frequency distribution of each parameter illustrates the same trends observed in Figure 5.19 and highlights the variability in shell size and translucency (mean grey value). Shell size and translucency (Figure 5.20) show high variability through the time series and show the relationship between shell size and translucency (extent of calcification) (Figures 5.20A and 20C). There is a greater proportion of whiter (less translucent, more calcified) shells during Dec 2006 - Jan 2007, Oct 2010 - March 2011, and Nov 2012 - Jan 2013, concurrent with a greater percentage of larger shell sizes (>300 μm). In contrast, a higher incidence of smaller shells (May 2007 - Jan 2008, Jan 2012 - Jul 2012) are accompanied by a higher incidence of lower mean grey values, indicative of greater translucency (less calcification). The proportion of the different sphericity groups is fairly stable through the record (Figure 5.20B), especially when compared to the variability observed in the MD and mean grey values datasets.

Statistical analysis of variability in *Neogloboquadrina pachyderma* morphology

To determine the main factors behind Np morphological variation a series of statistical analyses was carried out on the morphological parameters and the environmental data. For the morphological parameters, data collected by the manual method was used solely due to the large variability present in the secondary morphological parameters (circularity ratio and elongation ratio) calculated from surface area and maximum diameter (MD) measurements (see Chapter 4, 4.2.2.1) collected by automated microscopy. Np shell size was measured both as the MD and cross-sectional surface area (Figure 5.21). Significant correlation (r value between 0.959 and 0.996; Table 5.8) was found between MD and the square root of surface area in all 36 sets of samples collected by the manual method. The relationship can also be expressed as the slope of the regression, which varied between 0.760 and 0.918, with an average of 0.837 ± 0.04 for the time period between 2006 and 2013 (Table 5.8). These calculations indicate that both cross sectional area and MD can be used to represent shell size as the relationship between them is relatively constant due to the small variations in sphericity. In my study MD was used as a measure of shell size which allows comparison with previous studies (Moller et al. 2013, Kucera and Kennett, 2002).

In order to determine the distribution of the shell sizes across the whole time series as represented by MD, Anderson-Darling tests were carried out on each of the 32 sets of samples as listed in Table 5.8. The distribution of the shell sizes is shown in the

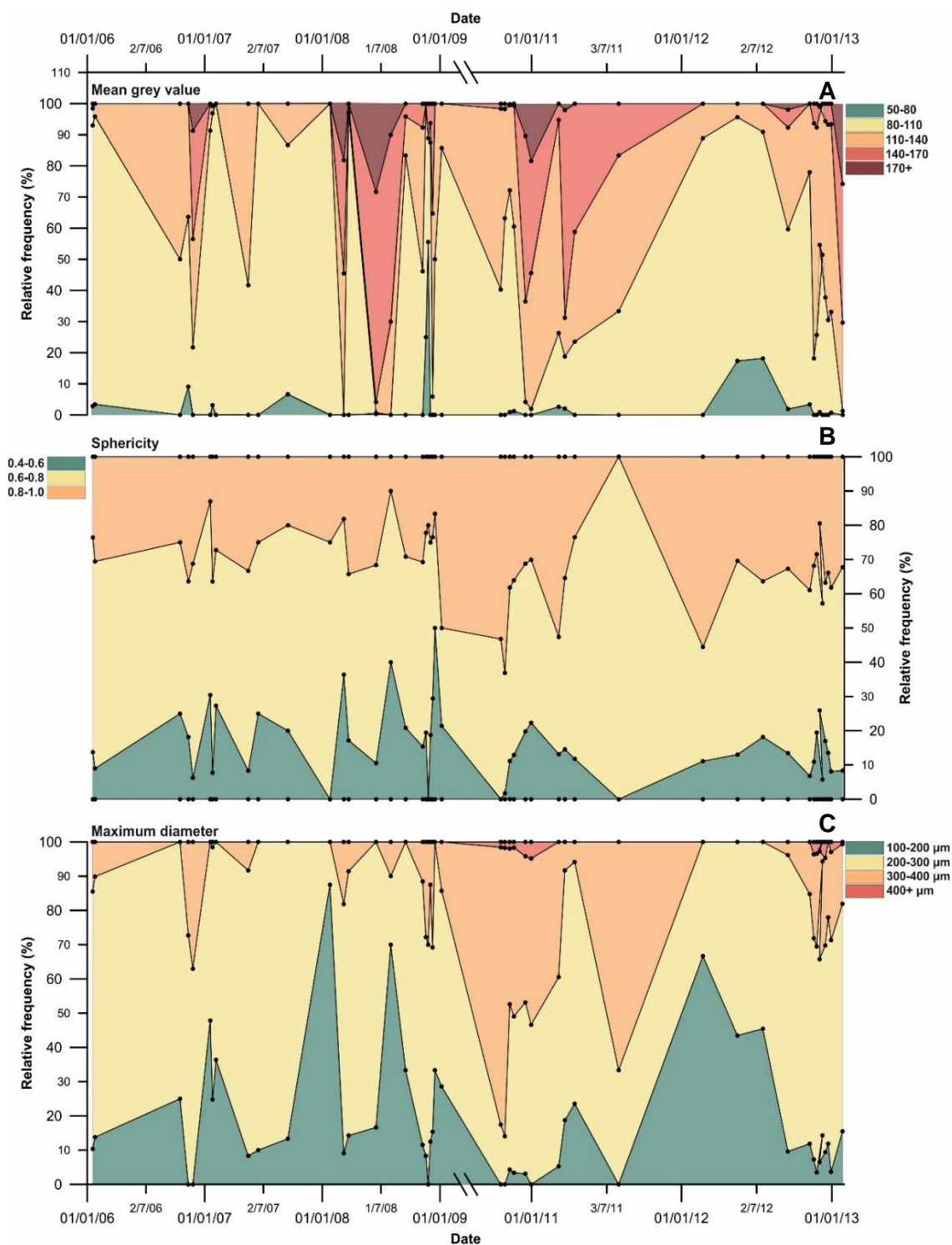


Figure 5.20: Relative frequency of mean grey values (A), sphericity (B) and maximum diameter (C) of Nps through the time series.

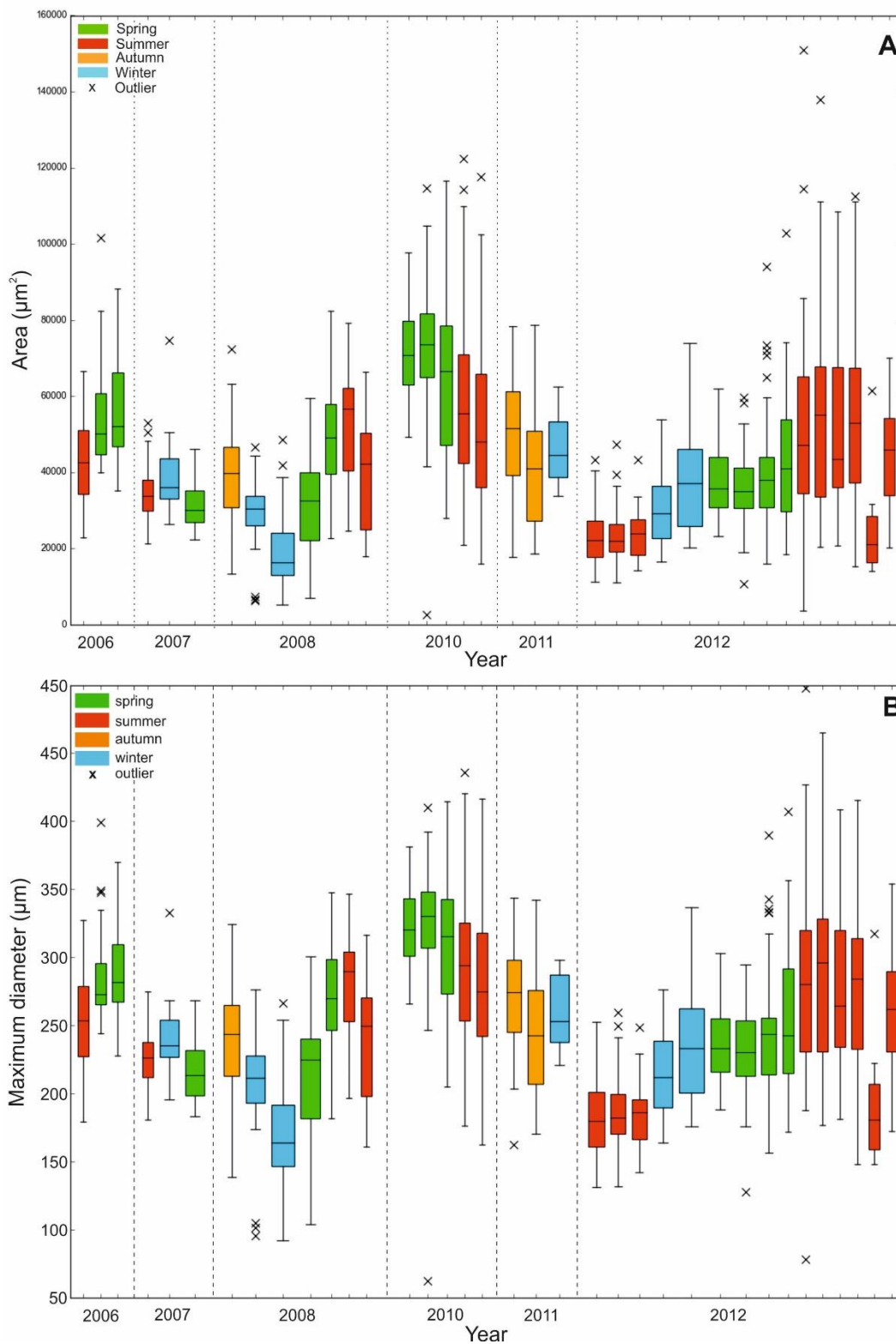


Figure 5.21: The Np surface area (A) and maximum diameter (B) record (collected by the manual morphological data collection method) mirror each other through the time-series. Phases represent time of year, as identified in Section 5.2.4. Dashed lines are visual divisions between the years. The width of each box is representative of the length of time the collection cup was open in the sediment trap: thinnest box is 7 days, widest box is 92 days. Gaps between boxes are indicative of gaps in the time series,

Table 5.8: Correlation (*r*) and slope of regression values between maximum diameter and surface area measurements (manual data collection method) 32 samples of the time series (four samples with less than 15 specimens/sample were removed following Section 5.2.2). Number of specimens in each sample and the *r* value at 95% statistical significance are also included in table.

| Date | Correlation | <i>r</i> value at 0.05 significance | Count | Slope of regression |
|-------------|--------------------|--|--------------|--------------------------------|
| 25/01/2006 | 0.980 | 0.250 | 62 | 0.804 |
| 11/11/2006 | 0.969 | 0.456 | 17 | 0.855 |
| 25/11/2006 | 0.982 | 0.304 | 38 | 0.819 |
| 25/01/2007 | 0.969 | 0.250 | 63 | 0.852 |
| 16/05/2007 | 0.968 | 0.456 | 17 | 0.877 |
| 16/09/2007 | 0.959 | 0.444 | 18 | 0.816 |
| 23/03/2008 | 0.988 | 0.304 | 39 | 0.86 |
| 16/06/2008 | 0.987 | 0.273 | 55 | 0.791 |
| 01/08/2008 | 0.988 | 0.288 | 48 | 0.868 |
| 16/09/2008 | 0.994 | 0.400 | 22 | 0.833 |
| 18/11/2008 | 0.977 | 0.273 | 49 | 0.833 |
| 06/01/2009 | 0.991 | 0.444 | 18 | 0.85 |
| 18/10/2010 | 0.981 | 0.250 | 64 | 0.803 |
| 28/10/2010 | 0.992 | 0.250 | 63 | 0.822 |
| 19/11/2010 | 0.983 | 0.250 | 63 | 0.903 |
| 17/12/2010 | 0.983 | 0.250 | 62 | 0.836 |
| 31/12/2010 | 0.982 | 0.250 | 62 | 0.866 |
| 08/03/2011 | 0.983 | 0.288 | 43 | 0.888 |
| 23/03/2011 | 0.995 | 0.400 | 23 | 0.904 |
| 23/01/2012 | 0.990 | 0.288 | 46 | 0.826 |
| 08/02/2012 | 0.983 | 0.304 | 42 | 0.807 |
| 16/05/2012 | 0.976 | 0.349 | 29 | 0.915 |
| 17/07/2012 | 0.990 | 0.381 | 24 | 0.828 |
| 16/09/2012 | 0.968 | 0.273 | 49 | 0.852 |
| 16/10/2012 | 0.980 | 0.304 | 38 | 0.863 |
| 08/11/2012 | 0.979 | 0.250 | 56 | 0.778 |
| 18/11/2012 | 0.985 | 0.250 | 65 | 0.76 |
| 02/12/2012 | 0.984 | 0.250 | 64 | 0.772 |
| 09/12/2012 | 0.986 | 0.273 | 50 | 0.78 |
| 23/12/2012 | 0.985 | 0.273 | 50 | 0.807 |
| 30/12/2012 | 0.989 | 0.250 | 64 | 0.819 |
| 27/01/2013 | 0.974 | 0.250 | 61 | 0.766 |

histograms with the accompanying Anderson-Darling p-values in Figure 5.22 (as log-transformed maximum diameter).

When the log-transformed MD data are plotted on a Normal Probability plot (normal Q-Q plots in Appendix 2) and tested for normality, four out of the 36 sets of samples display a non-normal distribution. This accounts for 11% of the entire dataset. The non-normally distributed samples are highlighted in Figure 5.22. The dominance of a unimodal distribution in 89% of the samples suggests that shell size can be represented by the log-transformed maximum diameter with confidence. As discussed in Moller et al. (2013) the log-transformed maximum diameter can be used as a measure of the mean MD of the population because it is not affected by sample size, thereby avoiding the possibility of skewed results deriving from small sample sizes. Levene's test for Equality of Variances was carried out on the log-transformed MD dataset covering the entire time-series (2006-2013) to investigate the consistency of the variance (dispersion of data points). The Levene's test reveals statistically significant difference ($p = <0.0001$, at 0.05 significance) indicating inter-annual variability in the range of test size between 2006 and 2013. The presence/absence of intra-annual variability can be determined by applying a Levene's test to a portion of the log-transformed MD dataset that belongs to 2012 (the most complete trap record). The test reveals a significant difference ($p = <0.0001$, at 0.05 significance) indicating intra-annual variability in the range of test sizes.

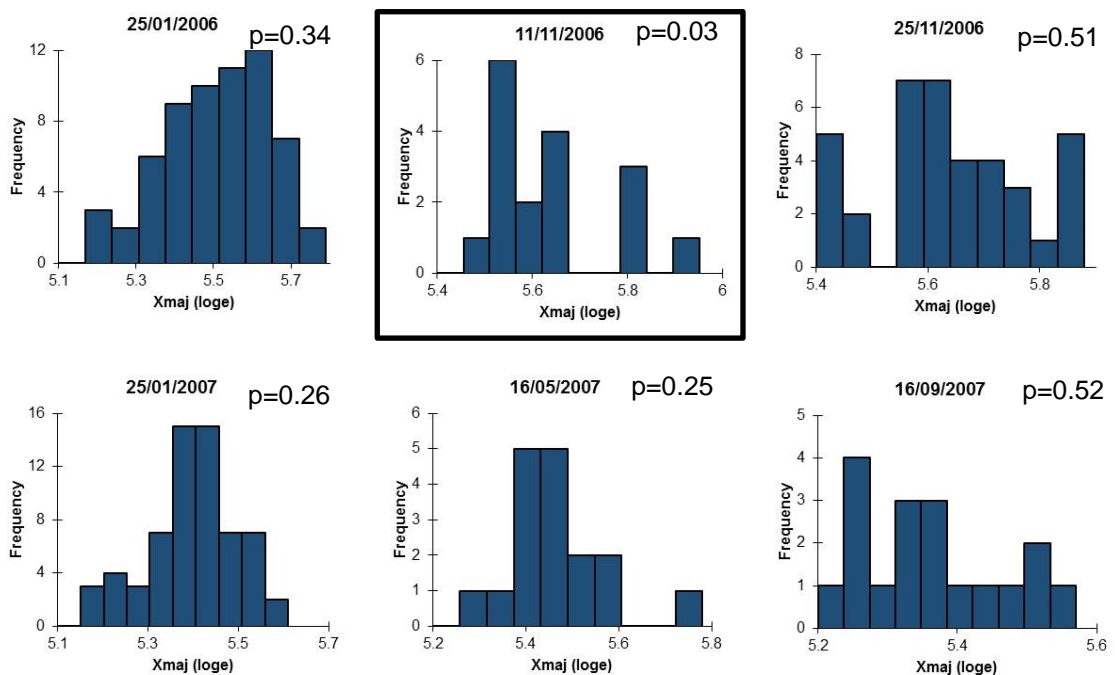


Figure 5.22: Histograms of the log-transformed maximum diameter values of each samples including the Anderson-Darling Normality test-derived p values. Non-normally distributed datasets are highlighted with black outline.

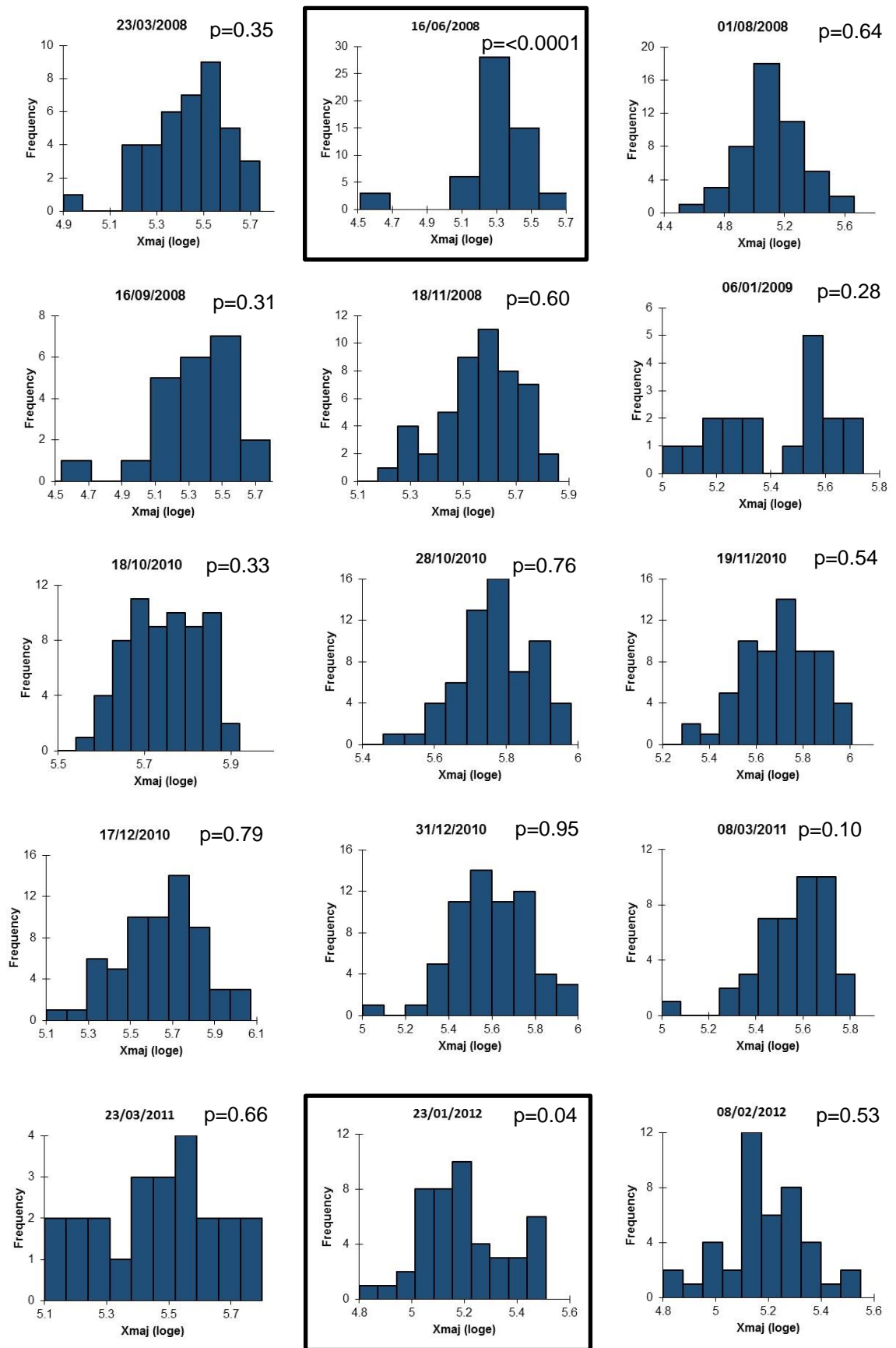


Figure 5.22 continued: Histograms of the log-transformed maximum diameter values of each samples including the Anderson-Darling Normality test-derived p values. Non-normally distributed datasets are highlighted with black outline.

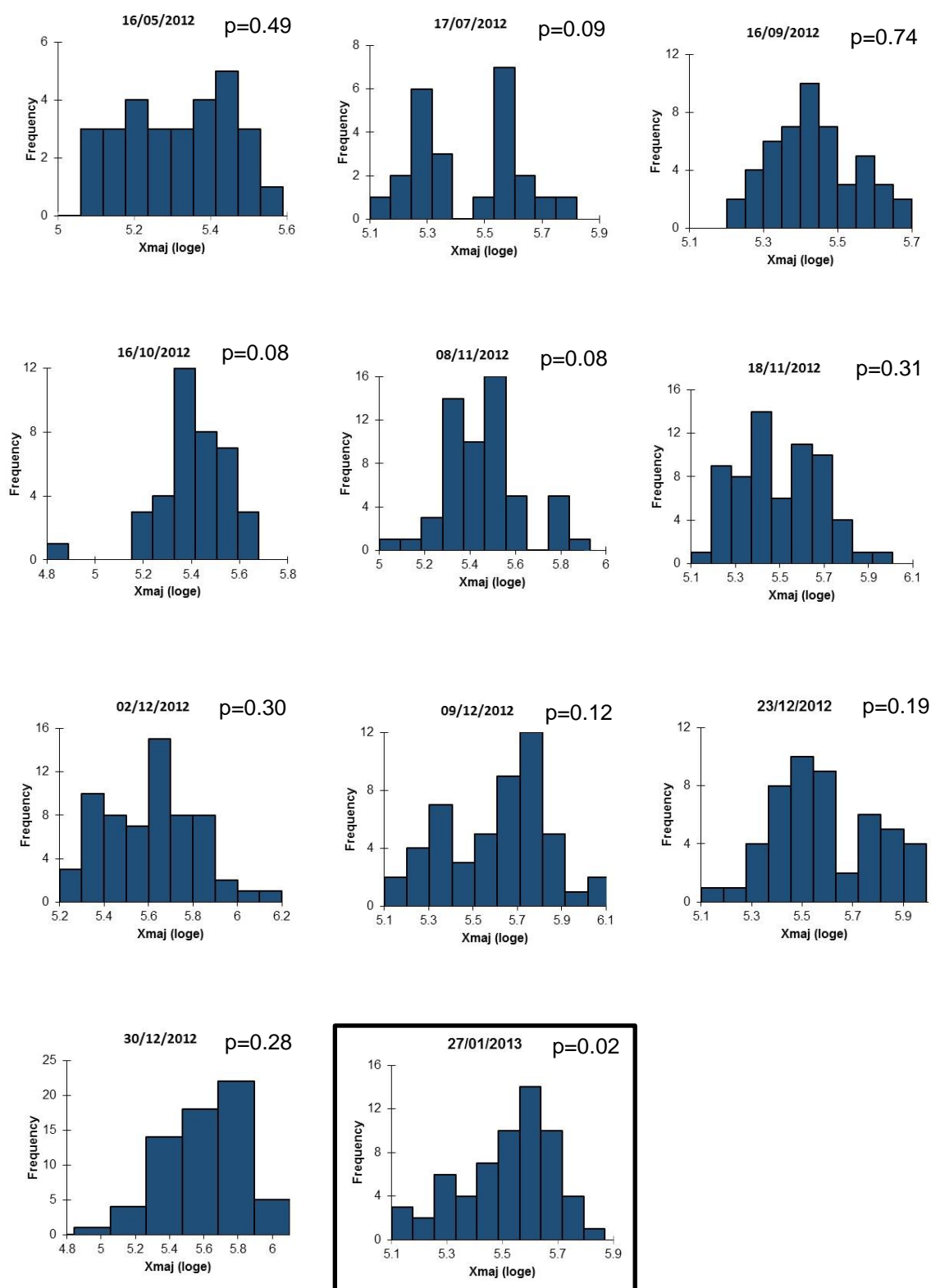


Figure 5.22 continued: Histograms of the log-transformed maximum diameter values of each samples including the Anderson-Darling Normality test-derived p values. Non-normally distributed datasets are highlighted with black outline.

Results of Principal Component Analyses

The distributions of the four size-invariant morphological parameters (circularity ratio, box ratio, elongation ratio and compactness coefficient, Table 5.9), which relate to body shape, were analysed within each sample (manually collected dataset) using principal component analysis (PCA) (representative sample shown in Figure 5.23). The visual representation of the PCA can reveal statistically defined clusters of points that can be attributed to different morphotypes (Figure 5.23). The presence of multiple clusters and thus multiple morphotypes can also be supported by undertaking Anderson-Darling test for normality on the first principle component site scores. A non-normal distribution of the scores suggest multiple morphotypes within a sample, as seen for example in the 16/09/2007 sample (Figure 5.23). Fourteen of the 32 samples display a non-normal distribution (Table 5.10) indicating that in those 14 samples multiple morphotypes are

Table 5.9: Definition of secondary morphological parameters, which relate to body shape as opposed to body size are derived from measured parameters (after Moller et al. 2013).

| Primary parameters | | Secondary morphological parameters | |
|--------------------|------------------|--|-------------------------|
| p | Perimeter | $R_c = A \cdot 4 \cdot \pi / p^2$ | Circularity ratio |
| A | Area | $R_e = 2 \cdot \sqrt{A} / (X_{\max} \cdot \sqrt{\pi})$ | Elongation ratio |
| X_{\max} | Maximum diameter | $B = X_{\min} / X_{\max}$ | Box ratio |
| X_{\min} | Minimum diameter | $C = p / 2 \cdot \sqrt{\pi} \cdot \sqrt{A}$ | Compactness coefficient |

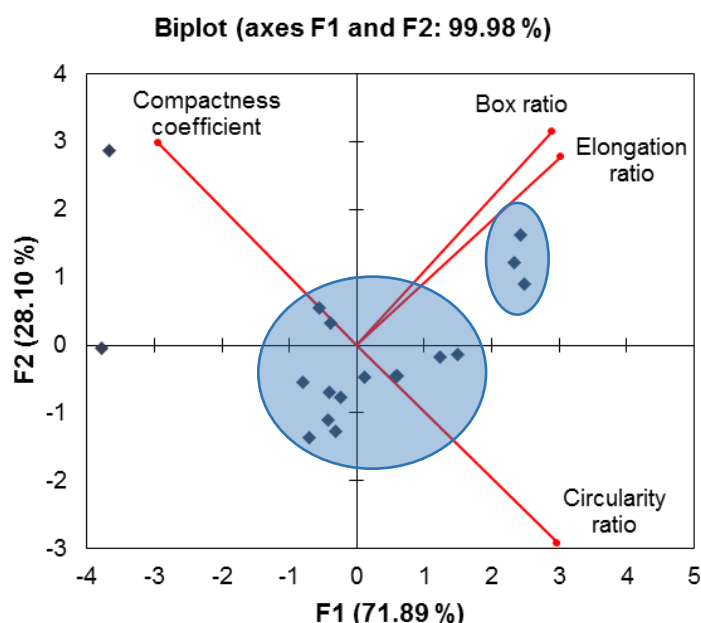


Figure 5.23: PCA biplot of 16/09/2007 normalised size-invariant morphological variables showing clustering of data points (blue circles). F1 is the first principle component axis. F2 is the second principle component axis. Brackets show the proportion of the variance explained by each component axis.

present. To assess the relationship between the body size and the body shape the log-transformed maximum diameter of each specimen was plotted against the first principal component scores (for example, Figure 5.24, rest in Appendix 3). The two parameters correlated with each other in 12 of the 32 samples (Table 5.10) (four samples were discounted from the total of 36 samples due to the number of specimens being less than 15, see Section 5.2.2). The linear correlation coefficients (*r* values) were between -0.48 and 0.51 , which suggests variable relationship between shape and size, i.e. positive correlation – as a specimen becomes larger it also becomes more rounded or in the case of negative correlations the specimens were more rounded the smaller they were. The result from the largest sample is shown in Figure 5.24.

To assess the relationship between the shape and the size parameters in each set of samples, PCA was performed on the mean values of the log-transformed maximum diameter and the mean values of each size-invariant morphological parameter of the 36 sets of data (Figure 5.25, Table 5.11). Three principal components explain 99.9% of the variability in the dataset. The first principal component (F1) is strongly correlated with the size-invariant variables (Table 5.11). It increases with increasing circularity, elongation and box ratio and increases with decreasing compactness coefficient. This suggests that these four criteria covary. F1 can therefore be viewed as a measure of circularity ratio, elongation ratio, box ratio, and compactness coefficient. F1 correlates most strongly with elongation ratio and box ratio with correlation coefficients of 0.819 and 0.792 (Table 5.11) indicating that the first principal component is primarily a measure of these two

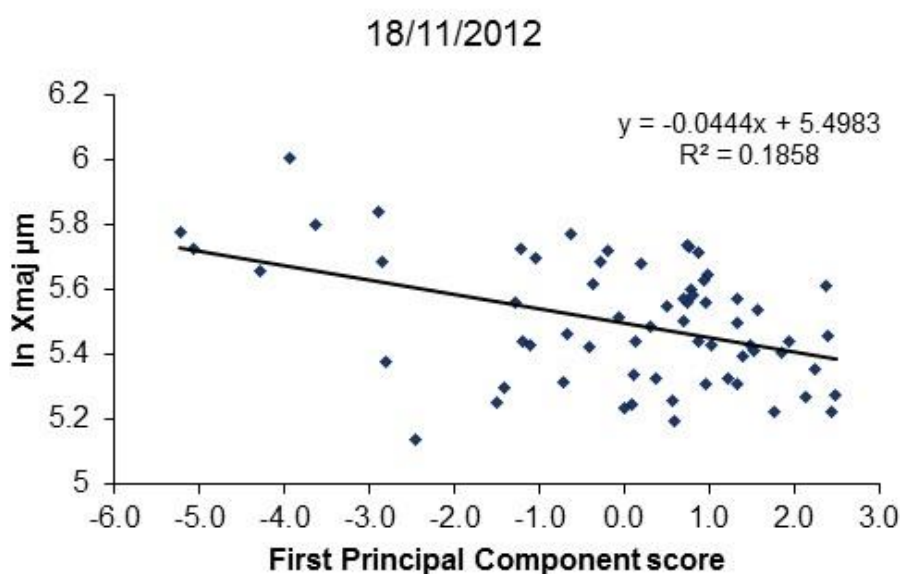


Figure 5.24: Relationship between log-transformed maximum diameter (*ln Xmaj*) and the first principle component scores of the PCA conducted on the normalised size-invariant morphological values. Figure shown is 18/11/2012 sample which contains the largest number of specimens analysed.

Table 5.10: Mid-date of collection period for sediment trap samples, number of data points per sample, Anderson-Darling p value of significance of the first principle component scores (F1) of the PCA conducted on the normalised size-invariant morphological dataset, and the correlation coefficient (r) calculated between the log-transformed maximum diameter (Xmaj) and the F1. Significant p-values and correlations highlighted in bold.

| Date | Count | Anderson-Darling p value | Xmaj(ln)-Size- invariant PCA F1 r value |
|------------|-------|-----------------------------|---|
| 25/01/2006 | 62 | 0.225 | -0.118 |
| 11/11/2006 | 17 | 0.517 | -0.110 |
| 25/11/2006 | 38 | 0.503 | -0.213 |
| 25/01/2007 | 63 | 0.203 | 0.043 |
| 16/05/2007 | 17 | 0.308 | -0.083 |
| 16/09/2007 | 18 | 0.045 | -0.035 |
| 23/03/2008 | 39 | 0.358 | -0.216 |
| 16/06/2008 | 55 | 0.030 | -0.338 |
| 01/08/2008 | 48 | 0.001 | 0.442 |
| 16/09/2008 | 22 | 0.373 | 0.081 |
| 18/11/2008 | 49 | 0.390 | 0.037 |
| 06/01/2009 | 18 | 0.114 | 0.262 |
| 18/10/2010 | 64 | 0.527 | -0.480 |
| 28/10/2010 | 63 | 0.009 | -0.324 |
| 19/11/2010 | 63 | 0.009 | 0.323 |
| 17/12/2010 | 62 | 0.054 | -0.025 |
| 31/12/2010 | 62 | 0.029 | 0.248 |
| 08/03/2011 | 43 | <0.0001 | 0.124 |
| 23/03/2011 | 23 | 0.180 | 0.508 |
| 23/01/2012 | 46 | 0.000 | 0.046 |
| 08/02/2012 | 42 | 0.016 | -0.214 |
| 16/05/2012 | 29 | 0.297 | 0.480 |
| 17/07/2012 | 24 | 0.006 | 0.136 |
| 16/09/2012 | 49 | 0.000 | -0.033 |
| 16/10/2012 | 38 | 0.103 | 0.010 |
| 08/11/2012 | 56 | 0.051 | -0.291 |
| 18/11/2012 | 65 | <0.0001 | -0.431 |
| 02/12/2012 | 64 | 0.151 | -0.351 |
| 09/12/2012 | 50 | 0.539 | -0.353 |
| 23/12/2012 | 50 | 0.051 | -0.148 |
| 30/12/2012 | 64 | 0.011 | -0.235 |
| 27/01/2013 | 61 | 0.004 | -0.389 |

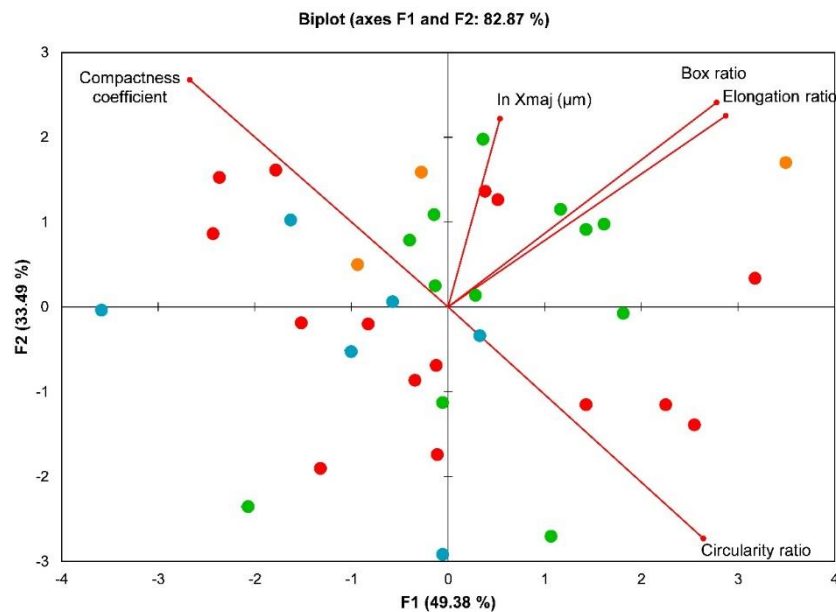


Figure 5.25: PCA biplot (F1-F2 scores) of the mean values of log-transformed maximum diameter and the mean values of each size-invariant morphological parameters covering the time series (2006-2013). Seasons are identified as: green-spring, red-summer, orange-autumn, and blue-winter.

variables and the observed variability in the dataset is related to changes in elongation in two dimensions, i.e. how elongate or round the specimens are, which relates to the ratio between the minor axis and major axis. The second principal component (F2) is also correlated with circularity ratio, elongation ratio, box ratio, and compactness coefficient, but to a lesser degree. Strongest correlation is recorded between circularity ratio and F2 (-0.641) (Table 5.11), so this component (F2) can be viewed as a measure of how close to a perfect sphere the specimens are. The third principal component (Figure 5.26 – F1-F3 biplot) only makes up 17% of the total variability in the dataset in comparison to the 49% and 33% of contribution of F1 and F2, respectively. However, it does show a strong positive correlation with maximum diameter ($r = 0.840$, Table 5.11 X_{maj}) suggesting that this component is a measure of specimen size. The biplot of the PCA results (Figure 5.25) reveal these strong correlations between the principal components and the variables. PCA biplots are used mainly to determine groupings of observations based on the positions of the variables with respect to the principle components. In Figure 5.25 the observations are scattered across both F1 and F2 and that observations which belong to the same seasons do not cluster together.

The dataset used for the PCA analysis was separated out based on the presence/absence of correlation between log-transformed MD and first principal component scores of PCA on size-invariant morphological parameters (e.g. Figure 5.24) within a given sample. Two PCAs were carried out on the datasets separated by the presence/absence of correlation between log-transformed maximum diameter and F1 of

Table 5.11: Eigenvalues and correlation between variables and principle component factors of the PCA run on the mean values values of log-transformed maximum diameter and the mean values of each size invariant morphological parameters of the time series.

| Eigenvalues | F1 | F2 | F3 |
|---|-----------|-----------|-----------|
| Eigenvalue | 2.469 | 1.675 | 0.852 |
| Variability (%) | 49.381 | 33.493 | 17.031 |
| Cumulative % | 49.381 | 82.874 | 99.905 |
| Correlations between variables and factors | | | |
| | F1 | F2 | F3 |
| Circularity ratio | 0.753 | -0.641 | 0.147 |
| Elongation ratio | 0.819 | 0.529 | -0.220 |
| Box ratio | 0.792 | 0.565 | -0.227 |
| Compactness coefficient | -0.762 | 0.628 | -0.157 |
| In Xmaj (μm) | 0.153 | 0.521 | 0.840 |

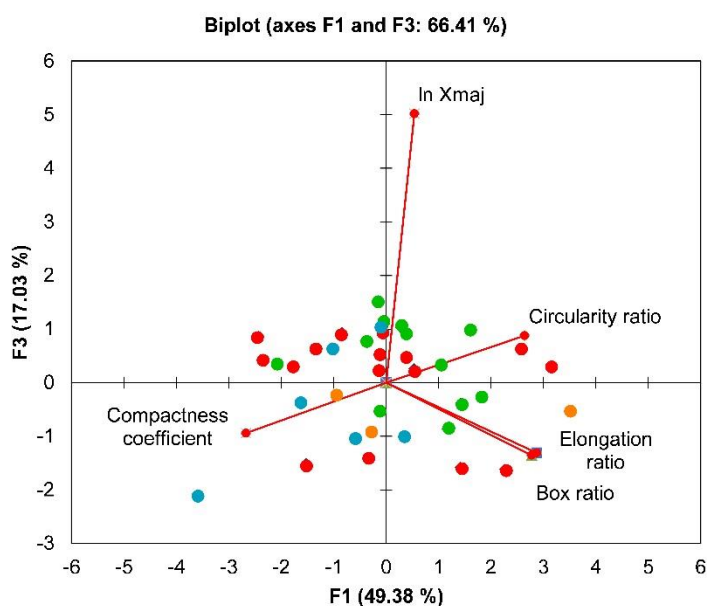


Figure 5.26: PCA biplot (F1-F3 scores) of the mean values of log-transformed maximum diameter and the mean values of each size-invariant morphological parameters covering the time series (2006-2013). Seasons are identified as: green-spring, red-summer, orange-autumn, and blue-winter.

the PCA conducted on the normalised size-invariant morphological dataset (Table 5.10). These showed similar results to the PCA that was carried out on the dataset which was not separated by the correlation (Table 5.10) (Figure 5.27). Neither PCA analysis show any clear clustering of points based on seasonal separation of the data (Figure 5.27A, B). Differences arise when the impact of the morphological variables is

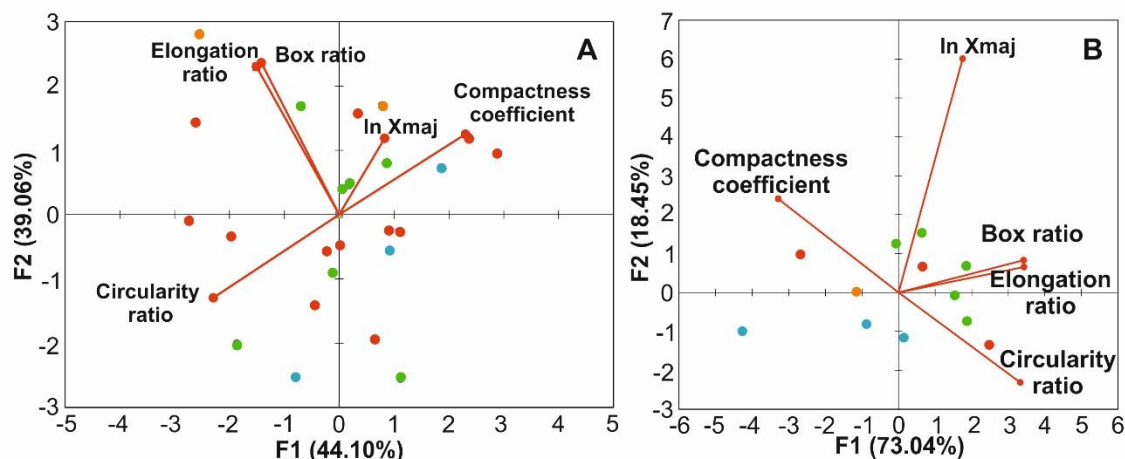


Figure 5.27: PCA biplots of the mean values of *log*-transformed maximum diameter and the mean values of each size-invariant morphological parameters belonging to samples where no correlation was found in Table 5.10 (A) and where correlation was identified (B). Seasons are identified as: green-spring, red-summer, orange-autumn, and blue-winter.

considered on the principle components. In the dataset where no correlation exists between the *log*-transformed MD and the first principal component scores of PCA on size-invariant morphological parameters 99% of the variability can be explained by three principal components (Table 5.11, Figure 5.27A) which is similar to the results of the PCA analysis conducted on the entire dataset together (Figure 5.25). Correlation between the morphological variables and the principal components (Table 5.11, Figure 5.27A) is also similar to the relationships identified in the PCA run on the data from the 32 sediment trap samples (Figure 5.25): F1 and F2 correlate strongly with size-invariant variables, F3 with *log*-transformed maximum diameter, but the directions of the correlations are the opposite (Figure 5.27A). In Figure 5.27A (dataset where samples show no relationship between shape and size) F1 is most strongly correlated with compactness coefficient and circularity ratio ($r = 0.867$ and -0.864 respectively), suggesting that it is a measure of how compact and perfectly spherical a specimen is. F2 shows similarly strong correlations with elongation ratio and box ratio ($r = 0.817$ and 0.837), therefore we can consider F2 to be a measure of how elongated a specimen is in two dimensions (box ratio is equal to the ratio between minimum diameter and maximum diameter). In the dataset where samples show a significant relationship between shape and size the first two principal components can explain over 90% of the variability (Table 5.11). Here F1 is strongly correlated with the size-invariant variables and F2 with the *log*-transformed maximum diameter (Figure 5.27B, Table 5.11). Similarly to the results of the PCA conducted on the entire dataset prior to splitting it up (Figure 5.25) F1 is most strongly correlated with elongation ratio and box ratio ($r = 0.941$ and 0.939 , respectively), therefore it can be considered to be a measure of these two

variables. F2 is a measure of specimen size as it is only correlated with log-transformed maximum diameter ($r= 0.83$). Hence, based on these findings, the results of the PCA conducted on the original dataset of 36 observations is highly influenced by the samples where a statistically significant relationship exists between the log-transformed MD (indicative of specimen size) and the size-invariant morphological parameters (indicative of shape). The lack of clustering into groups in any of the PCA biplots (Figures 5.25, 26, 27) indicates that the observed morphological variability (Figure 5.21, Section 5.2.2.3) is related to a combination of environmental parameters acting on the wellbeing of the foraminifera.

To summarise the findings of this section:

- Shell size (expressed as maximum diameter) displays intra-and inter-annual variability. Mean grey values, an expression of translucency and extent of calcification, shows intra-annual variability.
- Statistical analysis supports the use of log-transformed maximum diameter as a measure of Np size in a population.
- Inter-and intra-annual variability of Np size is supported by statistical analysis.
- Multiple morphotypes are identified in 14 out of 32 samples by PCA.
- Positive and negative linear correlation between body shape and body size is found in 12 out of 32 samples.
- PCA revealed that size-invariant morphological parameters, particularly elongation and box ratio exert the greatest influence on body shape.
- The results of the PCA conducted on the entire dataset (36 samples) are strongly influenced by samples where statistically significant correlation exists between body shape and body size.
- The PCA analyses revealed no clustering of data points related to the seasons the samples derive from suggesting that the morphological variability is the result of a combination of variable environmental parameters (food availability, temperature, sea ice, etc).

5.2.2.4 *Neogloboquadrina pachyderma stable isotopes*

The original goal of the project was to carry out novel single specimen stable isotope analysis on every sample (sediment trap cup) of the time series to provide a holistic record of Np stable isotope variability in the polar region of the Antarctic Peninsula. The variable collection period of the sediment cup and the single specimen analysis could allow the study of Np stable isotope variability related to short-and longer term environmental changes as well as the identification of inherent vital offsets (7 day

collection periods). To carry out single specimen stable isotope analysis, a minimum of 15 Np specimens, each weighing a minimum of 5 μg , are needed in each sample (see Chapter 4). However, some samples contained less than 15 specimens, and/or had specimens where the majority weighed less than 5 μg each, which prohibited the creation of a continuous stable isotope record. To overcome the problem, multi-specimen stable isotope analysis was carried out on the samples where single specimen analysis was not possible.

Multi-specimen stable isotope analysis

For the multi-specimen stable isotope analysis four to ten specimens were pooled together from the specific sample to provide approximately 40 μg carbonate for each analysis.

Approximately 1‰ variability is observed in both the *Neogloboquadrina pachyderma* $\delta^{18}\text{O}$ ($\delta^{18}\text{O}_{\text{np}}$) and the $\delta^{13}\text{C}$ ($\delta^{13}\text{C}_{\text{np}}$) records (Figure 5.28). The $\delta^{18}\text{O}_{\text{np}}$ record (Figure 5.27A) varies between +2.77‰ (17/07/2012) and +3.71‰ (11/11/2006) and has an average value of +3.29‰ \pm 0.21‰ (one standard deviation) through the time series. The $\delta^{13}\text{C}_{\text{np}}$ record (Figure 5.28B) varies between +0.167‰ (22/02/2012) and +1.02‰ (02/12/2012) with an average value of +0.56‰ \pm 0.20‰ (one standard deviation) for the 2006-2013 time series. Anderson-Darling tests for normality reveals that the $\delta^{18}\text{O}_{\text{np}}$ dataset is normally distributed ($p=0.333$), while the $\delta^{13}\text{C}_{\text{np}}$ is not normally distributed ($p=0.032$) (Figure 5.29) suggesting statistically greater variability within the $\delta^{13}\text{C}_{\text{np}}$ record through the time series compared to the $\delta^{18}\text{O}_{\text{np}}$ record.

Single specimen stable isotope analysis

Single specimen stable isotope analysis was carried out on samples which had >20 Np specimens. To assess the variability in the single specimen stable isotope records Levene's test for Equality of Variances was conducted separately on the oxygen and on the carbon isotope datasets. The Levene's test run on the $\delta^{18}\text{O}_{\text{np}}$ record shows that at least one of the variances is statistically different from another ($p=0.005$), which indicates that there is significant difference between the samples in the dispersion of the $\delta^{18}\text{O}_{\text{np}}$ values. $\delta^{18}\text{O}_{\text{np}}$ values show differences between the seasons (Figure 5.30A). Samples collected through the austral winter (May-September) have much lower $\delta^{18}\text{O}_{\text{np}}$ ratios compared to ones collected during the summer (December-February) months. In contrast to the $\delta^{18}\text{O}_{\text{np}}$ record, the Levene's test undertaken on the $\delta^{13}\text{C}_{\text{np}}$ dataset found no significant difference ($p=0.076$) between variances, suggesting that the intra-sample variance is consistent through the time series.

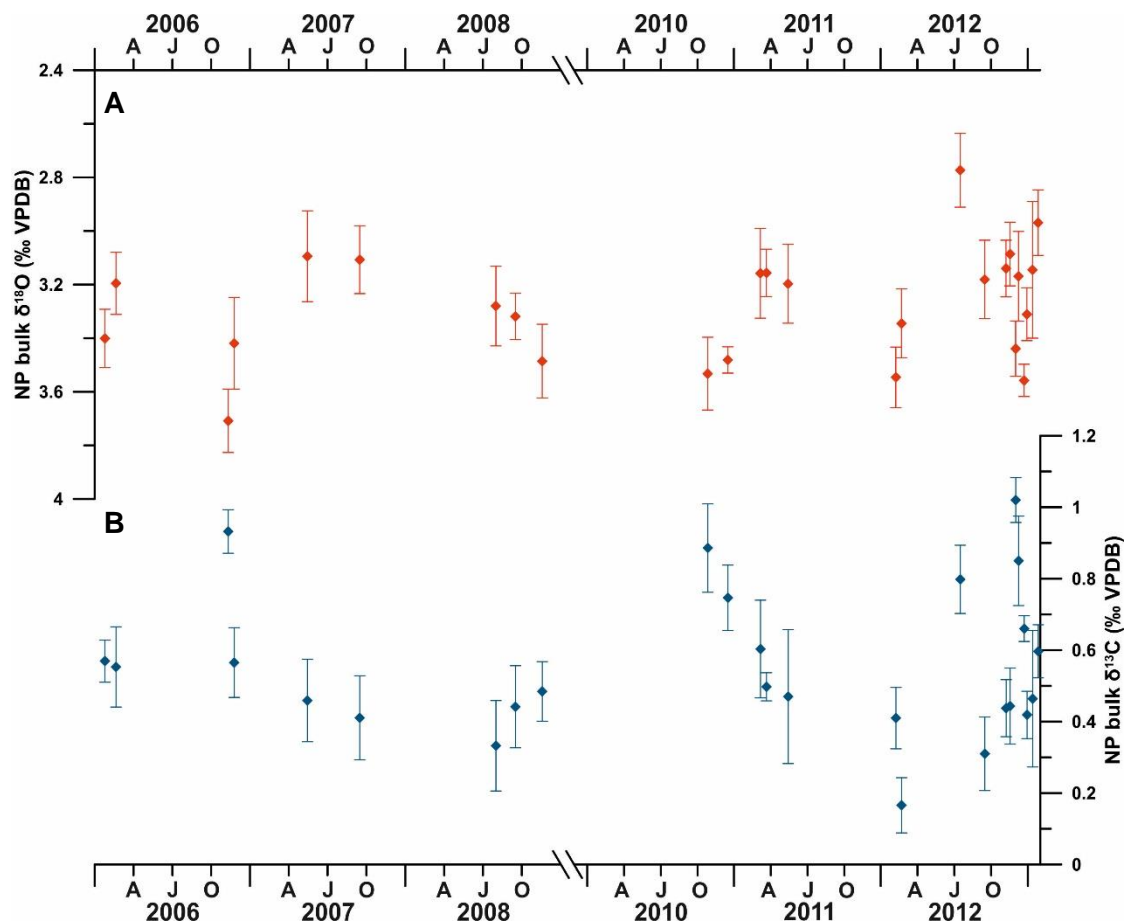


Figure 5.28: Multi-specimen *Neogloboquadrina pachyderma* stable isotope dataset (A: $\delta^{18}\text{O}$, B: $\delta^{13}\text{C}$). Error bars: ± 1 standard deviation. AJO: April, July, October.

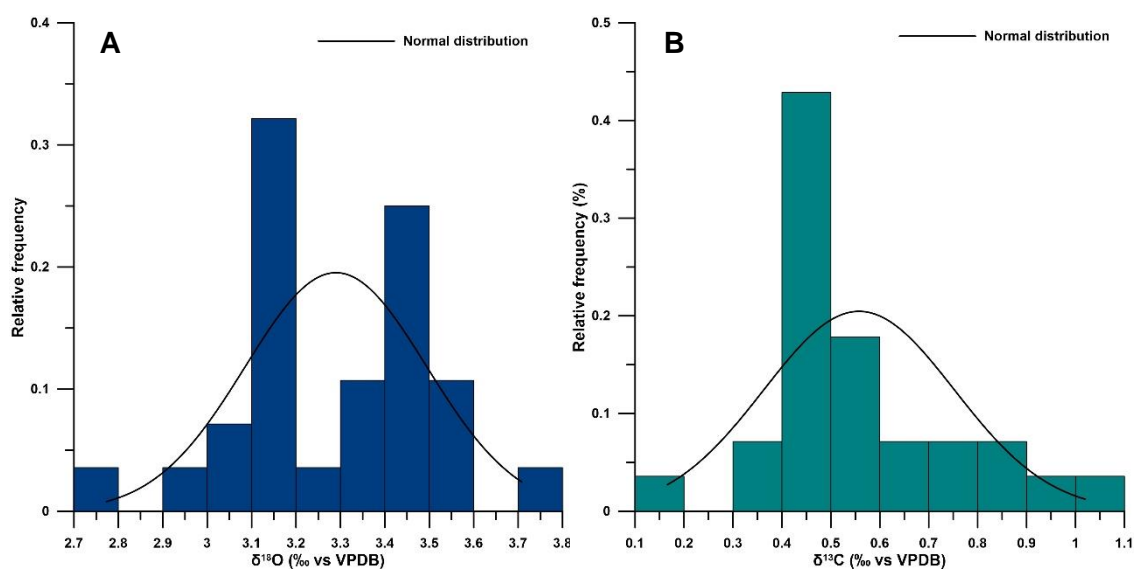


Figure 5.29: Relative frequency histogram of bulk $\delta^{18}\text{O}_{np}$ (A) and $\delta^{13}\text{C}_{np}$ (B) data sets. Black line represents the expected normal distribution. Anderson-Darling test for normality (results as *p*-values) revealed a normal distribution for $\delta^{18}\text{O}_{np}$ (A) and non-normal distribution for $\delta^{13}\text{C}_{np}$ (B). The latter dataset is skewed towards the lower values.

The range of both stable isotopes vary between the bulk and single specimen analysis. While the multi-specimen data displays only a 1‰ range in both isotope ratios, a 4‰ and a 2‰ range is recorded in the single specimen $\delta^{18}\text{O}_{\text{np}}$ and $\delta^{13}\text{C}$, respectively (Figure 5.30).

Predicted $\delta^{18}\text{O}$ calcite equilibrium

To constrain the approximate calcification depth of *Neogloboquadrina pachyderma* at Palmer Deep, and to determine any apparent vital effects in the oxygen isotope record, the equilibrium $\delta^{18}\text{O}$ ($\delta^{18}\text{O}_{\text{eq}}$) values can be calculated (Figure 5.31) using the following equation derived from Kim and O’Neil (1997) and Peeters et al., (2002):

$$\delta^{18}O_{\text{eq}} = 25.778 - 3.333 \times (43.704 + T)^{0.5} + \delta^{18}O_{\text{sw(PDB)}} \quad \text{Equation 7.}$$

where T is the seawater temperature and the $\delta^{18}\text{O}_{\text{sw(PDB)}}$ is the $\delta^{18}\text{O}$ of seawater expressed with respect to the Pee Dee Belemnite (PDB) scale. A correction for vital effects, which is related to temperature variability (Bausch et al., 1997), was not applied in the $\delta^{18}\text{O}_{\text{eq}}$ calculation as one of the objectives of the $\delta^{18}\text{O}_{\text{np}}$ assessment was the evaluation of vital effects. This can only be achieved if the $\delta^{18}\text{O}_{\text{np}}$ and $\delta^{18}\text{O}_{\text{eq}}$ measurements are compared without any vital effect correction factor. $\delta^{18}\text{O}_{\text{sw}}$ is usually expressed with respect to the Standard Mean Ocean Water (SMOW) scale and the conversion to PDB is achieved through the following (Bemis et al., 1998):

$$\delta^{18}O_{\text{sw(PDB)}} = 0.9998 \times \delta^{18}O_{\text{SMOW}} - 0.2 \quad \text{Equation 8.}$$

A number of factors need to be considered before the $\delta^{18}\text{O}_{\text{eq}}$ values can be calculated. In the polar regions, especially along the WAP, annual SST variability is small ($\sim 2^\circ\text{C}$) compared to the midlatitudes, and temperatures are generally low (-1.5 to 1.5°C), which means that temperature only has a small influence on the density and $\delta^{18}\text{O}$ of the seawater ($\delta^{18}\text{O}_{\text{sw}}$) (Meredith et al., 1999). Instead, salinity drives the annual variability of density and $\delta^{18}\text{O}_{\text{sw}}$. At the WAP the input of glacial meltwater and sea ice formation/melt determines the salinity- $\delta^{18}\text{O}_{\text{sw}}$ relationship. Glacial ice is isotopically very low (as low as -50‰) (Weiss et al., 1979, Rozanski et al., 1993), hence relatively small glacial runoff events can affect $\delta^{18}\text{O}_{\text{sw}}$. Sea ice formation (and the accompanying brine rejection) and sea ice melt (freshwater release) can alter the salinity of the seawater considerably, while having little impact on the $\delta^{18}\text{O}_{\text{sw}}$ (Meredith et al., 1999) resulting in a non-linear salinity- $\delta^{18}\text{O}_{\text{sw}}$ relationship in the high latitudes (Bausch et al., 1997). Therefore it is important, that we use $\delta^{18}\text{O}_{\text{sw}}$ values which derive from the same locality as the Np specimens and that the seasonal variability in $\delta^{18}\text{O}_{\text{sw}}$ is captured by actual measurements when calculating $\delta^{18}\text{O}_{\text{eq}}$ values. However, no $\delta^{18}\text{O}_{\text{sw}}$ values are available for the winter season

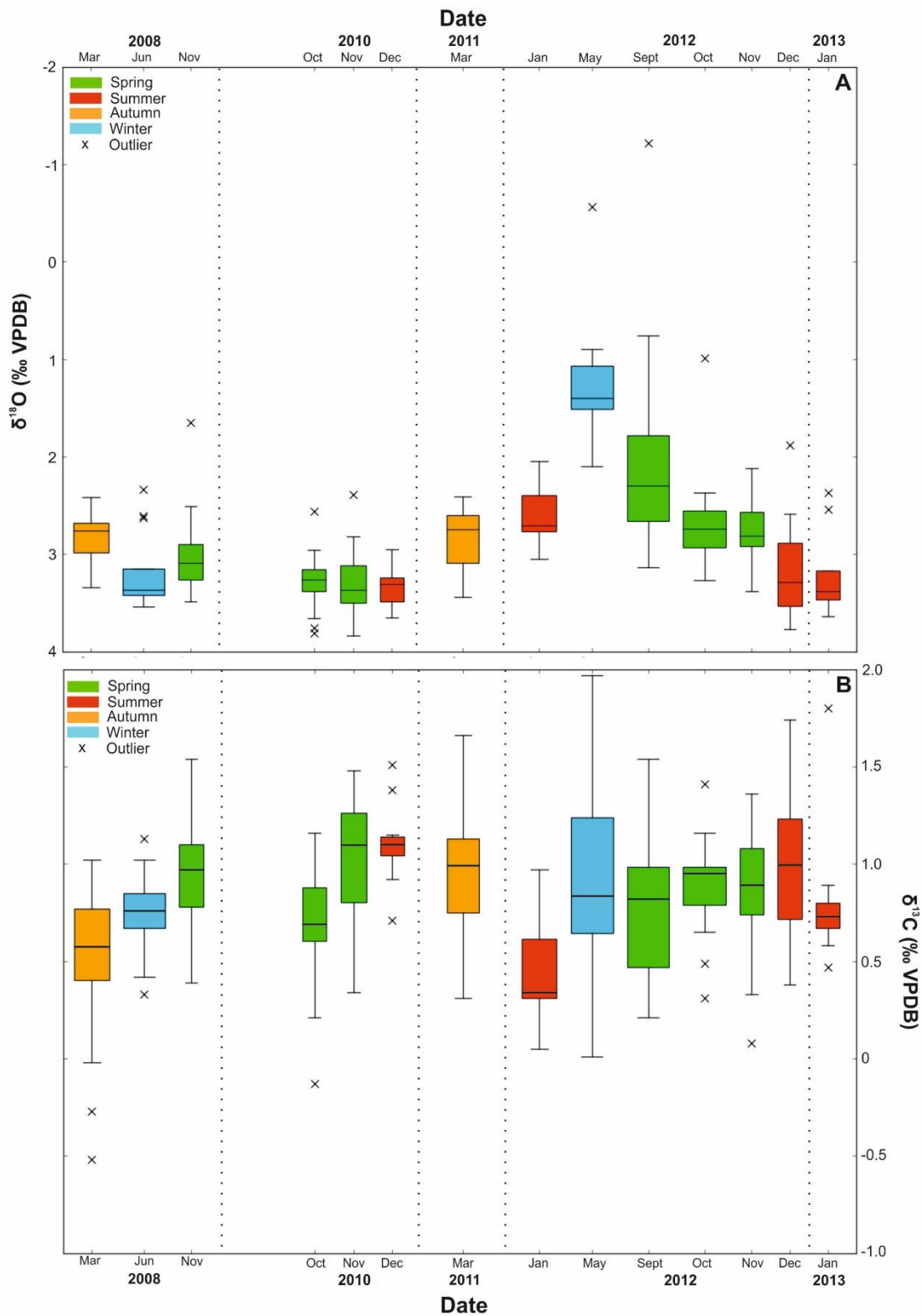


Figure 5.30: Boxplot of single specimen $\delta^{18}\text{O}$ (A) and $\delta^{13}\text{C}$ (B) record. Crosses represent outliers. Phases represent time of year, as identified in Section 5.2.4. Dashed lines are visual divisions between the years. The width of each box is representative of the length of time the collection cup was open in the sediment trap: thinnest box is 7 days, widest box is 92 days. Gaps between boxes are indicative of gaps in the time series,

at any depth, and only surface water data is available for the majority of the year. Depth-integrated $\delta^{18}\text{O}_{\text{sw}}$ data (collected by CTD) are only available from annual PAL-LTER cruises conducted in January of each year. To compensate for the lack of year-round $\delta^{18}\text{O}_{\text{sw}}$ data World Ocean Atlas 13 Salinity (Zweng et al., 2013) data were used to calculate expected $\delta^{18}\text{O}_{\text{sw}}$ values for the period between January and October using the following equation:

$$\delta^{18}\text{O}_{\text{sw}} = 0.3387 \times S - 11.796 \quad \text{Equation 9.}$$

Where *S* is salinity and $\delta^{18}\text{O}_{\text{sw}}$ is the $\delta^{18}\text{O}$ of seawater calculated with respect to SMOW. The equation is determined from observed relationship between $\delta^{18}\text{O}_{\text{sw}}$ and salinity (Meredith et al., 2017). An alternative $\delta^{18}\text{O}_{\text{sw}}$ equation (Equation 10) was used to calculate $\delta^{18}\text{O}_{\text{sw}}$ for the period between October and December. This is due to the introduction of glacial and sea ice melt into the surface water during the spring. Only surface values (0-50 m) were calculated for the October-December period as only surface water (0-50 m) $\delta^{18}\text{O}_{\text{sw}}$ measurements exist for this period.

$$\delta^{18}\text{O}_{\text{sw}} = 0.0458 \times S - 1.8883 \quad \text{Equation 10.}$$

The calculated $\delta^{18}\text{O}_{\text{sw}}$ values were used to calculate the $\delta^{18}\text{O}_{\text{eq}}$ values together with World Ocean Atlas 13 Temperature data (Locarnini et al., 2013) using Equation 7 and 8. The existence of measured (as opposed to calculated) $\delta^{18}\text{O}_{\text{sw}}$ depth profile means that summer conditions are represented well in the $\delta^{18}\text{O}_{\text{eq}}$ calculations (Figure 5.31). Due to the lack of winter $\delta^{18}\text{O}_{\text{sw}}$ data, and the lack of $\delta^{18}\text{O}_{\text{sw}}$ data below the surface between October and January, no winter (at any depths) and below surface spring $\delta^{18}\text{O}_{\text{eq}}$ values are calculated (Figure 5.32C).

The predicted isotopic equilibrium of $\delta^{18}\text{O}$ of calcite shows distinct seasonal variability at the surface and at depth, ranging from +2.83‰ to +3.64‰ at 0 m, and from +3.16‰ to +3.55‰ at 100 m water depth (Figure 5.31). The larger seasonal difference in the surface compared to deeper water is expected due to the greater variability in water temperature and salinity driven by the annual growth and melt of sea ice (Figures 5.32A, B). The predicted $\delta^{18}\text{O}_{\text{eq}}$ values at depth (50-100 m) show similar patterns to the measured $\delta^{18}\text{O}_{\text{np}}$ values between October and April (spring to early autumn). The $\delta^{18}\text{O}_{\text{eq}}$ and $\delta^{18}\text{O}_{\text{np}}$ values diverge in late autumn and the dissimilarity continues during winter. Equilibrium $\delta^{18}\text{O}$ at surface and at depth converge in late autumn, following the temperature profile indicative of the development of deeper mixing. This convergence of $\delta^{18}\text{O}_{\text{eq}}$ between surface and depth is accompanied by lower $\delta^{18}\text{O}_{\text{np}}$, which is up to 0.7‰ lower than $\delta^{18}\text{O}_{\text{eq}}$ values at 0 m and 50 m by the winter.

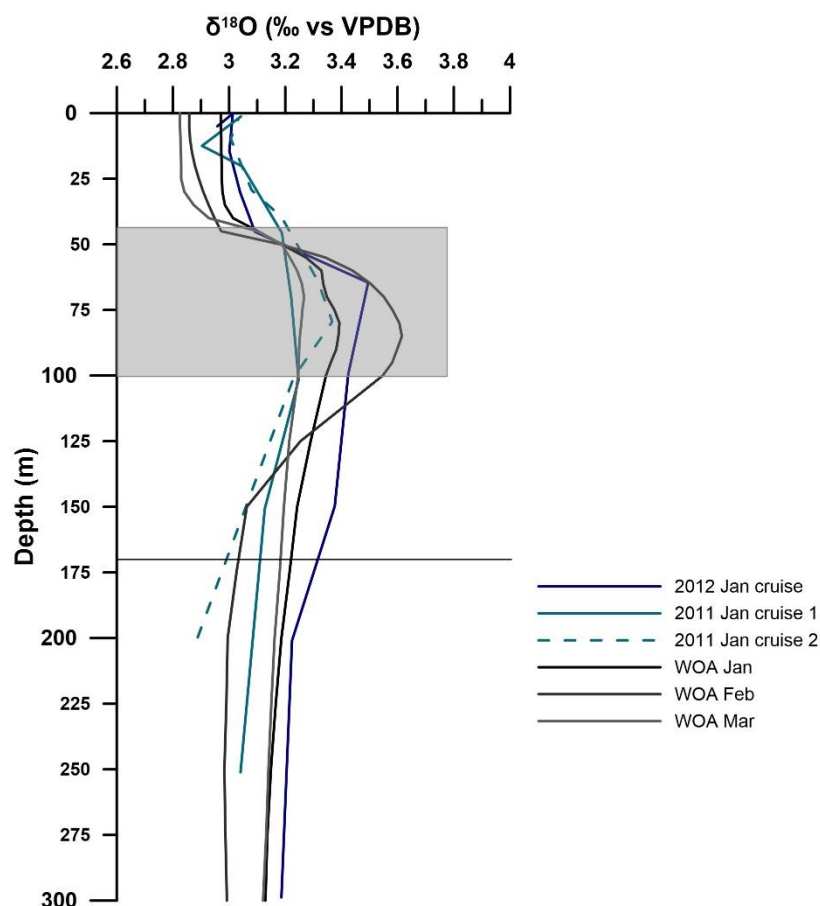


Figure 5.31: Equilibrium $\delta^{18}\text{O}$ depth profiles calculated from direct $\delta^{18}\text{O}_{\text{sw}}$ observations from Meredith et al. (2016) (blue lines) and from calculated $\delta^{18}\text{O}_{\text{sw}}$ data based on WOA13 salinity measurements (grey lines). Depth range of *Nps* calcification indicated by grey box. Grey horizontal line represents depth of the sediment trap.

Oxygen isotopes

The multi-specimen $\delta^{18}\text{O}_{\text{np}}$ record shows a 1‰ seasonal amplitude with lowest values between May and September (late autumn to winter) and highest values between November and January (late-spring to mid-summer) (Figure 5.33A). The single specimen $\delta^{18}\text{O}_{\text{np}}$ values show a similar pattern; however, the amplitude of difference between winter and summer values is larger, at ~2‰. Single specimen $\delta^{18}\text{O}_{\text{np}}$ represents an average $\delta^{18}\text{O}$ value that is acquired through the life-span of the individual foraminifera which can vary from several weeks to months depending on environmental conditions (Kozdon et al., 2009). Therefore within a sediment cup each single specimen $\delta^{18}\text{O}_{\text{np}}$ measurement represents conditions specific to that individual resulting in a range of values within a cup. Multi-specimen $\delta^{18}\text{O}_{\text{np}}$ analysis averages out the within-sample variance deriving from the probability that the specimens experienced different environmental conditions. Comparison of the mean single specimen $\delta^{18}\text{O}_{\text{np}}$ and the multi-

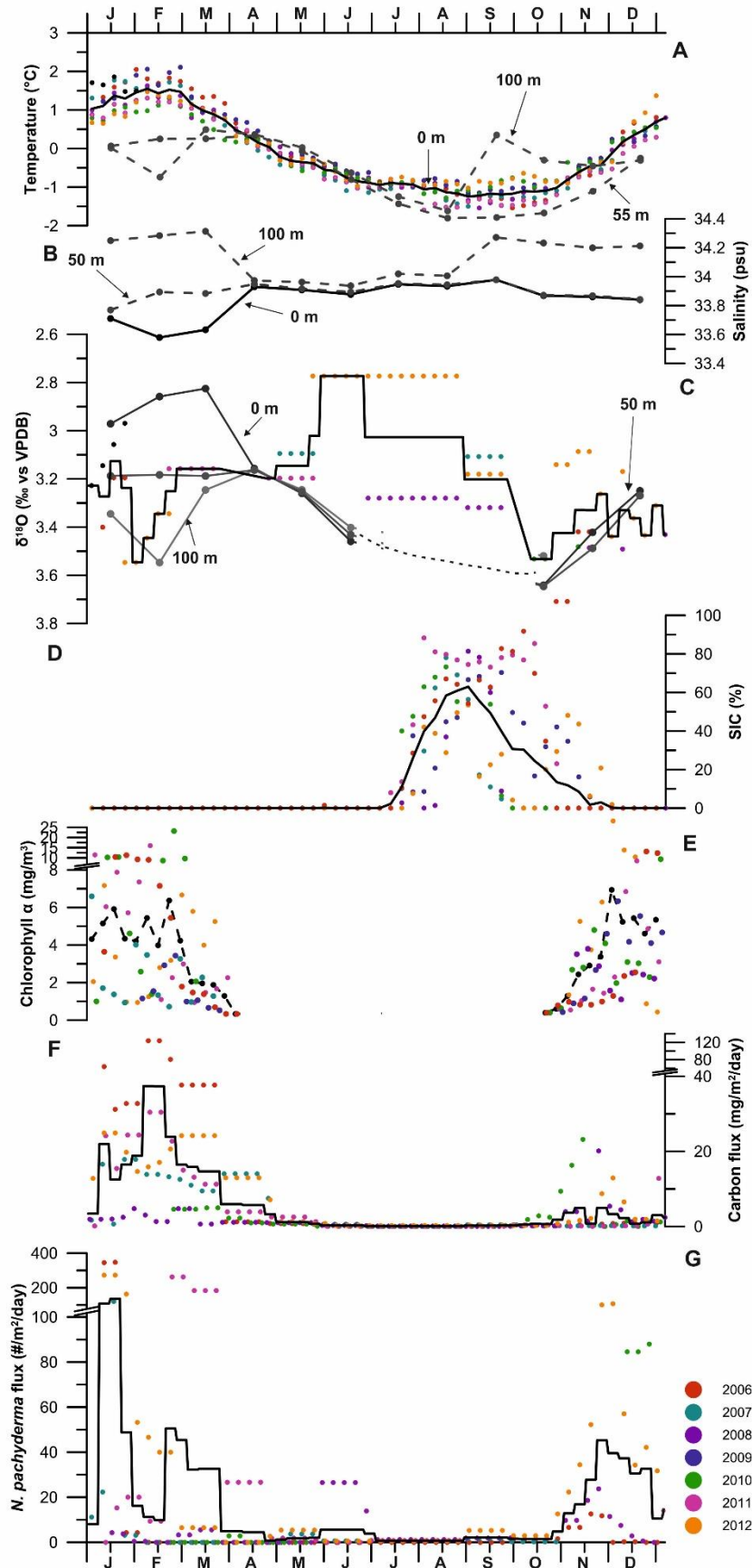


Figure 5.32: Weekly averaged and time shifted time series $\delta^{18}\text{O}$ record (black lines: average values of 2006-2012 period; colour dots: individual years). A) Satellite-derived weekly SST, average SST (black line) and WOA13 monthly temperature at 55 m and 100 m water depths (grey dashed lines). B) WOA13 monthly salinity record at surface (black line), 55 m and 100 m (grey dashed lines) water depths. C) Multi-specimen *Nps* $\delta^{18}\text{O}$ record, $\delta^{18}\text{O}_{\text{eq}}$ values at surface, 50 m and at 100 m water depths. D) Satellite-derived weekly sea ice concentration (SIC) and average SIC through the time series. E) Measured chlorophyll α concentration at 64.78°S, 64.07°W. F) Organic carbon flux record. G) *Nps* flux record (extremely high flux of October 2010 removed from calculation of average).

specimen $\delta^{18}\text{O}_{\text{np}}$ values is shown in Figure 5.33A. The average values of single specimen $\delta^{18}\text{O}_{\text{np}}$ are in most cases lower than the multi-specimen $\delta^{18}\text{O}_{\text{np}}$ values from the same sample set. The offset between the single and multi-specimen analyses is not consistent through the time series. The source of this offset most likely stems from how the average values of the single-specimen analyses are calculated. In the case of the mean value of a set of single specimen $\delta^{18}\text{O}_{\text{np}}$ measurements, every data point within the set has the same contribution to the final average value in terms of significance, i.e. if there are 10 specimens in the sample then each specimen makes up 10% of the final average value and there will be no weight or mass effects. The multi-specimen $\delta^{18}\text{O}_{\text{np}}$ values are measured by analysing between 4 and 10 specimens together in one vial. In the case of multi-specimen analysis, the contribution of each specimen to the final $\delta^{18}\text{O}_{\text{np}}$ value of the sample is proportional to the mass of each specimen. As higher mass/larger Np specimens tend to be characterised by a secondary crust (Kohfeld et al., 1996) with higher $\delta^{18}\text{O}_{\text{np}}$ values (Bausch et al., 1997), the resulting average $\delta^{18}\text{O}_{\text{np}}$ values of the multi-specimen analysis tend to show slightly higher $\delta^{18}\text{O}_{\text{np}}$ values than the mean of the single specimen $\delta^{18}\text{O}_{\text{np}}$ values (Figure 5.33A).

Lowest multi-specimen $\delta^{18}\text{O}_{\text{np}}$ values coincide with times of greatest water column mixing (between April and late October, Figure 5.32) when surface and subsurface temperatures are at their minimum. Np flux values are close to the minimum during this time. The lowest multi-specimen $\delta^{18}\text{O}_{\text{np}}$ values show the greatest offset from the calculated $\delta^{18}\text{O}_{\text{eq}}$ values observed between June and September which are similar between the surface and 100 m water depth during late autumn (Figure 5.32C). Multi-specimen $\delta^{18}\text{O}_{\text{np}}$ values gradually increase after the winter months and reach a maximum mid-spring, in October, before decreasing by a small amount ($\sim 0.2\text{‰}$) in November. During this time the $\delta^{18}\text{O}_{\text{np}}$ values are only $\sim 0.1\text{‰}$ lower than the equilibrium $\delta^{18}\text{O}$ values at 0-50 m and similar to $\delta^{18}\text{O}_{\text{eq}}$ values at 100 m water depth. Multi-specimen $\delta^{18}\text{O}_{\text{np}}$ values are relatively constant between late spring and mid-summer during the time of maximum Np flux and increased water column stratification. Only a $\sim 0.2\text{‰}$, variability is observed between late November and mid-January. $\delta^{18}\text{O}_{\text{np}}$ values increase once again when maximum stratification takes place (mid-Jan to mid-Feb). $\delta^{18}\text{O}_{\text{eq}}$ values at surface and 100 m water depth diverge during this time, by 0.6‰ and $\delta^{18}\text{O}_{\text{np}}$ show no offset from $\delta^{18}\text{O}_{\text{eq}}$ values between 50 and 100 m water depth. As the water column stratification diminishes and water temperatures at depth increase to above 0°C , $\delta^{18}\text{O}_{\text{np}}$ decreases by $\sim 0.4\text{‰}$ to approximately $+3.2\text{‰}$ (Feb-March) and remains stable during the autumn season until the early winter decrease takes place to $+2.8\text{‰}$ (May-June). A $\sim 0.5\text{‰}$ difference in $\delta^{18}\text{O}_{\text{np}}$ is observed between the winter months of 2008 and 2012

(Figure 5.32C), while a similar difference exists between observations in the spring of 2006 and 2012.

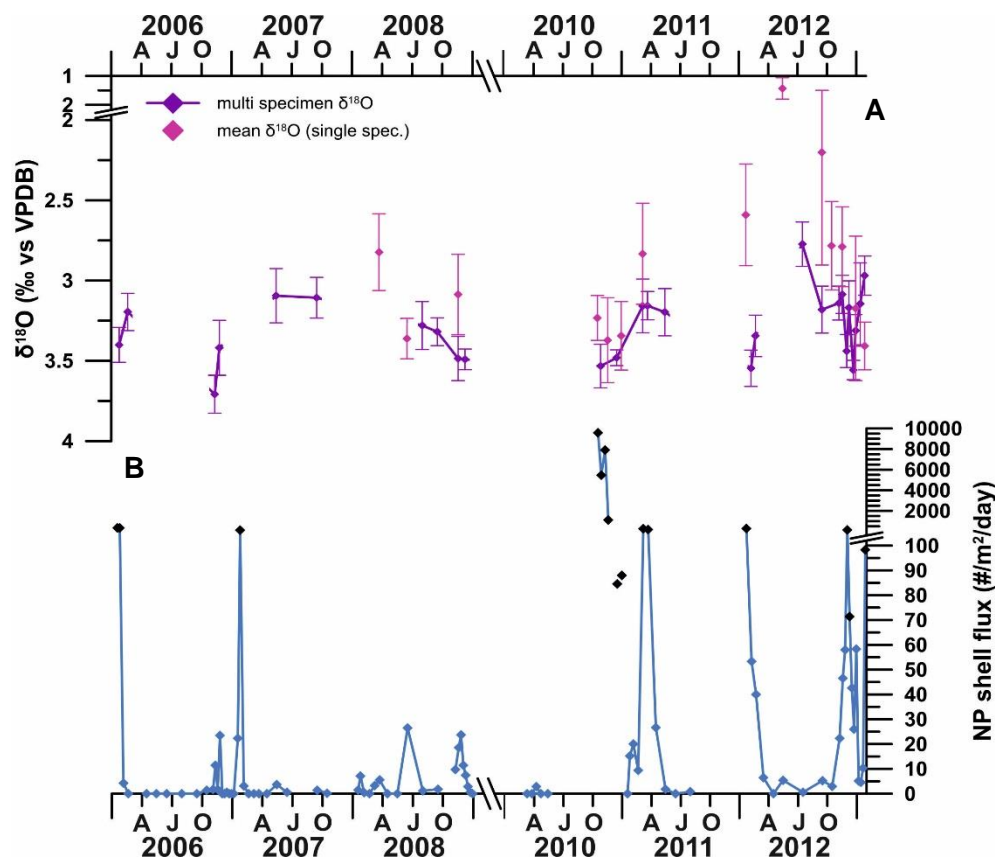


Figure 5.33: A) Multi-specimen (purple) and average single specimen (pink) Nps $\delta^{18}\text{O}$ record. Error bars on multi-specimen values represent one standard deviation of the measurement while error bars on average single-specimen values denote one standard deviation in the spread of the individual $\delta^{18}\text{O}$ values within the sample. B) Nps shell fluxes through the time series. AJJO: April, July, October.

5.2.3 A typical year at Palmer Deep

In order to describe the environmental parameters and their relation to each other the same weeks in the six different years (2006, 2007, 2008, 2010, 2011, and 2012) were averaged to make a composite year, described by weekly averages. The resulting model can be divided into six distinct phases (Figure 5.34) based on the intra-annual trend of the *Neogloboquadrina pachyderma* (Np) flux, as well as by the intra-annual trends shown by the environmental variables. Note that this averaging across the six years masks the inter-annual variation (e.g. timing of peak chlorophyll α concentrations varies year-on-year, timing of sea ice retreat varies year-on-year).

5.2.3.1 Phase 1 – Winter sea ice season

Phase 1 is defined by the lowest Np values of the year (Figure 5.34F), the onset of winter sea ice presence, peak Sea Ice Concentration (SIC), and subsequent reduction to ~20% SIC (Figure 5.34C). Sea ice occurs between July and October every year between 2006 and 2013 (Figure 5.34C). On average SIC peaks at the end of winter, during September; however, variability is found between the years. For example, maximum SIC is reached in August in 2007 compared to late October in 2006. Peak SIC rarely reaches 100% in the region, averaging around 70% between 2006 and 2013 (Figure 5.34C). Between July and October a SST minimum (Figure 5.34A) is associated with sea ice. By the end of the winter, sea water at 100 m water depth is warmer than at the surface due to the upward heat flux from the modified UCDW which is present deeper than the sampling depth (Smith and Klinck, 2002). At the same time, salinity at depth (100 m), is increased (Figure 5.34B) due to brine rejection during sea ice formation (Meredith et al., 2004), which also contributes to the deepening of the mixed layer and the erosion of the stratification. This period of sea ice presence between July and October coincides with the lowest organic carbon and nitrogen fluxes (close to zero $\text{mg}/\text{m}^2/\text{day}$) (Figure 5.34E).

5.2.3.2 Phase 2 - Sea ice break up season

The sea ice break up season is defined as a period of increasing Np flux (Figure 5.34F), decreasing SIC, from ~20% to zero (Figure 5.34C), and concomitant increasing Chlorophyll α (Chl α) concentration, from zero to ~3 mg/m^3 (Figure 5.34D). Towards the end of October SIC decreases (Figure 5.34C) and becomes more intermittent (Figure 5.34C, section 5.2.2.1) relating to changes in wind patterns (Meredith et al., 2017). Salinity at the surface and at 100 m water depth decreases by ~0.2 PSU following Phase 1 (Figure 5.34B), while SST and water temperature at 50 m increases in step with the decreasing water temperature at 100 m water depth (Figure 5.34A). This change in the water temperature across the 100 m water profile allows the mixed layer to begin to dissipate. The start of the shallow stratification of the water column and the release of nutrients from sea ice and glacial melt provides an ideal setting for diatom blooms. As a result Chl α concentration steadily rises during this phase (Figure 5.34D). An increase in organic carbon flux from 0 to ~5 $\text{mg}/\text{m}^2/\text{day}$ (Figure 5.34E) is also observed during this period. The timing of the development of this spring diatom bloom (November onwards) is also documented by satellite-derived Chl α and pigment biomass records (Smith et al., 2008).

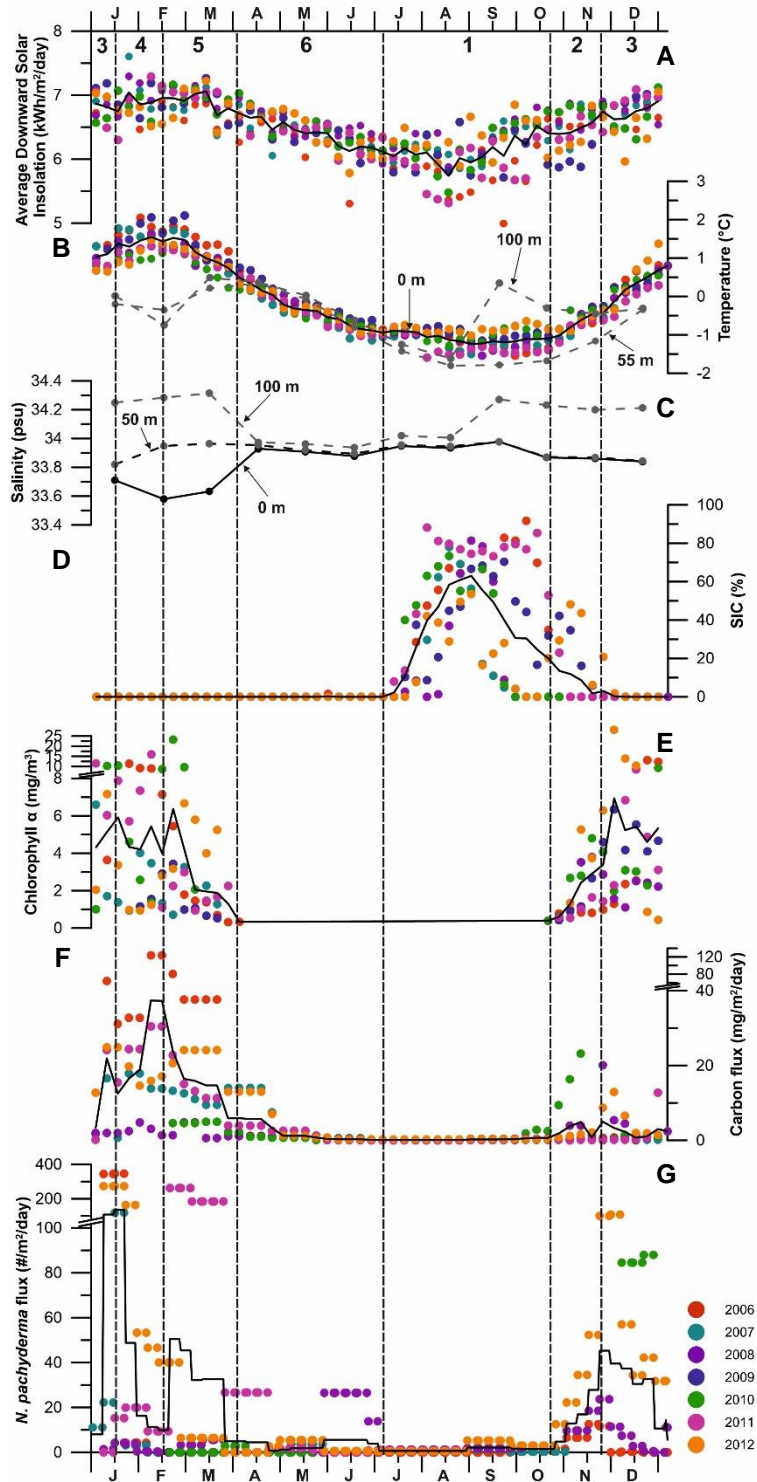


Figure 5.34: Weekly averaged and time-shifted time series flux record (black lines: average values, of 2006-2012 period; colour dots: individual years). A) Satellite-derived Average Downward Longwave Radiative Flux at 64.5°S, 66.0°W (NASA POWER, 2017); B) Annual satellite-derived weekly SST, average SST (black line) and WOA13 monthly temperature at 55 m and 100 m water depths (grey lines). C) WOA13 monthly salinity record at surface (black line), 50 m and 100 m (grey lines) water depths. D) Annual satellite-derived daily sea ice concentration, average SIC (black line). E) Chlorophyll α concentration (10-20 m), average Chl α concentration (black line). F) Average carbon flux (black line) and annual records. G) *Nps* flux record (extremely high flux of October 2010 removed from calculation of average). The low fluxes of early January and the sudden drop off at the end of December are due to the gaps in sampling periods. Dashed vertical lines represent the identified phases in section 5.2.3.

5.2.3.3 Phase 3 – Summer season

The summer season is defined by high Np flux (Figure 5.34F), steadily increasing SST (Figure 5.34A) and the complete disappearance of sea ice by the end of November (Figure 5.34C). During this phase between late November and mid-January SST continues to increase, reaching above 1°C, while water temperature at 100 m water depth continues to decrease, eventually equalling temperatures at 50 m depth by the end of December (Figure 5.34A). This increase in SST is accompanied by a steady decrease in surface water salinity (Figure 5.34B) due to glacial melt as air and ocean both warm. A result of the changes in temperature and salinity is the strengthening of the stratification of the water column at shallow depths (0-50 m). The melt of the sea ice and the development of the shallow stratification leads to increased primary productivity, which is reflected in the Chl α concentration (Figure 5.34D). Chl α concentration reaches its peak ($\sim 7 \text{ mg/m}^3$ on average) during this phase and remains steadily high during the summer months (Figure 5.34D). As a result of increased primary productivity organic carbon flux also increases by the end of this period (mid-January), reaching $\sim 21 \text{ mg/m}^2/\text{day}$ in January (Figure 5.34E). Inter-annual variability can be seen in both the Chl α concentration and organic carbon flux record during this phase. Chl α values vary from 1 to 29 mg/m^3 between 2006 and 2012 and show sudden, sharp increases even within individual years (Figure 5.34D), reflecting the rapid response of diatom blooms to changes in environmental drivers. Organic carbon flux varies in a similar fashion to Chl α , with values ranging from 2 to $65 \text{ mg/m}^2/\text{day}$ between November and January (Figure 5.34E), and sudden increases occur concomitantly with the Chl α concentration record.

5.2.3.4 Phase 4 - Late summer season

The late summer season is defined by decreasing Np flux (Figure 5.34F), increasing organic carbon flux (Figure 5.34E) and continuously increasing SST (Figure 5.34A). Between mid-January and mid-February SST reaches a maximum of $\sim 1.5^\circ\text{C}$ and temperatures at 100 m water depth continue to decrease leading to maximum stratification by mid-February (Figure 5.34A). This period of the year is characterised by the lowest surface salinities (33.6 PSU) (Figure 5.34B) due to the input of glacial meltwater from the coastal regions. Salinity at 50 m and 100 m water depth begins to increase (Figure 5.34B) which further strengthens the water column stratification. Chl α concentration remains steady on average between 4 and 6 mg/m^3 although inter-annual variability is prominent in the record (Figure 5.34D). Sustained primary productivity and the increased SST lead to a steady increase in the organic carbon flux, reaching a peak of $\sim 40 \text{ mg/m}^2/\text{day}$ (Figure 5.34E) by mid-February.

5.2.3.5 Phase 5 - Autumn season

Autumn is defined by increasing Np flux (Figure 5.34F), decreasing carbon flux (Figure 5.34E) and decreasing SST (Figure 5.34A). During the second half of February stratification decreases as SST starts to cool and water temperature at 50 and 100 m depths begins to increase (Figure 5.34A). The weakening of the water column stratification during this time is further driven by the increase in surface salinity and decrease in salinity at 100 m water depth (Figure 5.34B). The early part of this phase is characterised by another peak in chlorophyll α concentration (to over 6 mg/m²) which is then followed by a steady decrease reaching values close to 0 by the end of this phase in April (Figure 5.34D). The early peak in Chl α concentration is accompanied by a high organic carbon flux of ~30-40 mg/m²/day (Figure 5.34E). The organic carbon flux also begins to decrease towards the end of the phase but in a more gradual manner than the Chl α concentration values. These shifts in Chl α concentration and organic carbon flux values coincide with the falling SST and dissipating stratification.

5.2.3.6 Phase 6 – Early winter season

The early winter season is defined by the second lowest Np flux values (Figure 5.34F), further decreasing organic carbon flux (Figure 5.34E) and SST (Figure 5.34A) values. SST decreases as heat is lost to the atmosphere (Meredith et al., 2004) leading to the erosion of the stratification of the previous summer and to the deepening of the mixed layer. By the end of April, water column stratification completely disappears as SST in the upper 100 m of the water column equals out at ~0.5°C (Figure 5.34A). Similarly, surface salinity and salinity at 50 m and 100 m water depths become equal at ~ 34 PSU (Figure 5.34B) as a result of greater and deeper vertical mixing during this time. During this period organic carbon flux gradually reduces and reaches base levels close to zero by May (Figure 5.34E). By the end of this phase conditions are suitable for sea ice formation.

5.2.4 Annual flux patterns: What controls foraminiferal flux in the high latitudes?

Fluxes of Np, organic carbon and organic nitrogen are highest between November and February (phase 2-4, Figure 5.34E,F). Primary production and thus the marine ecosystem (e.g. phytoplankton, krill, fish, and larger marine organisms) on the continental shelf of the WAP is primarily driven by the seasonal cycle of sea ice, light availability (insolation), and atmospheric and oceanographic circulation (Smith et al., 1995; Prézelin et al., 2000; Prézelin et al., 2004; Ducklow et al., 2007). During November

to February, the Palmer Deep LTER sediment trap is located within the outer marginal ice zone (the outer edge of the seasonal sea ice), which is an area of high primary production (Smith and Nelson, 1985, Smiths et al., 2008), and where the availability of nutrients and the physical properties of the water column vary both temporally and spatially (Smith et al., 1995) in turn affecting biological communities. The extent of the sea ice off the shore of the WAP (and thus the location of the MIZ) shows high inter-annual variability (Figure 5.34C) which leads to the variation observed in the onset of primary production (Ducklow et al., 2007). Np flux at the mooring site shows a close relationship with Chl α concentrations (Figure 5.14, and 5.34), showing the importance of food availability for the Np fluxes.

Neogloboquadrina pachyderma shell flux shows two peaks during the year (Figure 5.34F). The first peak coincides with the sea ice melt, increasing solar insolation, the development of the spring chlorophyll bloom and the onset of water column stratification (phases 2 and 3). The second peak occurs around the time of maximum annual SST and surface salinity, when the water column is fully stratified (phase 5). Spearman's Correlation tests undertaken on the Np flux and the environmental variables (Section 5.2.2.2, Table 5.5) only identified statistically significant correlations between Np flux and organic carbon and organic nitrogen flux. However, statistically significant correlation was also found between Chl α concentration and organic carbon and nitrogen flux.

Chlorophyll α concentration reaches an early maximum between the end of November and early December when sea ice has retreated sufficiently and the surface ocean has begun to stratify (phases 2 and 3, Figure 5.34C, D). The development of the spring bloom coincides with the increase of Np flux (Figure 5.34E). Chlorophyll α concentrations remain above 5 mg/m³ between December and March (phases 3-5). The early part of phase 3 coincides with Np flux levels which are reduced and C_{org} and N_{org} flux values which are stable (Figure 5.34D,E). From January onwards (late phase 3), C_{org} and N_{org} increase rapidly, while Np flux reaches peak levels. By phase 3 sea ice typically disappears from the shelf area, and stratification is increased. The sustained presence of Chl α during this time can be attributed to glacial melt as it carries nutrients from the land and to micro-and macronutrients (iron, nitrate, and phosphate) from UCDW getting mixed into surface waters (Smiths et al., 1995; Ducklow et al., 2007; Martinson et al., 2008; Smith et al., 2008).

Although Chl α levels remain above 5 mg/m³ until the end of summer (phase 4), and C_{org} and N_{org} values consistently increase from mid-January to mid-February, Np flux drops off from its peak level to values similar those observed in spring (early phase 2 Figure 5.34). During phase 4 stratification becomes stable and SST increases rapidly (Figure

5.34B). The second Np flux peak (Figure 5.34F) takes place after Chl α and C_{org} and N_{org} reach their maximum and SST is at its peak (phase 5).

From those years in the record when the temporal coverage of water column sedimentation is almost complete, it is evident that Np shell flux displays a bimodal pattern, similar to that observed in the North Atlantic by Tolderlund and Bé (1971) and Jonkers et al. (2010). This suggests that permanent stratification does not control shell flux, rather the development of optimum growing conditions (food availability, timing of sea ice retreat and maximum SST). This bimodal flux pattern contrasts with studies conducted in the northern end of the AP, the Weddell Sea (Donner and Wefer, 1994) and in the Arctic, where a single summer peak in flux is observed (Kohfeld et al., 1996; Bausch et al., 1997; Simstich et al., 2003).

The results of the Spearman's Rank Correlation show that organic carbon and nitrogen flux values are positive correlated with SST and Chl α concentration, and negatively correlated with SIC, meaning that with increasing SST and Chl α and decreasing sea ice, biological productivity is increased (thus the increased organic carbon and nitrogen produced by primary production). The lack of significant correlation between Np flux values and environmental variables means that one parameter alone cannot influence the flux pattern. Rather it is the effects of the environmental variables on the food availability that determines Np flux, as the combination of SST, Chl α and sea ice determines the strength of the biological productivity, which is similar to the relationship observed in other high latitude regions (Donner and Wefer, 1994; Kohfeld et al., 1996; Mortyn and Charles; 2003; Kuroyanagi et al., 2011).

5.2.4.1 Inter-annual variability in Neogloboquadrina pachyderma shell flux

Triggers for increased Np flux are consistent each year (i.e. flux is always increased once sea ice melts), however, inter-annual variability is observed in the timing and amplitude of peak Np flux (Figure 5.13C). The timing of the first flux peak occurs in November in 2006-07, 2008-09 and in 2012-13, while in 2011-12, the first peak takes place earlier, in October. Flux is not available from 2007-08 and 2011-12. The timing of the second peak also varies between the years. In 2005-2006, 2006-07, 2007-08, 2011-12 and 2012-13 this occurs in January, while in 2010-11 it is in late February-March. Flux is not available for this time period during the 2009-10 season. The amplitude of the peak fluxes varies by three orders of magnitude during the six year record (Figure 5.13C). Summer 2007-08 shows the lowest peak fluxes (4 shells/m²/day in January), although samples from November and December are missing from the record. The greatest abundance of foraminifera is recorded in 2010-11 in October, with 9586 shells/m²/day. The timing of

the greatest fluxes of each year also varies between the years. In 2005-06, 2006-07, and 2011-12 highest abundances were reached in January, while in 2010-11 highest abundances were observed in October-November. In summer 2012-13 the fluxes of the two peaks are approximately equal (107 and 98 shells/m²/day). The differences in the timing and amplitude of the peak flux is partially driven by the relatively early sea ice melt in 2010 and also by the timing of the chlorophyll blooms.

5.2.5 The role of environmental variability on *Neogloboquadrina pachyderma* shell size and morphology

5.2.5.1 Morphotypes of *Neogloboquadrina pachyderma*

By assessing the shape and size of *Np* through the time series we can identify two main morphotypes, *Np*-A and *Np*-C (Figure 5.35) following from Chapter 5.1. *Np*-A is quadrate, rounded, and fairly spherical. It primarily has four visible chambers and a central aperture. It is visibly encrusted with a secondary crust and it is rather large (Figure 5.35A). These specimens are most abundant between September and February -austral spring and summer (Figure 5.36). *Np*-C is smaller, has thinner walls, generally quite lobate and elongated with four chambers and the aperture is in an off-centre position (Figure 5.35B). This morphotype does not have a secondary crust. It can be considered that *Np*-C is the pre-adult form of *Np*-A as it contains all the signs of pre-reproduction specimens, such as small, more translucent shell, elongated shape, and position of aperture (Hemleben, 1989; Kozdon et al., 2009). *Np*-C specimens are most abundant between March and August – austral autumn and winter (Figure 5.36). The presence of these two morphotypes (pre- and post-reproduction) in the sediment trap samples agrees well with sedimentary records from the region (Vautravers et al., 2013).

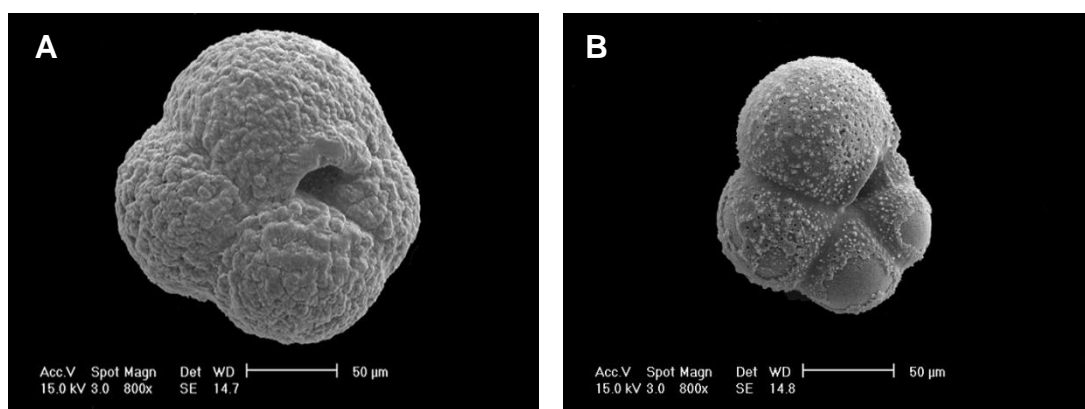


Figure 5.35: Scanning Electron Microscope images of *Np*-A (A) and *Np*-C (B) morphotypes of *Neogloboquadrina pachyderma*.

5.2.5.2 *Neogloboquadrina pachyderma* morphological variability and the role of environmental parameters

The results of the principal component analyses in section 5.2.2.3 revealed that seasonality alone cannot explain the morphological variability observed in the dataset. To determine what drives the morphological variability, redundancy analysis (RDA; see section 5.2.1.7) was carried out on the means of the size-normalised, size-dependent, size-invariant morphological data and the environmental parameters (Figure 5.37). This analysis shows a single dominant trend in the joint space of morphological variables and environmental parameters. The first canonical axis (F1) explains 84.9% of the joint variation. This axis is dominated by the size-dependent morphological variables, elongation ratio and circularity ratio and are linked to the concentration of sea ice, showing a negative correlation. This suggests, that the presence of sea ice and its increasing concentration has an adverse effect on the population, as smaller and less round specimens indicate the reduced chance of gametogenesis and development of a secondary crust.

The second canonical axis shows the effect of the opposing trends of chlorophyll and SST on the compactness coefficient. Positive correlation can be observed between SST and nitrogen and carbon fluxes (Figure 5.37). A negative correlation is observed between the compactness coefficient and SST, nitrogen and carbon fluxes, while a positive correlation is observed between chlorophyll concentration and the compactness coefficient. This trend shows the impact of productivity changes on the shape of the foraminifera, where greater chlorophyll α concentration (can be considered as food availability) results in more compact shells potentially indicating reproductive success and greater calcification (Kohfeld et al., 1996; Eynaud et al., 2009). Similar observations have been made in the North Atlantic and in the Arctic Sea as well (Eynaud et al., 2009; Moller et al., 2013), where nutrient concentrations and the availability of phytoplankton influence *Np* shell shape as well as size. However, it is worth noting, that F2 only explains 10% of the joint variance and therefore the observed relationships can only be considered weak. Additionally, the constrained and unconstrained variances of the RDA each account for 50% of the variability, thereby the environmental parameters are only responsible for 50% of the morphological variability meaning that other factors need to be considered to explain the total variability.

In summary, the presence/absence of sea ice and availability of food are the most important drivers behind *Np* abundance. A nearby sediment core record of *Np* abundance and morphology (Vautravers et al., 2013) supports this hypothesis.

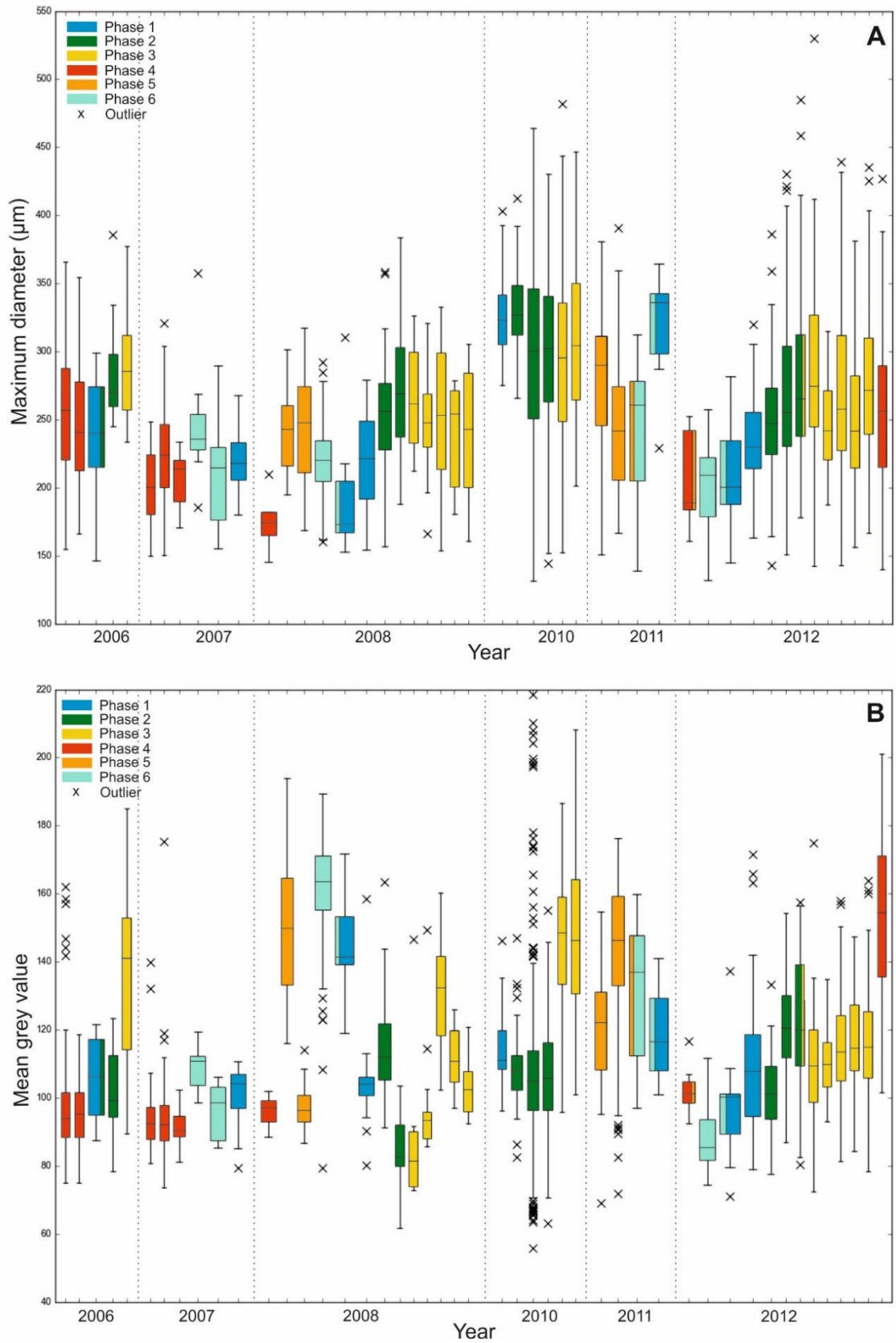


Figure 5.36: Maximum diameter (A) and transparency (B) time series record derived by automatic microscope system showing the difference in morphology between winter samples (blue boxes) through the record.

Specimens resembling *Np*-C were found to be dominating the sedimentary record between 26 and 72 ka BP, the last glacial period, suggesting the high mortality rate of pre-adult (pre-reproduction) *Np* in response to increased sea-ice extent and concentration. Therefore it can be considered that the prevalence of sea ice and the decreased food availability (as a result of shorter and/or less frequent sea ice melt episodes) create unfavourable conditions for *Np* to complete their life cycle. Mature, more robust *Np* survive these conditions to reproduce once the sea ice dissipates and/or food becomes plentiful but their relative abundance is reduced.

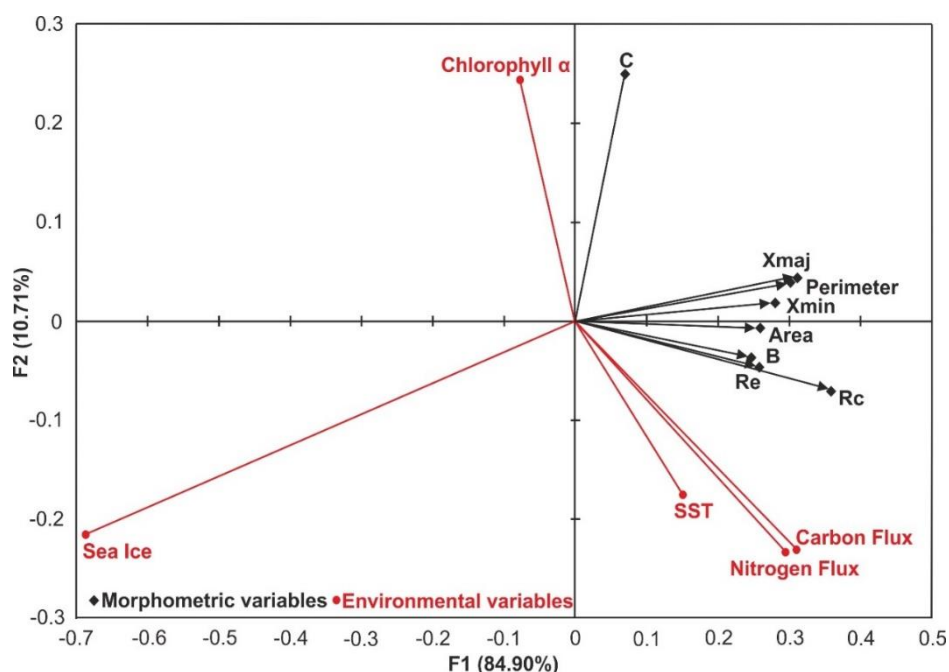


Figure 5.37: Redundancy Analysis biplot of the means of the normalised size-dependent and size-invariant morphological data (black) and the environmental parameters (red).

5.2.6 *Neogloboquadrina pachyderma* calcification and stable isotope variability

The $\delta^{18}\text{O}$ of foraminiferal calcite is determined by the equilibrium fractionation between calcite and seawater (which is a function of temperature), and by 'vital effects' which may create deviations from equilibrium (Niebler et al., 1999; Rohling and Cook, 1999; Section 4.1.5). Foraminifera secrete CaCO_3 from the surrounding seawater (Ravelo and Hillaire-Marcel, 2007) and the offset between $\delta^{18}\text{O}$ of foraminiferal calcite and the $\delta^{18}\text{O}$ of the seawater depends on the temperature. Although some species show isotopic equilibrium with seawater with very little deviation (e.g.: *G. tumida*, *G. bulloides*, *G. crassaformis*) (Niebler et al., 1999), *Neogloboquadrina pachyderma* has been observed to calcify in equilibrium (King and Howard, 2005; Jonkers et al., 2013; Sagawa et al., 2013; Asahi et al., 2015, Chapter 5.1) as well as out of equilibrium with seawater (Kohfeld et al., 1996;

Ortis et al., 1996; Bauch et al., 1997; Volkmann and Mensch, 2001; Bauch et al., 2002; Mortyn and Charles, 2003; Simstich et al., 2003; King and Howard, 2005; Kuroyanagi et al., 2011, Chapter 5.1); in the latter case the offset can vary from -0.4‰ (King and Howard, 2005) to -1.3‰ (Volkmann and Mensch, 2001). Additionally, offsets from equilibrium calcite vary between the ontogenic calcite (secreted prior to reproduction) and the secondary crust (precursor to gametogenesis) (Kozdon et al., 2009). A -0.5‰ to -1‰ offset from equilibrium was observed in the ontogenic calcite of Np specimens in the North Atlantic, while a positive vital offset of 0.8‰ was observed in the secondary crust of Np specimens in the same location (Kozdon et al., 2009). As the development of the secondary crust is a sign of reproduction and the final stage of the life cycle (Kucera, 2007), and it is assumed that Np dies shortly after gametogenesis (due to the break-up of the cytoplasm into isogametes (Hemleben et al., 1989), recovered tests that do not have a secondary crust can be considered to have died prior to reproduction. Therefore differences in vital offsets could be expected between Np-A and Np-C (see above Section 5.2.5) relating to where in its life cycle the specimen died.

The lack of consensus on Np vital offset and variability between morphotypes show the importance of identifying the presence/absence of vital offset at the study site prior to further assessment of the foraminifera-derived stable isotope record. Once the vital offset is assessed, the calcification depths of Np can be determined.

5.2.6.1 Depth and seasonality of calcification

As discussed in Bauch et al. (1997), the calcification depth is not necessarily the same as depth of habitat as Np migrate through the water column while they build their shells incorporating the signal of the water column along the way (Hemleben et al., 1989). Additionally, Np secretes a secondary calcite crust after gametogenesis when the organism sinks to deeper depths (Schiebel and Hemleben, 2005; Kozdon et al., 2009). As the secondary calcite crust can make up as much as 80% of the shell weight (Kohfeld et al., 1996; Stangeew, 2001) the $\delta^{18}\text{O}$ of the shell can be skewed towards deeper depths (higher $\delta^{18}\text{O}$). Therefore each specimen's $\delta^{18}\text{O}$ reflects a weighted average of $\delta^{18}\text{O}_{\text{sw}}$ along the part of the water column the specimen inhabited and calcified in.

To determine the calcification depth, first we need to know of any offset from $\delta^{18}\text{O}_{\text{eq}}$. By April, stratification dissipates and the water column is well mixed between 0 and minimum of 100 m (Figure 5.38), meaning the $\delta^{18}\text{O}_{\text{eq}}$ is uniform between these depths. During this time Np $\delta^{18}\text{O}$ follows the $\delta^{18}\text{O}_{\text{eq}}$ closely without any apparent offset. When the water column is stratified (December - March) an offset between surface $\delta^{18}\text{O}_{\text{eq}}$ and

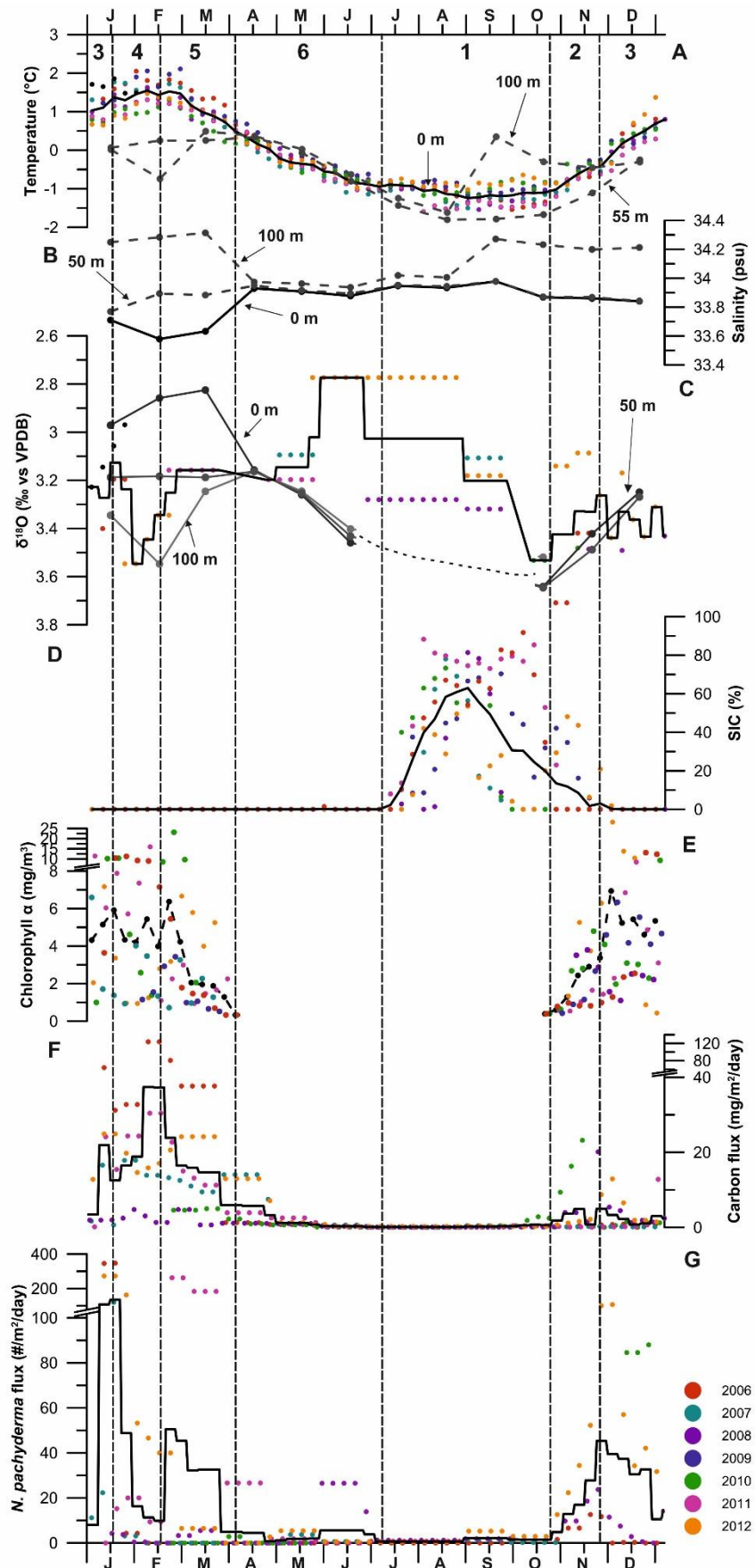


Figure 5.38: Legend as in Figure 5.31 with the addition of the phases of the year (dashed lines) as identified in section 5.2.3

Np $\delta^{18}\text{O}$ becomes evident (Figure 5.38C). At this time Np $\delta^{18}\text{O}$ seems to follow the same pattern as temperature below the surface mixed layer.

The depth at which Np calcifies can be constrained by the $\delta^{18}\text{O}_{\text{eq}}$ depth profiles, which are calculated from observed $\delta^{18}\text{O}_{\text{sw}}$, CTD salinity and temperature values and the modelled data from WOA13 (Figure 5.31). We identify the Np calcification depth during the summer months between 45 and 100 m, assuming no offset from $\delta^{18}\text{O}_{\text{eq}}$ due to vital effects (Figure 5.31). This depth is similar to previously published sediment trap record further south along the Antarctic Peninsula (Hendry et al., 2009) and to sediment trap (Kohfeld et al., 1996, Bauch et al., 1997) and plankton tow records (Carstens et al., 1997) in the Arctic region and fall within the shallower end of calcification depths identified in the South Atlantic sector of the Southern Ocean using plankton tows (Mortyn and Charles, 2003). Shallower calcification depths have been recorded in the northern Pacific regions (Ortiz et al., 1996; Kuroyanagi et al., 2011), although the calcification depth follows the depth of the mixed layer there too. During late autumn and winter (Figure 5.38: phase 6 and 1) the $\delta^{18}\text{O}_{\text{sw}}$ becomes slightly heavier as the temperature decreases and sea ice develops. This change in the $\delta^{18}\text{O}_{\text{sw}}$ results in the $\delta^{18}\text{O}_{\text{eq}}$ to also increase towards heavier values. Due to the lack of $\delta^{18}\text{O}_{\text{sw}}$ observations between April and October it is difficult to accurately determine the $\delta^{18}\text{O}_{\text{eq}}$ for these months. Surface $\delta^{18}\text{O}_{\text{eq}}$ should follow the changes in temperature and salinity until July, when sea ice formation begins; however, we can be less certain about $\delta^{18}\text{O}_{\text{eq}}$ below the mixed layer.

5.2.6.2 Intra- and inter-annual variability in *Neogloboquadrina pachyderma* $\delta^{18}\text{O}$

Np $\delta^{18}\text{O}$ values show large inter-annual variability during the winter; we observe a 0.5‰ difference between the winter months of 2008 and 2012, while a 0.2‰ difference exists between the 2007 and 2008 samples collected during August and September (Figure 5.30). Np $\delta^{18}\text{O}$ values follow the $\delta^{18}\text{O}_{\text{eq}}$ values between October and May, during the chlorophyll bloom (phase 2-5, Figure 5.38C) as more food allows greater growth. Np $\delta^{18}\text{O}$ diverge from $\delta^{18}\text{O}_{\text{eq}}$ after May and becomes lower until October (phase 6 and 1, Figure 5.38C).

This could be due to a number of reasons. One is the possibility that Np becomes dormant (hibernate and do not calcify or reproduce) during the winter season, therefore the shell $\delta^{18}\text{O}$ values reflect the conditions of the preceding autumn season. This could be the case when Np $\delta^{18}\text{O}$ remain relatively stable between March and September (only a 0.15‰ variability) as it did during 2007 (Figure 5.30, 5.38C). These specimens are larger and less transparent (thick calcite crust and/or presence of secondary crust) than usual for the time of the year (Figure 5.36). The thick calcite crust and/or presence of a

secondary crust in addition to the high $\delta^{18}\text{O}$ values in these specimens would suggest that the sediment trap captured mature Np that calcified at depth in equilibrium with seawater during the previous season, hence the difference between Np $\delta^{18}\text{O}$ and $\delta^{18}\text{O}_{\text{eq}}$. Mortality of these post-gametogenic specimens occurred during the winter when conditions became too hostile for the organism.

Another possibility to account for the lighter shell $\delta^{18}\text{O}$ with respect to $\delta^{18}\text{O}_{\text{eq}}$ is that the shell $\delta^{18}\text{O}$ reflects ontogenic calcite. The secondary crust secreted post-gametogenesis at deeper water depths than the original calcite layer typically has heavier $\delta^{18}\text{O}$ signature (Reiss, 1957; Hemleben et al., 1989; Kozdon et al., 2009). Np specimens that have not secreted the secondary crust (due to mortality prior to the formation of the crust or to unfavourable conditions), therefore have $\delta^{18}\text{O}$ compositions that are lighter than those with secondary crust (Kozdon et al., 2009). The relatively light Np $\delta^{18}\text{O}$ values (2.7‰) recorded between May and August of 2012 (Figure 5.30A) could reflect the lack of secondary crust. Ion microprobe analysis of Np specimens collected by plankton tows in the North Atlantic revealed that ontogenic calcite $\delta^{18}\text{O}$ in a shell can range from 1.1‰ to 3.0‰ and that the average ontogenic $\delta^{18}\text{O}$ values of the specimens do not reflect the changes of $\delta^{18}\text{O}_{\text{eq}}$ values with depth (Kozdon et al., 2009). Rather, the authors identified a 0.5 to 1‰ negative fractionation relative to surface water $\delta^{18}\text{O}_{\text{eq}}$. The negative offset of 0.8‰ identified by our study between the 2012 May-August Np $\delta^{18}\text{O}$ and corresponding $\delta^{18}\text{O}_{\text{eq}}$ falls within this range of offset. Additionally, specimens with light $\delta^{18}\text{O}_{\text{np}}$ (winter 2012 specimens) are smaller in size and more translucent, than specimens which calcified during the previous year and later on in the year too (Figure 5.36).

All of these data support the possibility that these specimens did not acquire a secondary crust and that these are not fully mature specimens. Accordingly, $\delta^{18}\text{O}_{\text{np}}$ values of these immature specimens reflect ontogenic calcite only and the offset from equilibrium $\delta^{18}\text{O}$ values is due to the disequilibrium fractionation related to the early stages of the foraminifera life cycle when calcification occurs rapidly requiring higher respiration rates (Berger et al., 1978; Hemleben et al., 1989; Spero and Lea, 1996). Foraminifera experience the greatest level of growth when food availability is high and $\delta^{18}\text{O}_{\text{sw}}$ is stable (Hemleben et al., 1989). At the WAP these conditions are fulfilled during the austral spring and summer, when nutrient Chl α concentrations are highest providing ample food. The large intra-annual variability observed in the Np flux record (Figure 5.38), with higher fluxes during the spring-summer, particularly in December and January, than in the rest of the year combined could potentially bias the $\delta^{18}\text{O}_{\text{np}}$ that would be derived from

core-top or sediment core samples to reflect spring-summer conditions and time of year. This has important implications for the interpretation of foraminifera-based paleo records. SST begins to increase during phase 2, which is preceded by the divergence of salinity between the surface and depth (Figure 5.38). The small changes in salinity, especially the decrease in the surface, indicate the introduction of freshwater. This would suggest the beginning of the stratification of the water column, however, SST and temperature below the surface do not begin to diverge until December. As discussed above, sea ice melt does not have a significant influence on the $\delta^{18}\text{O}_{\text{sw}}$, however, the influence of glacial meltwater would commence in December/January (when surface water $\delta^{18}\text{O}_{\text{sw}}$ become lighter due to the isotopically very light meltwater). Therefore $\delta^{18}\text{O}_{\text{sw}}$ and in turn $\delta^{18}\text{O}_{\text{eq}}$ values are expected to remain stable within the mixed layer during the spring and the early summer months (October to December). This is reflected in the *Np* $\delta^{18}\text{O}$ values which on average show no significant offset from the $\delta^{18}\text{O}_{\text{eq}}$ values at the surface or at depth (Figure 5.38). Because of the deep mixed layer it is not possible to accurately constrain the calcification depth during this time period beyond the fact that *Np* grow in the mixed layer. Inter-annual variability is present in the *Np* $\delta^{18}\text{O}$ specimens during October and November resulting in some offset from $\delta^{18}\text{O}_{\text{eq}}$. This can be attributed to the corresponding inter-annual variability in the sea ice cover. Higher than average sea ice cover was recorded in 2012 during this time, which could result in the lighter *Np* $\delta^{18}\text{O}$ values observed.

5.2.7 Seasonal variability of *Neogloboquadrina pachyderma* $\delta^{18}\text{O}$ derived from single specimen analysis

Single specimen $\delta^{18}\text{O}$ values show significant seasonal variability (Figure 5.30A, Figure 5.40, and Table 5.12) similar to that observed in the multi-specimen record. *Np* $\delta^{18}\text{O}$ values are highest during the summer months and are lower during both the previous and the following season (Figure 30A). The highest $\delta^{18}\text{O}_{\text{np}}$ values coincide with the largest test sizes (Figure 39A,B) and high proportion of encrusted specimens – as reflected by higher mean grey values that indicate greater calcification (Figure 39C). This indicates that a large proportion of the analysed specimens within the isotopically heaviest samples are adult organisms that went through their whole life cycle and secreted their secondary crust. These $\delta^{18}\text{O}$ values compare well with the multi-specimen $\delta^{18}\text{O}$ summer values (Figure 5.33) and show the same calcification depths of 45-100 m when compared to the $\delta^{18}\text{O}_{\text{eq}}$ values. Spring samples show increase in size and encrustation with time (evident in the 2012 samples) which is accompanied by increases in $\delta^{18}\text{O}$ values (Figure 5.39). Samples from the autumn months show the opposite: lower

Table 5.12: *P*-values of *F*-tests for equality of variance carried out on single specimen *Neogloboquadrina pachyderma* $\delta^{18}\text{O}$ data. *P*-values which indicate statistically significant difference are highlighted in bold.

| | 23/03/08 | 16/06/08 | 18/11/08 | 18/10/10 | 19/11/10 | 31/12/10 | 08/03/11 | 23/01/12 | 16/05/12 | 16/09/12 | 16/10/12 | 18/11/12 | 30/12/12 | 27/01/13 |
|----------|-------------|-------------|-------------|-------------|-------------|-------------|-------------|-------------|-------------|-------------|----------|----------|-------------|----------|
| 23/03/08 | 1.00 | | | | | | | | | | | | | |
| 16/06/08 | 0.02 | 1.00 | | | | | | | | | | | | |
| 18/11/08 | 0.42 | 0.01 | 1.00 | | | | | | | | | | | |
| 18/10/10 | 0.01 | 0.37 | 0.00 | 1.00 | | | | | | | | | | |
| 19/11/10 | 0.33 | 0.01 | 0.39 | 0.00 | 1.00 | | | | | | | | | |
| 31/12/10 | 0.34 | 0.04 | 0.26 | 0.04 | 0.20 | 1.00 | | | | | | | | |
| 08/03/11 | 0.11 | 0.00 | 0.12 | 0.00 | 0.19 | 0.06 | 1.00 | | | | | | | |
| 23/01/12 | 0.14 | 0.00 | 0.16 | 0.00 | 0.22 | 0.08 | 0.46 | 1.00 | | | | | | |
| 16/05/12 | 0.06 | 0.00 | 0.06 | 0.00 | 0.09 | 0.03 | 0.24 | 0.31 | 1.00 | | | | | |
| 16/09/12 | 0.00 | 0.00 | 0.00 | 0.00 | 0.00 | 0.00 | 0.00 | 0.01 | 0.04 | 1.00 | | | | |
| 16/10/12 | 0.28 | 0.01 | 0.33 | 0.00 | 0.41 | 0.17 | 0.31 | 0.31 | 0.16 | 0.00 | 1.00 | | | |
| 18/11/12 | 0.43 | 0.01 | 0.50 | 0.01 | 0.41 | 0.28 | 0.16 | 0.18 | 0.08 | 0.00 | 0.34 | 1.00 | | |
| 30/12/12 | 0.00 | 0.00 | 0.00 | 0.00 | 0.00 | 0.00 | 0.04 | 0.12 | 0.29 | 0.02 | 0.03 | 0.01 | 1.00 | |
| 27/01/13 | 0.12 | 0.30 | 0.10 | 0.38 | 0.08 | 0.19 | 0.03 | 0.04 | 0.02 | 0.00 | 0.07 | 0.10 | 0.01 | 1.00 |

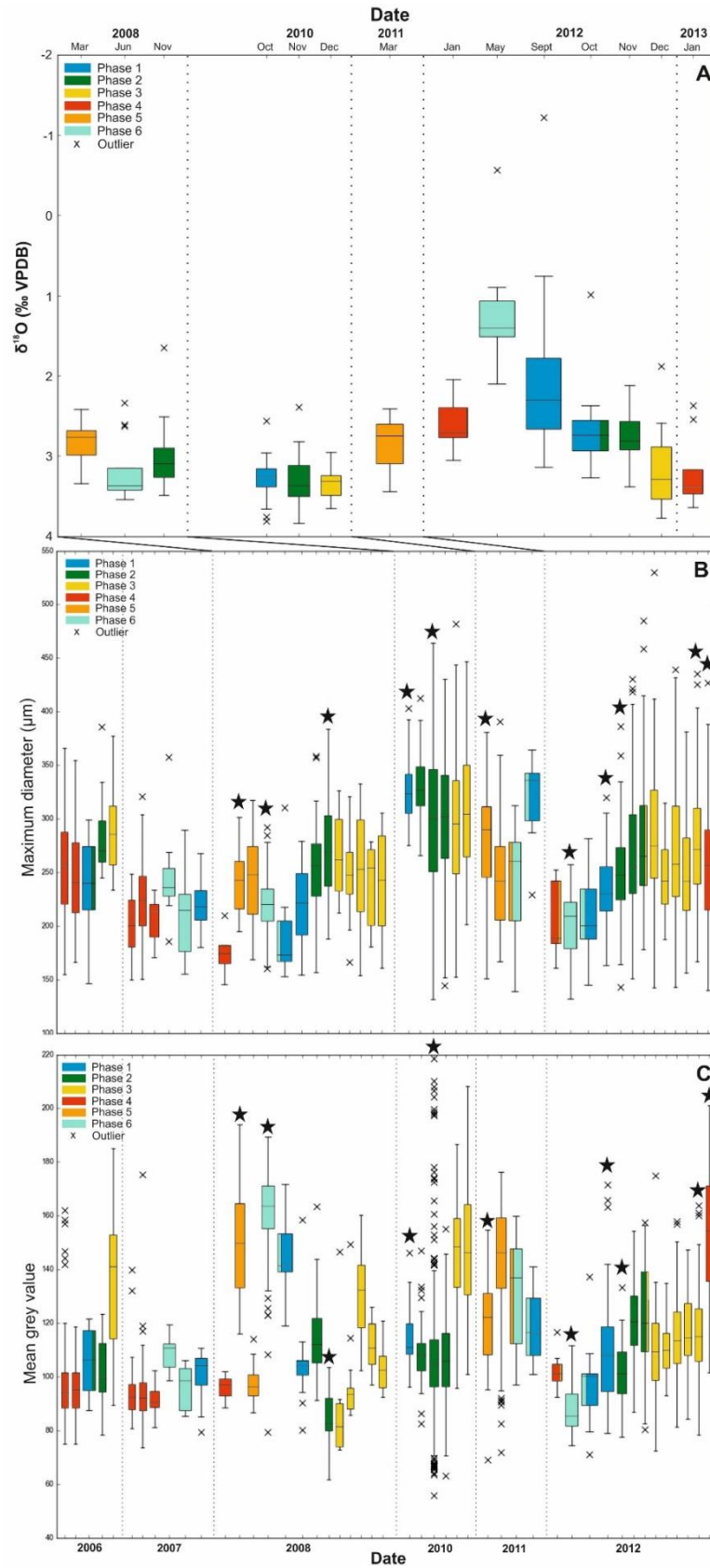


Figure 5.39: Single specimen *Nps* $\delta^{18}\text{O}$ (A), maximum diameter (B) and translucency (C) record. The morphometric dataset was created by the automatic microscope system. Black stars indicate the corresponding $\delta^{18}\text{O}$ dataset. Boxes are coloured according to the phases identified in section 5.2.3.

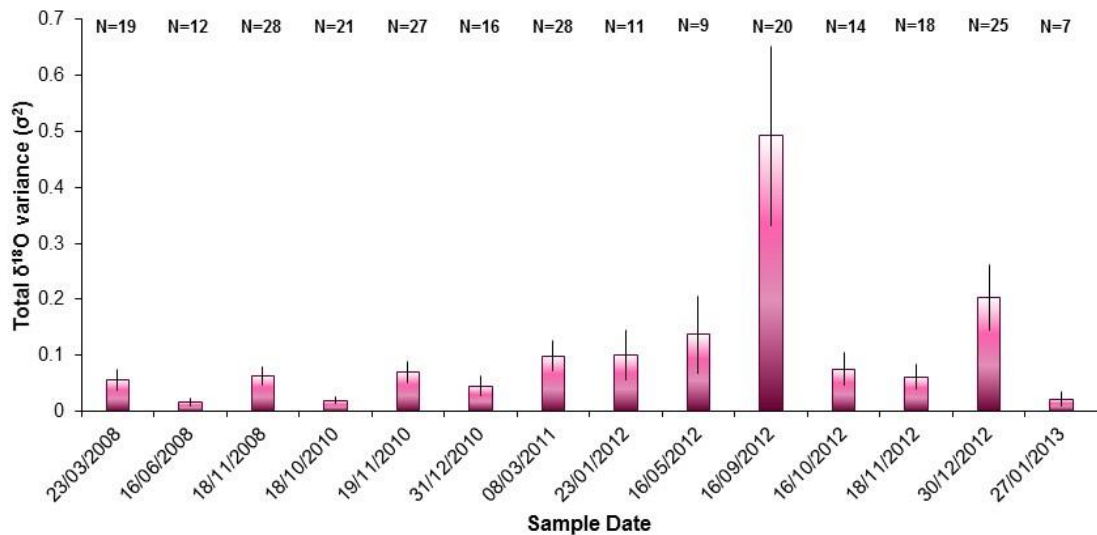


Figure 5.40: Variance of $\delta^{18}\text{O}$ of single specimen *Np* per sample. Error bars represent the standard error of the variance: $\sigma^2 \cdot \sqrt{2/(n-1)}$, where σ^2 is the variance and n is the number of observations.

stable isotope values than observed during the preceding summer (2010-2011) with corresponding decrease in size and encrustation. *Np* $\delta^{18}\text{O}$ values in the winter show two very different ranges. A 1.8‰ difference is observed between the average values recorded from the 2008 and 2012 winter samples (Figure 30A). The higher $\delta^{18}\text{O}$ values in the winter of 2008 are accompanied by mean shell sizes which fall in the lower range of shell sizes through the time series; however, the shells are some of the least translucent in the time series (Figure 5.39C). On visual inspection (under light microscope) these winter specimens showed a high degree of encrustation, and signs of secondary crust development (rounded test, central position of aperture). The development of the secondary crust in water depths between 45-100 m (Figure 5.31) reconciles the high $\delta^{18}\text{O}$ values.

The specimens of phases 6 and 1 of 2012 (Figure 5.39) which have the lightest single specimen $\delta^{18}\text{O}$ of the entire time series are small and the most translucent in comparison with the specimens captured in the following spring and summer (phases 2-4) of 2012 (Figure 5.39C). Visual inspection of the specimens revealed that no specimens appeared to have acquired a secondary crust. Additionally, the specimens displayed a wide range of shapes and in some instances the shells still contained chloroplast (visible by the orange coloration inside the shell). All of which suggest that these specimens perished in inhospitable conditions prior to reproduction.

5.2.7.1 Relationship between *Neogloboquadrina pachyderma* size and single specimen stable isotopes

Stable isotopes of foraminifera shells have been shown to co-vary with size (e.g. Berger et al., 1978; Bouvier-Soumagnac and Duplessy, 1985; Bauch et al., 1997; Niebler et al., 1999; Peeters et al., 2002; Hillaire-Marcel et al., 2004; Kuroyanagi et al., 2011). Previous studies have used the size-dependent differences in stable oxygen isotopic composition to deduce variability in water column stratification on the assumption that larger specimens lived deeper in the water column (Kuroyanagi et al., 2011). However, some studies (e.g. Jonkers et al., 2013) have failed to find a significant correlation between size and stable isotopes, which suggests that regional differences exist in this relationship as a result of different environmental controls. A lack of relationship between shell size and stable isotope would imply that between-sample and within-sample stable isotope variability are purely the result of environmental variability (chiefly temperature).

To investigate the existence of such size-dependent stable isotope variability in the WAP region, the single specimen stable isotope record was separated based on the minimum diameter of each shell. Due to the low shell flux the samples were not sieved into the usual shell size fractions of $<150\ \mu\text{m}$, $150\text{--}250\ \mu\text{m}$ and $>250\ \mu\text{m}$. Instead the size of each specimen was determined through the morphometric analysis prior to isotopic analysis. To make the results comparable to previous studies minimum diameter was employed as an indicator of size.

The dataset shows consistent size effect on both the $\delta^{18}\text{O}$ and $\delta^{13}\text{C}$ of *Np* (Figure 5.41) when the whole dataset is taken into consideration, although $\delta^{18}\text{O}$ shows a stronger correlation with size than $\delta^{13}\text{C}$, with a 0.52 and 0.23 r value respectively (sample size, n ,

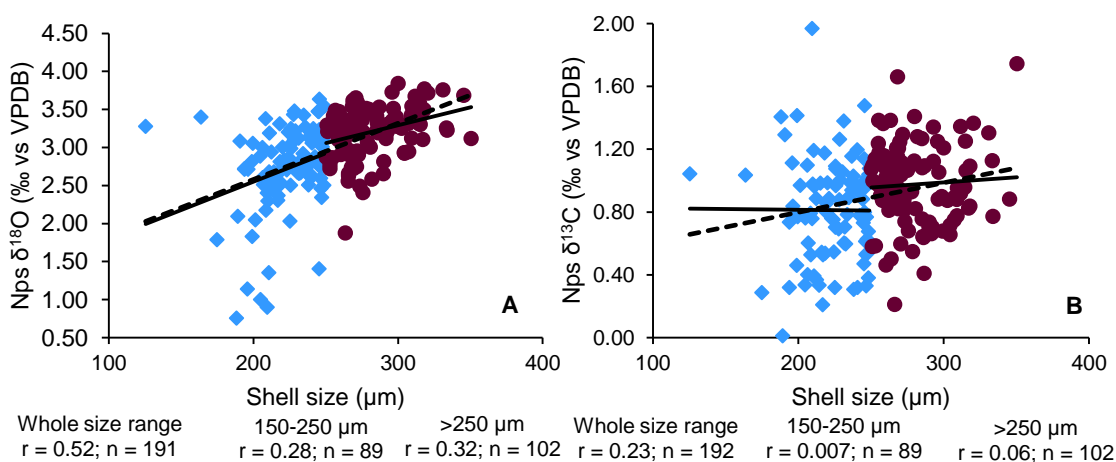


Figure 5.41: Regression diagrams between *Np* shell size (blue diamonds: $150\text{--}250\ \mu\text{m}$, purple dots: $>250\ \mu\text{m}$) and $\delta^{18}\text{O}$ (A) and $\delta^{13}\text{C}$ (B). Significant correlations (at 95% confidence) are detected between shell size and stable isotopes when the size fractions are not separated out (solid black line). r values denote the correlation coefficient, n denotes the number of specimens within the sample.

equals 191). When divided into two size fractions (150-250 μm and $>250\mu\text{m}$) $\delta^{18}\text{O}$ still shows correlation with size: $r=0.28$ and $r=0.32$ for 150-250 μm ($n = 89$) and $>250 \mu\text{m}$ ($n = 102$), respectively (Figure 5.41A). In comparison, the size effect disappears when the $\delta^{13}\text{C}$ dataset is separated into the two size fractions: $r=0.007$ (150-250 μm ; $n = 89$), $r=0.06$ ($>250 \mu\text{m}$; $n = 102$) (Figure 5.41B). An average of $\sim 0.15\text{‰}$ offset is observed between the small and large Np $\delta^{18}\text{O}$ throughout the record, although this is not a consistent offset. The variability in the offset between the smaller and larger size fraction suggests that the differences are largely related to variable oceanographic conditions, instead of size-specific kinetic/metabolic effects.

A similar variable offset relating to environmental variability has been observed in the North Pacific (Kuroyanagi et al., 2011). The offset varies between 0.01‰ (19/11/2010) and 0.72‰ (16/09/2012), with no discernible seasonal variability. This 0.15‰ average offset is comparable to previously published records in the Northern Hemisphere (Bauch et al., 1997 and Kuroyanagi et al., 2011). In comparison, the average offset between the small and large Np $\delta^{13}\text{C}$ is 0.04 , with a minimum of 0.01‰ (31/12/2010) and maximum of 0.44‰ (30/12/2012).

Larger specimens of Np (which are likely to weigh more) are more likely to calcify deeper in the water column, in colder and more saline waters giving rise to higher $\delta^{18}\text{O}_{\text{np}}$ values. In contrast, smaller specimens (smaller weight) are likely to calcify in shallower waters, with higher temperatures and lower salinity, leading to lower $\delta^{18}\text{O}_{\text{np}}$ values. Additionally, specimens with a secondary crust are more likely to be larger in size and heavier in weight – test weight can increase by up to 80% as a result of the secondary crust (Kohfeld et al., 1996). As the secondary crust is added in deeper waters, below the pycnocline (Kohfeld et al., 1996; Bauch et al., 1997; Kozdon et al., 2009) the $\delta^{18}\text{O}$ of Np with a thick secondary crust will have higher $\delta^{18}\text{O}$ values, as observed by Kozdon et al. (2009). Therefore the statistically significant differences between the $\delta^{18}\text{O}$ of the two size fractions of Np and the variable offset between the two size fractions can be attributed to calcification depth differences (and thus temperature and salinity) and to the presence/absence, as well as percent contribution of secondary crust to the total shell.

The size-specific Np $\delta^{13}\text{C}$ values (Figure 5.41B) (as identified by the statistically significant correlation coefficient of 0.23) agree with previously published records of size-specific Np $\delta^{13}\text{C}$ (Donner and Wefer, 1994; Volkmann and Mensch, 2001; Hillaire-Marcel et al., 2004). The correlation between size and $\delta^{13}\text{C}$ can be attributed to a number of factors: i) higher $\delta^{13}\text{C}$ of Dissolved Inorganic Carbon ($\delta^{13}\text{C}_{\text{DIC}}$), and $[\text{CO}_3^{2-}]$ in surface waters (Spero et al., 1997; Bemis et al., 2000); ii) impact of biological and kinetic fractionation on the $\delta^{13}\text{C}$ of smaller and larger specimens (Hemleben et al., 1989).

$\delta^{13}\text{C}_{\text{DIC}}$ is higher in the surface waters as a result of primary production, and lower at depth as a result of remineralisation (Broecker and Peng, 1982). Therefore smaller specimens that calcify closer to the surface should have higher $\delta^{13}\text{C}$ values. Carbonate ion concentration acts in the opposite direction on the foraminiferal $\delta^{13}\text{C}$ complicating the interpretation of the stable carbon isotope record.

Foraminifera calcify (and respire) faster during the early part of their life cycle, and as a result, smaller and younger specimens incorporate a greater amount of ^{12}C leading to lower shell $\delta^{13}\text{C}$ (Hemleben et al., 1989), this is clearly evidenced by the lower $\delta^{13}\text{C}_{\text{np}}$ values in the smaller specimens (Figure 5.30B). Respiration and calcification rate decrease after the early part of the life cycle which leads to the incorporation of a greater amount of ^{13}C into the shell increasing its $\delta^{13}\text{C}$ signature. Additionally, the secondary calcite crust is secreted in deeper waters with lower temperature, which would increase the shell $\delta^{13}\text{C}$. Similarly to the $\delta^{18}\text{O}_{\text{np}}$ record, the variable offset between the $\delta^{13}\text{C}$ of the small and large size fraction could be the result of differences between calcification depths, presence/absence of secondary crust and the life stage the specimen achieved prior to mortality.

5.2.8 Exceptional *Neogloboquadrina pachyderma* flux event of 2010: What is the role of the Southern Annular Mode and the El Niño-Southern Oscillation?

Anomalously large numbers of *Neogloboquadrina pachyderma* rained down into the sediment trap during October and November 2010 (ranging from 1100 to 9586 specimen/m²/day). These large values of *Np* flux are unprecedented in the six-year long time series and occur at an earlier time of the year than peak flux in the other years. The specimens of this event were some of the largest (with specimens up to ~450 μm in diameter; and averaging between ~300 μm and ~325 μm) and roundest specimens with high $\delta^{18}\text{O}_{\text{np}}$ (single specimen $\delta^{18}\text{O}_{\text{np}}$ averaging between $+3.23 \pm 0.14\text{‰}$ and $+3.37 \pm 0.26\text{‰}$). Additionally, a high proportion of the specimens showed signs of heavy encrustation, indicating the presence of a secondary crust. The flux, morphology and stable isotope record of this 2010 event indicate that the environmental conditions were perfect for *Np* growth and reproduction. However, the reasons behind this early flux event are not immediately clear from the record of environmental parameters.

The discussion in the previous sections highlighted that *Np* flux, morphology and stable isotope composition are all closely linked to sea ice extent and food availability (see Sections 5.2.3, 5.2.4, and 5.2.5). *Np* flux shows a close relationship with Chl α concentration (an indicator of primary production and food availability), while variability

in the timing of the onset of primary production is driven by the inter-annual variability of sea ice extent (Smith et al., 1997). The records show that differences in the timing and amplitude of peak Np flux between 2006 and 2012 are driven by the timing of the onset of sea ice melt. Additionally, the presence of sea ice as well as its extent are shown to have adverse effects on Np morphology, as the concentration of smaller sized specimens (that might not have gone through reproduction) is higher during sea ice periods. In contrast, increased Chl α concentration (and thus food availability) has a positive impact on Np morphology and reproductive success. Periods of increased food availability (spring-summer period and/or lower sea ice concentration) and greater reproductive success (evidenced by presence of secondary crust) result in higher $\delta^{18}\text{O}$ shell signature that also links Np $\delta^{18}\text{O}$ with the environmental variability. Based on these findings, the most likely explanation for the 2010 flux event is the combination of early sea ice retreat and/or low sea ice concentration and an early rise in primary production which made a significant amount of resources available for foraminifera growth and reproduction.

Sea ice has a complex but important relationship with the climate phenomenon El Niño Southern Oscillation (ENSO) and the Southern Annular Mode (SAM) (e.g. Turner et al., 2004) with the implication that some of the interannual variability in the Np flux, morphometric and stable isotope data may be driven by the impact of ENSO and the SAM on the WAP climate and oceanographic conditions.

5.2.8.1 Variability in sea ice advance and retreat due to Southern Annular Mode and El Niño-Southern Oscillation

Atmospheric variability in the WAP region on annual timescales is controlled by the twice-yearly poleward movement and intensification of the high latitude atmospheric low-pressure trough in the spring and the autumn, termed the semi-annual oscillation (SAO) (van Loon, 1967). The interactions between sea ice and the atmosphere due to the SAO drive the seasonal cycle of sea ice advance and retreat (e.g. Watkins and Simmonds, 1999; Stammerjohn et al., 2003). On inter-annual timescales, atmospheric variability and thus variability in sea ice advance and retreat are mostly controlled by the teleconnections between SAM/ENSO and the high latitudes because SAM/ENSO modulate the SAO (Watkins and Simmonds, 2000).

During the past thirty years co-variability between ENSO and SAM has increased (Kwok and Comiso, 2002; Fogt and Bromwich, 2006; Stammerjohn et al., 2008, Fogt et al., 2011; Clem and Fogt, 2013), meaning that the two processes change in-phase with each other more often: La Niña (El Niño) events occur at the same time as positive (negative)

phases of SAM (Fogt et al., 2011). The impact of ENSO and SAM on the strength of sea level pressure (SLP) anomalies and sea ice advance on the WAP also intensified during the same period (Stammerjohn et al., 2003; Stammerjohn et al., 2008b). As a result, negative SLP anomalies during austral summer and autumn are observed on the WAP during La Niña events and positive SAM (Figure 2.5), while positive SLP anomalies dominate when El Niño is in phase with negative SAM (Table 5.13). Concurrently, variability in WAP sea ice trends has been closely linked to the SLP anomalies. Earlier wind-driven sea ice retreat and later sea ice advance is associated with the development of strong negative SLP anomalies along the WAP (Table 5.13) supporting anomalously warm northerly winds in the Bellingshausen Sea as a result of the increasingly positive SAM and strong La Niña events since the 1990s. Conversely, positive SLP anomalies during the autumn months in the Amundsen Sea region are associated with cold southerly winds over the WAP region resulting in early sea ice advance (Table 5.13) (Stammerjohn et al., 2008a).

Table 5.13: Impact of co-varying El Niño-Southern Oscillation (ENSO) and Southern Annular Mode (SAM) on sea level pressure (SLP) anomaly over the West Antarctic Peninsula (WAP), wind direction over the WAP, and the length of the sea ice season along the WAP as a result of the interaction of the above (Stammerjohn et al., 2008a; Stammerjohn et al., 2008b; Meredith et al., 2017).

| | | |
|---------------------------------|-----------|-----------|
| ENSO | La Niña | El Niño |
| SAM | Positive | Negative |
| SLP anomaly over WAP | Negative | Positive |
| Wind direction | Northerly | Southerly |
| Length of sea ice season | Short | Long |

5.2.8.2 Recent trends in wind-driven sea ice variability in the Palmer region

The long term trends described in Section 5.2.3 are still prevalent along the WAP today (Meredith et al., 2017). Significant inter-annual variability in sea ice pattern was observed between 2010 and 2014 along the WAP (Figure 5.42) and the strong link between SLP anomalies, wind patterns and sea ice trends continued. Of particular relevance to the Palmer LTER sediment trap *Np* flux record is the impact of both the strongest positive SAM (Figure 5.43A) and a strong La Niña (Figure 5.43B) on sea ice distribution in 2010, in comparison to weaker SAM/El Niño years. The strong positive SAM and the strong La Niña gave rise to the development of very low SLP in the Bellingshausen Sea creating strong north-northwesterly winds between September 2010 and February 2011 (Figure 5.42A). These winds blew warm, moist air into the region reducing sea ice extent and duration resulting in an early spring retreat (early October) and late sea ice advance (Figure 5.13). The result of the low sea ice extent and short duration during the winter of

2010 was the low sea ice melt in the Palmer region in the austral spring-summer season of 2010-2011 (Meredith et al., 2017). The concentration of meteoric waters in near-shore areas (driven by the amount of precipitation) was increased as a result of the warm and moist northerly winds, which are more likely to contribute significant amount of precipitation (Meredith et al., 2017).

Increased meteoric water concentration supports strong southward geostrophic flow along the WAP by creating strong horizontal density gradients in salinity which in turn creates gradients in surface density due to the dominance of salinity on density at low temperature (Meredith et al., 2013). The geostrophic flow carries micronutrients (source of food for microorganisms) out of the northern WAP region to more southerly locations quicker (Meredith et al., 2013). The loss of micronutrients by the stronger geostrophic flow was most likely counteracted by the enhanced upwelling and eddy-transport of warm, nutrient-rich UCDW waters onto the continental shelf, which, created favourable conditions for phytoplankton (especially diatom) growth in the outer to midshelf region (Prézelin et al., 2004). Increased UCDW incursions onto the continental shelf of the WAP have become more common in recent decades (Martinson et al., 2008) and previous studies (Martinson et al., 2008; Martinson and McKee, 2012) have shown that enhanced upwelling is most likely to take place during positive SAM and coinciding La Niña events. The combination of the above processes created perfect conditions for the proliferation of Np, that resulted in the >1000 specimen/ m^2/day Np flux value observed in October and November 2010 (Figure 5.13C). These specimens were larger (maximum diameter values up to $450\mu\text{m}$, with averages of $300\mu\text{m}$ to $\sim 325\mu\text{m}$ Figure 5.36A), rounder (Figure 5.19B), and less translucent (mean grey value – Figure 5.36B) than Np from other years indicating greater reproductive success (presence of secondary crust) resulting in some of the highest $\delta^{18}\text{O}_{\text{np}}$ measurements ($+3.53\text{‰}$ in November 2010) between 2006 and 2013 (Figure 5.39A).

In comparison to 2010, 2012 was characterised by El Niño-like conditions over the Pacific Ocean (Figure 5.43D) (Wolter and Timlin, 1998; Wolter, 2016). Concurrently, SAM switched to a negative state after September 2012 (Figure 5.43C) (Marshall et al., 2016). The combination of the El Niño and the negative SAM gave rise to the development of a high SLP cell over the southern Bellingshausen/Amundsen Sea creating strong and persistent southerly winds over the WAP between October and December 2012 (Meredith et al., 2017). As a result of these winds, although 2012 had the lowest overall sea ice cover of the sediment trap collection period (Figure 5.13B), sea ice lingered in the region around the sediment trap site until late November as the

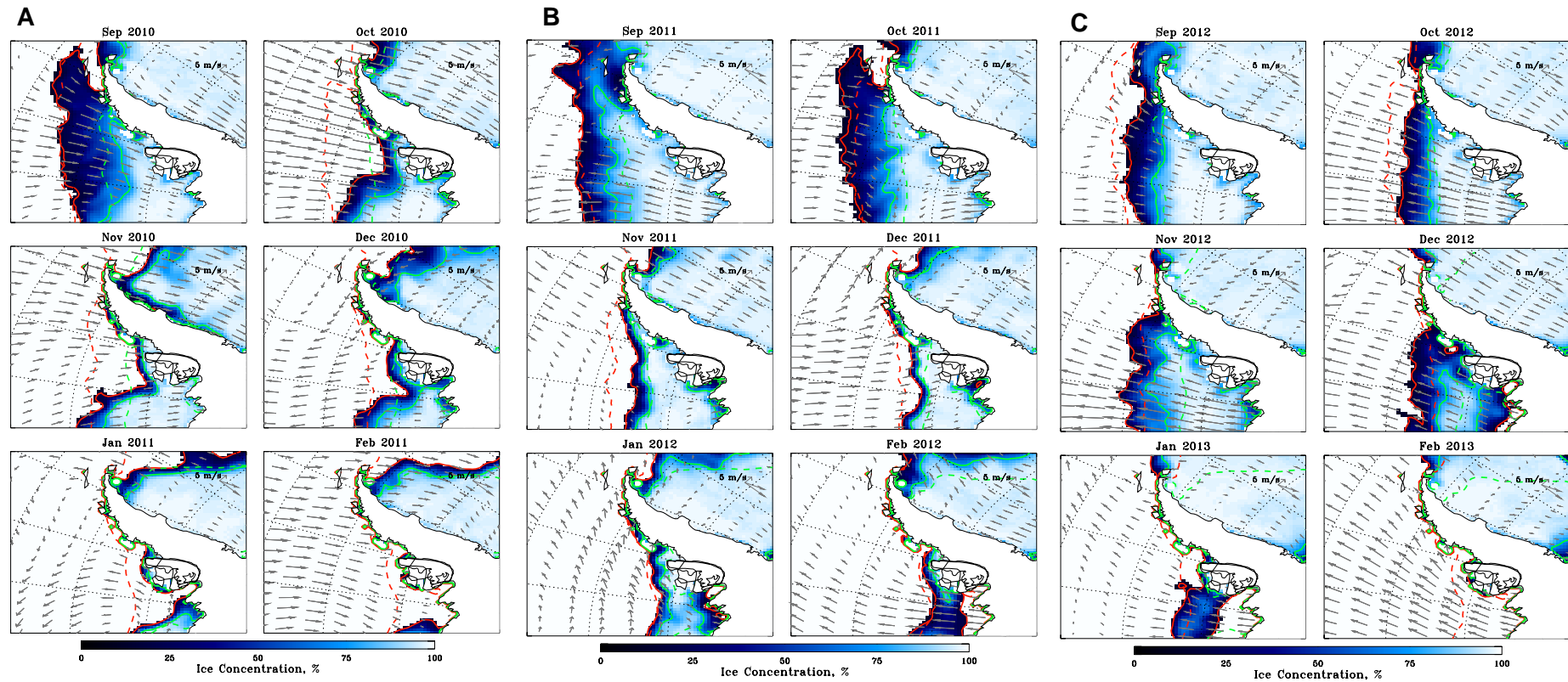


Figure 5.42: Sea ice concentration fields from Meredith et al. (2016). A) September 2010 to February 2011; B) September 2011 to February 2012; C) September 2012 to February 2013. Red lines show 15% concentration for the actual month (solid) and for the climatological mean (dashed) between 1979 and 2012. 75% concentration contours are marked in green.

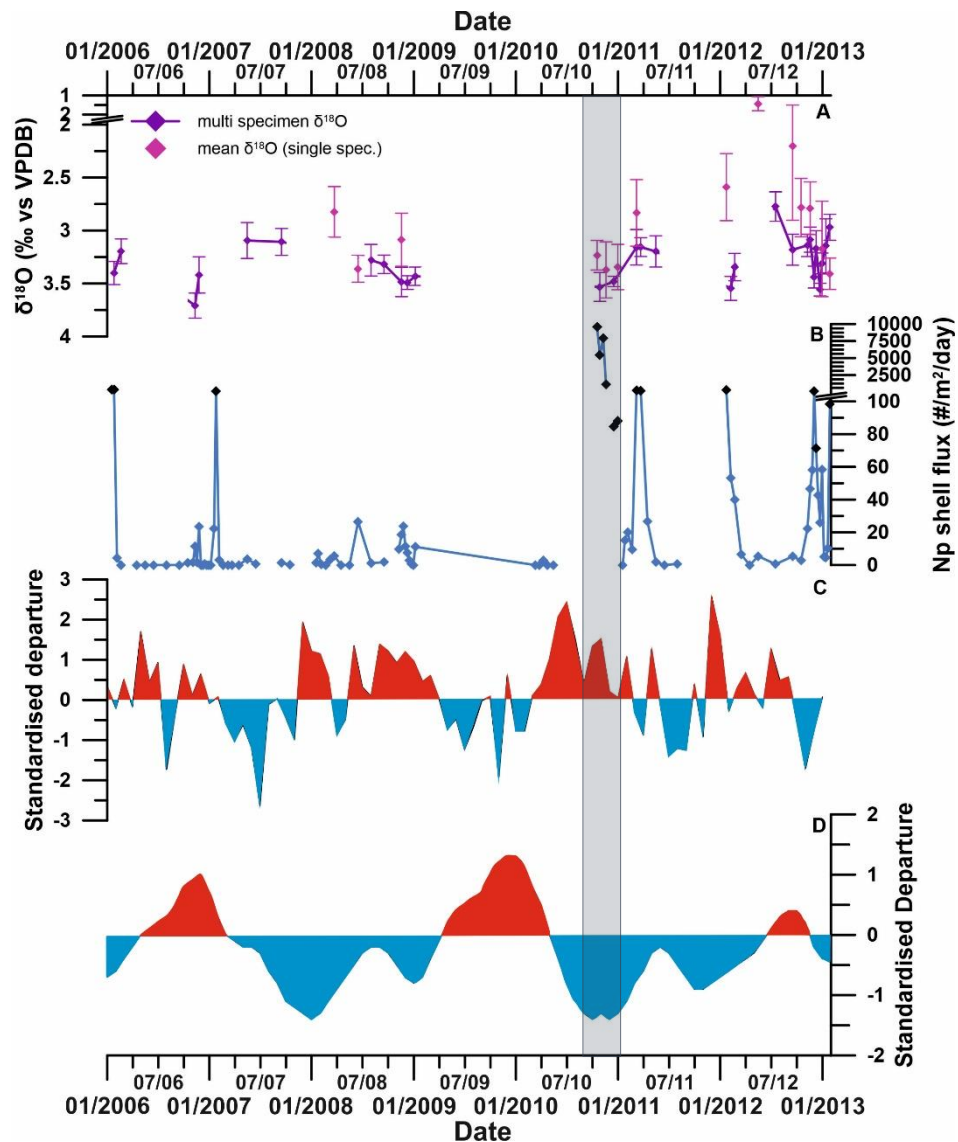


Figure 5.43: Multi-specimen and single specimen $\delta^{18}\text{O}_{np}$ (A) and *Neogloboquadrina pachyderma* flux record (B) from the Palmer-LTER sediment trap in relation to the SAM (C) and ENSO (D) index. SAM index is based on the departure from the zonal means between 40°S and 65°S (Marshall, 2003). Red sections show positive SAM period, blue sections show negative SAM periods in the top figure. The ENSO index based on the departure from the 1950-1993 reference period (Wolter, 2016). Red sections show El Niño conditions, blue sections show La Niña conditions in bottom figure. Note the co-variability between positive SAM and La Niña and vice versa for negative SAM and El Niño as well as the coinciding strong +SAM, La Niña, highest *Np* flux figures and high $\delta^{18}\text{O}_{np}$ measurements in the autumn of 2010 (box).

winds carried cold air over the sea ice (Figure 5.42C) (Meredith et al., 2017). The strong, cold southerly winds (arising from a dry region) limited the amount of precipitation over the WAP and the sea decreasing the near-shore meteoric water concentration, which in turn weakened the southward geostrophic flow (Meredith et al., 2013) limiting the amount of micronutrients carried out of the northern WAP region. Thus, *Np* flux between September and December 2012 was much lower than in 2010 (Figure 5.13), varying between 5 and 142 shell/ m^2 /day. The specimens that calcified during this period were

also on average smaller (lower maximum diameter: Figure 5.39B) than in 2010. The roundness (sphericity, Figure 5.19B) and the translucency (mean grey values, Figure 5.39C) of the shells were similar to 2010, indicating that those specimens that grew under these conditions still succeeded in completing their life cycles, completing gametogenesis and secreting their secondary crust. This is also reflected in the $\delta^{18}\text{O}_{\text{np}}$ measurements, which are similar to the 2010 measurements (Figure 5.39A). This reproductive success is most likely due to the high Chl α concentrations sustained by the weakened geostrophic flow.

Due to the significance and unusual characteristic of the Np flux values during the austral spring of 2010 we can attribute this event to the impact of the coinciding strong positive SAM and La Niña on the WAP. It is expected that northerly winds will become more persistent and stronger in the future as a response of a dominant positive SAM as anthropogenic forcings persist (Van Wessem et al., 2015) creating the possibility of shorter sea ice seasons and warmer SST in this region. These processes will create more favourable growing conditions for Np at the WAP, potentially increasing its abundance during the spring-summer period. The warmer seas and the greater food availability will allow Np to grow larger, and support greater reproductive success. This would have implications for the stable isotope record, as larger shells which have a secondary crust will make up more of the sediment that reaches the seafloor increasing the chances of preservation.

5.2.9 Synthesis and Conclusion

The main findings of the previous discussion sections are summarised in Figure 5.44. Under normal circumstances Np abundance displays a peak during the late spring-early summer (NDJ) period once the sea ice has completely retreated and chlorophyll concentration is increasing. During this time the majority of the Np appear to complete their full life cycle prior to mortality on account of their large (>275 μm maximum diameter) spherical tests indicative of secondary calcite crust formation following reproduction/gametogenesis. Due to the presence of the secondary calcite crust obtained at depth in the water column, $\delta^{18}\text{O}_{\text{np}}$ is the heaviest ($\sim 3.5\text{‰}$) in these specimens and therefore average sample values are heaviest at this time of the year. Small, elongated, non-encrusted specimens are also captured by the sediment trap during late spring-early summer, albeit in small numbers. These small specimens have lower $\delta^{18}\text{O}_{\text{np}}$ values which were obtained closer to the surface, as such these can be considered to be immature specimens that have not reproduced prior to mortality. As the phytoplankton

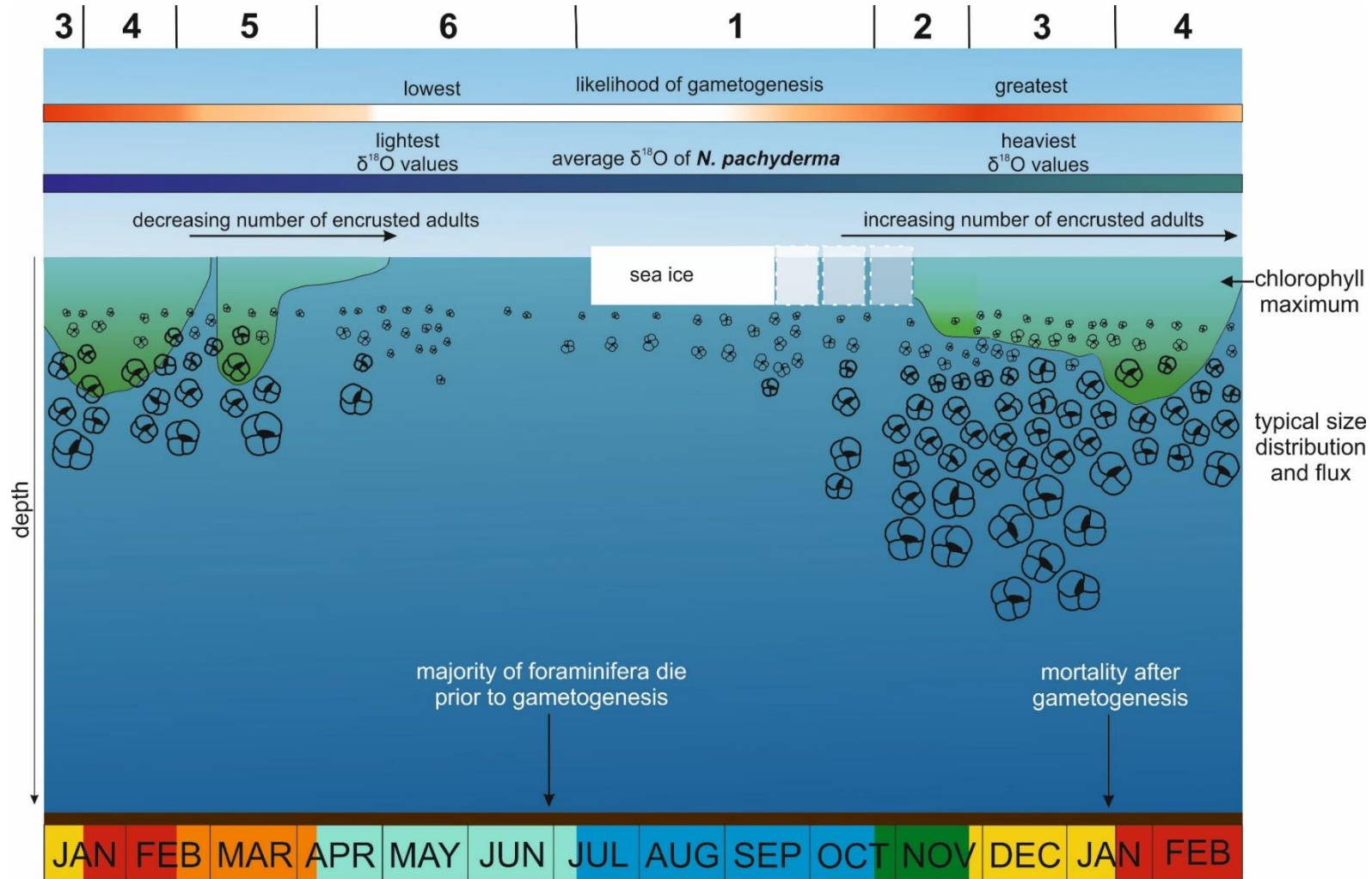


Figure 5.44: Synthesis figure of the seasonal average flux, morphology and stable isotope composition of *Np* in the continental shelf region of the WAP.

bloom and chlorophyll concentration increases and Np reaches deeper depths the flux decreases from its initial peak but still maintains high values, similarly to previous observations by Kohfeld et al. (1996) and Jonkers et al. (2013).

During the austral summer (phases 3 and 4) Np maintains a steady presence in the surface waters (small, elongated, immature specimens) as well as further down in the water column (large, spherical specimens with secondary crust) carrying lighter and heavier individual stable isotopic signatures, respectively. As chlorophyll concentrations and SSTs decrease and the water column stratification begins to break up during the austral autumn (phase 5-early 6), Np flux values decrease significantly. The proportion of encrusted to non-encrusted specimens in the sediment trap decreases during this period indicating that conditions are less favourable for Np to complete its life cycle. By the end of the austral autumn and the start of winter (phase 6), large encrusted specimens become very rare in the trap. Overall flux values reach very low levels and mostly small (<220 μm maximum diameter), elongated, thin-shelled pre-mature specimens with the lightest $\delta^{18}\text{O}$ values of the year reach the sediment trap. This time of the year is characterised by low food availability due to the lack of micronutrients and diminishing light, which together make it difficult for Np to reach the reproductive stage in its life cycle. However, some specimens must be able to survive the conditions and reproduce as Np remain present in the surface waters as shown by its more or less continuous presence in the trap.

During the winter months (phase 1) when sea ice is present above the sediment trap Np flux values remain close to zero (in some years it reaches zero). The specimens collected at this time of the year are small, albeit larger than during late autumn-early winter (phase 6). It is difficult to decipher where exactly the organisms live when sea ice occupies the surface waters. It is known that Np can survive and live within the brine channels of the sea ice (Spindler et al., 1996). It might be possible that the organisms go into a hibernation mode during the winter months and stop calcifying until conditions become suitable during early spring when sea ice begins to dissipate. This possibility is supported by the presence of medium sized (>220 μm) less elongated specimens which show a secondary crust by early spring (September) as soon as sea ice coverage decreases and SST increases. The presence of non-encrusted (most likely pre-gametogenic) specimens in the surface waters in late autumn – early winter (phase 6) when chlorophyll concentrations are close to zero, SSTs are very low, the water column is well mixed, and sea ice begins to form proves the fragility of Np in the high latitude regions. It supports previous suggestions about increased mortality rate prior to reproduction in unfavourable conditions during colder periods in the past 75 ka (Vautravers et al., 2013).

The above pattern of Np flux, morphology and stable isotope variability throughout the year can be modulated by extreme SAM and ENSO conditions, specifically during times of strong positive SAM coinciding with a strong La Niña as demonstrated by the austral spring 2010 samples. Our findings have important palaeoceanographic implications. Firstly, we suggest that when present non-encrusted Np specimens should not be mixed up with encrusted specimens when geochemical analysis is undertaken as the two different morphologies represent different depth habitats and seasons. Secondly, Np proxy records that only utilise encrusted specimens risk the possibility of only reconstructing austral spring and summer conditions and hence cannot draw conclusions about year-round conditions. Finally, the average annual Np flux value in a year not effected by strong SAM and ENSO is significantly lower than the annual flux value during a strong +SAM/La Niña year. Deposition of calcareous material to the seafloor is low in the high latitudes. Therefore it is possible that years with extreme flux values -due to the impact of the strong teleconnections with SAM and La Niña- could overwhelm average years in the sediment record. This would result in sediment cores recording primarily the years with extreme seasonal variability as opposed to average years with average conditions, skewing paleoreconstructions.

5.3 Investigating intermediate water mass variability in the Southern Ocean during the Holocene

The Southern Ocean and the southern mid-latitudes experienced wide scale climate variability during the long-term gradual cooling of the Holocene period (Masson et al., 2000). The Southern Westerly Winds (SWW) oscillated between periods of weaker and stronger strength (Lamy et al., 2010). Similarly, Antarctic Intermediate Waters (AAIW) experienced variability between lower and higher flow speeds during the Holocene that accompanied a gradual increase since the end of the deglacial period (Voigt et al., 2016). Along the Antarctic Peninsula, the flux of glacial meltwater from the glaciers of the West Antarctic Peninsula into the surrounding Bellingshausen Sea also showed periods of highs and lows during the past 13,000 years (Pike et al., 2013). El Niño-Southern Oscillation (ENSO) experienced variability during the Holocene, with reduced intensity between 4,000 and 5,000 yr BP compared to Early and Late Holocene conditions (Carré et al., 2014). Along with the intensity of ENSO, the spatial modes (determined by the location of maximum Sea Surface Temperature (SST) anomaly) also varied during the Holocene. Mollusc-derived $\delta^{18}\text{O}$ records indicate that strong La Niña events and moderate El Niño dominated ENSO from 6,700 and 7,500 yr BP. In comparison, prior to 8,000 yr BP and since 4,000 yr BP strong El Niño events and moderate La Niña events characterise ENSO (Carré et al., 2014).

In this chapter, a single specimen *Globorotalia inflata* stable isotope record is utilised to assess changes in the seasonality of oceanographic conditions in the mid-latitude regions around the Falkland Plateau, Scotia Sea. As shown in the previous chapter, single specimen foraminiferal stable isotopes are a useful proxy to assess changes in seasonality, as they can highlight changes in the range of conditions within a time period. The first two sections of this chapter describes the results of the *Globorotalia inflata* stable isotope analysis, while the rest of the sections assess the results to provide a thorough discussion on Holocene oceanographic variability in the Scotia Sea.

5.3.1 Comparison of paired and single specimen *Globorotalia inflata*

The aim of producing the downcore foraminifera $\delta^{18}\text{O}$ record at core site JR244 - GC528 on the Falkland Plateau (Figure 5.45) is to investigate variability in the seasonality of oceanographic conditions during the Holocene period. To achieve this, $\delta^{18}\text{O}$ values outside normal, or average, conditions need to be captured within a sample. The analysis of a number of individual (single specimen) foraminifera allows us to find these outliers which represent conditions experienced during the growing season of the individual

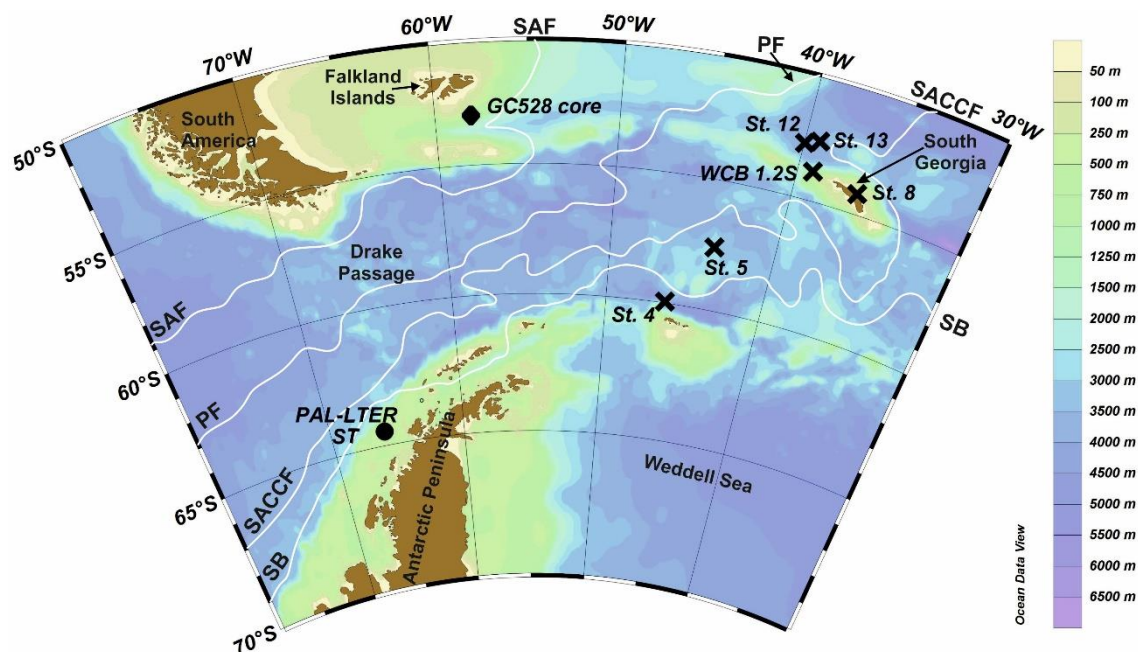


Figure 5.45: Bathymetry map of the Scotia Sea section of the Southern Ocean, highlighting the location of core JR244 - GC528 (black diamond), collected during the BAS cruise JR244, in relation to the localities of the samples utilised in previous two studies: black crosses represent samples discussed in chapter 5.1, black circle represents location of sediment trap samples of chapter 5.2. The main oceanic fronts are shown by the white lines: Subantarctic Front (SAF), Polar Front (PF), Southern Antarctic Circumpolar Current Front (SACCF), Southern Boundary of the ACC (SB).

organism. Although single specimen analysis is the best to capture ranges in conditions, if single foraminifera specimens are very small, with carbonate mass too low for analysis (<5 μg), it is possible to analyse pairs of specimens to increase the carbonate mass. However, extreme/outlier stable isotope values may be compromised as a result of the consolidation of each specimen's stable isotope signature, reducing the within-sample variability. As a result, paired specimen analysis may not provide the true range of $\delta^{18}\text{O}$ values. To determine its suitability for capturing seasonality, paired specimen isotope data must be compared to single specimen isotope data.

In this study, paired and single specimen *Globototalia inflata* $\delta^{18}\text{O}$ analyses were carried out and the statistical distribution of the datasets were compared (Table 5.14, 5.15 respectively). The eight samples of $\delta^{18}\text{O}$ analyses (Table 5.15), comprising paired analysis of *G. inflata* from sediment samples each covering one centimetre stratigraphic thickness, were grouped together and an Anderson-Darling test for Normality was carried out on the 213 data points. Each 1 cm time slice represents ~145 years (Roberts, 2016). Similarly, the 12 samples of single specimen $\delta^{18}\text{O}$ data (Table 5.15) were grouped together to test for normality using the Anderson-Darling test. The results of both tests ($p = 0.005$ and $p = <0.0001$ for combined paired sample dataset and combined single

Table 5.14: Summary statistics of paired specimen *Globorotalia inflata* $\delta^{18}\text{O}$ and $\delta^{13}\text{C}$ analyses from sediment core JR244 - GC528 (Falkland Plateau). *n*: number of data points; σ : standard deviation; σ^2 : variance; *SE* σ^2 : standard error of variance calculated as $\sigma^2 \times (2/(n-1))$.

| $\delta^{18}\text{O}$ Sample depth (cm) | Age | <i>n</i> | Mean | Median | σ | σ^2 | <i>SE</i> σ^2 |
|---|------|----------|-------|--------|----------|------------|----------------------|
| 1-2 | 1100 | 18 | +2.68 | +2.69 | 0.092 | 0.008 | 0.001 |
| 3-4 | 1150 | 30 | +2.73 | +2.71 | 0.1 | 0.01 | 0.001 |
| 13-14 | 2550 | 30 | +2.71 | +2.70 | 0.116 | 0.013 | 0.001 |
| 19-20 | 3250 | 31 | +2.64 | +2.63 | 0.095 | 0.009 | 0.001 |
| 25-26 | 3900 | 31 | +2.74 | +2.73 | 0.089 | 0.008 | 0.001 |
| 35-36 | 5250 | 28 | +2.66 | +2.69 | 0.115 | 0.013 | 0.001 |
| 45-46 | 6600 | 24 | +2.79 | +2.78 | 0.116 | 0.013 | 0.001 |
| 51-52 | 7700 | 21 | +2.76 | +2.74 | 0.125 | 0.016 | 0.002 |
| $\delta^{13}\text{C}$ | | | | | | | |
| 1-2 | 1100 | 18 | +1.54 | +1.54 | 0.119 | 0.014 | 0.002 |
| 3-4 | 1150 | 30 | +1.54 | +1.56 | 0.132 | 0.017 | 0.001 |
| 13-14 | 2550 | 29 | +1.53 | +1.55 | 0.136 | 0.018 | 0.001 |
| 19-20 | 3250 | 31 | +1.61 | +1.62 | 0.154 | 0.024 | 0.002 |
| 25-26 | 3900 | 31 | +1.63 | +1.63 | 0.133 | 0.018 | 0.001 |
| 35-36 | 5250 | 28 | +1.51 | +1.53 | 0.141 | 0.02 | 0.001 |
| 45-46 | 6600 | 24 | +1.55 | +1.58 | 0.137 | 0.019 | 0.002 |
| 51-52 | 7700 | 21 | +1.45 | +1.48 | 0.17 | 0.029 | 0.003 |

specimen sample dataset, respectively) show non-normal distributions which could either be a result of outliers or widely different ranges in the samples that make up the paired and single specimen dataset. Anderson-Darling tests were also carried out on the $\delta^{13}\text{C}$ datasets and revealed non-normal distribution of both the combined paired sample ($p = <0.0001$) and the combined single specimen sample ($p = 0.0002$) datasets. As a result, only non-parametric statistical tests can be carried out on the samples of paired and single specimen analyses.

To explore whether variability is reduced in the stable isotope data which derive from pairs of specimens, compared to those which derive from single specimens, the variance and the standard error of the variance of each sample is compared (Figure 5.46 and 5.47). The variance of single specimen $\delta^{18}\text{O}$ samples displays greater variability than the paired specimen $\delta^{18}\text{O}$ samples throughout the time-series (Figure 5.46). The paired specimen samples $\delta^{18}\text{O}$ variance is relatively stable, oscillating between 0.008 and 0.016 (3900 yr BP and 7720 yr BP, respectively) (Table 5.14, Figure 5.46A). In comparison, the single specimen samples $\delta^{18}\text{O}$ variance ranges between 0.005 (6100 yr BP) and 0.034 (8700 yr BP) (Table 5.15, Figure 5.46B), a 2.5-fold increase compared to the

Table 5.15: Summary statistics of single specimen *Globorotalia inflata* $\delta^{18}\text{O}$ and $\delta^{13}\text{C}$ dataset from sediment core JR244 - GC528. *n*: number of data points; σ : standard deviation; σ^2 : variance; *SE* σ^2 : standard error of variance calculated as $\sigma^2 \cdot (2/(n-1))$; *A*²: Anderson-Darling value; *p*: *p*-value of Anderson-Darling test. *P*-values <0.05 are highlighted. These samples are not normally distributed.

| $\delta^{18}\text{O}$ Sample | | | | | | | | | |
|------------------------------|------|----------|-------|--------|----------|------------|----------------------|-----------------------|----------|
| Depth (cm) | Age | <i>n</i> | Mean | Median | σ | σ^2 | <i>SE</i> σ^2 | <i>A</i> ² | <i>p</i> |
| 7-8 | 1700 | 30 | +2.61 | +2.62 | 0.106 | 0.011 | 0.001 | 0.219 | 0.823 |
| 9-10 | 2000 | 30 | +2.65 | +2.67 | 0.086 | 0.007 | 0.001 | 0.295 | 0.573 |
| 12-13 | 2400 | 30 | +2.62 | +2.63 | 0.100 | 0.010 | 0.001 | 0.340 | 0.474 |
| 14-18 | 2800 | 30 | +2.55 | +2.52 | 0.113 | 0.012 | 0.001 | 0.422 | 0.303 |
| 21-22 | 3450 | 30 | +2.59 | +2.56 | 0.098 | 0.010 | 0.001 | 0.325 | 0.508 |
| 27-28 | 4100 | 30 | +2.57 | +2.56 | 0.074 | 0.006 | 0.000 | 0.631 | 0.091 |
| 31-32 | 4700 | 30 | +2.63 | +2.64 | 0.090 | 0.008 | 0.001 | 0.325 | 0.509 |
| 37-38 | 5500 | 30 | +2.77 | +2.75 | 0.137 | 0.019 | 0.001 | 1.490 | 0.001 |
| 41-42 | 6100 | 29 | +2.62 | +2.61 | 0.075 | 0.005 | 0.000 | 0.179 | 0.910 |
| 49-50 | 7200 | 24 | +2.78 | +2.77 | 0.104 | 0.011 | 0.001 | 0.384 | 0.367 |
| 55-56 | 8700 | 27 | +2.85 | +2.84 | 0.183 | 0.034 | 0.003 | 1.452 | 0.001 |
| 59-60 | 9600 | 8 | +2.93 | +2.97 | 0.141 | 0.020 | 0.006 | 0.295 | 0.511 |
| $\delta^{13}\text{C}$ | | | | | | | | | |
| 7-8 | 1700 | 30 | +1.44 | +1.48 | 0.167 | 0.028 | 0.002 | 0.640 | 0.086 |
| 9-10 | 2000 | 30 | +1.51 | +1.53 | 0.178 | 0.032 | 0.002 | 0.456 | 0.249 |
| 12-13 | 2400 | 30 | +1.48 | +1.52 | 0.176 | 0.031 | 0.002 | 0.493 | 0.201 |
| 14-18 | 2800 | 30 | +1.43 | +1.41 | 0.181 | 0.037 | 0.003 | 0.487 | 0.208 |
| 21-22 | 3450 | 30 | +1.56 | +1.57 | 0.164 | 0.027 | 0.002 | 0.400 | 0.341 |
| 27-28 | 4100 | 30 | +1.48 | +1.45 | 0.191 | 0.036 | 0.003 | 0.277 | 0.630 |
| 31-32 | 4700 | 30 | +1.53 | +1.56 | 0.121 | 0.015 | 0.001 | 0.392 | 0.356 |
| 37-38 | 5500 | 30 | +1.54 | +1.54 | 0.150 | 0.022 | 0.002 | 0.404 | 0.333 |
| 41-42 | 6100 | 29 | +1.53 | +1.49 | 0.143 | 0.020 | 0.001 | 0.862 | 0.023 |
| 49-50 | 7200 | 24 | +1.57 | +1.57 | 0.141 | 0.020 | 0.002 | 0.415 | 0.309 |
| 55-56 | 8700 | 27 | +1.40 | +1.46 | 0.250 | 0.062 | 0.005 | 0.799 | 0.033 |
| 59-60 | 9600 | 8 | +1.53 | +1.57 | 0.176 | 0.031 | 0.009 | 0.435 | 0.220 |

paired specimen samples. The total $\delta^{13}\text{C}$ variance shows similar trends. The paired specimen samples $\delta^{13}\text{C}$ variance fluctuates between 0.018 (3900 yr BP) and 0.029 (7700 yr BP) (Table 5.14, Figure 5.47A), while the single specimen samples $\delta^{13}\text{C}$ variance varies between 0.015 (4700 yr BP) and 0.062 (8700 yr BP) (Table 5.15, Figure 5.47B), representing a greater than 3-fold increase in-between sample variances. These findings suggest that the paired and single specimen samples should not be analysed together as one time series because the paired specimen stable isotope analysis artificially reduces the within-sample variability by averaging out the extreme isotope measurements.

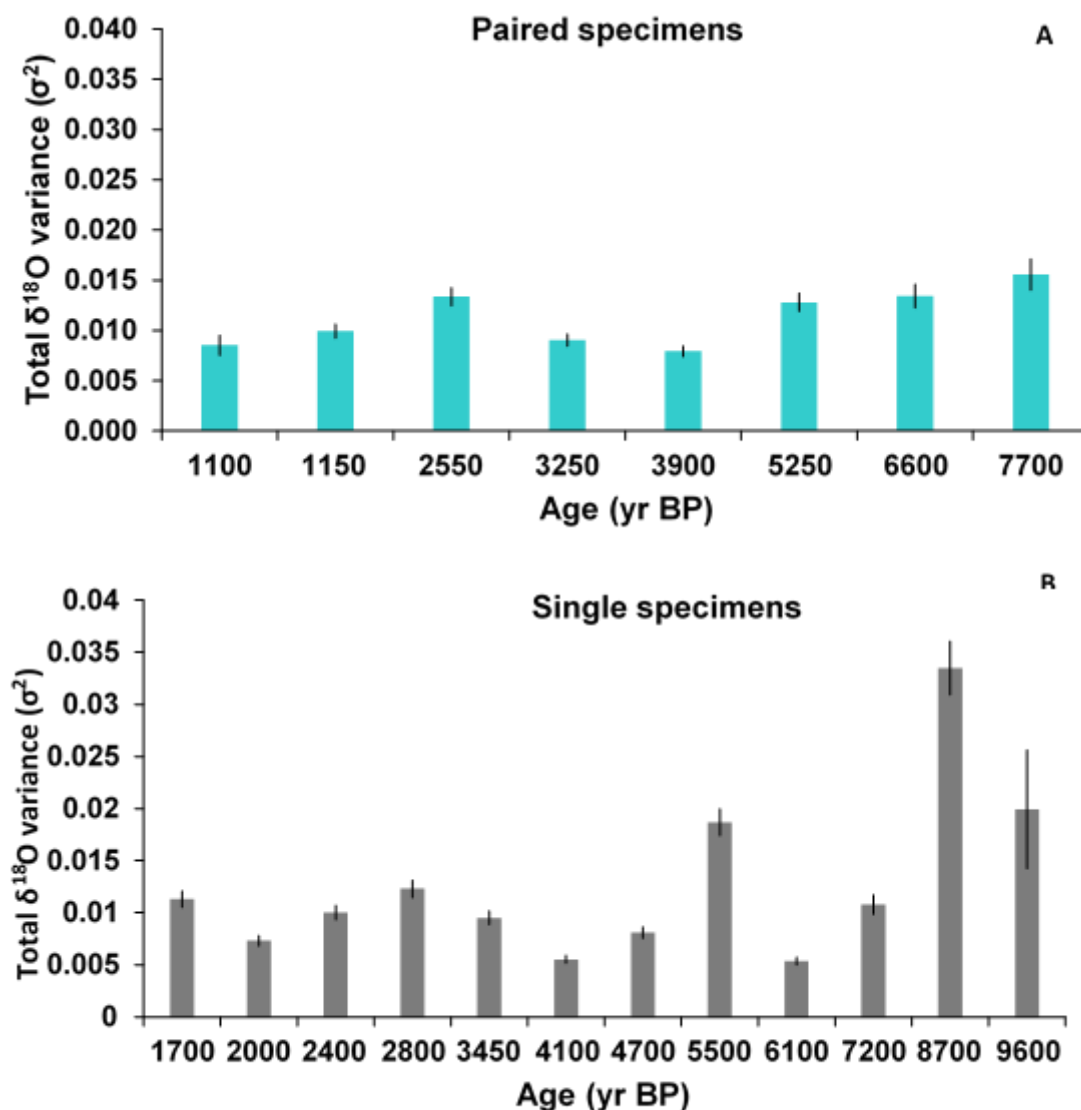


Figure 5.46: Comparison of total $\delta^{18}\text{O}$ variance between paired (A) and single specimen (B) *Globorotalia inflata* dataset from sediment core JR244 - GC528. Variance in the single specimen dataset displays greater degree of variability than in the paired specimen dataset. Error bars represent the standard error associated with the variance.

The simplest statistical comparison of paired and single specimen samples, each comprising multiple measurements, is carried out by analysing the position of the means of the two normally distributed datasets through a Student's t test. This approach reveals whether the groups are comparable or are different. However, the paired and single specimen sample stable isotope datasets are not normally distributed, hence the non-parametric version of the t test - the Mann-Whitney U test - needs to be applied. The Mann-Whitney U test uses the position of the median value as a summary of the data, which requires the dataset to be ranked. The results of the U test show statistically significant difference between the medians of the paired and single specimen sample datasets, for both the $\delta^{18}\text{O}$ ($p = 0.0001$) and $\delta^{13}\text{C}$ ($p = 0.0003$) datasets. These results

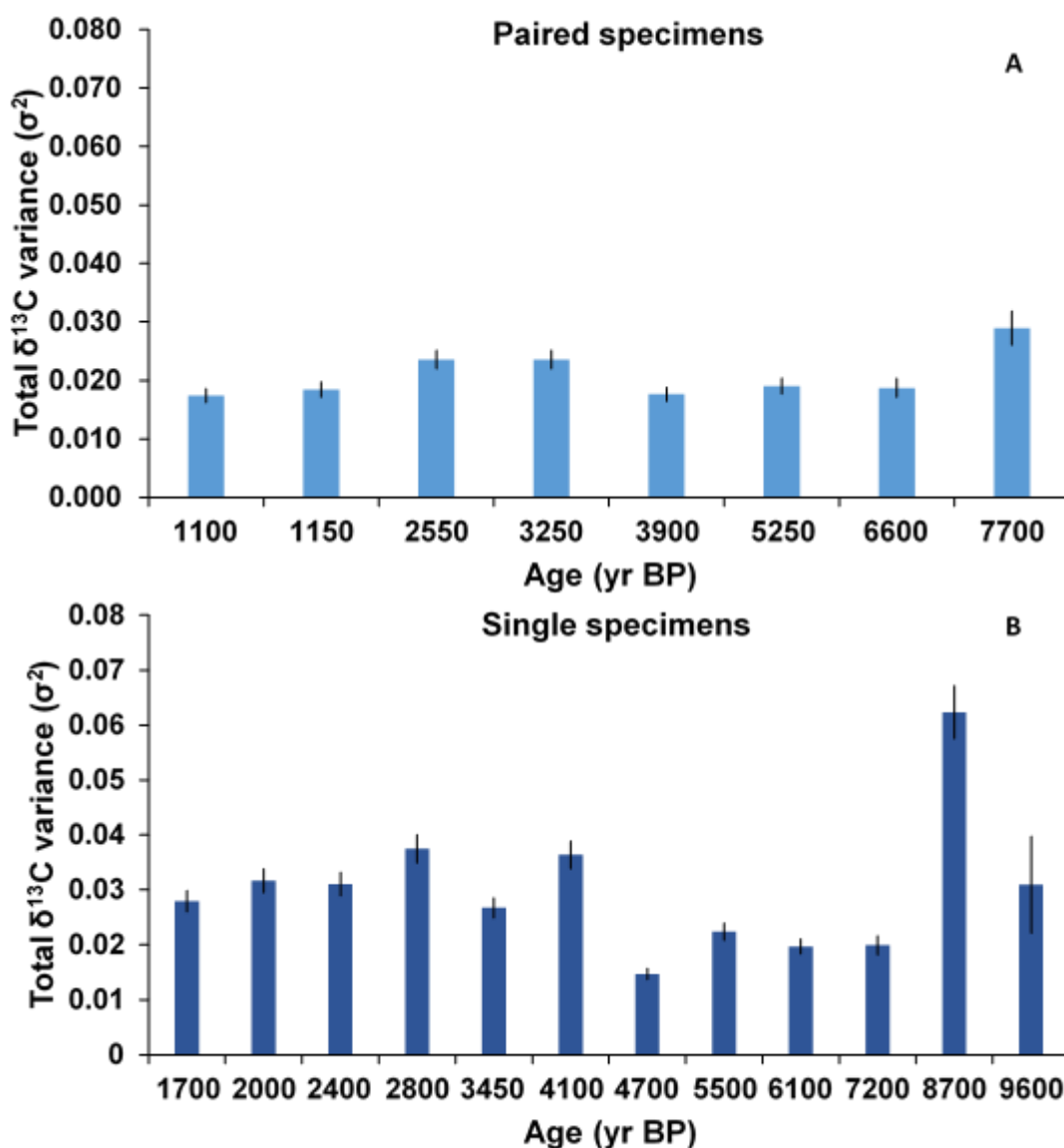


Figure 5.47: Comparison of total $\delta^{13}\text{C}$ variance between paired (A) and single specimen (B) *Globorotalia inflata* dataset from sediment core JR244 - GC528. Total variance of the paired specimen $\delta^{13}\text{C}$ samples is consistently smaller than the variance in the single specimen samples indicating that seasonality is artificially reduced by the analysis of pairs of specimens. Error bars represent the standard error of associated with the variance.

support the analysis of variances, and suggest that the paired and the single specimen dataset are significantly different and hence should not be grouped together for further analysis. Based on this result, further analysis of the stable isotope data from core JR244 - GC528 will focus solely on the single specimen data.

5.3.2 Single specimen stable isotope record of the Holocene

Box-whisker plots were employed to visualise the single specimen stable isotope record (Figure 5.48). These graphs illustrate the main trends in the record, by showing the median, 25%, 75%, minimum and maximum values, as well as the outliers. The outliers are determined based on the following (Eq.11):

$$OL = 1.5 \times IQR \quad \text{Equation 11}$$

where OL is the outlier and IQR is the inter-quartile range (the difference between the upper-quartile (75% value) and the lower-quartile (25% value)). The outliers represent data points which fall outside the normal variability, and can be treated as recording extreme seasonality.

One of the main features of the *Globorotalia inflata* single specimen stable isotope time series (Figure 5.48) is the difference in the within-sample range between the $\delta^{18}\text{O}$ and $\delta^{13}\text{C}$ datasets. The average range (maximum – minimum) in the $\delta^{18}\text{O}$ samples is 0.48‰, while in the $\delta^{13}\text{C}$ samples it is 0.68‰. This difference is even more evident when the interquartile range is compared: the $\delta^{18}\text{O}$ samples have an average interquartile range of 0.13‰; and the $\delta^{13}\text{C}$ samples have an average interquartile range of 0.23‰. Additionally, the total $\delta^{18}\text{O}$ within-sample variance fluctuates between 0.005 and 0.034 (Table 5.15), and the total $\delta^{13}\text{C}$ within-sample variance varies between 0.015 and 0.062 (Table 5.15). These differences in the within-sample ranges and variances shows that the $\delta^{18}\text{O}$ time series displays less overall variability than the $\delta^{13}\text{C}$ time series.

5.3.2.1 Single specimen oxygen isotope record

The total inter-sample variability in the median $\delta^{18}\text{O}$ (Figure 5.48A) is 0.37‰ between 9600 yr BP and 5500 yr BP (Table 5.15). During this period, both the median and the general trend of the data points decrease to lower $\delta^{18}\text{O}$ values (Figure 5.48A). The $\delta^{18}\text{O}$ record is stable between 4700 year BP and 1700 year BP, with 0.08‰ inter-sample variability between the median values (Table 5.15), which is outside the mass spectrometer's standard error of 0.05‰ associated with the analysis. The median $\delta^{18}\text{O}$ value decreases from +2.97‰ at 9600 yr BP to +2.66‰ at 2000 yr BP (Table 5.15). The highest $\delta^{18}\text{O}$ values are found in the early Holocene, at 9600 yr BP (Figure 5.48A), when the maximum reaches +3.11‰. In comparison, the lowest $\delta^{18}\text{O}$ value of +2.31‰ is found at 2800 yr BP (Figure 5.48A), in the late Holocene. The highest number of outliers (four) are found in the 8700 yr BP sample (Figure 5.48A). The variance (0.034) within the 8700 yr BP sample is also the greatest in the single specimen $\delta^{18}\text{O}$ time series (Table 5.15). The smallest variance (0.005) is found in the 6100 yr BP sample, which does not have any outliers.

For each sample a minimum of 30 *Globorotalia inflata* specimens were planned to be analysed. In reality, the number of specimens analysed per sample varied between 8 (9600 yr BP) and 30 (9 out of 12 samples, Table 5.15). The small specimen pool of 9600 yr BP sample was the result of low abundance and also specimen loss during transport. A primary concern when dealing with a small dataset is the increased variance due to

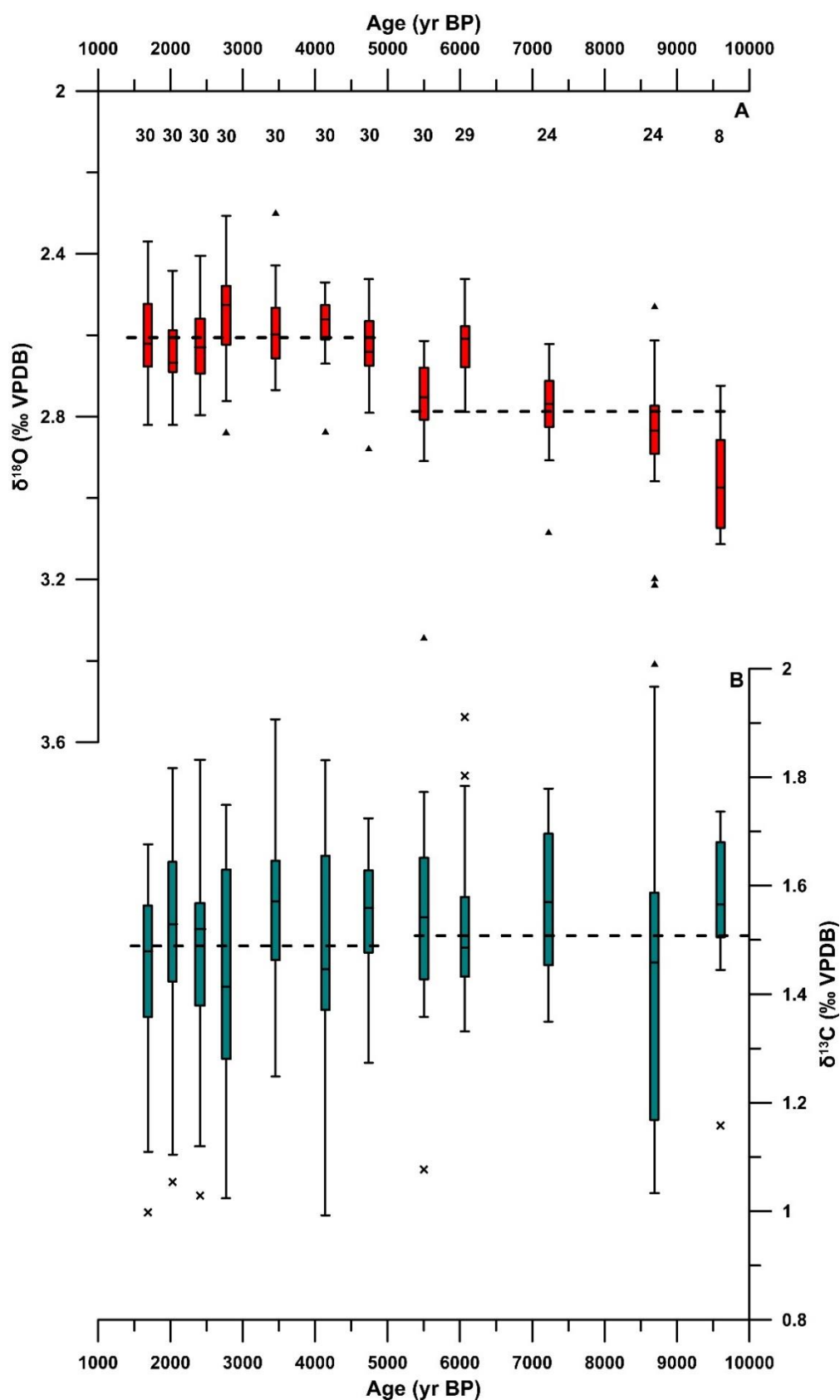


Figure 5.48: Single specimen stable isotope record of *Globorotalia inflata* from sediment core JR244 - GC528 (Falkland Plateau) during the Holocene represented as boxplots. A) $\delta^{18}\text{O}$, triangles represent outliers (data points outside the 1.5xIQR); number of single specimens analysed in each sample highlighted on top. B) $\delta^{13}\text{C}$, crosses represent outliers (data points outside the 1.5xIQR). Dotted lines are inter-sample mean values.

the small sample size. As expected, the variance of the sample with the smallest number of single specimens analysed is twice as large as the samples with 30 single shells analysed (0.2 vs 0.1, Table 5.15). However, some of the other samples' variances (e.g. 5500 yr BP, 0.019) are very similar to the variance of the 9600 yr BP sample (0.02). The largest $\delta^{18}\text{O}$ variance occurs at 8700 yr BP, where the sample included 27 single shell analyses (Table 5.15). This suggests that although the small number of data points in the 9600 yr BP sample is not ideal, it does not mask the overall inter-sample variability recorded in the $\delta^{18}\text{O}$.

The normality of each sample needs to be inspected in order to statistically analyse the changes in the single specimen $\delta^{18}\text{O}$ distribution during the Holocene. A series of Anderson-Darling tests reveal that the 8700 yr BP and 5500 yr BP $\delta^{18}\text{O}$ samples display non-normal distributions (Table 5.15). The large variance and the greater number of outliers identified in the 8700 yr BP sample supports the non-normal distribution and suggests that this sample is statistically different from the rest of the samples. Due to the non-normal distribution of two of the 12 samples, a non-parametric statistical analysis, the Kruskal-Wallis test, was used to investigate the presence/absence of statistically significant difference between the samples. The result ($p = <0.0001$), indicates that at least one sample median is statistically different from the median of at least one other sample, therefore the 12 samples (Table 5.15) do not belong to the same population. A series of pairwise Mann-Whitney U tests highlight the difference between the early and late Holocene samples (Table 5.16). The 9600, 8700 and 7200 yr BP samples are significantly different from every other sample apart from the 5500 yr BP one, while showing consistent relationships with each other and with 5500 yr BP (Table 5.16). The 6100 yr BP sample shows no significant difference in the median from the late Holocene samples of 1700, 2000, 2400, 2800, 3450, 4100 and 4700 yr BP (Table 5.16), while statistically significant difference in the median is identified between 6100 yr BP and the preceding three samples (Table 5.16). Significant difference is also recorded between the 2800 and 2000 yr BP as well as the 4100 and 2000 yr BP samples (Table 5.16).

5.3.2.2 Single specimen carbon isotope record

There is no visually apparent trend in the single specimen sample $\delta^{13}\text{C}$ time series compared to the $\delta^{18}\text{O}$ time series (Figure 5.48). The total inter-sample variability in the sample median $\delta^{13}\text{C}$ values during the Holocene is 0.16‰ (Figure 5.48B) (outside the mass spectrometer's standard error of 0.03‰ associated with the stable isotope analysis), found between the 3450 yr BP (highest median value of +1.57‰) and 2800 yr BP (lowest median value of +1.41‰) samples (Table 5.15). While the $\delta^{18}\text{O}$ time series can be divided into two parts (early and late Holocene), a division cannot be made in the

Table 5.16: Bonferroni corrected p values of pairwise Mann-Whitney U tests conducted on sediment core JR244 - GC528 single specimen *Globorotalia inflata* samples $\delta^{18}\text{O}$ and $\delta^{13}\text{C}$. Highlighted cells indicate statistically significant difference between samples ($p < 0.05$).

| $\delta^{18}\text{O}$ Age | 1700 | 2000 | 2400 | 2800 | 2450 | 4100 | 4700 | 5500 | 6100 | 7200 | 8700 |
|---|-------------|-----------|----------|----------|-----------|-----------|----------|----------|-----------|-------|------|
| 1700 | | | | | | | | | | | |
| 2000 | 1 | | | | | | | | | | |
| 2400 | 1 | 1 | | | | | | | | | |
| 2800 | 1 | 0.047 | 0.908 | | | | | | | | |
| 3450 | 1 | 1 | 1 | 1 | | | | | | | |
| 4100 | 1 | 0.041 | 1 | 1 | 1 | | | | | | |
| 4700 | 1 | 1 | 1 | 0.346 | 1 | 0.444 | | | | | |
| 5500 | 2.58300E-04 | 5.60E-03 | 6.82E-04 | 3.38E-06 | 4.964E-06 | 1.952E-07 | 7.78E-04 | | | | |
| 6100 | 1 | 1 | 1 | 0.414 | 1 | 0.678 | 1 | 7.62E-05 | | | |
| 7200 | 1.77E-04 | 1.464E-03 | 1.36E-04 | 3.97E-06 | 4.43E-06 | 8.92E-07 | 3.28E-04 | 1 | 3.173E-05 | | |
| 8700 | 7.94E-06 | 5.08E-05 | 9.90E-06 | 8.97E-07 | 1.26E-06 | 7.79E-07 | 2.98E-05 | 0.487 | 6.990E-06 | 1 | |
| 9600 | 2.92E-03 | 0.004 | 0.003 | 0.002 | 0.002 | 0.002 | 0.004 | 0.382 | 0.002 | 0.916 | 1 |
| $\delta^{13}\text{C}$ | | | | | | | | | | | |
| 1700 | | | | | | | | | | | |
| 2000 | 1 | | | | | | | | | | |
| 2400 | 1 | 1 | | | | | | | | | |
| 2800 | 1 | 1 | 1 | | | | | | | | |
| 3450 | 0.873 | 1 | 1 | 0.99 | | | | | | | |
| 4100 | 1 | 1 | 1 | 1 | 1 | | | | | | |
| 4700 | 1 | 1 | 1 | 1 | 1 | 1 | | | | | |
| 5500 | 1 | 1 | 1 | 1 | 1 | 1 | 1 | | | | |
| 6100 | 1 | 1 | 1 | 1 | 1 | 1 | 1 | 1 | | | |
| 7200 | 0.975 | 1 | 1 | 0.47 | 1 | 1 | 1 | 1 | 1 | 1 | |
| 8700 | 1 | 1 | 1 | 1 | 0.576 | 1 | 1 | 1 | 1 | 0.774 | |
| 9600 | 1 | 1 | 1 | 1 | 1 | 1 | 1 | 1 | 1 | 1 | 1 |

$\delta^{13}\text{C}$ time series as the sample medians do not change significantly through time (Figure 5.48B). Outliers in $\delta^{13}\text{C}$ are present in six of the 12 samples (Figure 5.48B). Only one sample (6100 yr BP) has more than one outlier; however, the two outliers in this sample do not correspond to the largest variance (Table 5.15). The largest variance (0.062) occurs at 8700 yr BP, while the smallest variance (0.015) belongs to the 4700 yr BP sample (Table 5.15). This total difference of 0.048 between the smallest and largest within-sample variance is larger than that found in the $\delta^{18}\text{O}$ time series as a whole (Section 5.3.1).

The results of the Anderson-Darling normality tests on the combined single specimen samples $\delta^{13}\text{C}$ dataset reveal that the 6100 yr BP and 8700 yr BP $\delta^{13}\text{C}$ samples have a non-normal distribution (Table 5.15) most likely as a result of the large variance (in the case of the 8700 yr BP sample, Table 5.15) and the greater number of outliers (6100 yr BP sample). The ensuing non-parametric Kruskal-Wallis test carried out on the combined single specimen samples $\delta^{13}\text{C}$ dataset revealed that there is significant difference ($p = 0.019$) between the medians of the $\delta^{13}\text{C}$ samples and that the samples do not belong to the same population. Pairwise Mann-Whitney U tests (Table 5.16) did not reveal which sample is significantly different from the others. This outcome suggests that although the samples do not belong to the same population, and hence display significant difference in their medians, the pairwise Mann-Whitney U test is not sensitive enough to detect the exact relationship between the samples. This result highlights the limitation of non-parametric statistical tests, which are known to be less sensitive than parametric tests (Corder and Foreman, 2014)

5.3.3 *Globorotalia inflata* stable isotope variability during the Holocene

The *Globorotalia inflata* single specimen sample $\delta^{18}\text{O}$ time series has an average of $\sim 0.2\text{‰}$ difference in the mean values between samples from 9600-5500 yr BP and 4700-1700 yr BP (Figure 5.48A), which is greater than the standard error of 0.05‰ associated with the analysis. The 9600-5500 yr BP period, here referred to as the Early Holocene (EH), has average *G. inflata* $\delta^{18}\text{O}$ values (between samples) of around $+2.79 \pm 0.13\text{‰}$, while the 4700-1700 yr BP period, here referred to as the Late Holocene (LH), has an average *G. inflata* $\delta^{18}\text{O}$ value of around $+2.6 \pm 0.1\text{‰}$ (between samples). The variance (range) of within-sample $\delta^{18}\text{O}$ values also shows significant difference between the EH and LH. Average EH within-sample variance is 0.018, and the average LH within-sample variance is half that of the EH, at 0.09. These differences in sample $\delta^{18}\text{O}$ averages and within-sample variances suggest different environmental conditions existed between the EH and LH intervals.

Contrary to the single specimen sample $\delta^{18}\text{O}$ time series, the *G. inflata* single specimen sample $\delta^{13}\text{C}$ time series is consistent between the EH and LH (Figure 5.48B). The between-sample average *G. inflata* $\delta^{13}\text{C}$ value is $+1.51 \pm 0.17\text{‰}$ in the EH, and the between-sample average $\delta^{13}\text{C}$ value is only 0.02‰ lower, at $+1.49 \pm 0.17\text{‰}$, in the LH. Additionally, the difference between the EH and LH $\delta^{13}\text{C}$ within-specimen variance is 0.02. Differences are more prominent in the $\delta^{13}\text{C}$ time series when the time period 4100-1700 yr BP is compared with 9600-8600 yr BP and 7200-4700 yr BP. When the time-series is grouped into these three time-slices a 0.06‰ difference exists between the average $\delta^{13}\text{C}$ values between 7200-4700 yr BP and 4100-1700 yr BP and a 0.08‰ difference in average $\delta^{13}\text{C}$ exists between the 9600-8700 yr BP and 7200-4700 yr periods. These differences are within the standard error associated with the mean values of the three time period (0.21‰ , 0.14‰ , and 0.18‰ for the 9600-8700 yr BP, 7200-4700 yr BP, and 4100-1700 yr BP period respectively). Similarly, the within-sample variance also displays greater offsets than the difference between the EH and LH variances when the record is divided into these three time-slices, with 0.013 (between 7200-4700 yr BP and 4100-1700 yr BP) and 0.027 (9600-8700 yr BP and 7200-4700 yr BP) difference recorded between the average within-sample variances.

The different trends in *Globorotalia inflata* $\delta^{18}\text{O}$ and $\delta^{13}\text{C}$ suggest that the two records are driven by different processes that acted at different times through the Holocene. Additionally, the statistically significant differences identified between the single specimen samples in both the $\delta^{18}\text{O}$ and $\delta^{13}\text{C}$ time series (Section 5.3.2.1, 5.3.2.2) indicate that environmental conditions changed throughout the Holocene. The following section discusses the potential environmental processes responsible for the isotope variability, and how the single specimen *G. inflata* stable isotope time series compares with existing Southern Ocean Holocene records of air temperatures, wind strength, Antarctic Intermediate Water strength, and glacial meltwater discharge.

5.3.4 *Globorotalia inflata* as an Antarctic Intermediate Water proxy species

Globorotalia inflata is a deep-dwelling planktonic foraminifera (Bé, 1969) that mainly calcifies in the thermocline during austral spring (Bé, 1969; King and Howard, 2005; Wilke et al., 2006). A large-scale study of South Atlantic thermocline temperatures based on *G. inflata* identified the calcification depth of this species to be between 350-400 m (Groeneveld and Chiessi, 2011). Specimens recovered from the northern part of the Falkland Plateau (48.91°S 57.88°W , north of Falkland Islands) were shown to have calcified at 368 m water depth and at 3.88°C water temperature (Groeneveld and

Chiessi, 2011). This assessment puts *G. inflata* calcification within intermediate water masses (Figure 5.49), specifically, within Antarctic Intermediate Water.

To constrain the approximate calcification depth of *Globorotalia inflata* in sediment core JR244 - GC528, and to determine any apparent vital effects in the oxygen isotope record, the equilibrium $\delta^{18}\text{O}$ ($\delta^{18}\text{O}_{\text{eq}}$) values were calculated. Previous studies of *G. inflata* identified calcification more or less in equilibrium, with a large variability ($\pm 0.4\text{‰}$) (Niebler et al., 1999, Wilke et al., 2006). Due to this variability, it is recommended that vital effects are investigated at each location.

Monthly temperature and salinity data for the sediment core location were obtained from World Ocean Atlas 13 (WOA13, Locarnini et al., 2013; and Zweng et al., 2013; <http://doi.org/10.7289/V5NZ85MT>). Seawater $\delta^{18}\text{O}$ ($\delta^{18}\text{O}_{\text{sw}}$) was estimated assuming a linear relationship (Eq. 1) between salinity (S) and $\delta^{18}\text{O}_{\text{sw}}$ based on regional $\delta^{18}\text{O}_{\text{sw}}$ data covering the area between 55.07°S 58.29°W and 56.13°S 57.67°W, obtained from the Global Seawater Oxygen-18 Database (Schmidt et al., 1999; <https://data.giss.nasa.gov/o18data/>). The area (between 53.13°S 53.38°W and 53.13°S 56.38°W) selected for salinity values from the WOA13 (Zweng et al., 2013) experiences a small, 0.26 PSU, seasonal variability. The relationship between salinity and $\delta^{18}\text{O}_{\text{sw}}$ is linear in the open ocean (Meredith et al., 1999), therefore it is reasonable to enlist only one set of equations to calculate $\delta^{18}\text{O}_{\text{sw}}$ (Eq. 12), as opposed to the two utilised in Chapter 5.2:

$$\delta^{18}\text{O}_{\text{sw}} = 0.1698 \times S - 5.9533 \quad \text{Equation 12.}$$

The calculated $\delta^{18}\text{O}_{\text{sw}}$ values were converted to the Pee Dee Belemnite (PDB) scale following Bemis et al. (1998) (Eq. 13),

$$\delta^{18}\text{O}_{\text{sw(PDB)}} = 0.9998 \times \delta^{18}\text{O}_{\text{SMOW}} - 0.2 \quad \text{Equation 13.}$$

where $\delta^{18}\text{O}_{\text{smow}}$ is the calculated $\delta^{18}\text{O}_{\text{sw}}$ value (Eq. 12) expressed on the Standard Mean Ocean Water (SMOW) scale. The $\delta^{18}\text{O}_{\text{eq}}$ values were calculated following Kim and O'Neil (1997) and Peeters et al. (2002) temperature and $\delta^{18}\text{O}$ relationship (Eq. 14):

$$\delta^{18}\text{O}_{\text{eq}} = 25.778 - 3.333 \times (43.704 + T)^{0.5} + \delta^{18}\text{O}_{\text{sw(PDB)}} \quad \text{Equation 14}$$

where T is the seawater temperature and $\delta^{18}\text{O}_{\text{sw(PDB)}}$ is the calculated $\delta^{18}\text{O}_{\text{sw}}$ value (Eq. 13) expressed with respect to the PDB scale.

The $\delta^{18}\text{O}_{\text{eq}}$ profile (Figure 5.50) of the austral spring months (September, October and November) shows steadily increasing $\delta^{18}\text{O}$ values with depth. Surface water (0-100 m) values are lowest in November due to increasing SST. $\delta^{18}\text{O}_{\text{eq}}$ values vary between

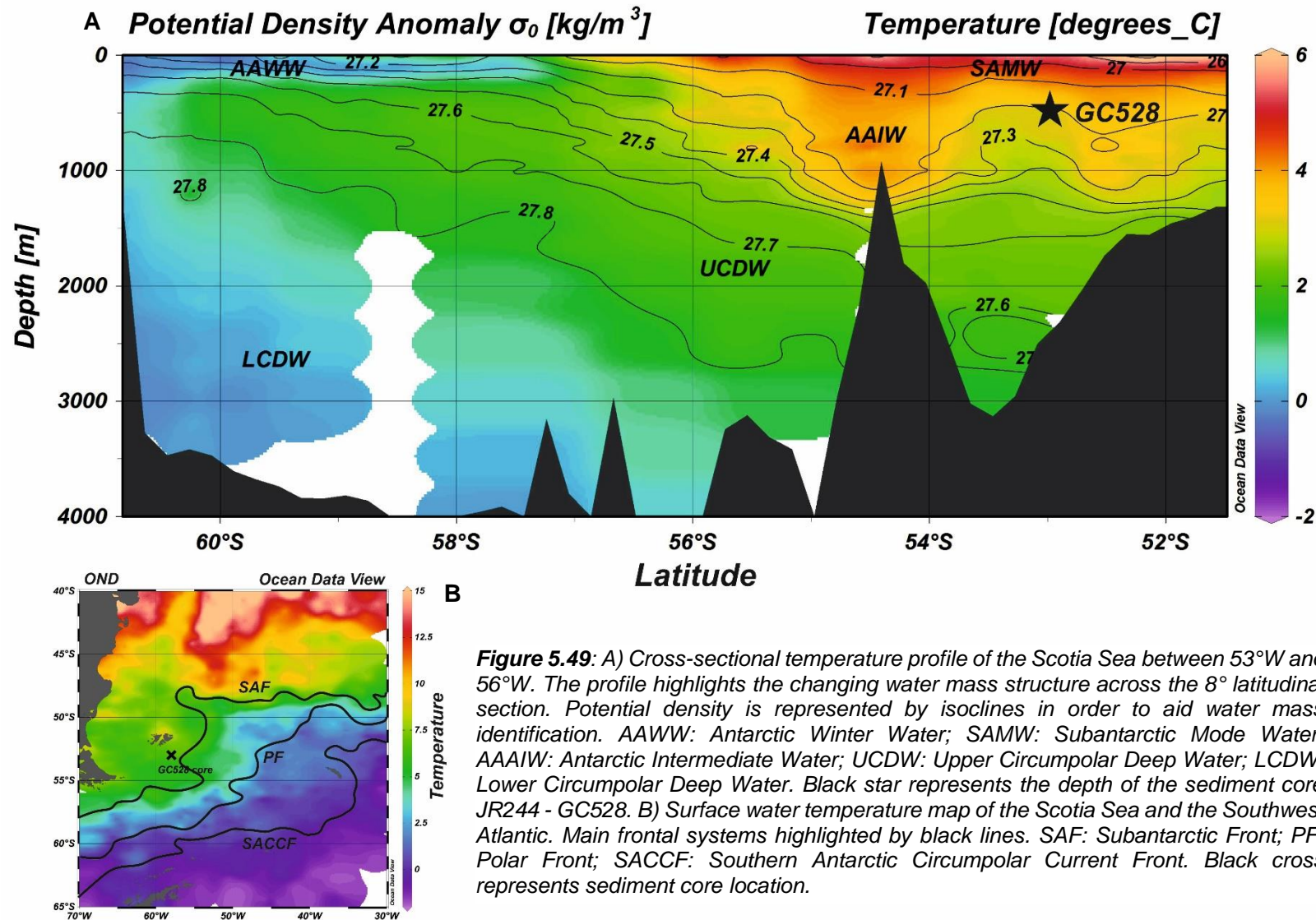


Figure 5.49: A) Cross-sectional temperature profile of the Scotia Sea between 53°W and 56°W. The profile highlights the changing water mass structure across the 8° latitudinal section. Potential density is represented by isoclines in order to aid water mass identification. AAWW: Antarctic Winter Water; SAMW: Subantarctic Mode Water; AAIW: Antarctic Intermediate Water; UCDW: Upper Circumpolar Deep Water; LCDW: Lower Circumpolar Deep Water. Black star represents the depth of the sediment core JR244 - GC528. B) Surface water temperature map of the Scotia Sea and the Southwest Atlantic. Main frontal systems highlighted by black lines. SAF: Subantarctic Front; PF: Polar Front; SACCF: Southern Antarctic Circumpolar Current Front. Black cross represents sediment core location.

+2.29‰ and +2.67‰ in the spring months between 300 and 400 m water depths (Figure 5.50). Highest $\delta^{18}\text{O}_{\text{eq}}$ values within this depth interval are found in October, increasing from +2.61‰ at 300 m to +2.67‰ at 400 m (Figure 5.50). As the $\delta^{18}\text{O}_{\text{eq}}$ values are based on temperature and salinity values from the WOA13 (which reflect average climatologies between 1955 and 2005) we can only make reasonable assumptions on *Globorotalia inflata* calcification for the late Holocene (4700-1700 yr BP), when water temperatures and salinities closely resembled those found today.

Late Holocene *Globorotalia inflata* single specimen $\delta^{18}\text{O}$ values vary approximately between +2.4‰ and +2.8‰ (Figure 5.48A), with an average of around +2.6‰. Deep-dwelling planktonic foraminifera species, like *G. inflata*, calcify more or less in equilibrium with the surrounding seawater, but with a significant standard deviation ($\pm 0.4\text{‰}$) (Fairbanks et al., 1982; Niebler et al., 1999; Wilke et al., 2006). Previous studies of *G.*

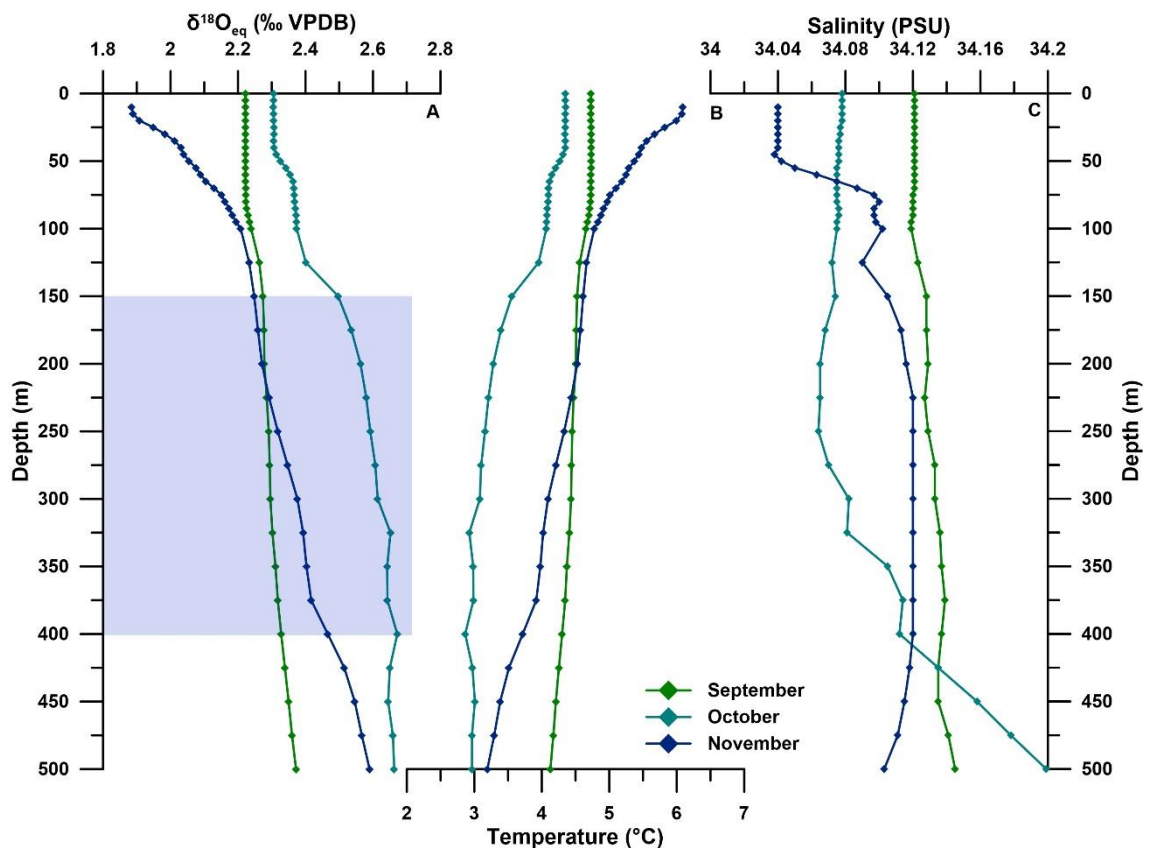


Figure 5.50: A) Equilibrium $\delta^{18}\text{O}$, B) Temperature and C) Salinity at the location of sediment core JR244 - GC528. $\delta^{18}\text{O}_{\text{eq}}$ values for September (green), October (light blue) and November (dark blue) between the surface and 500 m water depth show the most likely calcification depth of between 150 and 400 m water depth for *Globorotalia inflata*. Surface values in November are highly skewed by the introduction of low salinity waters while temperature and salinity values for September show the lack of vertical stratification during that month. Published *G. inflata* $\delta^{18}\text{O}$ values (with $\pm 0.4\text{‰}$ standard deviation; Niebler et al., 1999) fall on the $\delta^{18}\text{O}_{\text{eq}}$ values corresponding to October supporting previous suggestions of spring-time calcification (King and Howard, 2005). $\delta^{18}\text{O}_{\text{eq}}$ are based on $\delta^{18}\text{O}$ -salinity relationship drawn from regional $\delta^{18}\text{O}_{\text{sw}}$ values from the Global Seawater Oxygen-18 database (Schmidt et al., 1999) and salinity and temperature values from WOA 13 (Loncarnini et al., 2013; Zweng et al., 2013).

inflata placed its main calcification depth within the thermocline, however, calcification does continue as the organism descends to deeper depths (Fairbanks et al., 1982; Wilke et al., 2006). Based on the continuous calcification below the thermocline (Fairbanks et al., 1982) and the $\delta^{18}\text{O}_{\text{eq}}$ profile (Figure 5.50) we can place the LH *G. inflata* main calcification depth between 150 m and 400 m, with calcification taking place mostly in October. The timing and the depth of calcification agrees well with plankton tow (Mortyn and Charles, 2003) and core top records from the South Atlantic (Chiessi et al., 2007; Groeneveld and Chiessi, 2011). By comparing the identified calcification depth range (150-400 m) with the WOA13 temperature and salinity data (Figure 5.49 and 5.50B, C) it can be confirmed that *G. inflata* calcification takes place within the AAIW, which makes the species suitable for the investigation of AAIW variability.

5.3.5 Does *Globorotalia inflata* stable isotope variability reflect changes in local or regional environmental conditions?

The region of the Falkland Plateau, between 52°19'S and 53°21'S (Figure 5.51), is characterised by the transition from a coastal environment dominated by Shelf Water to an open ocean environment dominated by Transition Zone Water (TZW) (Sirota and Sundakov, 2014). The TZW separates coastal Shelf Waters from AAIW carried by the Falkland Current onto the Plateau (Figure 5.51). Long-term oceanography records from the southern parts of the Falklands Plateau, spanning the time period between 2002 and 2014, reveal that seasonal temperature and salinity variability within the TZW penetrate only to 130-140 m water depth, and warm temperature anomalies in the shelf region are also restricted to this depth (Sirota and Sundakov, 2014). In contrast, negative temperature anomalies of ~0.4°C were recorded within the whole depth transect (surface to >330 m) in 2002 and 2010 (Sirota and Sundakov, 2014). The sediment core location (53°S 58°W) is under the influence of TZW at the surface (0 to ~200 m, Figure 5.51) and of the AAIW in the deeper layers (below 200 m) (Arkhipkin et al., 2004). The modern oceanographic record of Sirota and Sundakov (2014) supports the findings that *G. inflata* calcification takes place within AAIW. Seasonal temperature and salinity variability is and Sundakov, 2014), hence it is reasonable to suggest that the *G. inflata* (calcifying restricted to the top 130-140 m, and seasonal variability below 140 m is negligible (Sirota below 150 m) stable isotope record does not reflect local seasonal surface or deeper water variability. This suggestion is also supported by the fact that *G. inflata* predominantly reproduces during the austral spring (e.g. King and Howards, 2005). Core JR244 - GC528 has an average sedimentation rate of 6.9 cm/kyr during the Holocene (Roberts, 2016), meaning that on average a 1 cm stratigraphic thickness contains ~145

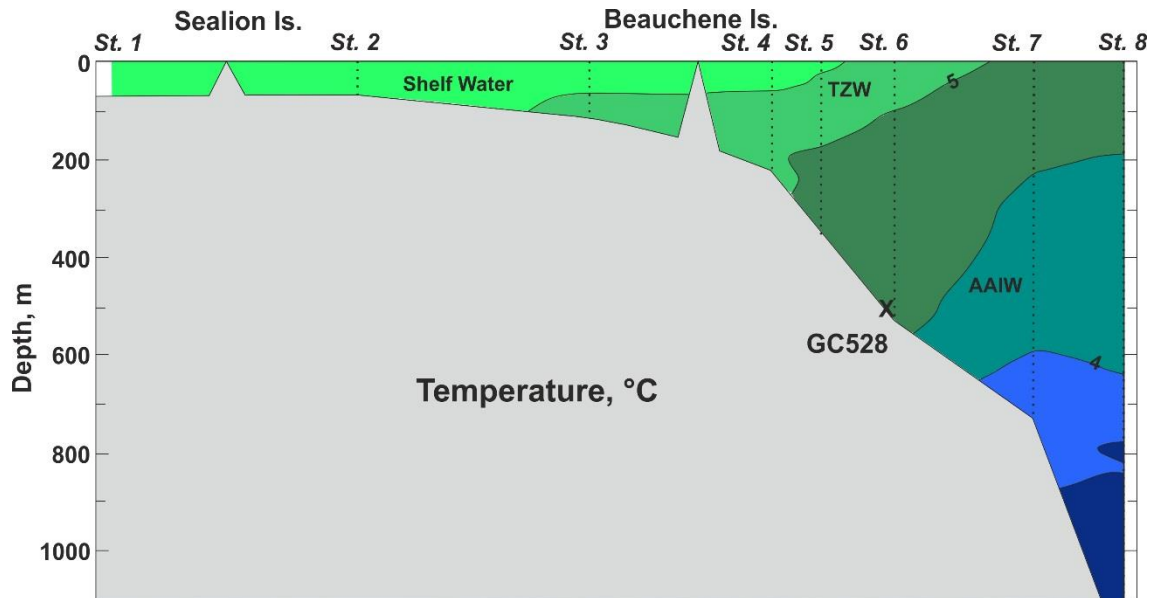


Figure 5.51: October temperature depth profile of Falkland Plateau between 52°19'S and 53°21'S (Sirota and Sundakov, 2014). Sediment core location is located between St.5 and St.6 which is bathed in AAIW at depths below 200 m.

years of sediment and thus preserved foraminifera, hence, it is unlikely that intra-annual variability will be preserved.

The stable isotope record might reflect local interannual variability, however, the ~0.4°C temperature anomaly (equal to <math><0.1\text{‰}</math> change in G. inflata calcification depths. The *G. inflata* G. inflata calcification depths (Sirota and Sundakov, 2014). Hence, it can be considered that at this location the *G. inflata*

Holocene paleoclimate records from the Southeast Pacific and South Atlantic (e.g. Holmgren and Bjorck, 2013; Lamy et al., 2011; Varma et al., 2011) show a steady decline in oceanic and atmospheric temperatures between 9000 yr BP and present day in response to declining solar insolation levels. In contrast, benthic foraminiferal

been steady since 7,500 yr BP, and increased between ~10,000 yr BP and 7,500 yr BP (Roberts et al., 2016). Constant intermediate water temperature at calcification depth would have resulted in steady *G. inflata* $\delta^{18}\text{O}$. The increasing intermediate water temperature between ~10,000 yr BP and 7,500 yr BP would be reflected as a decrease in *G. inflata* $\delta^{18}\text{O}$ at this time. Therefore, it can be considered, that the decreasing *G. inflata* $\delta^{18}\text{O}$ between 9,600 yr BP and 7,200 yr BP are the result of the warming AAIW after the deglaciation. However, as AAIW temperature remained steady since 7,500 yr BP (Roberts et al., 2016), another driver needs to be considered for the decreasing *G. inflata* $\delta^{18}\text{O}$ from 7,200 yr BP to 4,700 yr BP (Figure 5.48A).

If the temperature decline observed elsewhere in the South Atlantic (Holmgren and Bjorck, 2013) was reflected in the *G. inflata* $\delta^{18}\text{O}$ data, we could expect steadily increasing $\delta^{18}\text{O}$ values. However, the *G. inflata* $\delta^{18}\text{O}$ values decrease between the EH and the LH (Figure 5.48A), therefore we can discount temperature as the main force behind the *G. inflata* $\delta^{18}\text{O}$ trend past 7,500 yr BP. The two main drivers of foraminiferal $\delta^{18}\text{O}$ are the temperature of the seawater and the $\delta^{18}\text{O}_{\text{sw}}$ (Ravelo and Hillaire-Marcel, 2007). Therefore, as *G. inflata* $\delta^{18}\text{O}$ do not seem to respond to the observed temperature change by Holmgren and Bjorck (2013), it can be considered that the *G. inflata* $\delta^{18}\text{O}$ is impacted by changes in $\delta^{18}\text{O}_{\text{sw}}$, primarily, by changes in AAIW $\delta^{18}\text{O}_{\text{sw}}$ in response to variability of source waters with different $\delta^{18}\text{O}_{\text{sw}}$ signature.

5.3.6 Temperature- and size-dependency in single specimen *Globorotalia inflata* $\delta^{18}\text{O}$ measurements

Depth-integrated plankton tow records (Wilke et al., 2006) from the eastern South Atlantic show that *Globorotalia inflata* $\delta^{18}\text{O}$ increase with depth following the decreasing trend in temperature, however, there is also a 0.3‰ offset in $\delta^{18}\text{O}$ between smaller (150-250 μm) and larger (250-355 μm) size fractions showing higher $\delta^{18}\text{O}$ in larger specimens (Figure 5.52). These plankton tow findings suggest continued shell growth and calcification with increasing depth mostly controlled by local hydrography, as opposed to a limited and restricted calcification depth. A similar temperature- $\delta^{18}\text{O}$ relationship was identified in a number of other studies (e.g. Ganssen and Kroon, 2000; King and Howard, 2005; Chiessi et al., 2007), as was the size- $\delta^{18}\text{O}$ relationship (e.g. Lončarić et al., 2006; Metcalfe et al., 2015) which supports the existence of size- and temperature-related isotope variability in *G. inflata*.

Due to limited abundance, *Globorotalia inflata* specimens were not separated into specific size fractions and, hence, size-related isotope variability cannot be discounted from the stable isotope data. Tentative assumptions on the scale of the impact of size on

JR244 - GC528 *G. inflata* $\delta^{18}\text{O}$ can be made using visual observation. Specimens from the EH period (particularly prior to 6100 yr BP) were less abundant and generally smaller than specimens from LH samples. Based on the size- $\delta^{18}\text{O}$ relationship it would be expected that smaller shells would provide lower $\delta^{18}\text{O}$ values, however, the GC528 *G. inflata* $\delta^{18}\text{O}$ results show higher average $\delta^{18}\text{O}$ values in the EH and lower average values in the LH (Figure 5.53A), which suggest that there is no size-dependency in the *G. inflata* $\delta^{18}\text{O}$ record. Additionally, AAIW temperature has remained relatively stable since ~7,500 yr BP at this location (Roberts et al., 2016), which suggests that variability in *G. inflata* $\delta^{18}\text{O}$ is not

In contrast to the long-term Holocene record, the average within-sample $\delta^{18}\text{O}$ variability (which indicates interannual variability during the sampling period: ~145 years/cm) could be impacted by both the temperature- and size-dependence of *Globorotalia inflata* $\delta^{18}\text{O}$. These impacts are particularly relevant in the EH samples where large size-variability could not be avoided due to low *G. inflata* abundance in the sediments.

It could be hypothesised that the greater within-sample variance of the EH samples at 9600, 8700 and 5500 yr BP (Figure 5.46B) is the result of greater decadal variability during the ~145 year sedimentation period represented by one sample. ENSO intensity was close to modern levels during the EH (Carré et al., 2014) which would have

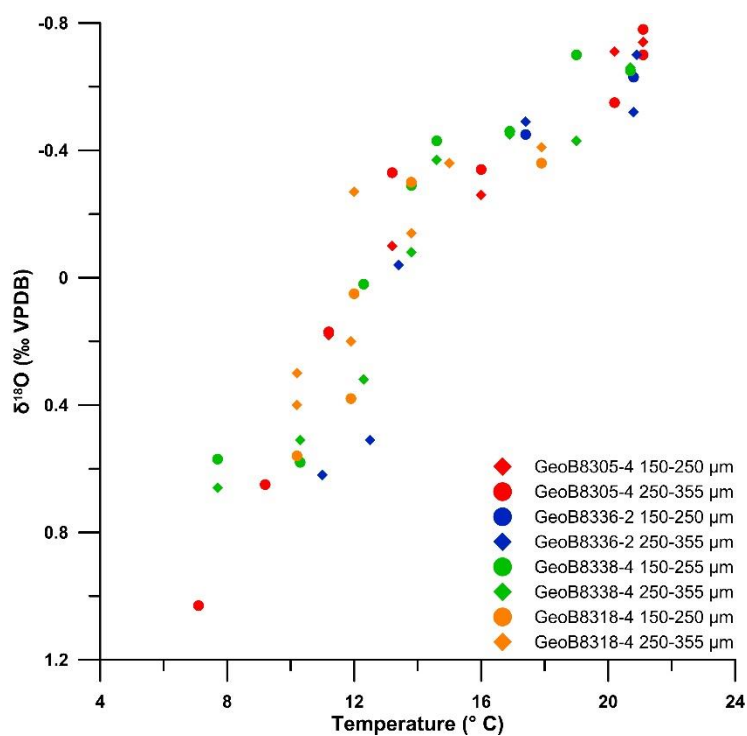


Figure 5.52: *Globorotalia inflata* $\delta^{18}\text{O}$ and seawater temperature relationship at four locations in the South Atlantic (Wilke et al., 2006) shows the linear trend of increasing $\delta^{18}\text{O}$ with decreasing temperature (increasing depth). Specimens are separated by size groups (150-250 μm : diamonds, 250-355 μm : circles) highlighting the biological impact of shell size on $\delta^{18}\text{O}$ values: larger shell size results in higher shell $\delta^{18}\text{O}$.

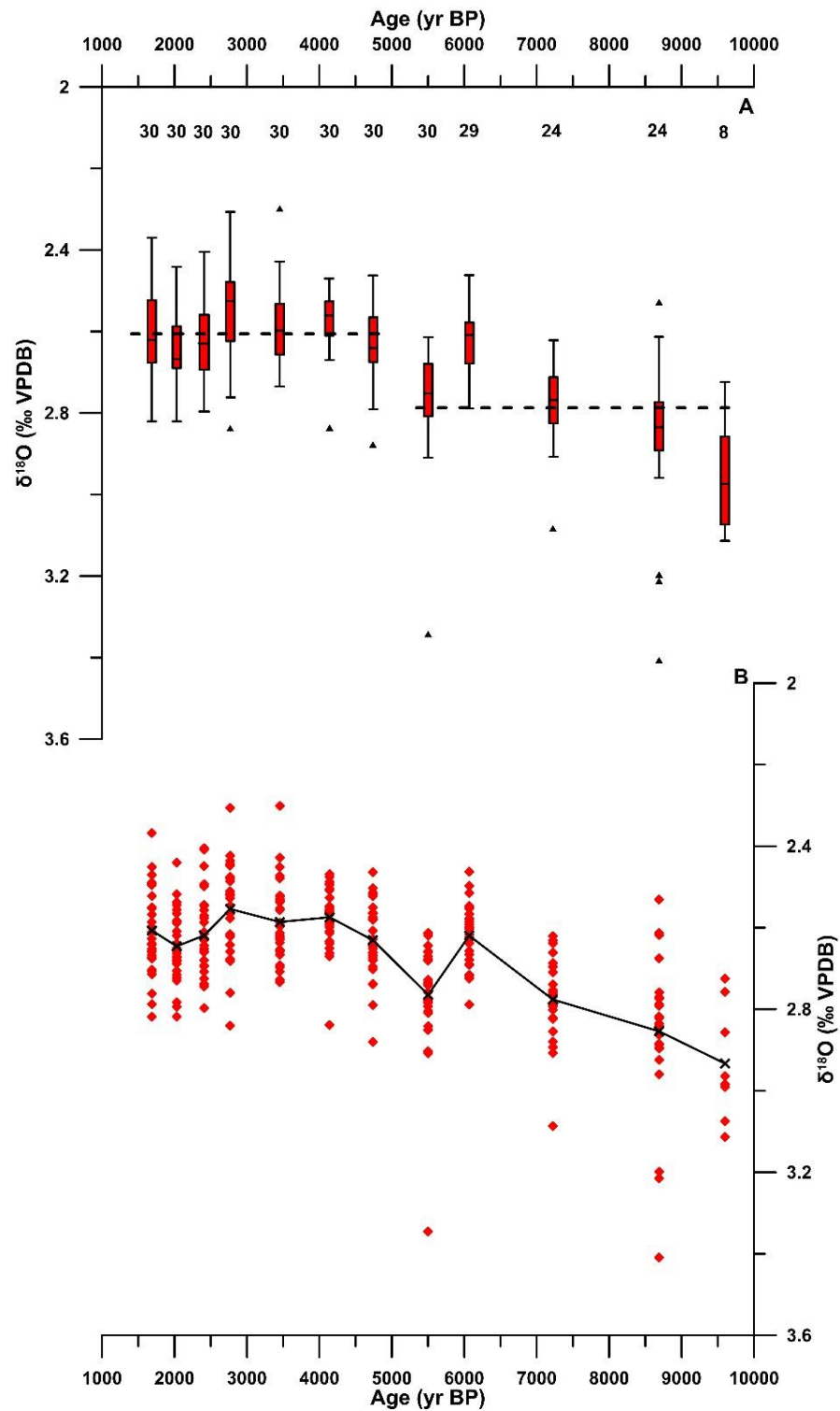


Figure 5.53: Core JR244 - GC528 (Falkland Plateau) A) Single specimen *Globorotalia inflata* $\delta^{18}\text{O}$ represented as box-whisker plots. Dashed lines: average mean values of 9600-5500 yr BP (early Holocene) and 4700-1700yr BP (late Holocene) intervals. Triangles: outliers as identified in Figure 5.48. B) Raw single specimen *G. inflata* $\delta^{18}\text{O}$ record. Black crosses: mean values, solid black line: mean trend.

increased short-term climate variability. The increased presence of outliers in the 8700yr BP sample (4 out of 24 data points, Figure 5.53A) supports the possibility of greater decadal variability during the EH. The 5500 yr BP sample contains an outlier (+3.35‰) which is ~0.7‰ higher than the second highest measurement (Figure 5.53B) which is most likely responsible for the higher variance. The 9600 yr BP sample had low sample size (8 specimens) hence its variance most likely reflects this, as opposed to larger decadal variability. A record of water column stratification and density gradient inferred from a deep-water core in the South Atlantic identified a breakdown of salinity-driven stratification after 10,000 yr BP, and a weaker density gradient sustained by differences in temperature between the deep and intermediate waters (Roberts et al., 2016). Decreasing deep-water salinity values after between 11,000 yr BP and ~9,000 yr BP drove the breakdown of stratification, as salinity at intermediate depth at core JR244 - GC528 remained steady (Roberts et al., 2016). As the JR244 – GC528 core site is situated on the Falkland Plateau and is not bathed in deep waters, such as North Atlantic Deep Water or Antarctic Bottom Water, the changes in stratification across the South Atlantic during the EH (Roberts et al., 2016) would not have impacted the *G. inflata* $\delta^{18}\text{O}$ record. Without higher resolution sediment records and increased within-sample specimen numbers, it is not possible to interpret the single specimen record any further. In conclusion, the temperature- and size-dependence of *Globorotalia inflata* means that the small (~0.48‰) average within-sample range across the Holocene is most likely the result of different calcification patterns between individual specimens. This is in agreement with the $\pm 0.4\%$ oxygen isotope disequilibrium (vital effect) identified in the *G. inflata* species, which is linked to physiological and ecological effects (Niebler et al., 1999).

5.3.7 The role of biological and chemical processes on *Globorotalia inflata* $\delta^{13}\text{C}$

Culture studies have shown that foraminiferal $\delta^{13}\text{C}$ is directly related to $\delta^{13}\text{C}_{\text{DIC}}$ (Spero, 1992). $\delta^{13}\text{C}_{\text{DIC}}$ is higher in the surface water due to the preferential uptake of ^{12}C during primary production, while it is lower at depth where organic matter is remineralised (Broecker and Peng, 1982). As a result, foraminiferal $\delta^{13}\text{C}$ is expected to decrease with depth, with the decreasing $\delta^{13}\text{C}_{\text{DIC}}$. The concentration of CO_3^{2-} ($[\text{CO}_3^{2-}]$) in the seawater also affects the $\delta^{13}\text{C}$ of foraminiferal calcite (Spero et al., 1997), where an increase in seawater $[\text{CO}_3^{2-}]$ results in decreased foraminiferal $\delta^{13}\text{C}$. $[\text{CO}_3^{2-}]$ is higher in surface waters than at intermediate depth in the South Atlantic (Wilke et al., 2006) and thus it is expected that foraminiferal $\delta^{13}\text{C}$ increases with depth within the water column. $\delta^{13}\text{C}_{\text{DIC}}$

and $[\text{CO}_3^{2-}]$ act in opposite direction on the foraminiferal $\delta^{13}\text{C}$ complicating the interpretation of planktonic foraminiferal $\delta^{13}\text{C}$. *Globorotalia inflata* secretes its shell continuously through the water column (Lončarić et al., 2006; Wilke et al., 2006) therefore the total shell $\delta^{13}\text{C}$ is influenced by a range of $\delta^{13}\text{C}_{\text{DIC}}$ and $[\text{CO}_3^{2-}]$ values across its depth range. This continuous calcification across water depths means that specimens which calcify in shallower depths (smaller shells) have different $\delta^{13}\text{C}$ than those that reach deeper depths during calcification (larger specimens).

Coupled with the impact of different $\delta^{13}\text{C}_{\text{DIC}}$ and $[\text{CO}_3^{2-}]$ at different depths is the impact of biological and kinetic fractionation on the $\delta^{13}\text{C}$ of smaller and larger specimens. Foraminifera calcify and, thus, respire faster during the early stages of their life cycle which results in lower $\delta^{13}\text{C}$ values in smaller and younger shells (Hemleben et al., 1989). This well-established size-dependence of foraminiferal $\delta^{13}\text{C}$ has been found in *G. inflata* (Figure 5.54) (e.g. Wefer and Berger, 1991; Elderfield et al., 2002; Wilke et al., 2006; Metcalfe et al., 2015) which – together with the impact of $\delta^{13}\text{C}_{\text{DIC}}$ and $[\text{CO}_3^{2-}]$ on foraminiferal $\delta^{13}\text{C}$ – can potentially explain the lack of long-term variability in the single specimen *G. inflata* $\delta^{13}\text{C}$ time series from core JR244 - GC528 (Table 5.15, Figure 5.48B). *G. inflata* analyses could not be limited to specific size fractions (due to low

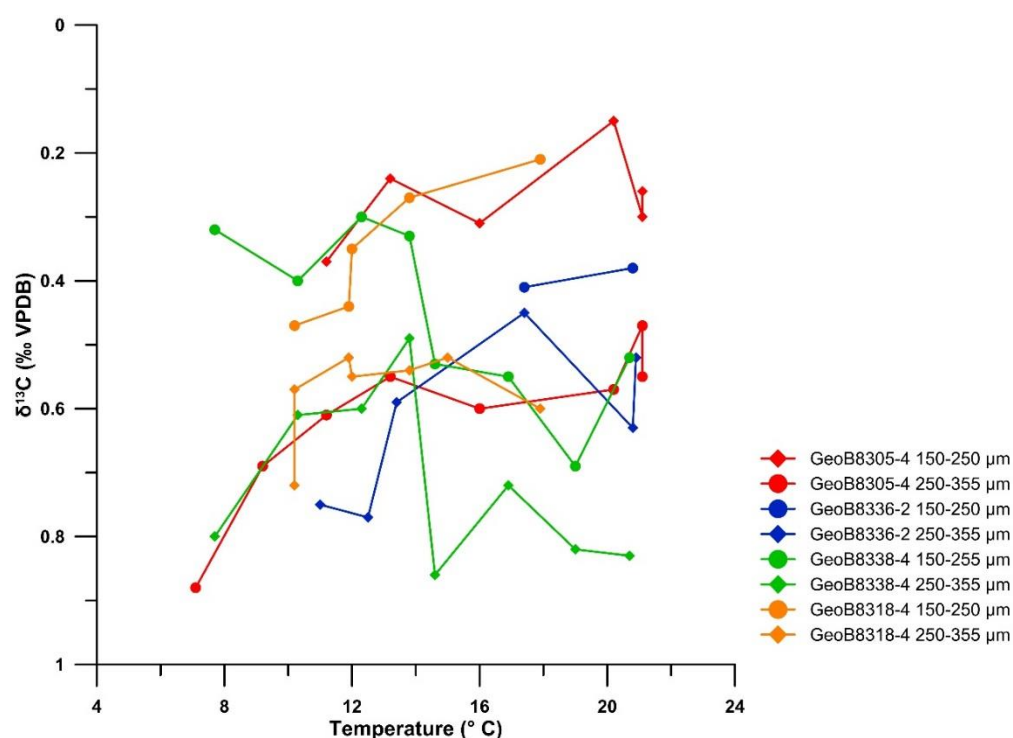


Figure 5.54: *Globorotalia inflata* $\delta^{13}\text{C}$ vs Temperature in the South Atlantic (Wilke et al., 2006) shows the consistent offset in $\delta^{13}\text{C}$ between small (150-250 μm) and large (250-355 μm) specimens. The relationship between sizes highlights the danger in mixing size fractions during analysis. The size-dependency is not constrained to surface waters (high temperatures) but is also a feature at depth (lower temperatures).

abundance) so it is possible that some of the within-sample range observed in the single specimen $\delta^{13}\text{C}$ is also due to the size-dependence of $\delta^{13}\text{C}$. Local changes in $\delta^{13}\text{C}_{\text{DIC}}$ due to changes in primary production and upwelling/advection of waters with different $\delta^{13}\text{C}$ (Ravelo and Hillaire-Marcel, 2007) can also be a factor behind the variability in the within-sample range (Figure 5.48B: minimum of 0.43‰ of the 7200 yr BP sample versus the 0.93‰ of the 8700 yr BP sample and an average within-sample range of 0.68‰) observed in the single specimen sample *G. inflata* $\delta^{13}\text{C}$ time series. Without direct observations of the $\delta^{13}\text{C}_{\text{DIC}}$ and $[\text{CO}_3^{2-}]$ of the water masses that the *G. inflata* calcified in during its life cycle it is not possible to draw further robust interpretations from the *G. inflata* $\delta^{13}\text{C}$ time series.

5.3.8 A changing regime of Antarctic Intermediate Water sources during the Holocene

One of the primary features of Holocene Southern Ocean climate is the gradual cooling of the atmosphere from the Early Holocene Climate Optimum (~11,000-9500 yr BP) to the present (Figure 5.55B; Masson et al., 2000; Bentley et al., 2009) as a direct response to decreasing high latitude winter-spring solar insolation (Figure 5.55A; Renssen et al., 2005). Decreasing air temperatures transferred down to both surface and intermediate waters and, as a result, intermediate water temperature in the Pacific Ocean was ~1.5°C warmer during the middle Holocene Thermal Maximum (8000-6000 yr BP) than in the 21st Century (Rosenthal et al., 2013).

The temperature and $\delta^{18}\text{O}$ of seawater are the two main determining factors of foraminiferal $\delta^{18}\text{O}$ (Ravelo and Hillaire-Marcel, 2007). Increasing seawater temperature decreases the $\delta^{18}\text{O}_{\text{foram}}$ at a rate of -0.22‰/1°C (Epstein et al., 1953). The JR244 - GC528 *Globorotalia inflata* single specimen sample stable isotope record shows decreasing values (Figure 5.48A) from 9600 yr BP (2.93‰ mean value) to 2700 yr BP (2.55‰ mean value). This is concurrent with decreasing intermediate water temperatures in the Pacific Ocean (Rosenthal et al., 2013) and steady AAIW temperature at the *G. inflata* $\delta^{18}\text{O}$ core site since ~7,500 yr BP following a period of steady increase since the Last Glacial Maximum as inferred from benthic foraminiferal $\delta^{18}\text{O}$ (Roberts et al., 2016). The period of increasing AAIW temperature until ~7,500 yr BP could explain the decreasing *G. inflata* $\delta^{18}\text{O}$ values from 9,600 yr BP to 7,200 yr BP. However, *G. inflata* $\delta^{18}\text{O}$ continued to decrease until 4,100-4,600 yr BP, when the benthic foraminiferal $\delta^{18}\text{O}$ record indicate steady AAIW temperatures (Roberts et al., 2016) suggesting a response to changes in $\delta^{18}\text{O}$ of AAIW. The $\delta^{18}\text{O}$ of AAIW in the Scotia Sea is mainly driven by the balance in the contribution of different source waters, namely the

Subantarctic Mode Water (SAMW) and Antarctic Winter Water (AAWW) (Garabato et al., 2009), which have widely different temperatures, salinities and hence $\delta^{18}\text{O}$ signatures (Meredith et al., 1999).

The SAMW portion of AAIW derives from the South Pacific (Hanawa and Talley, 2001) and is formed through the deep convection of the thick winter mixed layers in the southeast Pacific on the northern side of the ACC (Garabato et al., 2009). Part of the SAMW is advected south and east from its formation area flowing through the Drake Passage and, as it does, it cools (from $>10^{\circ}\text{C}$ to $4\text{-}5^{\circ}\text{C}$) and becomes denser forming one part of the AAIW (Meredith et al., 1999). The $\delta^{18}\text{O}$ of the SAMW portion of the AAIW (-0.15‰ , Table 5.17) will therefore reflect the formation region (midlatitude regions off southeast Chile) and the modification the water mass has experienced by the time it reached the Scotia Sea (Hanawa and Talley, 2001).

In contrast to the mid latitude-derived SAMW, AAWW contributes very cold ($<1.5^{\circ}\text{C}$, and can reach -1°C south of the Polar Front, Table 5.17) and fresh (~ 33.9 PSU) water to AAIW (Meredith et al., 1999). AAWW forms by the seasonal warming of the surface waters of the along the Antarctic Peninsula and its properties are mostly determined by the contribution of precipitation and glacial meltwater (Meredith et al., 1999; Meredith et al., 2013). As both precipitation and glacial meltwater have isotopic signatures that are much lower than average seawater, increased concentration of either of these meteoric inputs can dramatically alter the $\delta^{18}\text{O}$ of AAWW. AAWW is subducted along isopycnals as it is advected northwards (Garabato et al., 2009), eventually reaching intermediate water depth levels between the PF and the SAF where it freshens AAIW through isopycnal mixing (Meredith et al., 1999). Although no $\delta^{18}\text{O}$ values have been determined for the AAWW core contribution at the SAF, a sharp decrease in $\delta^{18}\text{O}$ of AAIW due to the addition of AAWW (decreasing from -0.22‰ to -0.27‰) has been observed by Meredith et al. (1999) highlighting the potential of AAWW to alter AAIW $\delta^{18}\text{O}$.

Based on the hypothesis that the JR244 - GC528 core-derived *Globorotalia inflata* $\delta^{18}\text{O}$ (Figure 5.48A) reflects AAIW $\delta^{18}\text{O}$ and on the observations of SAMW and AAIW/AAWW

Table 5.17: Temperature (*T*), salinity (*S*) and $\delta^{18}\text{O}$ properties of Antarctic Intermediate Water (AAIW), Subantarctic Mode Water (SAMW) and Antarctic Winter Water (AAWW) in the Scotia Sea (Talley, 1996; Meredith et al., 1999; Garabato et al., 2003; Meredith et al., 2010). The impact of additional volume of SAMW and AAWW on AAIW properties is highlighted in the last column.

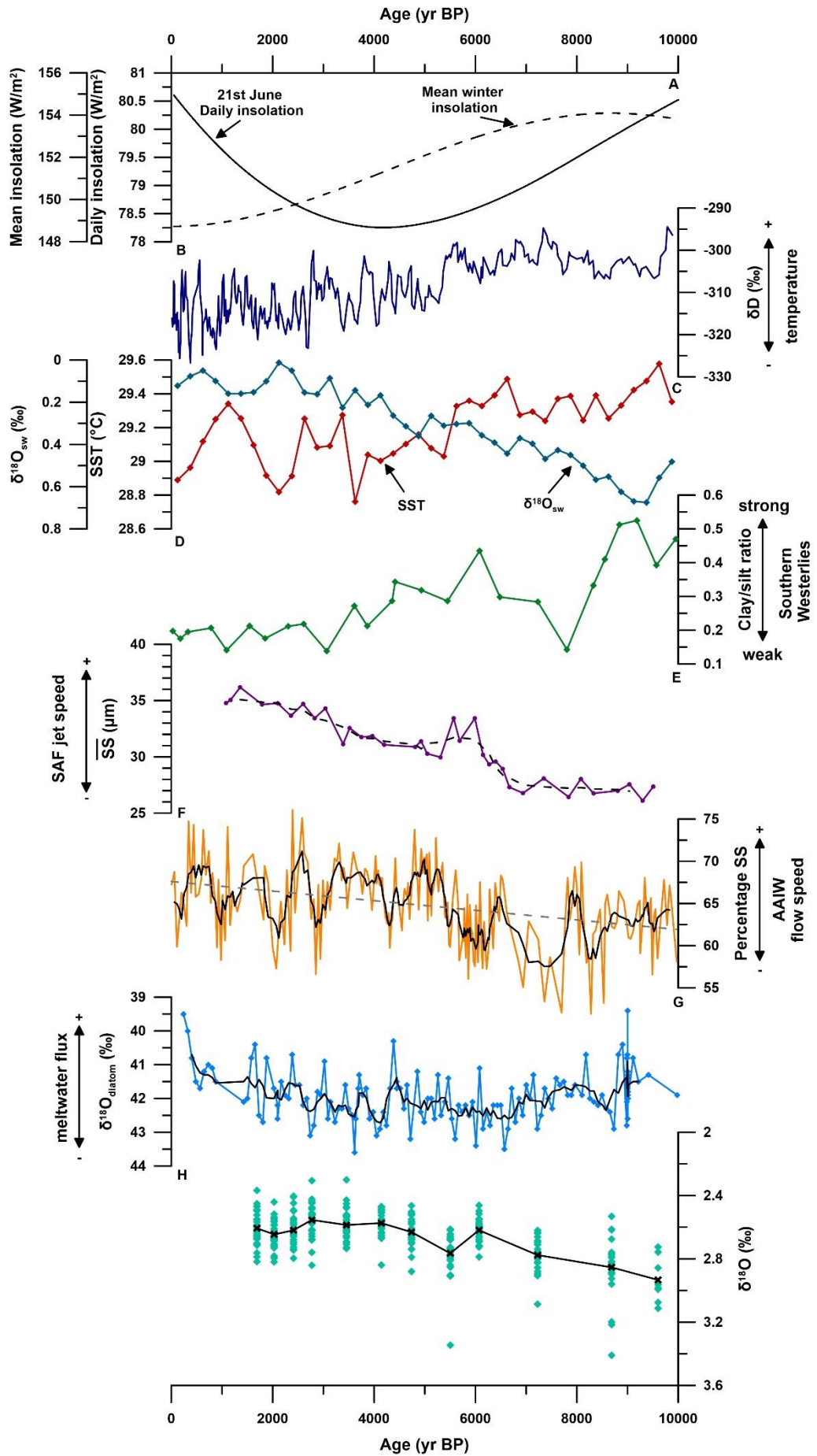
| Water mass | <i>T</i> ($^{\circ}\text{C}$) | <i>S</i> (PSU) | $\delta^{18}\text{O}$ (‰ VMSO) | Impact of increased contribution to AAIW |
|------------|---------------------------------|----------------|-----------------------------------|--|
| AAIW | $\sim 2.5\text{-}3$ | 34.15 | -0.21 | |
| SAMW | ~ 4.5 | 34.4 | -0.15 | $\uparrow T, \uparrow S, \uparrow \delta^{18}\text{O}$ |
| AAWW | < 1.5 | < 34 | -0.27 | $\downarrow T, \downarrow S, \downarrow \delta^{18}\text{O}$ |

properties (Meredith et al., 1999, Garabato et al., 2009), it is suggested that AAIW experienced variability during the Holocene. The higher *G. inflata* $\delta^{18}\text{O}$ values of the EH (average +2.79‰, Figure 5.53A) indicate not only the colder AAIW temperatures of the very earliest parts of the Holocene (Roberts et al., 2016) but also a greater contribution of more saline, warmer and isotopically higher SAMW to AAIW, compared with fresher and colder AAWW, increasing the $\delta^{18}\text{O}$ of AAIW (Table 5.17) resulting in higher *G. inflata* $\delta^{18}\text{O}$ compared with the LH. The decrease in *G. inflata* $\delta^{18}\text{O}$ after 4700 yr BP to average levels of around +2.6‰ (Figure 5.53A) could be attributed to increased contribution of fresher and isotopically lower AAWW to AAIW, compared to SAMW, decreasing the $\delta^{18}\text{O}$ signature of AAIW (Table 5.17) and thus that of *G. inflata*. The variability in the relative contribution of the two water masses to AAIW between the Early and Late Holocene is most likely the result of changes in AAWW formation along the Antarctic Peninsula during the Holocene relating to changes in climatic conditions instead of a mixture of SAMW and AAIW variability as SAMW formation was consistent after 8000 yr BP (Kalansky et al., 2015).

In the following two sections Holocene climate variability and its influence on SAMW and AAWW formation is explored together with the resulting impact on AAIW properties and, thus, the observed *G. inflata* $\delta^{18}\text{O}$ variability (Figure 5.53A).

5.3.8.1 SAMW variability and its impact on AAIW properties and *Globorotalia inflata* $\delta^{18}\text{O}$ due to Holocene climate variability in the Southeast Pacific

In the Southeast Pacific, the Early Holocene Climate Optimum (after ~11,000 yr BP) was characterised by high SSTs (Kilian and Lamy, 2012), while dry and warm climatic conditions prevailed over South America (Unkel et al., 2010). These conditions were the result of stronger southern westerly winds (SWW) (Figure 5.55D) — which were positioned in a more southerly location compared to the mid-to late Holocene (Kalansky et al., 2015) — combined with higher temperatures (Figure 5.55C) (Kilian and Lamy, 2012). As a result, SAMW formation in the Pacific Ocean was enhanced during this period (Kalansky et al., 2015). Enhanced SAMW formation and contribution to AAIW within the Scotia Sea, would have increased the $\delta^{18}\text{O}$ signature of the AAIW due to the more positive $\delta^{18}\text{O}$ signature of SAMW compared with AAIW. The increased contribution of SAMW to AAIW combined with the warming AAIW observed at JR244 – GC528 core site (Roberts et al., 2016) would have increased the $\delta^{18}\text{O}$ of *Globorotalia inflata*, as observed between 10,000 and 8000 yr BP (Figure 5.53). Warm conditions prevailed until ~8500 yr BP, after which temperatures decreased by ~1.5°C (Kilian and Lamy, 2012)



and precipitation levels increased. The SAMW formation region in the Pacific Ocean was effected by the Northern Hemisphere 8200 yr BP event which caused short-term cooling (Rohling and Pälike, 2005) that lasted until ~7900 yr BP.

The period between 7500 yr BP and 5500 yr BP was characterised by steadily decreasing precipitation levels in the Southeast Pacific region as a result of slowly decreasing SWW strength (Figure 5.55D; Lamy et al., 2010). This led to decreased SAMW formation and/or transport after 8000 yr BP compared with the very early stages of the Holocene (Kalansy et al., 2015), which would have led to a decrease in its contribution to AAIW development east of the Drake Passage, reducing the flow strength and volume of AAIW between 8000 and 6000 yr BP (Figure 5.55F, Voigt et al., 2016). A cooling of SAMW in response to the long-term Holocene cooling (Scott et al., 2004, Kilian and Lamy, 2012) must have been accompanied by some variability in the salinity of the water column as *G. inflata* $\delta^{18}\text{O}$ measurements show variability after the earliest part of the EH — decreasing at 7200 and 6100 yr BP then increasing at 5500 yr BP (Figure 5.53, 10H). It is possible that the variability is the result of increasing but variable influence and contribution of AAWW to AAIW properties relative to SAMW.

The Late Holocene period (5500 yr BP to present) experienced continuing temperature decrease (Lamy et al., 2002) along with variable, but weaker SWW strength over the SAMW formation region (Lamy et al., 2010, Figure 5.55D). During this period glaciers in the Southern Andes underwent periodic re-advances (Glasser et al., 2004; Wenzens, 2005) indicating highly variable, but consistently colder climate conditions compared to the EH. The highly variable climate was most likely due to the intensification of ENSO after low ENSO variance between 5,000 and 4,000 yr BP (Carré et al., 2014). The climatic cooling trend was also reflected in intermediate water temperatures which decreased by ~1.5°C after 6000 yr BP in the Pacific Ocean (Rosenthal et al., 2013). In contrast, SAMW formation and/or transport in the Southeast Pacific remained steady during the LH at earlier levels (Kalansky et al., 2015) even in the face of these variable

Figure 5.55: A) Daily (21st June) solar insolation values at 50°S between 1950 and 10,000 yr BP (solid line) and mean winter (21st March to 21st September) solar insolation values (dashed line) at 50°S for the same time period (Laskar et al., 2004). B) Taylor Dome deuterium record (3-point average) from Ross Embayment, Antarctica indicating decreasing air temperatures across the Holocene (Steig et al., 1998). C) Multi-core reconstruction of Western Tropical Pacific SST (red) and $\delta^{18}\text{O}_{\text{sw}}$ (blue) based on *Globigerinoides ruber* Mg/Ca and $\delta^{18}\text{O}$ (Scott et al., 2004) D) Clay/silt ratio from the Southeast America (53°S) indicative of the strength of the Southern Westerlies (Lamy et al., 2010). E) Mean sortable silt grain size from core JR244 - GC528, indicative of SAF jet speed (Roberts et al., 2017). F) Sortable silt (% 63-10 μm) record from Southwest Atlantic indicative of AAIW strength; solid black line: 5-point running average, grey dashed line: linear trend through the Holocene (Voigt et al., 2016). G) Diatom $\delta^{18}\text{O}$ record from Palmer Deep, West Antarctic Peninsula, as a proxy for glacial meltwater flux; solid black line: 5-point average (Pike et al., 2013). H) Single specimen *G. inflata* $\delta^{18}\text{O}$ record from the JR244 - GC528 core, Falkland Plateau; black crosses indicate mean values within samples.

environmental conditions. This suggests, that the observed increase in AAIW flow speed and volume (Figure 5.55F, Voigt et al., 2016) along with the increasing SAF jet speed (Figure 5.55E; Roberts et al., 2017;) and the decrease in *Globorotalia inflata* $\delta^{18}\text{O}$ values after 5500 yr BP (Figure 5.53) is likely related to the increased influence/input of AAWW to AAIW properties.

5.3.8.2 AAWW variability and its impact on AAIW properties and *Globorotalia inflata* $\delta^{18}\text{O}$ due to Holocene climate variability at the Antarctic Peninsula and South Atlantic

The Antarctic Peninsula (AP) and South Atlantic section of the Southern Ocean were impacted differently to the Southeast Pacific during the Early Holocene. The Early Holocene Climate Optimum was present at high latitudes, as evidenced by ice-core-derived temperature records (e.g. Masson et al., 2000; Figure 5.55B), however, it was shorter lived (~11,000-9500 yr BP) than in lower latitudes. In the South Atlantic, salinity-driven stratification of the glacial period began to break down ~10,000 yr BP, leading to the reversal of temperature inversion between the intermediate and the deep waters of the South (Roberts et al., 2016). The period between 9500 yr BP and 5500 yr BP was characterised by continuing deglaciation across the AP (Bentley et al., 2006), however, the rate of glacial discharge along the West Antarctic Peninsula (WAP) experienced a slowdown (Pike et al., 2013, Figure 5.55G) compared to the early deglaciation. Large regional differences (during the time period 9500-5500 yr BP) also existed between the apparently colder South Atlantic-Southern Ocean (Bianchi and Gersonde, 2004) and the warmer AP (Domack, 2002) where sea ice cover also decreased (Leventer et al., 2002; Barbara et al., 2016).

The consistent, though slower glacial discharge after 9500 yr BP would have promoted AAWW formation along the AP contributing to AAIW generation further north in the Scotia Sea. Prior to 8000 yr BP, SAMW, with its increased formation rate (see 5.3.8.1) would have had a greater influence on AAIW properties than AAWW especially as glacial discharge slowed down around 9000 yr BP (Pike et al., 2013). As SAMW transport decreased towards the end of the EH, the constant advection of AAWW towards AAIW formation regions would have caused AAIW $\delta^{18}\text{O}$ to decrease thereby causing *G. inflata* $\delta^{18}\text{O}$ to decrease (Figure 5.53), however, the small variability observed in the *G. inflata* record indicates that the relative contribution of AAWW and SAMW to AAIW was variable. Altogether, the overall high (average 2.79‰) *G. inflata* $\delta^{18}\text{O}$ during the EH suggest that although AAWW (low $\delta^{18}\text{O}$) influenced AAIW properties at that time, SAMW (high $\delta^{18}\text{O}$) exerted a greater impact and reinforced the influence of the increasing water

temperatures as observed at the core site between ~10,500 and 7,500 yr BP (Roberts et al., 2016).

Following the transitional period after the Early Holocene Climate Optimum, the period between 4500 to 2800 yr BP experienced warmer temperatures at the WAP (Hodgson et al., 2004). This warming was accompanied by increased primary productivity (Schmidt et al., 1990), decreased sea ice cover (Shevenell et al., 1996; Domack et al., 2003) and increased, but variable glacial meltwater discharge along the WAP (Figure 5.55G; Pike et al., 2013; Swann et al., 2017) as a result of the intensification of ENSO variability and events following a period of low ENSO variance from 5,500 to 4,500 yr BP (Carré et al., 2014). The latest Holocene period since 2800 yr BP experienced even higher levels of glacial meltwater discharge (Figure 5.55G; Pike et al., 2013) and seasonally highly variable sea ice cover (Domack et al., 2002) at the WAP due to atmospheric warming relating to continuing strong ENSO activity in the Pacific Ocean (Carré et al., 2014). As a result of the increased glacial discharge after 5000 yr BP (Pike et al., 2013), AAWW formation would have been invigorated, increasing its relative proportion in AAIW formation in the Scotia Sea at a time when AAIW temperature was relatively stable at the core site (Roberts et al., 2016), thereby decreasing AAIW and thus *Globorotalia inflata* $\delta^{18}\text{O}$ (Figure 5.55H). This is supported by increasing AAIW flow speeds after the EH; indicated by sortable silt records from two locations in the South Atlantic (Figure 5.55E; F, Voigt et al., 2016; Roberts et al., 2017) as well as by the increasing volume of AAIW after the mid-Holocene (Voigt et al., 2016) when SAWM formation was steady (Kalansky et al., 2015).

Assessment of Holocene climate variability and its impact on SAMW and AAWW formation during the Holocene shows that there is a clear link between *Globorotalia inflata* $\delta^{18}\text{O}$ at core site JR244 - GC528 on the Falkland Plateau and climatic conditions further afield. The observed 0.2‰ offset in *G. inflata* single specimen sample $\delta^{18}\text{O}$ between the EH and the LH (Figure 5.53) is likely the result of the combination of an Early Holocene (~10,500-7,500 yr BP) increase in AAIW temperature at the core site and the variable relative proportion and influence of SAMW and AAWW to AAIW at the core site. On average, SAMW had a greater relative contribution to AAIW during the EH reinforcing the warming AAIW following the deglaciation (Roberts et al., 2016), leading to high *G. inflata* $\delta^{18}\text{O}$ (Figure 5.53A). In contrast, AAWW made up a greater proportion of AAIW in the LH, decreasing average *G. inflata* $\delta^{18}\text{O}$.

5.3.9 Summary and Conclusion

Here the aim was to investigate variability in the seasonality of oceanographic conditions during the Holocene period through the use of single specimen *Globorotalia inflata* stable isotope analysis. Statistical analysis reveals significant difference in within-sample $\delta^{18}\text{O}$ variance (which are outside the analytical error) and significantly different environmental conditions between the Early Holocene and Late Holocene period which is also reflected by the $\sim 0.2\text{‰}$ difference in average $\delta^{18}\text{O}$ between the Early and Late Holocene period. *G. inflata* calcifies within Antarctic Intermediate Waters (AAIW) on the Falklands Plateau below 150 m water depth. AAIW shows no significant seasonal variability which together with the one peak flux of *G. inflata* per year (austral spring) means that the stable isotope record is not a reflection of intra-annual variability, nor does it reflect local oceanographic conditions. Instead it is proposed that the *G. inflata* at the core location records changes in AAIW properties in response to source water variability. Due to the temperature- and size-dependence of *G. inflata* the $\sim 0.48\text{‰}$ average within-sample $\delta^{18}\text{O}$ variability identified from the single specimen $\delta^{18}\text{O}$ measurements is most likely the result of different calcification patterns between individual specimens related to vital effects.

The Holocene AAIW source water variability is investigated by comparing the impact of changing Subantarctic Mode Water (SAMW) and Antarctic Winter Water (AAWW) – the source waters of AAIW – on *Globorotalia inflata* $\delta^{18}\text{O}$ which is then assessed in terms of Holocene Southern Ocean climate variability. SAMW, which derives from the South Pacific, contributes relatively warm ($\sim 4.5\text{ °C}$) waters to AAIW with a $\delta^{18}\text{O}$ signature (-0.15‰) that is relatively higher than the core AAIW $\delta^{18}\text{O}$ (-0.21‰). In contrast, AAWW, which derives from the Antarctic Peninsula, contributes cold ($< 1.5\text{ °C}$) and fresh (< 34 PSU) waters to AAIW with a $\delta^{18}\text{O}$ signature (-0.27‰) that is lower than the core AAIW $\delta^{18}\text{O}$. The assessment of Holocene climate variability and its impact on SAMW and AAWW formation revealed that during the Early Holocene SAMW provided a greater contribution to AAIW than AAWW, increasing AAIW $\delta^{18}\text{O}$, which together with the increasing AAIW temperatures resulted in the high (average of around $+2.79\text{‰}$) *G. inflata* $\delta^{18}\text{O}$ between 9600 and 5500 yr BP. The relative contribution of fresher and isotopically lower AAWW increased after 4700 yr BP as a result of the increased glacial meltwater discharge along the Antarctic Peninsula and decreased SAMW formation (compared to the Early Holocene). This increased AAWW formations decreased AAIW $\delta^{18}\text{O}$ in the Scotia Sea, resulting in the lower (average of around $+2.6\text{‰}$) *G. inflata* $\delta^{18}\text{O}$ between 4700 and 1700 yr BP at a time when AAIW temperatures were relatively stable. This assessment shows the clear link between *G. inflata* $\delta^{18}\text{O}$ at the Falkland Plateau and oceanographic changes along the Antarctic Peninsula during the Holocene. Additionally,

this study highlights the applicability of *G. inflata* $\delta^{18}\text{O}$ as a proxy for intermediate water variability across the Southern Ocean.

6 Conclusions and Recommendations

This thesis provides insights into the use of single specimen foraminiferal stable isotope analysis to study changes in seasonality in high latitude regions. In this final chapter, the aims and objectives set out in Chapter 1 will be assessed against the findings of the studies contained in Chapter 5.1, 5.2, and 5.3. Additionally, recommendations will be made on the single specimen foraminiferal stable isotope method when applied in the high latitudes, as well as on the analysis of morphological variability and foraminiferal abundance.

6.1 *Neogloboquadrina pachyderma* abundance, stable isotope composition, vital effects, and calcification depth variability in the Scotia Sea: results from vertical plankton hauls

Single specimen stable isotope analysis was carried out on modern *Neogloboquadrina pachyderma* (Np) specimens that were collected by vertical plankton hauls in the Scotia Sea. The aim of this chapter was to assess the variability in the stable isotope record across the mid to high latitudes of the Scotia Sea in order to provide a region-specific record of vital effects. Additionally, variability in the abundance and morphotypes of Np was also assessed.

Neogloboquadrina pachyderma abundance varies by up to two orders of magnitude between the most southerly station south of the Southern Boundary of the Antarctic Circumpolar Currents and one of the most northerly station located on the southern edge of the Polar Front. Alongside the equatorward increase in Np numbers, the depth of peak Np abundance at each stations increased from south to north across the study area. The pattern of Np flux and depth of peak Np numbers at the stations is consistent with previous plankton tow studies conducted in the Atlantic sector of the Southern Ocean (Mortyn and Charles, 2003) and confirms the role of temperature and chlorophyll α concentration on Np flux.

Previous studies of Southern Ocean *Neogloboquadrina pachyderma* highlighted the existence of a number of different morphotypes and genotypes within the species which were linked to different environmental conditions (Kennett, 1968; Darling et al., 2004) and parts of the foraminiferal life cycle (Vautravers et al., 2013). To avoid the possibility of morphology-related isotope variability prior to the single specimen isotope analysis, the *Neogloboquadrina pachyderma* specimens were inspected under light microscope

and separated into morphotypes. Three morphotypes were identified (Np-A, Np-B, and Np-C), with the first two representing adult forms (with a secondary crust) whose distribution is separated by the Southern Antarctic Circumpolar Current. In contrast, the third morphotype represents juvenile, pre-gametogenic specimens that dominated the assemblage at one station west of South Georgia.

Similarly to Np abundance, a latitudinal gradient is present in $\delta^{18}\text{O}_{\text{np}}$ as a result of the south to north temperature increase across the study area. $\delta^{18}\text{O}_{\text{np}}$ differences across the Scotia Sea are also linked to differences in shell size/weight and morphotypes, as heavier specimens have higher $\delta^{18}\text{O}_{\text{np}}$, and the juvenile, Np-C specimens show the lowest $\delta^{18}\text{O}_{\text{np}}$. The relationship between size and $\delta^{18}\text{O}_{\text{np}}$ is similar to that observed in Np by previous studies (e.g. Bausch et al., 1997; Hillaire-Marcel et al., 2004).

The Scotia Sea displays a wide range of oceanographic variability (see Chapter 5.1.3 and 5.1.4), the result of which is variability in the depth of the mixed layer and the pycnocline across the study area and the depth of peak Np abundance. Foraminiferal calcite equilibrium $\delta^{18}\text{O}$ is closely linked to temperature, and as a result, it varies spatially and with depth. Both calcification depths and vital effects - the deviation from equilibrium calcification due to biological and or kinetic processes (Ravelo and Hillaire-Marcel, 2007) - show variability across the Scotia Sea in relation to morphotypes and local hydrography. The juvenile morphotype (Np-C), which calcifies within the mixed layer shows a negative offset of $\sim 0.6\text{‰}$ from mixed layer $\delta^{18}\text{O}_{\text{eq}}$. In contrast, Np-A morphotypes show variable calcification depths and vital offsets. Calcification in equilibrium below the mixed layer by Np-A was observed at three stations, two of which were open ocean settings, and one an enclosed bay. This equilibrium calcification below the mixed layer agrees well with another Np study in the northern Pacific (Asahi et al., 2015), while other plankton tow studies observed negative fractionations of up to 1‰ (e.g. Bausch, et al., 1997; Volkmann and Mensch, 2001; Mortyn and Charles, 2003). Some Np-A specimens also show calcification in equilibrium within the mixed layer at all the stations where they were present, as well as out of equilibrium (-0.46‰ vital offset) within the mixed layer at one station. This variable offset from $\delta^{18}\text{O}_{\text{eq}}$ is most likely the result of calcification, and secretion of the secondary crust within the mixed layer supporting previous suggestions that it is not temperature-driven, but instead controlled by biological processes (Jonkers et al., 2016; Fenhrenbacher et al., 2017).

6.2 Seasonal variability of *Neogloboquadrina pachyderma* abundance, morphology, and stable isotope composition at the West Antarctic Peninsula

A complete assessment of *Neogloboquadrina pachyderma* abundance, morphology, and single specimen isotope variability over a period of six year (2006-2013) at the continental shelf off Palmer Deep, West Antarctic Peninsula was presented in this chapter. The aim of this chapter was to create a modern record of seasonal and interannual variability of Np properties in relation to environmental changes in the high latitude regions.

Neogloboquadrina pachyderma flux displays both intra- and inter-annual variability in the sediment trap record. Flux varies from near zero to over 300 tests/m²/day between the winter and summer months, with two distinct pulses occurring, one in austral late spring and one in late summer. The first peak Np flux takes place soon after the winter sea ice dissipates and coincides with the early chlorophyll bloom. The peak Np flux occurs during the second chlorophyll bloom when surface water temperatures are the highest and the water column is stratified. Although Np flux decreases in-between the two blooms it remains above values observed during the winter months. The bimodal pattern of Np flux and the pattern of environmental properties during the year suggest that the development of optimum growing conditions created by a combination of environmental variables determine the Np shell flux. These include food availability, maximum SST, and timing of sea ice retreat that determine the strength of the biological productivity. The bimodal Np flux pattern has previously been observed in the North Atlantic (Rolund and Bé, 1971; Jonkers et al., 2010), while in the Arctic (Kohfeld et al., 1996; Simstich et al., 2003) and in the northern Weddell Sea (Donner and Wefer, 1994) a single peak flux was recorded highlighting the importance of the optimum growing conditions for Np abundance.

The study site is located within the outer marginal ice zone, an area of high biological productivity (Smith et al., 2008). The availability of nutrients and the physical properties of the water column vary both temporally and spatially in this region (Smith et al., 1995). In particular, the extent of the sea ice off the shore of the WAP shows high inter-annual variability (Stammerjohn et al., 2008a). As a result, the timing and amplitude of the Np flux varies year-on-year. The timing of the first peak flux moves from November to October in 2011-12 compared to the other years, the second peak flux moves from late January to late February in 2010-11, while the amplitude varies by three orders of magnitude between 2007-08 and 2010-11 as a direct result of changes in the timing of sea ice melt and development of the chlorophyll bloom.

Two distinct morphotypes of *Neogloboquadrina pachyderma* were identified in the sediment trap samples, an adult morphotype, Np-A, and a juvenile morphotype, Np-C (following from Chapter 5.1). Along with flux, Np morphology also displays both intra- and inter-annual variability. Largest Np specimens are found in the spring-summer months, and show differences in size between the years, with the highest Np peak flux specimens of Nov-Jan 2010-11 obtaining the largest shell sizes. Similarly to size, the translucency of the specimens also shows intra-annual variability showing greater calcification of summer specimens compared to winter ones. Detailed statistical analysis revealed that the morphological variability in the sediment trap record is driven by sea ice and chlorophyll concentration, similarly to Np flux. Increased sea ice concentration/longer sea ice season together with lower chlorophyll concentration creates unfavourable conditions for Np to complete their life cycle. Only if Np specimens are already mature, more robust can they survive these conditions to reproduce once sea ice melts and nutrients concentrations are higher, although their overall flux will be reduced.

Neogloboquadrina pachyderma calcification depth varies between 45 and 100 m during the summer months, assuming no vital offset, which falls within existing studies of Np calcification depths in the Southern Ocean (Mortyn and Charles, 2003) and in the Antarctic Peninsula (Hendry et al., 2009). Np $\delta^{18}\text{O}$ values show inter- and inter-annual variability, similarly to flux and morphology; displaying a maximum of 0.5‰ difference between winter values of 2008 and 2012, and a more than 3‰ difference between May and December 2012 Np $\delta^{18}\text{O}$ values. The relationship between Np $\delta^{18}\text{O}$ and $\delta^{18}\text{O}_{\text{eq}}$ also shows variability, as Np $\delta^{18}\text{O}$ follows $\delta^{18}\text{O}_{\text{eq}}$ between October and May but diverges during the winter season. The inter-annual variability is most likely the result of a number of reasons, including the mortality of post-gametogenic specimens that became dormant during the winter season leading to higher $\delta^{18}\text{O}_{\text{np}}$ values between March and September and years with low intra-annual variability, and negative offset from $\delta^{18}\text{O}_{\text{eq}}$. Another possibility is the presence of small, juvenile, Np-C morphotypes that have not secreted their calcite crust leading to the low $\delta^{18}\text{O}_{\text{np}}$ (relating to the ontogenic calcite), such as those during the winter season of 2012. The single specimen Np $\delta^{18}\text{O}$ record shows a clear link between morphology, environmental conditions, and $\delta^{18}\text{O}$. Heaviest $\delta^{18}\text{O}_{\text{np}}$ values coincide with the largest test sizes, and the greatest number of specimens that obtained their secondary crust at the end of their life cycle, during times of optimum growing conditions. The annual record of $\delta^{18}\text{O}_{\text{np}}$ and size show a clear seasonal trend, with increasing size, encrustation, and $\delta^{18}\text{O}_{\text{np}}$ from spring to summer followed by decreasing size, encrustation, and $\delta^{18}\text{O}_{\text{np}}$ from the autumn as growing conditions deteriorate (SST and chlorophyll concentration decrease and sea ice concentration

increases). An overall synthesis of seasonal variability in flux, morphology, and $\delta^{18}\text{O}$ can be found in Chapter 5.2.9 (Figure 5.45).

The sediment trap record highlighted the impact of atmospheric teleconnections between El Niño-Southern Oscillation/Southern Annular Mode (ENSO/SAM) and high latitude atmospheric settings. A positive SAM coinciding with a strong La Niña in 2010 led to anomalously low sea level pressure over the Bellingshausen Sea crating strong north-northwesterly winds between September 2010 and February 2011 that resulted in an early sea ice retreat and late sea ice advance (Meredith et al., 2017). Simultaneously, the upwelling of nutrient-rich, warm Upper Circumpolar Current (UCDW) waters over the continental shelf increased in recent times due to ENSO/SAM (Martinshon and McKee, 2012) creating more favourable conditions for phytoplankton growth (Prézelin et al., 2004). The result of these atmospheric and oceanographic conditions was the proliferation of larger, rounder, and more encrusted *Neogloboquadrina pachyderma* with high $\delta^{18}\text{O}_{\text{np}}$ in the spring of 2010, leading to a flux of over 1000 specimen/m²/day, an anomalous number in the six-year long record. These 2010 samples emphasised the impact of ENSO/SAM on the marine ecosystem around the Antarctic Peninsula. Additionally, it also showed how sediment samples can be overwhelmed by anomalous years with very high number of Np potentially skewing paleoceanographic reconstructions.

6.3 Investigating intermediate water mass variability in the Southern Ocean during the Holocene

Single specimen isotope analysis was carried out on *Globorotalia inflata* specimens collected from a sediment core recovered from the Falkland Plateau in the Scotia Sea. The aim of this chapter is to use the foraminiferal isotope record to investigate intermediate water variability relating to environmental and climatic changes in the southern high latitudes during the Holocene period.

The single specimen *Globorotalia inflata* record displays a statistically significant variability in within-sample $\delta^{18}\text{O}$ range during the Holocene, as well as significantly different environmental conditions between the Early and Late Holocene period. The single specimen $\delta^{18}\text{O}$ record shows an average of $\sim 0.48\text{‰}$ within-sample range across the Holocene which is linked to different calcification patterns between individual specimens, particularly, as *G. inflata* specimens have a large variability in vital offsets ($\pm 0.4\text{‰}$) related to physiological and ecological effects (Niebler et al., 1999). Significant within-sample variability in Early Holocene samples were outside the $\pm 0.4\text{‰}$ range and thus could be a sign of greater decadal variability at those times. However, the resolution

of the sediment core and the within-sample specimen numbers prevents more detailed interpretation of these higher within-sample variability.

Globorotalia inflata was identified as an intermediate water species, supporting previous assessments in the southern mid latitudes (Wilke et al., 2006; Groeneveld and Chiessi, 2011). At the Falkland Plateau *G. inflata* was shown to calcify within Antarctic Intermediate Water (AAIW) below 150 m water depth making it a useful species to study changes in this water mass over longer periods. A modern assessment of oceanographic conditions around the Falkland Plateau (Sirota and Sundakov, 2014) revealed that AAIW does not show significant seasonal variability at this location. As such, the average 0.2‰ *G. inflata* $\delta^{18}\text{O}$ variability between the Early and Late Holocene can be considered as the result of changes in AAIW properties in response to source water variability.

Antarctic Intermediate Water is primarily made up of Subantarctic Mode Water (SAMW) and Antarctic Winter Water (AAWW) (Garabato et al., 2009), and thus, its $\delta^{18}\text{O}$ signature is determined by the balance between these two water masses with widely different temperatures, salinities, and thus $\delta^{18}\text{O}$ values (Meredith et al., 1999). The portion of SAMW that enters the Drake Passage is warmer ($\sim 4.5^\circ\text{C}$) and isotopically heavier (-0.15‰) than the core AAIW (-0.21‰). In contrast, AAWW is colder, fresher, and isotopically lighter ($<1.5^\circ\text{C}$, <34 PSU, less than -0.27‰) than the core AAIW. Hence, variability between the contributions of the two source waters have a clear impact on AAIW $\delta^{18}\text{O}$, and as a consequence, *G. inflata* $\delta^{18}\text{O}$.

A detailed assessment of Holocene climate variability revealed that during the Early Holocene SAMW provided a greater contribution to AAIW formation than AAWW resulting in the higher average *G. inflata* $\delta^{18}\text{O}$ values ($+2.8\text{‰}$) recorded between 9600 and 5500 yr BP. After this period, increased glacial meltwater discharge along the Antarctic Peninsula increased the contribution of AAWW to AAIW at the same time as SAMW formation decreased relative to the Early Holocene. As a result, AAIW $\delta^{18}\text{O}$ decreased, as seen in the lower average *G. inflata* $\delta^{18}\text{O}$ values ($+2.6\text{‰}$) between 4700 and 1700 yr BP. The *G. inflata* $\delta^{18}\text{O}$ record shows a strong link between high latitude oceanographic processes and mid latitude water mass variability and highlights the possibility of using this proxy to study long term intermediate water variability in the Southern Ocean.

6.4 Recommendations to improve methods

In this thesis I utilised single specimen foraminiferal $\delta^{18}\text{O}$ to attempt to investigate changes in seasonality in the high latitudes. Single specimen foraminiferal $\delta^{18}\text{O}$ has been used successively in tropical regions, where species are larger in size, and intra- and

inter-annual variability is large thanks to monsoon and ENSO activities (Koutavas et al., 2006; Khider et al., 2011; Scroton et al., 2011; Ford et al., 2015). In this section I aim to summarise my findings relating to the single specimen method as well as to the morphological and abundance studies.

Recommendations for single specimen foraminiferal isotope analysis:

- Analysis of a minimum of 30, preferably 50, specimens in each sample to ensure statistically significant results in statistical analysis.
- Each Foraminifera specimen, especially when small polar species like *Neogloboquadrina pachyderma* is used, should be weighed to ensure carbonate mass is enough for isotope analysis. Although it is a time-consuming exercise, by doing this, it is possible to limit the number of unreliable isotope results.
- Separate *Neogloboquadrina pachyderma* specimens into morphotypes to limit the possibility of morphotype-related isotope variability. In particular, remove juvenile specimens from samples prior to analysis as the $\delta^{18}\text{O}$ of ontogenic calcite is significantly lower than the secondary crust due to biological processes (changes relating to physical processes will be masked).
- If *Neogloboquadrina pachyderma* is used to reconstruct long term seasonality, it is important to constrain genotypic variability, which is linked to frontal boundaries.
- Use of Quantile-Quantile plots (if possible) would aid the assessment of difference in distribution between two time periods (see Ford et al., 2015).

Recommendations for morphometric analysis:

- Weigh every shell analysed for morphometrics to be able to determine changes in density.
- If possible, use a combination of individually mounted specimens and automated microscope setup, where a camera moves on a platform and takes photos of individual specimens. This would reduce errors relating to different orientations of the specimens.
- Use automated image analysis techniques to speed up image processing.
- Explore the use of Fourier shape analysis (Healy-Williams, 1992; Eynaud et al., 2009) to identify morphotypes.

Recommendations for plankton tow studies:

- Use of MOCNESS nets (Multiple Opening and Closing Net, with and Environmental Sensing System) similarly to Kohfeld et al. (1996), and Mortyn and

Charles (2003). A MOCNESS net can be equipped with sensors that measure in situ water temperature, salinity, fluorescence, and water flow through the nets, providing truly concomitant foraminiferal abundance numbers and water property data. It also rescinds the need for a separate CTD to measure these properties, although water samples for $\delta^{18}\text{O}_{\text{sw}}$ would need to be collected by a CTD. The net captures samples at distinct, separate depth intervals giving a picture of foraminifera species and abundance variability across a range of depths.

- Use of a flow meter in order to calculate true foraminiferal abundance (in $\#/m^3$ of seawater).

Recommendations for single specimen analysis of sediment core samples:

- Consider the location of the site, ensure that the area experiences sufficient seasonal variability.
- Ideally, for a polar study choose a site that is located close to the coast. This will allow the identification of varying glacial meltwater input.
- Choose a foraminifera species that calcifies in the surface waters or within the mixed layer and one that is present all-year round. Seasonal variability in large-scale atmospheric variability, and surface water parameters will be reflected in the surface water calcifying foraminifera.
- Preferably undertake a modern assessment of the habitat, calcification depth, and time of peak abundance of the chosen foraminifera species to understand the region-specific foraminiferal variability.
- Choose a high resolution sediment core (e.g. 1cm/10 years). This would enable the assessment of within-sample seasonal variability by limiting the number of years each cm of the core represents.

7. References

- Abelmann, A. et al. 2015. The seasonal sea-ice zone in the glacial Southern Ocean as a carbon sink. *Nature Communications*, 6, 8136.
- Allen, C. S. et al. 2010. A record of Holocene glacial and oceanographic variability in Neny Fjord, Antarctic Peninsula. *Holocene* 20(4), pg. 551-564.
- Allen, C. S. et al. 2011. Last glacial–interglacial sea-ice cover in the SW Atlantic and its potential role in global deglaciation. *Quaternary Science Reviews* 30(19–20), pg. 2446-2458.
- Arkhipkin, A. I. et al. 2004. The influence of seasonal environmental changes on ontogenetic migrations of the squid *Loligo gahi* on the Falkland shelf. *Fisheries Oceanography* 13(1), pg. 1-9.
- Arrigo, K. R. et al. 2008. Coastal Southern Ocean: A strong anthropogenic CO₂ sink. *Geophysical Research Letters* 35(21), L21602, doi:10.1029/2008GL035624.
- Asahi, H. et al. 2015. Seasonal variability of $\delta^{18}\text{O}$ and $\delta^{13}\text{C}$ of planktic foraminifera in the Bering Sea and central subarctic Pacific during 1990-2000. *Paleoceanography* 30(10), pg. 1328-1346.
- B. Brown, M. and Forsythe, A. 1974. Robust Tests for Equality of Variances. *Journal of the American Statistical Association* 69, pg. 364-367.
- Barbara, L. et al. 2016. Environmental responses of the Northeast Antarctic Peninsula to the Holocene climate variability. *Paleoceanography* 31(1), pg. 131-147.
- Barker, P. F. and Camerlenghi, A. 2002. *Glacial History of the Antarctic Peninsula from Pacific Margin Sediments*. In: *Barker, P.F., Camerlenghi, A., Acton, G.D., and Ramsay, A.T.S. (Eds.), Proceedings of the Ocean Drilling Program, Scientific Results, 178*. [Online]. <http://www-odp.tamu.edu/publications/178_SR/VOLUME/SYNTH/SYNTH.PDF>. Available on: [Accessed: 14/09/2017].
- Bauch, D. et al. 1997. Oxygen isotope composition of living *Neogloboquadrina pachyderma* (sin) in the Arctic Ocean. *Earth and Planetary Science Letters* 146(1-2), pg. 47-58.
- Bauch, D. et al. 2000. The imprint of anthropogenic CO₂ in the Arctic Ocean: evidence from planktic $\delta^{13}\text{C}$ data from watercolumn and sediment surfaces. *Deep Sea Research Part II: Topical Studies in Oceanography* 47(9), pg. 1791-1808.
- Bauch, D. et al. 2002. Carbon isotopes and habitat of polar planktic foraminifera in the Okhotsk Sea: the 'carbonate ion effect' under natural conditions. *Marine Micropaleontology* 45(2), pg. 83-99.
- Be, A. W. H. 1980. GAMETOGENIC CALCIFICATION IN A SPINOSE PLANKTONIC FORAMINIFER, *GLOBIGERINOIDES-SACCULIFER* (BRADY). *Marine Micropaleontology* 5(3), pg. 283-310.
- Bemis, B. E. et al. 1998. Reevaluation of the oxygen isotopic composition of planktonic foraminifera: Experimental results and revised paleotemperature equations. *Paleoceanography* 13(2), pg. 150-160.
- Bemis, BE, et al. 2000 Temperature influence on the carbon isotopic composition of *Globigerina bulloides* and *Orbulina universa* (planktonic foraminifera). *Marine Micropaleontology*. 38(3-4) pg. 213-228.

- Bentley, M. J. et al. 2006. Geomorphological evidence and cosmogenic $^{10}\text{Be}/^{26}\text{Al}$ exposure ages for the Last Glacial Maximum and deglaciation of the Antarctic Peninsula Ice Sheet. *Geological Society of America bulletin*. 118(9), pg. 1149-1159.
- Bentley, M. J. et al. 2009. Mechanisms of Holocene palaeoenvironmental change in the Antarctic Peninsula region. *Holocene* 19(1), pg. 51-69.
- Benz, V et al. 2016: Last Glacial Maximum sea surface temperature and sea-ice extent in the Pacific sector of the Southern Ocean. *Quaternary Science Reviews*, 146, pg. 216-237.
- Berben, S. M. P. et al. 2017. A late-Holocene multi-proxy record from the northern Norwegian margin: Temperature and salinity variability. *Holocene* 27(6), pg. 822-834.
- Berger, W. H. et al. 1978. Stable isotopes in deep-sea carbonates: Box core ERDC-92, West Equatorial Pacific. *Oceanologica Acta* 1(2), pg. 203-216.
- Bianchi, C. and Gersonde, R. 2004. Climate evolution at the last deglaciation: the role of the Southern Ocean. *Earth and Planetary Science Letters* 228(3-4), pg. 407-424.
- Boltovskoy, E. 1971. Ecology of the planktonic Foraminifera living in the surface layer of Drake Passage. *Micropaleontology* 17(1), pg. 53-68.
- Boltovskoy, E. et al. 1996. Planktic foraminifera from the southwestern Atlantic (30 degrees-60 degrees S): Species-specific patterns in the upper 50 m. *Marine Micropaleontology* 28(1), pg. 53-72.
- Bouvier-Soumagnac, Y. and Duplessy, J.-C. 1985. Carbon and oxygen isotopic composition of planktonic foraminifera from laboratory culture, plankton tows and recent sediment; implications for the reconstruction of paleoclimatic conditions and of the global carbon cycle. *The Journal of Foraminiferal Research* 15(4), p. 302.
- Broecker, W. S. and Peng, T. 1982. *Tracers in the sea*. Lamont-Doherty Geological Observatory, Columbia University. 690 pages.
- Broecker, W. S. and Peng, T. H. 1974. Gas exchange rates between air and sea. *Tellus* 26(1-2), pg. 21-35.
- Bromwich, D. H. et al. 2013. Central West Antarctica among the most rapidly warming regions on Earth. *Nature Geoscience* 6(2), pg. 139-145.
- Bé, A.W.H., 1962. Quantitative multiple opening-and-closing plankton samplers: *Deep-Sea Research*. 9, pg. 144-151.
- Bé, A. W. H. 1969. *Planktonic Foraminifera*. In *Folio 11: Distribution of Selected Groups of Marine Invertebrates in Waters South of 35 ° S Latitude*. New York, pg. 9-12.
- Bé, A.W.H., 1980. Gamelogenic calcification in a spinose planktonic foraminifer, *Globigerinoides sacculifer* (Brady): *Marine Micropaleontology*. 5, pg. 283-310.
- Bé, A.W.H., and Spero, H.J., 1981. Shell regeneration and biological recovery of planktonic foraminifera after physical injury induced in laboratory culture: *Micropaleontology*. 27, pg. 305-316.
- Caromel, A. G. M. et al. 2015. Morphological Change During The Ontogeny Of The Planktic Foraminifera. *Journal of Micropalaeontology*. pg. 2-19.

- Carré, M. et al., 2014. Holocene history of ENSO variance and asymmetry in the eastern tropical Pacific. *Science* 345 (6200). pg. 1045-1048.
- Carstens, J. et al. 1997. Distribution of planktic foraminifera at the ice margin in the Arctic (Fram Strait). *Marine Micropaleontology* 29(3), pg. 257-269.
- Charles, C. D. and Fairbanks, R. G. 1990. Glacial to interglacial changes in the isotopic gradients of Southern Ocean surface water. In: Bleil, U. and Thiede, J. eds. *Geological History of the Polar Oceans: Arctic Versus Antarctic*. Norwell, Massachusetts: Kluwer Academic Publishers, pg. 519-538.
- Chiessi, C. M. et al. 2007. Signature of the Brazil-Malvinas Confluence (Argentine Basin) in the isotopic composition of planktonic foraminifera from surface sediments. *Marine Micropaleontology* 64(1-2), pg. 52-66.
- Clarke, A. et al. 2007. Introduction. Antarctic ecology from genes to ecosystems: the impact of climate change and the importance of scale. *Philosophical Transactions of the Royal Society B-Biological Sciences* 362(1477), pg. 5-9.
- Clem, K. R. and Fogt, R. L. 2013. Varying roles of ENSO and SAM on the Antarctic Peninsula climate in austral spring. *Journal of Geophysical Research-Atmospheres* 118(20). pg. 11,481-11,492.
- Cleroux, C. et al. 2007. Deep-dwelling foraminifera as thermocline temperature recorders. *Geochemistry Geophysics Geosystems* 8, pg 1-19.
- Cleroux, C. et al. 2013. Reconstructing the upper water column thermal structure in the Atlantic Ocean. *Paleoceanography* 28(3), pg. 503-516.
- CLIMAP Project Members, 1976. The surface of the ice-age earths. *Science*. 191, pg. 1131-1137.
- Cook, A. J. et al. 2005. Retreating glacier fronts on the Antarctic Peninsula over the past half-century. *Science* 308(5721), pg. 541-544.
- Cook, A. J. et al. 2016. Ocean forcing of glacier retreat in the western Antarctic Peninsula. *Science* 353(6296), pg. 283-286.
- Dalziel, I. W. D. et al. 2013. The Scotia Arc: Genesis, Evolution, Global Significance. *Annual Review of Earth and Planetary Sciences, Vol 41* 41, pg. 767-793.
- Darling, K. F. et al. 2006. A resolution for the coiling direction paradox in *Neogloboquadrina pachyderma*. *Paleoceanography* 21(2). PA2011.
- Darling, K. F. et al. 2004. Molecular evidence links cryptic diversification in polar planktonic protists to quaternary climate dynamics. *Proceedings of the National Academy of Sciences of the United States of America* 101(20), pg. 7657-7662.
- Deacon, G. E. R. 1937. *The Hydrology of the Southern Ocean*. Cambridge, U.K.: Cambridge University Press, pg. 124.
- Dingle, R. V. and Lavelle, M. 1998. Antarctic Peninsula cryosphere: Early Oligocene (c. 30 Ma) initiation and a revised glacial chronology. *Journal of the Geological Society* 155, pg. 433-437.
- Domack, E. W. 2002. A synthesis for site 1098: Palmer Deep. In: Barker, P.F. et al. eds. *Proceedings of the ocean drilling program, scientific results*. Texas A&M University: Ocean Drilling Program.

- Domack, E. W. et al. 2003. Environmental setting of the Antarctic Peninsula. *Antarctic Peninsula Climate Variability: Historical and Paleoenvironmental Perspectives* 79, pg. 1-13.
- Donner, B. and Wefer, G. 1994. Flux and stable isotope composition of *Neogloboquadrina pachyderma* and other planktonic foraminifers in the Southern Ocean (Atlantic sector). pg. *Deep-Sea Research* 1 41(11/12), pg. 1733-1743.
- Ducklow, H. et al. 2012. The Marine System of the Western Antarctic Peninsula. *Antarctic Ecosystems*. John Wiley & Sons, Ltd, pg. 121-159.
- Ducklow, H. W. 2008. Long-term studies of the marine ecosystem along the west Antarctic Peninsula Preface. *Deep-Sea Research Part II-Topical Studies in Oceanography* 55(18-19), pg. 1945-1948.
- Ducklow, H. W. et al. 2007. Marine pelagic ecosystems: The West Antarctic Peninsula. *Philosophical Transactions of the Royal Society B-Biological Sciences* 362(1477), pg. 67-94.
- Eagles, G. 2010. The age and origin of the central Scotia Sea. *Geophysical Journal International* 183(2), pg. 587-600.
- Elderfield, H. and Ganssen, G. 2000. Past temperature and delta O-18 of surface ocean waters inferred from foraminiferal Mg/Ca ratios. *Nature* 405(6785), pg. 442-445.
- Elderfield, H. et al. 2002. The relationship between shell size and Mg/Ca, Sr/Ca, $\delta^{18}\text{O}$, and $\delta^{13}\text{C}$ of species of planktonic foraminifera. *Geochemistry, Geophysics, Geosystems* 3(8), pg. 1-13.
- Emery, W. J. 1977. Antarctic Polar Frontal Zone from Australia to the Drake Passage. *Journal of Physical Oceanography* 7, pg. 811-822.
- Emiliani, C. 1955. Pleistocene Temperatures. *The Journal of Geology* 63(6), pg. 538-578.
- Epstein, S. et al. 1953. REVISED CARBONATE-WATER ISOTOPIC TEMPERATURE SCALE. *Geological Society of America Bulletin* 64(11), pg. 1315-1325.
- Epstein, S. and Mayeda, T. 1953a. Variation of O-18 content of waters from natural sources. *Geochimica et Cosmochimica Acta* 4(5), pg. 213-224.
- Epstein, S. et al. 1977. Oxygen and Hydrogen Isotopic Ratios in Plant Cellulose. *Science* 198(4323), pg. 1209-1215.
- Erez, J. 1978. *The influence of differential production and dissolution of the stable isotope composition of planktonic foraminifera*. Ph.D Thesis. Woods Hole-MIT Joint Program.
- Erez, J. a Luz, B. 1983. Experimental paleotemperature equation for planktonic foraminifera. *Geochimica et Cosmochimica Acta* 47(6), pg. 1025-1031.
- Etourneau, J. et al. 2013. Holocene climate variations in the western Antarctic Peninsula: evidence for sea ice extent predominantly controlled by changes in insolation and ENSO variability. *Climate of the Past* 9, pg. 1431-1446.
- Evans, D. G. et al. 2014. The imprint of Southern Ocean overturning on seasonal water mass variability in Drake Passage. *Journal of Geophysical Research: Oceans* 119(11), pg. 7987-8010.
- Eynaud, F. 2011. Planktonic foraminifera in the Arctic: Potentials and issues regarding modern and quaternary populations. *IOP Conference Series: Earth and Environmental Science* 14(1). 012005.

- Eynaud, F. et al. 2009. Morphological variability of the planktonic foraminifer *Neogloboquadrina pachyderma* from ACEX cores: Implications for Late Pleistocene circulation in the Arctic Ocean. *Micropaleontology* 55(2-3), pg. 101-116.
- Fairbanks, R. G. 1989. A 17,000-year glacio-eustatic sea level record: influence of glacial melting rates on the Younger Dryas event and deep-ocean circulation. *Nature* 342(6250), pg. 637-642.
- Fairbanks, R. G. et al. 1980. VERTICAL-DISTRIBUTION AND ISOTOPIC COMPOSITION OF LIVING PLANKTONIC-FORAMINIFERA IN THE WESTERN NORTH-ATLANTIC. *Science* 207(4426), pg. 61-63.
- Fairbanks, R. G. et al. 1982. VERTICAL-DISTRIBUTION AND ISOTOPIC FRACTIONATION OF LIVING PLANKTONIC-FORAMINIFERA FROM THE PANAMA BASIN. *Nature* 298(5877), pg. 841-844.
- Faure, G. 1986. *Principles of Isotope Geology*. New York, NY: John Wiley and Sons Inc., pg. 335.
- Fehrenbacher, J. S. et al. 2017. Link between light-triggered Mg-banding and chamber formation in the planktic foraminifera *Neogloboquadrina dutertrei*. *Nature Communications* 8, 15441.
- Feldmeijer, W. et al. 2013. The effect of chemical pretreatment of sediment upon foraminiferal-based proxies. *Geochemistry Geophysics Geosystems* 14(10), pg. 3996-4014.
- Fogt, R. L. a Bromwich, D. H. 2006. Decadal variability of the ENSO teleconnection to the high-latitude South Pacific governed by coupling with the southern annular mode. *Journal of Climate* 19(6), pg. 979-997.
- Fogt, R. et al. 2011. Understanding the SAM influence on the South Pacific ENSO teleconnection. *Climate Dynamics* 36(7-8), pg. 1555-1576.
- Ford, H. L. et al. 2015. Reduced El Nino-Southern Oscillation during the Last Glacial Maximum. *Science* 347(6219), pg. 255-258.
- Frew, R. D. et al. 1995. Oxygen isotope study of water masses in the Princess Elizabeth Trough, Antarctica. *Marine Chemistry* 49(2), pg. 141-153.
- Ganssen, G. M. and Kroon, D. 2000. The isotopic signature of planktonic foraminifera from NE Atlantic surface sediments: implications for the reconstruction of past oceanic conditions. *Journal of the Geological Society, London* 157(3), pg. 693-699.
- Ganssen, G. M. et al. 2011. Quantifying sea surface temperature ranges of the Arabian Sea for the past 20 000 years. *Climate of the Past* 7(4), pg. 1337-1349.
- Garabato, A. C. N. et al. 2002. Modification and pathways of Southern Ocean Deep Waters in the Scotia Sea. *Deep-Sea Research Part I-Oceanographic Research Papers* 49(4), pg. 681-705.
- Garabato, A. C. N. et al. 2003. Water mass conversion, fluxes, and mixing in the Scotia Sea diagnosed by an inverse model. *Journal of Physical Oceanography* 33(12), pg. 2565-2587.
- Garabato, A. C. N. et al. 2009. Variability of Subantarctic Mode Water and Antarctic Intermediate Water in the Drake Passage during the Late-Twentieth and Early-Twenty-First Centuries. *Journal of Climate* 22(13), pg. 3661-3688.
- Glasser, N. F. et al. 2004. Late Pleistocene and Holocene palaeoclimate and glacier fluctuations in Patagonia. *Global and Planetary Change* 43(1), pg. 79-101.

- Gleiber, M. R. et al. 2012. Time series of vertical flux of zooplankton fecal pellets on the continental shelf of the western Antarctic Peninsula. *Marine Ecology Progress Series* 471, pg. 23-36.
- Gonfiantini, R. 1986. Chapter 3 - ENVIRONMENTAL ISOTOPES IN LAKE STUDIES A2 - FRITZ, P. In: Fontes, J.C. ed. *The Terrestrial Environment*, B. Amsterdam: Elsevier, pg. 113-168.
- Gordon, A. L. and Huber, B. A. 1984. Thermohaline stratification below the Southern Ocean sea ice. *Journal of Geophysical Research: Oceans* 89(C1), pg. 641-648.
- Goudeau, M. L. S. et al. 2015. Seasonality variations in the Central Mediterranean during climate change events in the Late Holocene. *Palaeogeography Palaeoclimatology Palaeoecology* 418, pg. 304-318.
- Groeneveld, J. and Chiessi, C. M. 2011. Mg/Ca of *Globorotalia inflata* as a recorder of permanent thermocline temperatures in the South Atlantic. *Paleoceanography* 26, PA2203.
- Houghton J. T. et al. 2001. Climate change 2001: The scientific basis. *Contribution of Working Group I to the Third Assessment Report of the Intergovernmental Panel on Climate Change*. Cambridge University Press, Cambridge. pg. 881.
- Hammer, Ø. and Harper, D. A. T. 2006. *Paleontological Data Analysis*. Blackwell Publishing, pg. 351.
- Hammer, Ø. et al. 2001. PAST: Paleontological statistics software package for education and data analysis. *Palaeontologia Electronica* 4(1), pg. 9.
- Hanawa, K. and D.Talley, L. 2001. Chapter 5.4 Mode waters. In: Siedler, G. et al. eds. *International Geophysics*. Vol. 77. Academic Press, pg. 373-386.
- Hanslik, D. et al. 2010. Quaternary Arctic Ocean sea ice variations and radiocarbon reservoir age corrections. *Quaternary Science Reviews* 29(25-26), pg. 3430-3441.
- Harangozo, S. A. 2000. A search for ENSO teleconnections in the west Antarctic Peninsula climate in Austral winter. *International Journal of Climatology* 20(6), pg. 663-679.
- Hartley, H. O. 1950. THE USE OF RANGE IN ANALYSIS OF VARIANCE. *Biometrika* 37(3-4), pg. 271-280.
- Healy-Williams, N. and Williams, D. F. 1981. FOURIER-ANALYSIS OF TEST SHAPE OF PLANKTONIC-FORAMINIFERA. *Nature* 289(5797), pg. 485-487.
- Healy-Williams, N. 1992. Stable isotope differences among morphotypes of *Neogloboquadrina pachyderma* (Ehrenberg): implications for high-latitude palaeoceanographic studies. *Terra Nova* 4(6), pg. 693-700.
- Hemleben, C. et al. 1977. Test morphology, organic layers and chamber formation of the planktonic foraminifer *Globorotalia menardii* (d'Orbigny): *Journal of Foraminiferal Research*. 7, pg. 1-25.
- Hemleben, C. and Spindler, M. 1983. Recent advances in research on living planktonic foraminifera *Utrecht Micropaleontological bulletins* 30, pg. 141-170.
- Hemleben, C. et al. 1989. *Modern Planktonic Foraminifera*. New York: Springer-Verlag, pg. 376.
- Hendry, K. R. and Rickaby, R. E. M. 2008. Opal (Zn/Si) ratios as a nearshore geochemical proxy in coastal Antarctica. *Paleoceanography* 23(2). PA2218.

- Hendry, K. R. et al. 2009. Controls on stable isotope and trace metal uptake in *Neogloboquadrina pachyderma* (sinistral) from an Antarctic sea-ice environment. *Earth and Planetary Science Letters* 278(1-2), pg. 67-77.
- Heroy, D. C. et al. (2007). Holocene climate change in the Bransfield Basin, Antarctic Peninsula: evidence from sediment and diatom analysis. *Antarctic Science*, 20, pg. 69–87.
- Hibbert, F. D. et al. 2010. British Ice Sheet dynamics inferred from North Atlantic ice-rafted debris records spanning the last 175 000 years. *Journal of Quaternary Science* 25(4), pg. 461-482.
- Hilbrecht, H. 1996. Extant Planktic Foraminifera and the Physical Environment in the Atlantic and Indian Oceans: An Atlas based on CLIMAP and Levitus (1982) Data. Zurich: *Mitteilungen aus dem Geologischen Institut der Eidgen. Technischen Hochschule und der Universität Zürich, Neue Folge*, pg. 93
- Hillaire-Marcel, C. et al. 2004. Size-dependent isotopic composition of planktic foraminifers from Chukchi Sea vs. NW Atlantic sediments—implications for the Holocene paleoceanography of the western Arctic. *Quaternary Science Reviews* 23(3), pg. 245-260.
- Hodgson, D. A. et al. 2004. Paleolimnological studies from the Antarctic and sub-Antarctic islands In: Pienitz, R. et al. eds. *Developments in paleoenvironmental research volume 8. Long-term environmental change in Arctic and Antarctic Lakes* Springer, pg. 419-474.
- Hoefs, J. 1997. *Stable Isotope Geochemistry*. Berlin: Springer-Verlag. pg. 286.
- Hoffmann, G. and Heimann, M. 1997. Water isotope modeling in the Asian monsoon region. *Quaternary International* 37(Supplement C), pg. 115-128.
- Holmgren, S. U. et al. 2013. Holocene environmental changes on Nightingale Island, South Atlantic, based on diatom floristic changes in an infilled pond. *Palaeogeography Palaeoclimatology Palaeoecology* 378, pg. 45-51.
- Horel, J. D. and Wallace, J. M. 1982. PLANETARY-SCALE ATMOSPHERIC PHENOMENA ASSOCIATED WITH THE SOUTHERN OSCILLATION - REPLY. *Monthly Weather Review* 110(10), pg. 1497-1497.
- Hoskins, B. J. and Karoly, D. J. 1981. THE STEADY LINEAR RESPONSE OF A SPHERICAL ATMOSPHERE TO THERMAL AND OROGRAPHIC FORCING. *Journal of the Atmospheric Sciences* 38(6), pg. 1179-1196.
- Huber, R. et al. 2000. Shell size variation of the planktonic foraminifer *Neogloboquadrina pachyderma* sin. in the Norwegian–Greenland Sea during the last 1.3 Myrs: implications for paleoceanographic reconstructions. *Palaeogeography, Palaeoclimatology, Palaeoecology* 160(3–4), pg. 193-212.
- Jacobs, S. S. and Comiso, J. C. 1997. Climate variability in the Amundsen and Bellingshausen Seas. *Journal of Climate* 10(4), pg. 697-709.
- Jennings, A. E. et al. 2017. Ocean forcing of Ice Sheet retreat in central west Greenland from LGM to the early Holocene. *Earth and Planetary Science Letters* 472, pg. 1-13.
- Johnson, S. 2006. *Stephen Johnson on Digital Photography*. O'Reilly Media, Incorporated. pg. 320.
- Jolliffe, I. T. 2002. *Principal Component Analysis*. New York Springer-Verlag. pg. 488.

- Jongman, R. H. G. et al. 1995. *Data analysis in community and landscape ecology. 2nd Edition.* Cambridge, University of Cambridge. pg. 299.
- Jonkers, L. et al. 2010. Seasonal stratification, shell flux, and oxygen isotope dynamics of left-coiling *N. pachyderma* and *T. quinqueloba* in the western subpolar North Atlantic. *Paleoceanography* 25, pg. 13.
- Jonkers, L. et al. 2013. Seasonal patterns of shell flux, $\delta^{18}\text{O}$ and $\delta^{13}\text{C}$ of small and large *N. pachyderma* (s) and *G. bulloides* in the subpolar North Atlantic. *Paleoceanography* 28(1). pg. 164-174.
- Jonkers, L. et al. 2015. Lunar periodicity in the shell flux of planktonic foraminifera in the Gulf of Mexico. *Biogeosciences* 12(10), pg. 3061-3070.
- Jonkers, L. et al. 2016. Chamber formation leads to Mg/Ca banding in the planktonic foraminifer *Neogloboquadrina pachyderma*. *Earth and Planetary Science Letters* 451. pg. 177-184.
- Kalansky, J. et al. 2015. Southern Ocean contributions to the Eastern Equatorial Pacific heat content during the Holocene. *Earth and Planetary Science Letters* 424, pg. 158-167.
- Kennett, J. P. 1968. Latitudinal Variation in *Globigerina pachyderma* (Ehrenberg) in Surface Sediments of the Southwest Pacific Ocean. *Micropaleontology* 14(3), pg. 305-318.
- Ketten, D.R., and Edmond, J.M.. 1979. Gametogenesis and calcification of planktonic foraminifera: *Nature*. 278, pg. 546-548.
- Khider, D. et al. 2011. Assessing El Nino Southern Oscillation variability during the past millennium. *Paleoceanography* 26, pg. 20. PA3222
- Kilian, R. and Lamy, F. 2012. A review of Glacial and Holocene paleoclimate records from southernmost Patagonia (49-55 degrees S). *Quaternary Science Reviews* 53, pg. 1-23.
- Kim, S.-T. and O'Neil, J. R. 1997. Equilibrium and nonequilibrium oxygen isotope effects in synthetic carbonates. *Geochimica et Cosmochimica Acta* 61(16), pg. 3461-3475.
- King, J. C. 1994. RECENT CLIMATE VARIABILITY IN THE VICINITY OF THE ANTARCTIC PENINSULA. *International Journal of Climatology* 14(4), pg. 357-369.
- King, J. C. and Turner, J. 1997. *Antarctic Meteorology and Climatology*. Cambridge: Cambridge University Press. pg. 409
- King, J. C. et al. 2003. Antarctic peninsula climate variability and its causes as revealed by analysis of instrumental records. *Antarctic Peninsula Climate Variability: Historical and Paleoenvironmental Perspectives* 79, pg. 17-30.
- King, J. C. et al. 2013. Antarctic Peninsula Climate Variability and Its Causes as Revealed by Analysis of Instrumental Records. *Antarctic Peninsula Climate Variability: Historical and Paleoenvironmental Perspectives*. American Geophysical Union, pg. 17-30.
- Kipp, N. G. 1976. New Transfer Function for Estimating Past Sea-Surface Conditions from Sea-Bed Distribution of Planktonic Foraminiferal Assemblages in the North Atlantic. In: Cune, R.M. and Hays, J.D. eds. *Investigation of Late Quaternary Paleoceanography and Paleoclimatology*. Geological Society of America. Vol. 145.
- Kohfeld, K. E. et al. 1996. *Neogloboquadrina pachyderma* (sinistral coiling) as paleoceanographic tracers in polar oceans: Evidence from northeast water Polynya plankton tows, sediment traps, and

- surface sediments. *Paleoceanography* 11(6), pg. 679-699.
- Koutavas, A. et al. 2006. Mid-Holocene El Nino-Southern Oscillation (ENSO) attenuation revealed by individual foraminifera in eastern tropical Pacific sediments. *Geology* 34(12), pg. 993-996.
- Koutavas, A. and Joanides, S. 2012. El Nino-Southern Oscillation extrema in the Holocene and Last Glacial Maximum. *Paleoceanography* 27. PA4208.
- Kozdon, R. et al. 2009. Intratest oxygen isotope variability in the planktonic foraminifer *N. pachyderma*: Real vs. apparent vital effects by ion microprobe. *Chemical Geology* 258(3-4), pg. 327-337.
- Kroopnick, P. et al. 1972. Total CO₂, ¹³C, and dissolved δ¹⁸O at Geosecs II in the North Atlantic. *Earth and Planetary Science Letters* 16(1), pg. 103-110.
- Kroopnick, P. M. 1985. The distribution of ¹³C of ΣCO₂ in the world oceans. *Deep Sea Research Part A. Oceanographic Research Papers* 32(1), pg. 57-84.
- Kucera, M. and Kennett, J. P. 2002. Causes and consequences of a middle Pleistocene origin of the modern planktonic foraminifer *Neogloboquadrina pachyderma* sinistral. *Geology* 30(6), pg. 539-542.
- Kucera, M. 2007. Chapter Six Planktonic Foraminifera as Tracers of Past Oceanic Environments. *Developments in Marine* 1, pg. 213-262.
- Kuroyanagi, A. et al. 2011. Seasonal variation in the oxygen isotopic composition of different-sized planktonic foraminifer *Neogloboquadrina pachyderma* (sinistral) in the northwestern North Pacific and implications for reconstruction of the paleoenvironment. *Paleoceanography* 26. PA4215.
- Kwok, R. and Comiso, J. C. 2002. Southern Ocean climate and sea ice anomalies associated with the Southern Oscillation. *Journal of Climate* 15(5), pg. 487-501.
- Lamy, F. et al. 2001. Holocene rainfall variability in southern Chile: a marine record of latitudinal shifts of the Southern Westerlies. *Earth and Planetary Science Letters* 185(3-4), pg. 369-382.
- Lamy, F. et al. 2010. Holocene changes in the position and intensity of the southern westerly wind belt. *Nature Geoscience* 3(10), pg. 695-699.
- Lamy, F. et al. 2002. High- and low-latitude climate control on the position of the southern Peru-Chile Current during the Holocene. *Paleoceanography* 17(2). pg. 16-1 – 16-10. PA1028.
- Larter, R. D. et al. 2011. *RRS James Clark Ross, Cruise JR244: Marine Geoscience and Physical Oceanography, Southern Weddell Sea and South Orkney Continental Shelf, January to March 2011*. British Antarctic Survey, Cambridge.
- Lea, DW. et al. (1995) *Calcium-uptake and Calcification Rate in the Planktonic Foraminifer Orbulina universa*. *Journal of Foraminiferal Research*. 25(1) pg.14-23.
- Leduc, G. et al. 2009. Modes of eastern equatorial Pacific thermocline variability: Implications for ENSO dynamics over the last glacial period. *Paleoceanography* 24, PA3202.
- Lefebvre, W. and Goosse, H. 2005. Influence of the Southern Annular Mode on the sea ice-ocean system: the role of the thermal and mechanical forcing. *Ocean Science* 1(3), pg. 145-157.
- Lefebvre, W. et al. 2004. Influence of the Southern Annular Mode on the sea ice-ocean system. *Journal of Geophysical Research-Oceans* 109(C9), C09005.

- Lehman, S. J. and Keigwin, L. D. 1992. SUDDEN CHANGES IN NORTH-ATLANTIC CIRCULATION DURING THE LAST DEGLACIATION. *Nature* 356(6372), pg. 757-762.
- Lehmann, E. L. and Romano, J. P. 2005. *Testing Statistical Hypotheses*. New York, USA: Springer-Verlag pg. 786.
- Levene, H. 1960. Robust tests for equality of variances. In: Olkin, I. and Hotelling, H. eds. *Contributions to Probability and Statistics: Essays in Honor of Harold Hotelling*. Stanford University Press, pg. 278–292.
- Leventer, A. et al. 1993. Diatom evidence for late Holocene climatic events in Granite Harbor, Antarctica, *Paleoceanography*, 8, pg. 373–386.
- Leventer, A. et al. 2002. Laminations from the Palmer Deep: A diatom-based interpretation. *Paleoceanography* 17(3), pg. PAL 3-1-PAL 3-15.
- Leventer, A. et al. 2006. Marine sediment record from East Antarctica margin reveals dynamics of ice-sheet recession. *GSA Today*. 16. 10.1130/GSAT01612A.1.
- Li, Z. X. 2000. Influence of Tropical Pacific El Niño on the SST of the Southern Ocean through atmospheric bridge. *Geophysical Research Letters* 27(21), pg. 3505-3508.
- Little, M. G. et al. 1997. Rapid palaeoceanographic changes in the Benguela Upwelling System for the last 160,000 years as indicated by abundances of planktonic foraminifera. *Palaeogeography Palaeoclimatology Palaeoecology* 130(1-4), pg. 135-161.
- Livermore, R. et al. 2005. Paleogene opening of Drake Passage. *Earth and Planetary Science Letters* 236(1-2), pg. 459-470.
- Locarnini, R. A. et al. 2013. *World Ocean Atlas 2013, Volume 1: Temperature*. Silver Spring, MD: NOAA, pg. 40.
- Lohmann, G. P. 1995. A MODEL FOR VARIATION IN THE CHEMISTRY OF PLANKTONIC-FORAMINIFERA DUE TO SECONDARY CALCIFICATION AND SELECTIVE DISSOLUTION. *Paleoceanography* 10(3), pg. 445-457.
- Lončarić, N. et al. 2006. Oxygen isotope ecology of recent planktic foraminifera at the central Walvis Ridge (SE Atlantic). *Paleoceanography* 21(3), PA3009.
- Malmgren, B. et al. 1972. Biometric Analysis of Phenotypic Variation: *Globigerina pachyderma* (Ehrenberg) in the South Pacific Ocean. *Micropaleontology* 18(2), pg. 241-248.
- Malmgren, B. A. 1983. RANKING OF DISSOLUTION SUSCEPTIBILITY OF PLANKTONIC-FORAMINIFERA AT HIGH-LATITUDES OF THE SOUTH-ATLANTIC OCEAN. *Marine Micropaleontology* 8(3), pg. 183-191.
- Marshall, G. 2016. *The Climate Data Guide: Marshall Southern Annular Mode (SAM) Index (Station-based)*. [Online]. Available on: <https://climatedataguide.ucar.edu/climate-data/marshall-southern-annular-mode-sam-index-station-based> [Accessed]: 5/05/2016.
- Marshall, G. J. 2003a. Trends in the southern annular mode from observations and reanalyses. *Journal of Climate* 16(24), pg. 4134-4143.
- Marshall, G. J. 2003b. Trends in the Southern Annular Mode from Observations and Reanalyses. *Journal of Climate* 16(24), pg. 4134-4143.

- Marshall, G. J. and Bracegirdle, T. J. 2015. An examination of the relationship between the Southern Annular Mode and Antarctic surface air temperatures in the CMIP5 historical runs. *Climate Dynamics* 45(5-6), pg. 1513-1535.
- Marshall, G. J. et al. 2006. The impact of a changing Southern Hemisphere Annular Mode on Antarctic Peninsula summer temperatures. *Journal of Climate* 19(20), pg. 5388-5404.
- Martinson, D. G. and McKee, D. C. 2012. Transport of warm Upper Circumpolar Deep Water onto the western Antarctic Peninsula continental shelf. *Ocean Science* 8(4), pg. 433-442.
- Martinson, D. G. et al. 2008. Western Antarctic Peninsula physical oceanography and spatio-temporal variability. *Deep-Sea Research Part II-Topical Studies in Oceanography* 55(18-19), pg. 1964-1987.
- Massom, R. A. et al. 2006. Extreme anomalous atmospheric circulation in the West Antarctic Peninsula region in Austral Spring and Summer 2001/02, and its profound impact on sea ice and biota. *Journal of Climate* 19(15), pg. 3544-3571.
- Masson, V. et al. 2000. Holocene climate variability in Antarctica based on 11 ice-core isotopic records. *Quaternary Research* 54(3), pg. 348-358.
- Matsumoto, K. et al. 2001. Similar glacial and Holocene Southern Ocean hydrography, *Paleoceanography*, 16(5), pg. 445-454.
- Matthews, A. J. and Meredith, M. P. 2004. Variability of Antarctic circumpolar transport and the Southern Annular Mode associated with the Madden-Julian Oscillation. *Geophysical Research Letters* 31(24), L24312.
- McCartney, M. S. 1977. Subantarctic Mode Water. In: Angel, M.V. ed. *A Voyage of Discovery: George Deacon 70th Anniversary Volume*. Oxford: Pergamon Press, pg. 103-119.
- McConnaughey, T. 1989. ^{13}C and ^{18}O isotopic disequilibrium in biological carbonates: II. In vitro simulation of kinetic isotope effects. *Geochimica et Cosmochimica Acta* 53(1), pg. 163-171.
- Meredith, M. P. et al. 1999. Distribution of oxygen isotopes in the water masses of Drake Passage and the South Atlantic. *Journal of Geophysical Research-Oceans* 104(C9), pg. 20949-20962.
- Meredith, M. P. et al. 2004a. Impact of the 1997/98 ENSO on upper ocean characteristics in Marguerite Bay, western Antarctic Peninsula. *Journal of Geophysical Research-Oceans* 109(C9). C09013
- Meredith, M. P. et al. 2004b. Changes in the ocean transport through Drake Passage during the 1980s and 1990s, forced by changes in the Southern Annular Mode. *Geophysical Research Letters* 31(21), L21305.
- Meredith, M. P. and King, J. C. 2005. Rapid climate change in the ocean west of the Antarctic Peninsula during the second half of the 20th century. *Geophysical Research Letters* 32(19). L19604.
- Meredith, M. P. et al. 2008a. Variability in the freshwater balance of northern Marguerite Bay, Antarctic Peninsula: Results from $\delta\text{O}-18$. *Deep-Sea Research Part II-Topical Studies in Oceanography* 55(3-4), pg. 309-322.
- Meredith, M. P. et al. 2008b. On the interannual variability of ocean temperatures around South Georgia, Southern Ocean: Forcing by El Niño/Southern Oscillation and the Southern Annular Mode.

Deep-Sea Research Part II-Topical Studies in Oceanography 55(18-19), pg. 2007-2022.

Meredith, M. P. et al. 2010. Changes in the freshwater composition of the upper ocean west of the Antarctic Peninsula during the first decade of the 21st century. *Progress in Oceanography* 87(1-4), pg. 127-143.

Meredith, M. P. et al. 2011. SUSTAINED MONITORING OF THE SOUTHERN OCEAN AT DRAKE PASSAGE: PAST ACHIEVEMENTS AND FUTURE PRIORITIES. *Reviews of Geophysics* 49, RG4005.

Meredith, M. P. et al. 2013. The Freshwater System West of the Antarctic Peninsula: Spatial and Temporal Changes. *Journal of Climate* 26(5), pg. 1669-1684.

Meredith, M. P. et al. 2017. Changing distributions of sea ice melt and meteoric water west of the Antarctic Peninsula. *Deep-Sea Research Part II-Topical Studies in Oceanography* 139, pg. 40-57.

Metcalfe, B. et al. 2015. Late Pleistocene glacial-interglacial shell-size-isotope variability in planktonic foraminifera as a function of local hydrography. *Biogeosciences* 12(15), pg. 4781-4807.

Moller, T. et al. 2013. The effect of sea surface properties on shell morphology and size of the planktonic foraminifer *Neogloboquadrina pachyderma* in the North Atlantic. *Palaeogeography Palaeoclimatology Palaeoecology* 391, pg. 34-48.

Montes-Hugo, M. et al. 2009. Recent Changes in Phytoplankton Communities Associated with Rapid Regional Climate Change Along the Western Antarctic Peninsula. *Science* 323(5920), pg. 1470-1473.

Morard, R. et al. 2011. Worldwide Genotyping in the Planktonic Foraminifer *Globocoinella inflata*: Implications for Life History and Paleoceanography. *Plos One* 6(10). e26665.

Morard, R. et al. 2016. Tracing shifts of oceanic fronts using the cryptic diversity of the planktonic foraminifera *Globorotalia inflata*. *Paleoceanography* 31(9), pg. 1193-1205.

Mortyn, P. G. and Charles, C. D. 2003. Planktonic foraminiferal depth habitat and delta O-18 calibrations: Plankton tow results from the Atlantic sector of the Southern Ocean. *Paleoceanography* 18(2). 1037.

Mosby, H. 1934. The waters of the Atlantic Antarctic Ocean. *Scientific Results of the Norwegian Antarctic Expedition* 11. Pg.1-131.

Moy, C. M. et al. 2002. Variability of El Nino/Southern Oscillation activity at millennial timescales during the Holocene epoch. *Nature* 420(6912), pg. 162-165.

Mulitza, S. et al. 1997. Planktonic Foraminifera as recorders of past surface-water stratification. *Geology* 25(4) pg. 335-338.

Niebler, H. S. and Gersonde, R. 1998. A planktic foraminiferal transfer function for the southern South Atlantic Ocean. *Marine Micropaleontology* 34(3-4), pg. 213-234.

Niebler, H.-S. et al. 1999. *Oxygen Isotope Values of Planktic Foraminifera: A Tool for the Reconstruction of Surface Water Stratification*. pg. 165-189.

Ninnemann, U. S. a Charles, C. D. 1997. Regional differences in Quaternary Subantarctic nutrient cycling: Link to intermediate and deep water ventilation. *Paleoceanography* 12(4), pg. 560-567.

Orsi, A. H. and Whitworth III, T. 2005. *Hydrographic Atlas of the World Ocean Circulation*

Experiment (WOCE). Volume 1: Southern Ocean. Southampton, U.K.: International WOCE Project Office.

Orsi, A. H. et al. 1995. ON THE MERIDIONAL EXTENT AND FRONTS OF THE ANTARCTIC CIRCUMPOLAR CURRENT. *Deep-Sea Research Part I-Oceanographic Research Papers* 42(5), pg. 641-673.

Ortiz, J. D. et al. 1996. Deep-dwelling planktonic foraminifera of the northeastern Pacific Ocean reveal environmental control of oxygen and carbon isotopic disequilibria. *Geochimica et Cosmochimica Acta* 60(22), pg. 4509-4523.

Panizzo, V. et al. 2013. Sea ice diatom contributions to Holocene nutrient utilization in East Antarctica, *Paleoceanography*, 29, pg. 328–342.

Peck, V. L. et al. 2015. Oceanographic variability on the West Antarctic Peninsula during the Holocene and the influence of upper circumpolar deep water. *Quaternary Science Reviews* 119, pg. 54-65.

Peeters, F. J. C. et al. 2002. The effect of upwelling on the distribution and stable isotope composition of *Globigerina bulloides* and *Globigerinoides ruber* (planktic foraminifera) in modern surface waters of the NW Arabian Sea. *Global and Planetary Change* 34(3), pg. 269-291.

Peterson, R. G. and Whitworth, T. 1989. THE SUB-ANTARCTIC AND POLAR FRONTS IN RELATION TO DEEP-WATER MASSES THROUGH THE SOUTHWESTERN ATLANTIC. *Journal of Geophysical Research-Oceans* 94(C8), pg. 10817-10838.

Pflaumann, U. et al. 1996. SIMMAX: A modern analog technique to deduce Atlantic sea surface temperatures from planktonic foraminifera in deep-sea sediments. *Paleoceanography* 11(1), pg. 15-35.

Philander, S. G. H. 1983. EL-NINO SOUTHERN OSCILLATION PHENOMENA. *Nature* 302(5906), pg. 295-301.

Pike, J. et al. 2013. Glacial discharge along the west Antarctic Peninsula during the Holocene. *Nature Geoscience* 6(3), pg. 199-202.

Poppe, L. J. et al. 2000. Grain-size analysis of marine sediments: Methodology and data processing. In: Poppe, L.J. ed. *USGS East-Coast sediment analysis: Procedures, database, and georeferenced displays* USGS, Coastal and Marine Geology, Woods Hole Field Center.

Portilho-Ramos, R. D. et al. 2014. PLANKTONIC FORAMINIFERAL VARIATIONS IN THE SOUTHWESTERN ATLANTIC SINCE THE LAST GLACIAL-INTERGLACIAL CYCLE. *Palaios* 29(1-2), pg. 38-44.

Prezelin, B. B. et al. 2000. The linkage between Upper Circumpolar Deep Water (UCDW) and phytoplankton assemblages on the west Antarctic Peninsula continental shelf. *Journal of Marine Research* 58(2), pg. 165-202.

Prezelin, B. B. et al. 2004. Physical forcing of phytoplankton community structure and primary production in continental shelf waters of the Western Antarctic Peninsula. *Journal of Marine Research* 62(3), pg. 419-460.

Pritchard, H. D. et al. 2012. Antarctic ice-sheet loss driven by basal melting of ice shelves. *Nature* 484(7395), pg. 502-505.

Pritchard, H. D. and Vaughan, D. G. 2007. Widespread acceleration of tidewater glaciers on the

- Antarctic Peninsula. *Journal of Geophysical Research-Earth Surface* 112, F03S29.
- Rasmusson, E. M. and Wallace, J. M. 1983. METEOROLOGICAL ASPECTS OF THE EL-NINO SOUTHERN OSCILLATION. *Science* 222(4629), pg. 1195-1202.
- Ravelo, A. C. and Hillaire-Marcel, C. 2007. Chapter Eighteen: The Use of Oxygen and Carbon Isotopes of Foraminifera in Paleoceanography. In: Hillaire-Marcel, C. and De Vernal, A. eds. *Developments in Marine Geology*. Vol. 1. Elsevier, pg. 735-764.
- Reiss, Z. 1957. The Bilamellidea, now superfamily and remarks on Cretaceous globorotaliids. *Cushman Found. Foram. Res. Contr* 8, pg. 127-145.
- Renssen, H. et al. 2005. Holocene climate evolution in the high-latitude Southern Hemisphere simulated by a coupled atmosphere-sea ice-ocean-vegetation model. *Holocene* 15(7), pg. 951-964.
- Renwick, J. A. 2005. Persistent positive anomalies in the Southern Hemisphere circulation. *Monthly Weather Review* 133(4), pg. 977-988.
- Reynolds, R. W. et al. 2002. An Improved In Situ and Satellite SST Analysis for Climate. *Journal of Climate* 15(13), pg. 1609-1625.
- Reynolds, R. W. and Smith, T. M. 1994. Improved Global Sea Surface Temperature Analyses Using Optimum Interpolation. *Journal of Climate* 7(6), pg. 929-948.
- Roberts, J. 2016. *Insights into Glacial Terminations from a South Atlantic Perspective*. Ph.D Thesis. University of Cambridge.
- Roberts, J. et al. 2016. Evolution of South Atlantic density and chemical stratification across the last deglaciation. *Proceedings of the National Academy of Sciences*. 113. (3). pg. 514-519.
- Roberts, J. et al. 2017. Deglacial changes in flow and frontal structure through the Drake Passage. *Earth and Planetary Science Letters*, 474. pp. 397-408.
- Rohling, E. J. and Bigg, G. R. 1998. Paleosalinity and $\delta^{18}\text{O}$: A critical assessment. *Journal of Geophysical Research: Oceans* 103(C1), pg. 1307-1318.
- Rohling, E. J. and Cooke, S. 1999. Stable oxygen and carbon isotopes in foraminiferal carbonate shells. In: Sen Gupta, B.K. ed. *Modern Foraminifera*. Dordrecht: Springer Netherlands, pg. 239-258.
- Rohling, E. J. and Palike, H. 2005. Centennial-scale climate cooling with a sudden cold event around 8,200 years ago. *Nature* 434(7036), pg. 975-979.
- Rosenthal, Y. et al. 2013. Pacific Ocean Heat Content During the Past 10,000 Years. *Science* 342(6158), pg. 617-621.
- Rozanski, K. et al. 1993. Isotopic Patterns in Modern Global Precipitation. In: Swart, P.K. et al. eds. *Climate Change in Continental Isotopic Records*. Washington, DC: American Geophysical Union, pg. 1-36.
- Sagawa, T. et al. 2013. Seasonal variations in planktonic foraminiferal flux and oxygen isotopic composition in the western North Pacific: Implications for paleoceanographic reconstruction. *Marine Micropaleontology* 100, pg. 11-20.
- Salmon, K. H. et al. 2015. Upper ocean mixing controls the seasonality of planktonic foraminifer fluxes and associated strength of the carbonate pump in the oligotrophic North Atlantic. *Biogeosciences* 12(1), pg. 223-235.

- Savidge, D. K. and Amft, J. A. 2009. Circulation on the West Antarctic Peninsula derived from 6 years of shipboard ADCP transects. *Deep-Sea Research Part I-Oceanographic Research Papers* 56(10), pg. 1633-1655.
- Schiebel, R. and Hemleben, C. 2005. Modern Planktic Foraminifera. *Paläontologische Zeitschrift* 79(1), pg. 135-148.
- Schmidt, G. A. et al. 1999. *Global Seawater Oxygen-18 Database - v1.22* [Online]. <https://data.giss.nasa.gov/o18data/> Available on: [Accessed: 07/2016].
- Schmidt, D. N. et al. 2004a. Size distribution of Holocene planktic foraminifer assemblages: biogeography, ecology and adaptation. *Marine Micropaleontology* 50(3-4), pg. 319-338.
- Schmidt, D. N. et al. 2004b. The evolutionary history of size variation of planktic foraminiferal assemblages in the Cenozoic. *Palaeogeography Palaeoclimatology Palaeoecology* 212(1-2), pg. 159-180.
- Schmidt, R. et al. 1990. Holocene diatom flora and stratigraphy from sediment cores of two Antarctic lakes (King George Island). *Journal of Paleolimnology* 3(1), pg. 55-74.
- Scropton, N. et al. 2011. Persistent El Nino-Southern Oscillation variation during the Pliocene Epoch. *Paleoceanography* 26.
- Shackleton, N. J. and Opdyke, N. D. 1973. Oxygen isotope and palaeomagnetic stratigraphy of Equatorial Pacific core V28-238: Oxygen isotope temperatures and ice volumes on a 105 year and 106 year scale. *Quaternary Research* 3(1), pg. 39-55.
- Shevenell, A. et al. 1996. Record of Holocene palaeoclimate change along the Antarctic Peninsula: evidence from glacial marine sediments, Lallemand Fjord. *Papers and Proceedings of the Royal Society of Tasmania*, 130 (2). pg. 55-64.
- Shevenell, A. E. et al. 2011. Holocene Southern Ocean surface temperature variability west of the Antarctic Peninsula, *Nature*, 470, pg. 250–254.
- Simstich, J. et al. 2003. Paired $\delta^{18}\text{O}$ signals of *Neogloboquadrina pachyderma* (s) and *Turborotalita quinqueloba* show thermal stratification structure in Nordic Seas. *Marine Micropaleontology* 48(1–2), pg. 107-125.
- Sirota, A. and Sundakov, A. 2014. *Seasonal variation in oceanographic conditions on the eastern and southern parts of the shelf and continental slope of the Falklands Islands in 1999-2014*. Marine Satellite Technologies. pg.26.
- Skvarca, P. and De Angelis, H. 2013. Impact Assessment of Regional Climatic Warming on Glaciers and Ice Shelves of the Northeastern Antarctic Peninsula. *Antarctic Peninsula Climate Variability: Historical and Paleoenvironmental Perspectives*. American Geophysical Union, pg. 69-78.
- Sloyan, B. M. and Rintoul, S. R. 2001. Circulation, renewal, and modification of Antarctic mode and intermediate water. *Journal of Physical Oceanography* 31(4), pg. 1005-1030.
- Smith, D. A. and Klinck, J. M. 2002. Water properties on the west Antarctic Peninsula continental shelf: a model study of effects of surface fluxes and sea ice. *Deep-Sea Research Part II-Topical Studies in Oceanography* 49(21), pg. 4863-4886.
- Smith, J. A. et al. 2010. The presence of polynyas in the Weddell Sea during the Last Glacial Period

- with implications for the reconstruction of sea-ice limits and ice sheet history. *Earth and Planetary Science Letters* 296(3-4), pg. 287-298.
- Smith, R. C. et al. 1995. The Palmer LTER: A long-term ecological research program at Palmer Station, Antarctic. *Oceanography* 8(3), pg. 77-86.
- Smith, R. C. et al. 2008. Bellingshausen and western Antarctic Peninsula region: Pigment biomass and sea-ice spatial/temporal distributions and interannual variability. *Deep Sea Research Part II: Topical Studies in Oceanography* 55(18), pg. 1949-1963.
- Smith, W. O. and Nelson, D. M. 1985. Phytoplankton Bloom Produced by a Receding Ice Edge in the Ross Sea: Spatial Coherence with the Density Field. *Science* 227(4683), pg. 163-166.
- Spero, H. J. and Parker, S. L. 1985. Photosynthesis in the symbiotic planktonic foraminifer *Orbulina universa*, and its potential contribution to oceanic primary productivity. *The Journal of Foraminiferal Research* 15(4), pg. 273-281.
- Spero, H. J. and Williams, D. F. 1990. EVIDENCE FOR SEASONAL LOW-SALINITY SURFACE WATERS IN THE GULF OF MEXICO OVER THE LAST 16,000 YEARS. *Paleoceanography* 5(6), pg. 963-975.
- Spero, H. J. 1992. Do planktic foraminifera accurately record shifts in the carbon isotopic composition of seawater ΣCO_2 ? *Marine Micropaleontology* 19(4), pg. 275-285.
- Spero, H. J. and Lea, D. W. 1993. Intraspecific stable isotope variability in the planktic foraminifera *Globigerinoides sacculifer*: Results from laboratory experiments. *Marine Micropaleontology* 22(3), pg. 221-234.
- Spero, H. J. and Lea, D. W. 1996. Experimental determination of stable isotope variability in *Globigerina bulloides*: implications for paleoceanographic reconstructions. *Marine Micropaleontology* 28(3), pg. 231-246.
- Spero, H. et al. 1997. Effect of seawater carbonate concentration on foraminiferal carbon and oxygen isotopes. *Nature* 390, pg. 497-500.
- Spindler, M. 1990. A COMPARISON OF ARCTIC AND ANTARCTIC SEA ICE AND THE EFFECTS OF DIFFERENT PROPERTIES ON SEA ICE BIOTA. *Geological History of the Polar Oceans: Arctic Versus Antarctic* 308, pg. 173-186.
- Spindler, M. 1996. On the salinity tolerance of the planktonic foraminifera *Neogloboquadrina pachyderma* from Antarctic sea ice. *Proceedings of the NIPR Symposium on Polar Biology* 9, pg. 85-91.
- Spindler, M. et al. 1978. LIGHT AND ELECTRON-MICROSCOPIC OBSERVATIONS OF GAMETOGENESIS IN *HASTIGERINA-PELAGICA* (FORAMINIFERA). *Journal of Protozoology* 25(4), pg. 427-433.
- Spindler, M. et al. 1979. LUNAR PERIODICITY OF REPRODUCTION IN THE PLANKTONIC FORAMINIFER *HASTIGERINA-PELAGICA*. *Marine Ecology Progress Series* 1(1), pg. 61-64.
- Stammerjohn, S. E. et al. 2003. Ice-atmosphere interactions during sea-ice advance and retreat in the western Antarctic Peninsula region. *Journal of Geophysical Research-Oceans* 108(C10). 3329.
- Stammerjohn, S. E. et al. 2008a. Sea ice in the western Antarctic Peninsula region: Spatio-temporal variability from ecological and climate change perspectives. *Deep-Sea Research Part II-Topical Studies in Oceanography* 55(18-19), pg. 2041-2058.

- Stammerjohn, S. E. et al. 2008b. Trends in Antarctic annual sea ice retreat and advance and their relation to El Niño-Southern Oscillation and Southern Annular Mode variability. *Journal of Geophysical Research-Oceans* 113(C3). C03S90.
- Stangeew, E. 2001. *Distribution and isotopic composition of living planktonic foraminifera N. pachyderma (sinistral) and T. quinqueloba in the high latitude North Atlantic*. Ph.D. Thesis. Universität zu Kiel, Germany.
- Stehman, C. F. 1972. Planktonic Foraminifera in Baffin Bay, Davis Strait and the Labrador Sea. *Maritime Sediments* Vol 8(1). pg 13-19.
- Steinhardt, J. et al. 2015. Reconciling single-chamber Mg/Ca with whole-shell delta O-18 in surface to deep-dwelling planktonic foraminifera from the Mozambique Channel. *Biogeosciences* 12(8), pg. 2411-2429.
- Stephens, M. A. 1974. EDF Statistics for Goodness of Fit and Some Comparisons. *Journal of the American Statistical Association* 69(347). pg. 730-737.
- Stephens, M. A. 1986. Tests Based on EDF Statistics. In: d'Agostino, R.B. and Stephens, M.A. eds. *Goodness-of-Fit Techniques*. New York: Marcel Dekker, pg. 97-193.
- Stott, L. et al. 2004. Decline of surface temperature and salinity in the western tropical Pacific Ocean in the Holocene epoch. *Nature* 431(7004), pg. 56-59.
- Swann, G. E. A. et al. 2013. Seasonally resolved diatom delta O-18 records from the West Antarctic Peninsula over the last deglaciation. *Earth and Planetary Science Letters* 364, pg. 12-23.
- Swann, G. E. A. et al. 2017. Temporal controls on silicic acid utilisation along the West Antarctic Peninsula. *Nature Communications* 8, pg. 14645.
- Talley, L. D. 1996. Antarctic Intermediate Water in the South Atlantic. *The South Atlantic: Present and Past Circulation*. Berlin, Heidelberg: Springer Berlin Heidelberg, pg. 219-238.
- Taylor, F. and McMinn, A., 2001. Evidence from diatoms for Holocene climate fluctuation along the East Antarctic margin. *Holocene*, 11(4) Pg. 455-466
- Taylor, F., J. et al. 2001. Holocene paleoclimate change in the Antarctic Peninsula: Evidence from the diatom, sedimentary and geochemical record, *Marine Micropaleontology*. 41, pg. 25–43.
- Thompson, D. W. J. and Wallace, J. M. 2000. Annular modes in the extratropical circulation. Part I: Month-to-month variability. *Journal of Climate* 13(5), pg. 1000-1016.
- Tolderlund, D. S. et al. 1971. Seasonal Distribution of Planktonic Foraminifera in the Western North Atlantic. *Micropaleontology* 17(3), pg. 297-329.
- Tolderlund, D.S, and Bd, A.WJJ, 1971. Seasonal distribution of planktonic foraminifera in the western North Atlantic: *Micropaleontology*. 17, pg. 297-329.
- Townend, J. 2002. *Practical Statistics for Environmental and Biological Scientists*. Chichester, UK: John Wiley & Sons Ltd, t. 288.
- Turner, J. 2004. The El Niño-southern oscillation and Antarctica. *International Journal of Climatology* 24(1), pg. 1-31.
- Turner, J. et al. 2016. Absence of 21st century warming on Antarctic Peninsula consistent with

natural variability. *Nature* 535(7612), pg. 411-415.

Unkel, I. et al. 2010. Records of environmental changes during the Holocene from Isla de los Estados (54.4°S), southeastern Tierra del Fuego. *Global and Planetary Change* 74(3–4), pg. 99-113.

Upton, G. and Cook, I. 1996. *Understanding Statistics*. OUP Oxford. pg. 672.

van Loon, H. 1967. The half-yearly oscillations in middle and high southern latitudes and the coreless winter *Journal of the Atmospheric Sciences* 24(5), pg. 472-486.

van Wessem, J. M. et al. 2015. Temperature and Wind Climate of the Antarctic Peninsula as Simulated by a High-Resolution Regional Atmospheric Climate Model. *Journal of Climate* 28(18), pg. 7306-7326.

Varma, V. et al. 2011. Solar-forced shifts of the Southern Hemisphere Westerlies during the Holocene. *Climate of the Past* 7(2), pg. 339-347.

Vaughan, D. G. et al. 2003. Recent rapid regional climate warming on the Antarctic Peninsula. *Climatic Change* 60(3), pg. 243-274.

Vautravers, M. J. et al. 2013. Palaeoenvironmental records from the West Antarctic Peninsula drift sediments over the last 75 ka. In: Hambrey, M.J., Barker, P. F., Barrett, P. J., Bowman, V., Davies, B., Smellie, J. L. & Tranter, M. eds. *Antarctic Palaeoenvironments and Earth-Surface Processes*. London: Geological Society, London, Special Publications, pg. 263-276.

Venables, H. et al. 2012. Fronts and habitat zones in the Scotia Sea. *Deep Sea Research II*, 59-60. pg. 14-24.

Vincent, E. and Berger, W. H. 1981. Planktonic foraminifera and their use in Paleoclimatology. In: Emiliani, C. ed. *The oceanic lithosphere. The sea*. Vol. 7. Hoboken, N. J.: Wiley-Interscience, pg. 1025-1119.

Voigt, I. et al. 2016. Holocene changes in Antarctic Intermediate Water flow strength in the Southwest Atlantic. *Palaeogeography Palaeoclimatology Palaeoecology* 463, pg. 60-67.

Volkman, R. a Mensch, M. 2001. Stable isotope composition ($\delta^{18}\text{O}$, $\delta^{13}\text{C}$) of living planktic foraminifers in the outer Laptev Sea and the Fram Strait. *Marine Micropaleontology* 42(3-4), pg. 163-188.

von Gyldenfeldt, A. B. et al. 2000. Estimation of the catchment area of a sediment trap by means of current meters and foraminiferal tests. *Deep-Sea Research Part II-Topical Studies in Oceanography* 47(9-11), pg. 1701-1717.

Watkins, A. B. and Simmonds, I. 1999. A late spring surge in the open water of the Antarctic sea ice pack. *Geophysical Research Letters* 26(10), pg. 1481-1484.

Watkins, J. 2016. *JR304: Ecosystems, Western Core Box & Moorings Incorporating CGS projects 95, 99 and 101*. Cambridge, UK: British Antarctic Survey.

Wefer, G. and Berger, W. H. 1991. Isotope paleontology: growth and composition of extant calcareous species. *Marine Geology* 100(1), pg. 207-248.

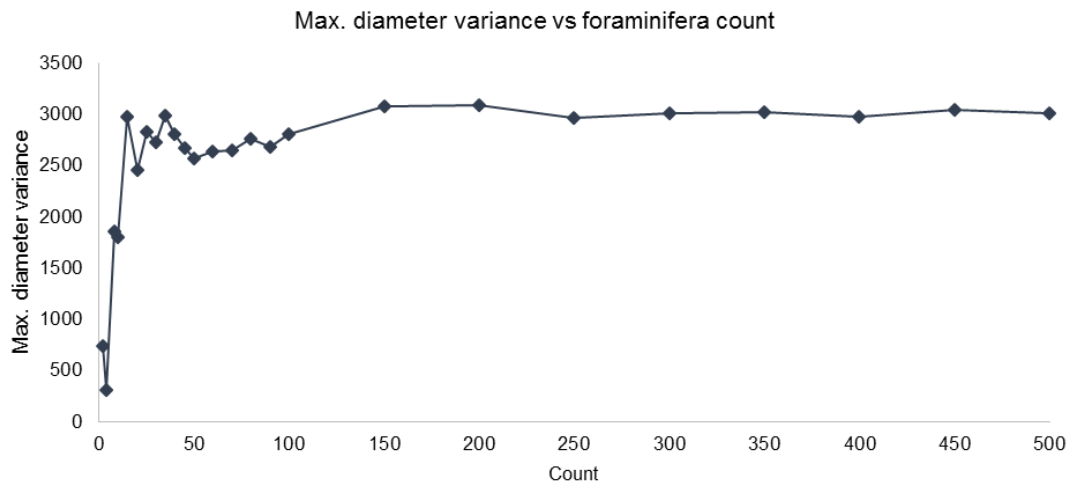
Weiss, R. F. et al. 1979. Geochemical studies of the Weddell Sea. *Deep Sea Research Part A. Oceanographic Research Papers* 26(10), pg. 1093-1120.

- Wenzens, G. 2005. *Glacier advances east of the Southern Andes between the Last Glacial Maximum and 5,000 BP compared with lake terraces of the endorheic Lago Cardiel (49°S, Patagonia, Argentina)*. *Zeitschrift für Geomorphologie*, NF 49(4) pg. 433-454.
- White, W. B. and Peterson, R. G. 1996. An Antarctic circumpolar wave in surface pressure, wind, temperature and sea-ice extent. *Nature* 380(6576), pg. 699-702.
- Whitworth, T. 1980. ZONATION AND GEOSTROPHIC FLOW OF THE ANTARCTIC CIRCUMPOLAR CURRENT AT DRAKE PASSAGE. *Deep-Sea Research Part a-Oceanographic Research Papers* 27(7), pg. 497-507.
- Wilke, I. et al. 2006. The influence of seawater carbonate ion concentration CO_3^{2-} on the stable carbon isotope composition of the planktic foraminifera species *Globorotalia inflata*. *Marine Micropaleontology* 58(4), pg. 243-258.
- Williams, D. F. et al. 1988. Shape and isotopic differences between conspecific foraminiferal morphotypes and resolution of paleoceanographic events. *Palaeogeography, Palaeoclimatology, Palaeoecology* 64(3), pg. 153-162.
- Wit, J. C. et al. 2010. Approaches to unravel seasonality in sea surface temperatures using paired single-specimen foraminiferal $\delta^{18}O$ and Mg/Ca analyses. *Paleoceanography* 25, PA4220.
- Wolter, K. 2016. *Multivariate ENSO index* [Online]. Earth System Research Laboratory, NOAA: Available on: <https://www.esrl.noaa.gov/psd/enso/mei/> [Accessed: 15/05/2016].
- Wolter, K. and Timlin, M. S. 1998. Measuring the strength of ENSO events: How does 1997/98 rank? *Weather* 53(9), pg. 315-324.
- Yuan, X. J. 2004. ENSO-related impacts on Antarctic sea ice: a synthesis of phenomenon and mechanisms. *Antarctic Science* 16(4), pg. 415-425.
- Zweng, M. M. et al. 2013. *World Ocean Atlas 2013, Volume 2: Salinity*. Silver Spring, MD: NOAA, pg. 39.

Appendix

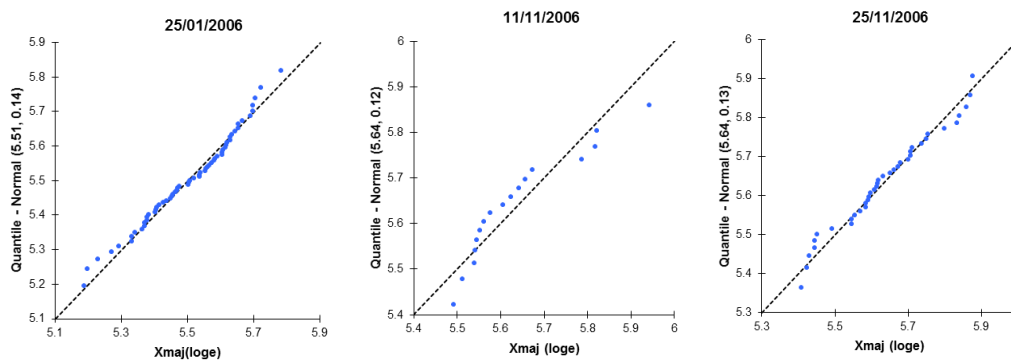
A1. Palmer LTER Rarefaction curve

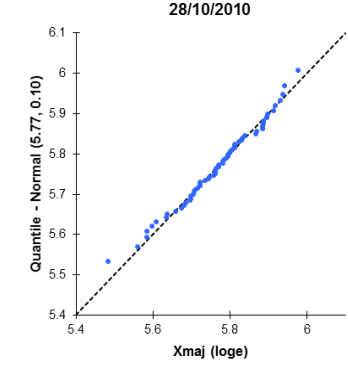
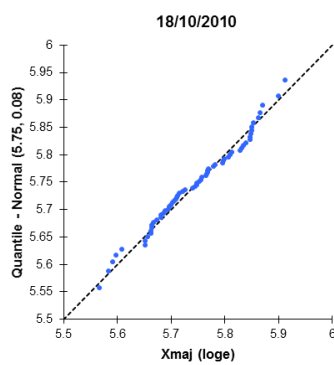
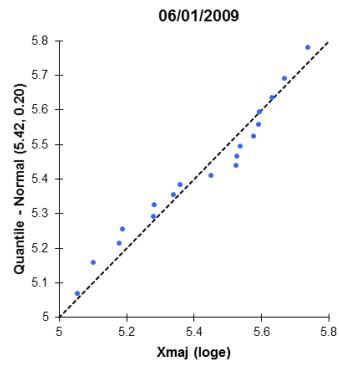
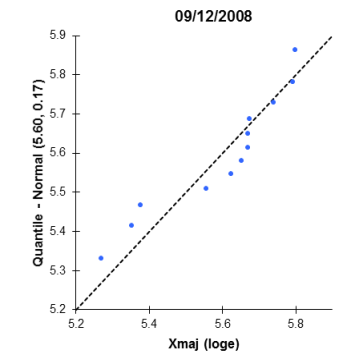
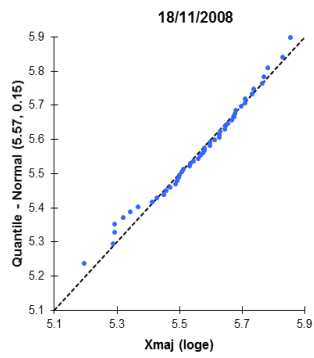
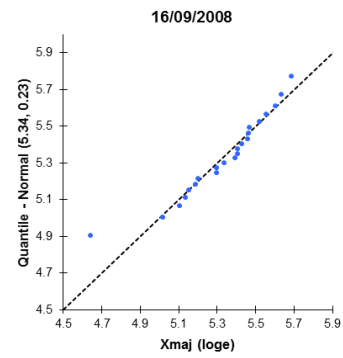
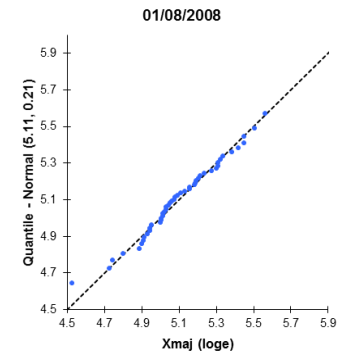
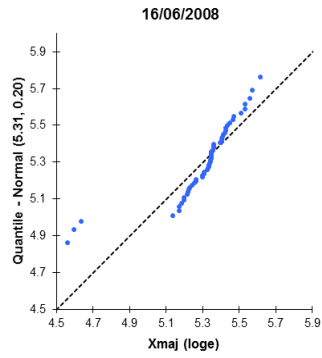
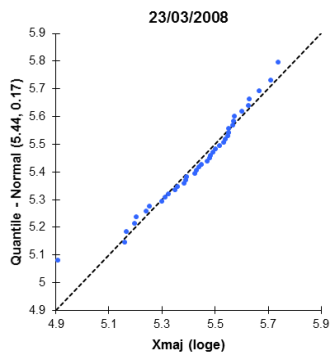
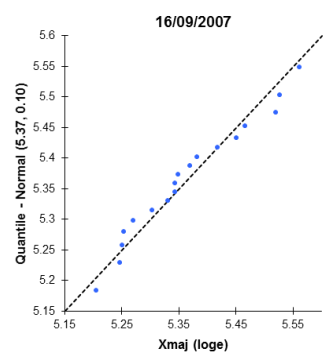
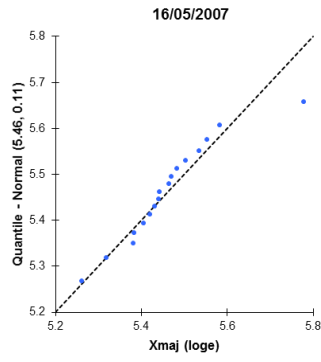
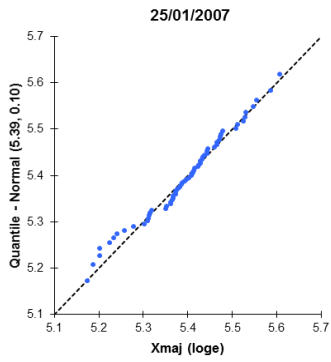
Rarefaction curve to determine number of specimens required per sample for reliable statistical analysis. *Neogloboquadrina pachyderma* maximum diameter variance values from 09/11/2010 sample are plotted against number of foraminifera.

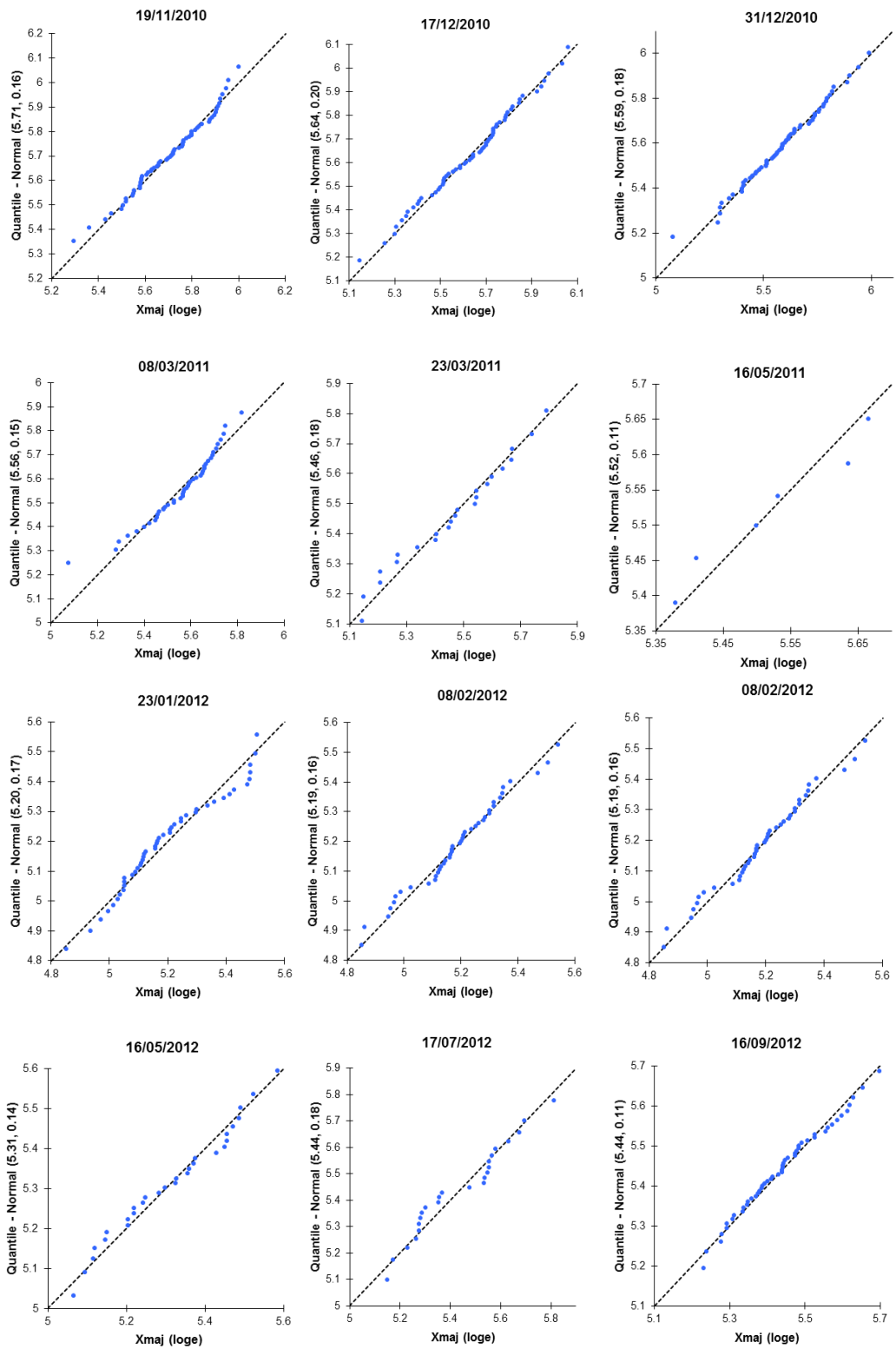


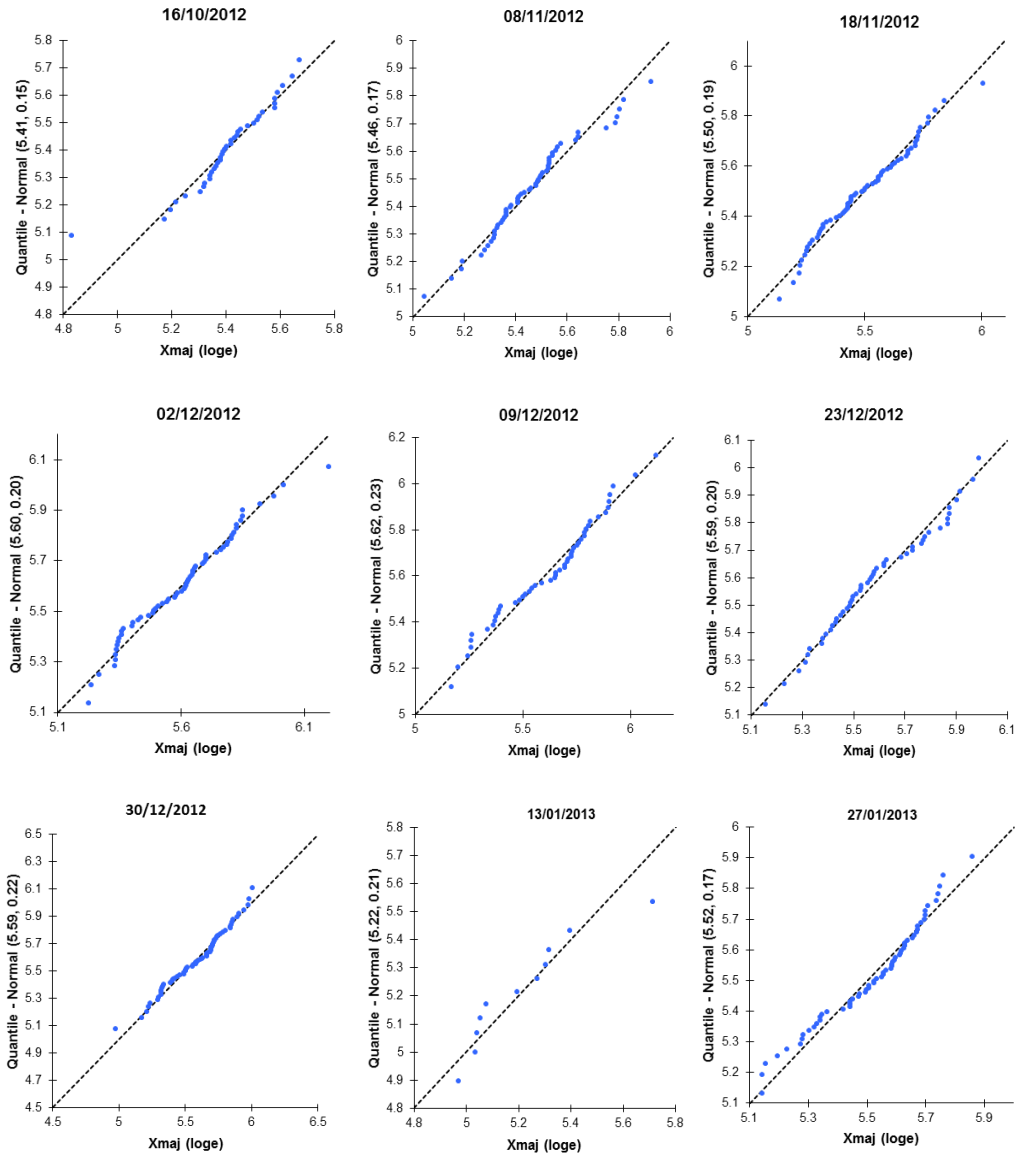
A2. Palmer LTER Normal Probability Plots

Normal probability Q-Q plots showing the distribution of the *Neogloboquadrina pachyderma* log-transformed maximum diameter values against a normal distribution (Chapter 5.2.2.3).









A3. Palmer LTER correlations between Xmaj and PCA F1 score

Correlations between log-transformed maximum diameter values of *Neogloboquadrina pachyderma* and the first principal component score of the PCA analysed on the four size-invariant morphological parameters (circularity ratio, box ratio, elongation ratio and compactness coefficient, Table 5.9

